Eduardo Nuno Borges Pereira

Processes of Cracking in Strain Hardening in Cementitious Composites

UMinho|2012

Universidade do Minho
Escola de Engenharia

Eduardo Nuno Borges Pereira

Processes of Cracking in Strain Hardening in Cementitious Composites

Julho de 2012

Universidade do Minho
Escola de Engenharia

Eduardo Nuno Borges Pereira

Processes of Cracking in Strain Hardening in Cementitious Composites

Tese de Doutoramento
Doutoramento em Engenharia Civil

Trabalho realizado sob a orientação do
Prof. Joaquim António de Oliveira Barros
e do
Prof. Gregor Fischer

Julho de 2012

DECLARAÇÃO

Nome:
Eduardo Nuno Borges Pereira

Endereço electrónico: eduardo.pereira@civil.uminho.pt
Telefone: 253311964 / 963046121

Número do Bilhete de Identidade: 11367403

Título dissertação □/tese □
Processes of Cracking in Strain Hardening Cementitious Composites

Orientador(es):
Prof. Joaquim António de Oliveira Barros
Prof. Gregor Fischer

Ano de conclusão: 2012

Designação do Mestrado ou do Ramo de Conhecimento do Doutoramento:
Doutoramento em Engenharia Civil

Universidade do Minho, ___/___/______

Assinatura: ____

Summary

The recent technological development of a great variety of fibers has been creating new opportunities for the improvement of fiber reinforced cementitious composites (FRCC) as structural materials. Their design nowadays aims at the development of materials with exceptional energy dissipation ability and extreme tensile performance. The intention is to mitigate the limitations of conventional concrete deriving from its quasi-brittle nature, often revealed by the catastrophic collapse of structures during extreme loading events or the early loss of functional properties of structural members due to insufficient durability.

In the past few decades the research carried out in the FRCC field has suggested different approaches to the design of these materials. In particular, when the FRCC is designed to develop strain-hardening in tension and multiple cracking, these materials are typically classified as Strain Hardening Cementitious Composites. Two main properties are often equated when defining the composition and fiber reinforcement used, and these are ductility and strength. The results available in the literature suggest that a trade-off between these two exists. The examples of cementitious composites showing higher tensile strengths are often of moderate ductility, whereas the examples of the most ductile cementitious composites show moderate tensile strengths. In a broad perspective, these composites are generally classified as Ultra High Performance Fiber reinforced Cement-based Composites (UHPFRCC).

In the perspective of structural design, strain-hardening ability in tension is often referred to as the most relevant feature of SHCC materials. The structural problems that can be effectively solved by using these materials are numerous and diverse. Strain-hardening in tension is the result of the ability of the material to develop multiple cracks. This relevant material property represents a dual advantage in engineering applications: while more cracking develops at the same prescribed tensile deformation, the individual crack openings are much smaller, often invisible to the naked eye. The resulting benefits in terms of durability and preservation of functional properties of the structural elements are evident. Conversely, higher energy dissipation ability exists at the level of a single crack, which is multiplied by the large number of cracks typically developed. The result is a material that can be designed

to exhibit high toughness, among other beneficial material features.

The mechanical behavior of FRCC is the result of a delicate balance of multiple factors. The interfacial bonding and fiber pull-out properties, the material parameters of the fibers and of the matrix, the distribution of material flaw sizes in the matrix, the fiber orientation and their dispersion in the matrix play an important role in the resulting composite mechanical behavior. The study of the influence of all these parameters separately is complex, given that they perform in a highly coupled manner. Considerable knowledge exists about the micro-mechanisms and composite behavior of these materials, and a group of experimental testing procedures are already widely accepted as effective to characterize their mechanical behavior. However, this research field is still undergoing significant technological and scientific developments.

This research is focused on the characterization of the cracking processes in SHCC materials. The strategy followed considers mostly the material meso-scale, although micro- and macro-scales are also included, but with less significance. The objective is to contribute to extend the knowledge about the nature of the cracking initiation and propagation mechanisms in these composites, as well as to contribute to the development of the numerical strategies dedicated to the simulation of the structural behavior of SHCC members. To this purpose, alternative testing procedures are proposed to characterize the cracking processes in SHCC. These include alternative specimen geometries, test setups, and the use of innovative techniques of high resolution analysis of deformations, based on digital imaging. The last part of this research is dedicated to exploring classical elasto-plasticity to the simulation of the structural behavior of SHCC under generic tri-axial states of stress. Lastly, some indications for future developments and refinements of the present research are suggested.

Resumo

Os compósitos de matriz cimentícia com endurecimento em tração têm demonstrado desenvolvimentos substanciais no passado recente. As enormes vantagens que representam relativamente aos betões convencionais, ou até mesmo quando comparados com os betões reforçados com fibras convencionais, justificam os intensos esforços de investigação e desenvolvimento que lhe têm sido dedicados.

No passado recente, a investigação no domínio dos materiais compósitos de matriz cimentícia tem seguido diferentes estratégias para a definição da sua composição. Estas estratégias estão fundamentalmente dirigidas para o desenvolvimento de elevado desempenho em tração, nomeadamente através da capacidade de formação de múltiplas fendas e de endurecimento em tração após a formação da primeira fenda. As duas principais propriedades mecânicas que são equacionadas no desenho destes materiais são a ductilidade e a resistência à tração. De acordo com os resultados publicados por diversos autores, parece haver um equilíbrio entre estas duas propriedades, verificando-se que os exemplos existentes de compósitos com maior resistência à tração demonstram moderada ductilidade, e em contrapartida os exemplos de compósitos de maior ductilidade revelam moderada resistência à tração.

Considerando o comportamento estrutural dos materiais compósitos de matriz cimentícia, o endurecimento em tracção é considerado como a propriedade mais importante destes materiais. O tipo de problemas estruturais que podem ser solucionados recorrendo a estes materiais são numerosos, e provavelmente novas aplicações surgirão num futuro próximo, dadas as suas excepcionais vantagens mecânicas. O endurecimento em tracção resulta da capacidade do material para desenvolver múltiplas fendas em tracção, sem fracturar. Esta importante propriedade material representa uma dupla vantagem em termos estruturais: enquanto o número de fendas originadas para o mesmo nível de deformação é muito superior, a abertura de fenda observada é muito inferior aos valores que tipicamente se verificam em betões convencionais, sendo quase sempre invisíveis a olho nu. Deste comportamento material resultam benefícios claros em termos de durabilidade e preservação das propriedades funcionais dos elementos estruturais. Em simultâneo, dado que a capacidade de dissipação de energia durante o processo de fendilhação ao nível de uma única fenda é substancialmente superior,

o elevado número de fendas originado confere a estes materiais elevada tenacidade.

O comportamento mecânico dos compósitos de matriz cimentícia resulta de um equilíbrio delicado de múltiplos factores. As propriedades mecânicas das fibras utilizadas, das fases que constituem a matriz, da interface fibra-matriz, da distribuição de defeitos na matriz, da orientação preferencial das fibras e sua dispersão na matriz, entre outras, todas desempenham um papel crucial nas propriedades mecânicas do compósito resultante. O estudo de todos estes parâmetros de forma isolada é praticamente impossível, dado que todos eles se relacionam de forma bastante complexa. Existem já sólidos conhecimentos quanto à mecânica microestrutural e os procedimentos a seguir na definição da composição dos compósitos de matriz cimentícia. No entanto, dada a complexidade do seu comportamento e a crescente exigência das aplicações a que se destinam, existe ainda uma permanente actualização do conhecimento deste tipo de materiais e um contínuo desenvolvimento das suas capacidades e propriedades mecânicas. O potencial do conceito associado aos materiais de matriz cimentícia não se encontra ainda totalmente explorado, e são previsíveis desenvolvimentos futuros de elevado interesse para a engenharia estrutural.

O presente trabalho insere-se neste contexto de aprofundamento da documentação do comportamento mecânico e dos processos de fendilhação nos materiais de matriz cimentícia. A estratégia definida considera fundamentalmente a meso-escala do material, ainda que a micro-escala e a macro-escala sejam também frequentemente invocadas ao longo deste trabalho. O objectivo principal é o de contribuir para aprofundar o conhecimento actual acerca da natureza dos mecanismos de iniciação e propagação de fendas nestes materiais, assim como de contribuir para o desenvolvimento de estratégias numéricas para a simulação do comportamento estrutural destes materiais. Para este fim, são propostos procedimentos de ensaio alternativos ou complementares aos já existentes e utilizam-se ferramentas inovadoras para a documentação de deformações com elevada resolução, baseadas na análise de imagens digitais. A última parte deste trabalho é ainda dedicada à utilização dos conceitos clássicos de elasto-plasticidade para a simulação do comportamento estrutural destes materiais quando submetidos a estados de tensão tri-axiais. Por fim são enumeradas algumas sugestões para desenvolvimentos futuros, baseadas nos resultados obtidos neste trabalho.

Preface

This thesis was prepared and submitted at the University of Minho in partial fulfillment of the requirements to obtain the *Philosophiæ Doctor* degree in Civil Engineering.

The research reported in this thesis, conducted at the University of Minho and at the Technical University of Denmark from March 2007 to June 2012, deals with the mechanics of cracking in fiber reinforced cementitious composites and is composed of six Chapters and one Appendix.

Guimaraes, 02 July 2012

Eduardo Nuno Borges Pereira

Acknowledgements

The authorship of this thesis is far from being restricted to the single subscriber that appears in the first page. A multitude of enriching and insightful influences have combined, to form the cement that binds together many different pieces of a puzzle left unfinished, and for which I only gave my humble contribution with a few pieces.

The financial support by the Foundation for Science and Technology of Portugal (FCT) is greatly acknowledged, through grant SFRH / BD / 36515 / 2007, funded by POPH - QREN, the Social European Fund and the MCTES, and DTU-Byg for their support as part of this project.

The guidance and insightful advice of my supervisors is greatly acknowledged. Professor Joaquim Barros was the great responsible for this expedition, the one who challenged me from the first moment and kept my spirit unrest until the conclusion. Professor Gregor Fischer was the responsible of the greatest change in my professional attitude, and I deeply thank him for showing me how to focus on the essential and to look for the answers where they can be found. Curiously, after some reflection the benefit was even greater in my personal life.

The administrative staff in the University of Minho was unexcelled. In my absence, everything was always taken care of with great professionalism, and they were always generously available to help.

The supportive and helpful attitude of the technicians of the laboratory and of the IT department at DTU is also acknowledged, because they transformed the impossible into a reality many times and made our tasks more pleasant and fun to carry out. The help and advice of the administrative staff is also greatly acknowledged, for their hospitality and permanent help in transposing obstacles.

To all my friends in Denmark, I leave here my deepest gratitude. Thank you for making me feel like at home, since the first minute I arrived, and to help me

growing a little more as a person. You made me immune to the gray color in the sky and the gray feelings in the heart, and even immune to heavy flying objects!! I felt privileged to meet you and become your friend, and I am sure that the great moments we have spent together, sometimes sweet and other times bitter, will remain in my memory for the rest of my existence.

To my friends in Portugal, I was absent, I know, but I am ready to compensate for the lost time. You kept me inspired, and our common past is a great heritage that I care for and that guides my attitude every day! Thank you for your friendship.

To my family I would like to leave, in these last few lines, my deepest and emotioned 'thank you'. I know I have been a quite difficult person and that I have shared with you the most bitter parts of this great experience. But you, your unconditional support, your patience, your love and care, you made all this happen...you kept me going, no matter how difficult the obstacles were! So, in the end, I did nothing ... you did it all!

Contents

CHAPTER 1

Introduction

1.1 Background

Concrete has been, in existence, a key material in changing forms for thousands of years. Probably the oldest form of concrete ever used was discovered in the floor of a hut in Israel, dated around 7000 BC [Idorn, 1997]. This concrete was prepared by burning limestone to produce quicklime, then mixed with water and stone, and then left to set. The knowledge about lime-based concretes spread to Egypt and Ancient Greece, and later to the Romans. The ancient roman constructions remain, in our days, as inspiring examples of optimal usage of concrete in strong and durable preeminent structures [Neville, 1996]. The word ”concrete” derives from the Latin ”concretus”, which means ”grown together” or ”compounded” [Idorn, 1997].

Concrete occupies a privileged position amongst the most important structural materials of our days. To imagine the modern world and all the complex transportation systems and infrastructures constructed by man without concrete is challenging. Probably the weight of the tradition and the knowledge that came to our days through history is the guarantee of its indisputable position of importance. Even though, concrete is an extremely versatile construction material. Unlike other construction materials, concrete possesses excellent resistance to water, which makes it an ideal material for building structures to control, transport and store water. Furthermore, the plastic consistency of the freshly produced concrete allows the easy forming of structures with complex shapes and sizes. It is also a cheap and readily available material, since its principal components are inexpensive and commonly accessible in most parts of the world [Mehta and Monteiro, 2006].

As a composite, concrete may be considered as a three-phase material, where a cement-matrix phase, composed of water, smaller particles ($D_n < 125\ \mu$m) and cement, binds the larger particles belonging to the aggregate phase. The third phase consists of the interfacial transition zone (ITZ), with special properties resulting from the different conditions affecting the packing of particles, the wall effects and the short range interaction forces occurring in particulate suspensions. The mechanical properties of the composite are the result of the coupled behavior of these three phases. If the properties of the main components solely are considered (cement matrix and aggregates) many of the concrete properties, either in terms of deformability or strength, do not follow the laws of mixtures[Mehta and Monteiro, 2006]. The complete understanding of this behavior is complex, and requires a closer look to different scale-sizes of the material structure, specially the important role of the interfacial transition zone separating aggregates and the cement paste. Different properties and features of the concrete mechanical behavior can be explained at distinct scale-sizes, from the atomic scale to the largest civil construction scale-size [van Mier, 1997], which is often classified as a multi-scale character.

Concrete is known to be a tension-weak material, with a tensile strength much lower than the compressive strength (typically 10%) and very limited tensile strain capacity. Cracks and internal flaws exist even prior to loading, and the mechanical behavior of concrete under distinct loading conditions is mostly governed by the influence of these initial flaws and weak regions on the initiation and propagation of cracks. Also, the great difference between the nature and mechanical properties of aggregates and the cementitious materials in the concrete matrix induce important stress gradients at the transition regions between the different phases. The moderate tensile hardening prior to the attainment of the ultimate tensile capacity and the subsequent rapid tensile softening characterize the so-called quasi-brittle behavior of concrete [Karihaloo et al., 1993; Landis and Shah, 1995]. The original use of fibers in concrete mixtures was intended to delay and control the onset and propagation of cracks. The first applications of fibers to building materials can be traced back to the Egyptians, by using straw to reinforce mud bricks, and evidence exists of the use of asbestos fibers to reinforce clay pots about 5000 years ago [Mehta and Monteiro, 2006]. But it was over the past 40 years that the use of fiber reinforced cements and concretes has been steadily increasing. The first widely used cementitious composite was the asbestos cement, which was developed in the 1900's with the invention of the Hatschek process. Since then, a wide variety of fibers have been used with hydraulic cements, such as steel, glass, carbon, Kevlar, polypropylene, polyethylene, polyvinyl alcohol, and other natural fibers like sisal, jute or cellulose [Bentur and Mindess, 2006]. Although initially the intention was to significantly increase the tensile and flexural strengths of concrete, over time the developed fiber reinforced mortars and concretes offered little improvement in strength when compared with the corresponding mixtures without fibers, mostly due to the difficulties associated with the incorporation of sufficient volumes of fibers[Mehta and Monteiro, 2006]. Only in recent years a number of innovative fiber reinforced formulations have shown the ability to significantly improve the strength and deformability of cement-based materials, when compared with the traditional quasi-brittle behavior of concrete. SIFCON was first proposed [Lankard, 1984] to overcome the difficulties encountered in dispersing enough amounts of fibers in the mixtures to significantly improve their tensile properties. Interesting improvement of the tensile strength and deformability were achieved using this procedure, although at the expense of the addition of fiber volumes exceeding 15%. Tensile strengths of 35 MPa at a tensile strain of 1.2% have been reported with SIFCON mixtures containing a fiber volume of 17% [Naaman, 1992].

1.1.1 Ultra High Performance Fiber Reinforced Cement-based Composites (UHPFRCC)

The motivation of the first applications of fibers to cementitious matrices was the enhancement of the strength of concrete and the mitigation of the undesired effects of concrete brittleness on the material behavior. The distinction between the concepts of material strength and material toughness was not clear, and the mixture compositions were simply the result of an attempt to maximize the fiber content. Over time, the developed fiber reinforced mortars and concreteswere unable to significantly improve strength when compared with the corresponding mixtures without fibers. Soon it became generally recognized that the most significant effect of fiber addition was the enhancement of toughness [Li, 2002; Mehta and Monteiro, 2006]. With the gradual extending of the Fracture Mechanics concepts to the cracking behavior of concrete, and in particular to the Fiber Reinforced Concrete (FRC) mechanics, significant break-through improvements were achieved in characterizing and designing fiber reinforced cementitious composite mixtures. The broader concept of Fiber Reinforced Cementitious Composites (FRCC) is nowadays conveniently used, while including the wide variety of different cementitious matrices existing in the more recently developed FRCC materials. The ability of fibers to significantly increase tensile ductility and strength of FRCC, whether in the shape of continuous or discrete fibers, has been recognized mainly after the work of Aveston [Aveston et al., 1972]. In recent years, carefully designed mixtures of fiber reinforced cementitious composites have been showing the ability to develop strain-hardening behavior in tension and considerable tensile deformation, with reasonable amounts of randomly oriented discrete fibers. The term high performance fiber reinforced cement composite (HPFRCC) was first introduced by [Reinhardt and Naaman, 1992] to define the materials that exhibit a significant post-cracking strain hardening phase and show considerable deformability, independently of the tensile, flexural or compressive strengths. The term high performance was employed earlier to characterize concretes with certain improved functional properties, such as fire resistance, freeze-thaw resistance, improved density, abrasion resistance, chloride penetration resistance, limited shrinkage or creep, etc. In the case of fiber reinforced concretes this term was used to distinguish a special class of FRCC, in which the tensile behavior enhancement resulting from the fiber addition was superior to the typically obtained effect of toughness increase. The general classification was proposed to distinguish three main classes of FRCC depending on the tensile response of these materials [Naaman, 2008]:

- The class that includes the composites exhibiting hardening in direct tension (HPFRCC);
- The class including the composites that, although not exhibiting hardening in direct tension, show deflection-hardening response, the Deflection Hardening Fiber Reinforced Cement Composites (DHFRCC);
- The class that includes the composites that merely show moderate toughness increase when compared to unreinforced mixtures, showing deflection softening response.

In Figure 1.1 the critical fiber volume in tension, $\mathrm{V}_{\mathrm{f,crit}}^{\mathrm{tension}}$, represents the minimum amount of fibers in the FRC mixture leading to a tensile-hardening response. The critical fiber volume in bending, $\mathrm{V}_{\mathrm{f,crit}}^{\mathrm{bending}}$, represents the minimum amount of fibers in the mixture leading to a deflection-hardening response.

Different types of HPFRCC may be found in the literature, examples of mixtures developed over time with different types of materials and showing distinct mechanical responses, such as Ductal® [Orange et al., 1999] or CERACEM [Maeder et al., 2004], as a result of industrial initiatives. Other representative examples developed in academic or other research institutions are CARDIFRC® [Benson and Karihaloo, 2005], high performance multimodal fiber reinforced cement composite (HPMFRCC) [Rossi, 1997] or later $\mathrm{CEMTEC}^{®}_{\mathrm{multiscale}}$ [Boulay et al., 2004], Hybrid-Fibre Concrete (HFC) [Marković, 2006] , Ultra High Performance Fiber Reinforced Concrete (UHPFRC) [Wille et al., 2011] and ECC [Li et al., 2001]. The FRCC material design is nowadays aiming at the development of materials with exceptional energy dissipation ability and enhanced tensile behavior. The aim is to mitigate the limitations of conventional concrete deriving from its quasi-brittle nature, often revealed by the catastrophic collapse of structures during extreme loading events or the early loss of

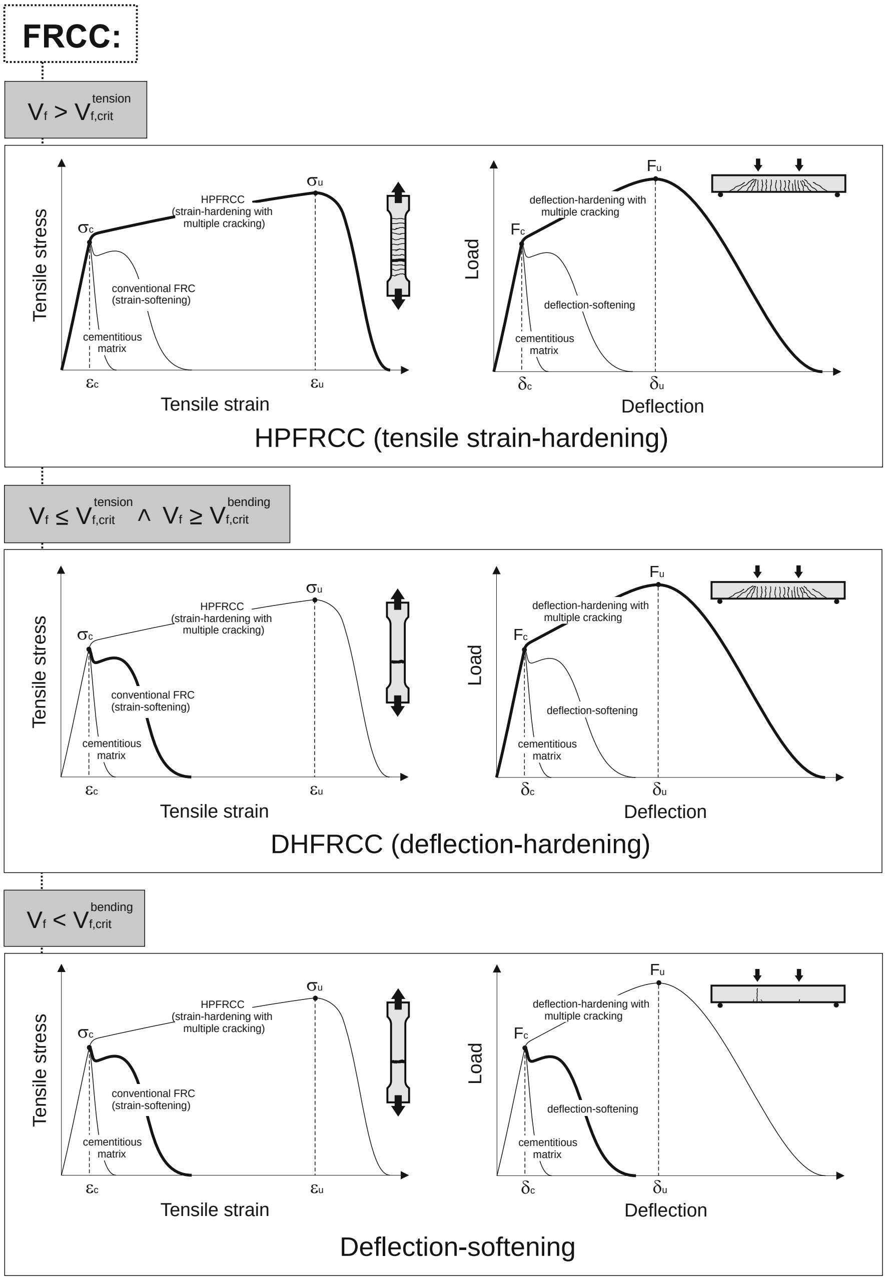

Figure 1.1: Classification of FRCC type according to the material tensile behavior in direct tension and in bending.

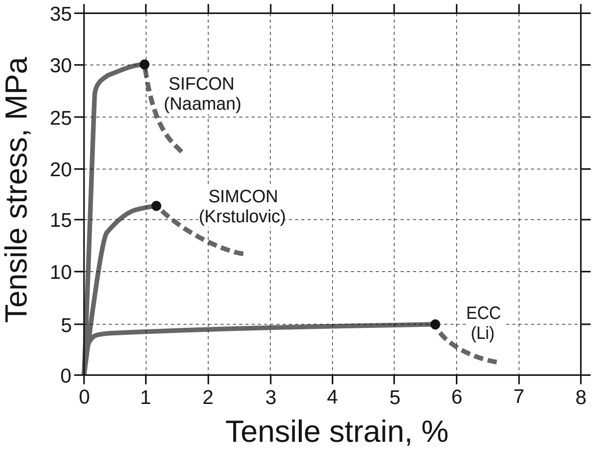

Figure 1.2: Distinction of different types of UHPFRCC and illustration of the trade-off between tensile strength and ductility [Naaman, 2008].

functional properties due to insufficient resilience or durability. The examples above referred respond to these challenges in different ways. The two main characteristics that distinguish the tensile behavior of the different examples of UHPFRCC referred are the tensile strength and the ultimate tensile strain. In general, a trade-off seems to exist between these two properties [Wu and Li, 1994; Naaman, 2008], as shown in Figure 1.2 where three representative tensile responses of distinct FRCC types are presented: SIFCON [Naaman, 1992], SIMCON [Krstulovic-Opara and Malak, 1997] and ECC [Li, 2003].

1.1.2 Engineered Cementitious Composites (ECC): concept and applications

Engineered Cementitious Composites (ECC) is a class of cement based materials typically reinforced with Polyvinyl Alcohol (PVA) fibers and containing fiber volume fractions below 2%. ECC consists of a special group of UHPFRCC showing high tensile strain hardening ability (between 3% and 7% of ultimate tensile strain) at ultimate tensile strengths between 4 and 6 MPa [Li, 2002, 2003]. Pseudo-strain hardening behavior in tension exhibited by ECC is the consequence of the development of multiple cracks under tensile loading, and of tensile hardening at the level of a single crack. This material property represents a dual advantage in engineering applications: while more cracks develop at the same tensile deformation, the individual crack openings are significantly smaller. The result of this multiple cracking behavior is enhanced durability and improved preservation of functional properties at structural level. In addition, high energy dissipation ability exists at the level of a single crack, which is amplified by the large number of cracks typically developed. ECC materials are therefore designed to exhibit high toughness and significant tolerance to damage in tension. Compressive strengths between 40 MPa and 80 MPa can be obtained, depending on the mixture composition. The utilization of ECC as a replacement of conventional concrete in structural elements was demonstrated to significantly improve the mechanical performance of these structures, by considerably delaying the loss of structural integrity due to excessive deformation and preventing brittle failure [Fischer and Li, 2003b, 2007; Leung et al., 2007; Parra-Montesinos and Wight, 2000].

The typical pseudo-strain hardening behavior obtained when ECC specimens are tested in direct tension is presented in Figure 1.3 [Lin and Li, 1997; Fischer and Li, 2003a].

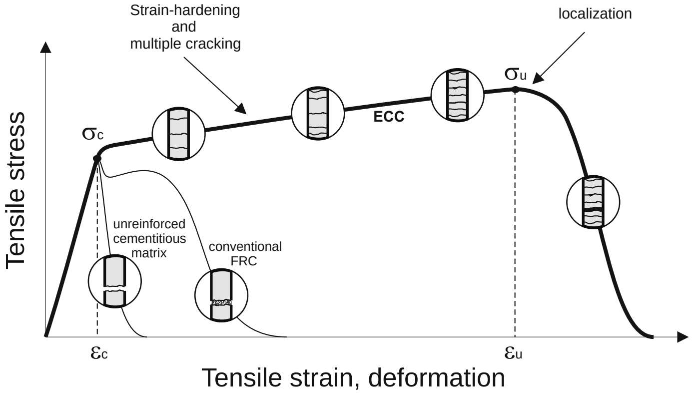

Figure 1.3: Typical pseudo-strain hardening behavior and multiple cracking evolution of ECC materials tested in direct tension.

The composite mechanical behavior in tension of ECC is the result of a delicate balance of multiple factors. The interfacial bonding and fiber pull-out properties, the material parameters of the fibers and of the matrix, the distribution of flaw sizes in the matrix, the fiber orientation and their dispersion in the matrix, these all play an important role in the resulting composite mechanical behavior. A performance oriented design procedure, based on micro-mechanics and fracture mechanics, was proposed to achieve saturated pseudo strain-hardening behavior, before the eventual localization and tensile rupture. It is based on two performance criteria, which are measures of energy exchange during steady state flat crack propagation and stress level to initiate micro-cracks [Li et al., 2002; Li, 2003; Kanda and Li, 2006]. These concepts will be further explored in Chapter 2.

In recent years ECC has been utilized in large scale applications. The significantly higher cost of the material when compared to conventional concrete has been limiting a more widespread utilization of ECC as a simple replacement of conventional concrete. However the full potential of the material is not explored when the simple replacement of conventional concrete is considered. ECC utilization is particularly advantageous in special situations where ductile/deformable materials are required, tight control of crack growth and enhanced resistance to bursting or spalling, or significant corrosion protection are required. One example is the application of ECC to construct, repair or replace the mechanical expansion joints between simply supported spans of bridges and viaducts, as shown in Figure 1.4.a. The application of ECC in this first case led to the significant reduction of the intensive deterioration caused by traffic loading, resulting in reduced maintenance needs and lower repair costs during service life [Lepech and Li, 2009; Làrusson and Fischer, 2011]. In Figure 1.4.b the 972 m long cable-stayed Mihara Bridge in Hokkaido, Japan, is shown. A 40 mm thick continuous ECC overlay was applied on top of the steel deck during construction, after the revision of the design requirements and to increase fatigue resistance [Kunieda and Rokugo, 2006; Li, 2011]. Multiple applications of ECC can also be found on retrofitting water-retaining structures. ECC protection layers were applied, either directly or by projection, to repair cracked or deteriorated surfaces of concrete dams, retaining walls and water channels [Rokugo et al., 2009]. In a different direction, extrusion processes especially designed to the extrusion of pipes made of fiber reinforced cementitious materials have been developed using ECC [Stang and Li, 1999]. The process was successfully used in the production of pipelines, and the properties obtained were competitive when compared to the alternative solution, made of plastic.

The ductile behavior of ECC can also be effectively utilized to reduce the risk of catastrophic collapse of structures. One example is the use of ECC in the construction of infrastructures located at areas where seismic activity is relevant. ECC can be adopted to increase shear strength, displacement capacity and damage tolerance in members subjected to large inelastic deformations during seismic events. Applications include members with shear-dominant response such as beam-column connections, low-rise walls, coupling beams and flexural members subjected to large displacement reversals [Parra-Montesinos, 2005]. In Japan, ECC has been recently utilized in high-rise buildings, to produce hybrid reinforced ECC coupling beams, dampers and other structural elements (Figure 1.6) destined to provide the structure with the necessary energy dissipation ability during seismic events. Two examples are the 41-story Nabeaure Yokohama tower [Li, 2011] and the 27-story Glorio Poppongi

a) b)

Figure 1.4: Structural applications of ECC materials: a) link slab as continuous joint in simply supported viaduct and b) ECC overlay in the cable-stayed Mihara bridge.

residential high-rise building in central Tokyo [Kunieda and Rokugo, 2006; Rokugo et al., 2009]. In this last example the precast coupling beams were 500 mm wide, 900 mm high and 1650 mm long (Figure 1.6). The coupling beams were designed to withstand drifts of 1/30 under severe earthquakes and remain reusable without considerable repair after the earthquake [Rokugo et al., 2009].

1.2 Research significance and objectives

The understanding of the tensile behavior of strain hardening cementitious composites has been the subject of numerous research studies for the past three decades. Since the work of Aveston, Cooper and Kelly [Aveston et al., 1972] dealing with the analytical study of the conditions necessary to the attainment of multiple cracking in fiber reinforced brittle matrix composites, it was realized that the typical quasi-brittle behavior of concrete could be altered and ductile failure in tension could, in principle, be obtained in a systematic fashion. The addition of fibers into cement-based composites could be more ambitious than the simple improvement of the material toughness.

As a very desirable material property, tensile strain hardening ability became the utmost challenge in FRCC development. As described previously, pseudo-strain hardening ability and significant tensile deformability were successfully achieved using relatively low fiber volume fractions, exemplified with ECC. To achieve this behavior, the design process of strain hardening cementitious composites was meticulously studied. In general, this study is based on two criteria, one mechanical and the other

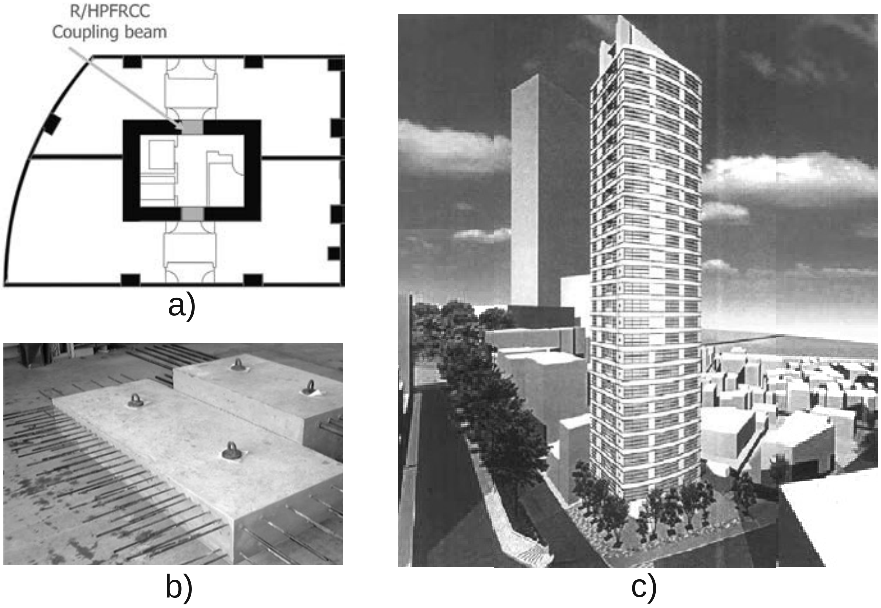

Figure 1.5: Structural application of ECC materials in the construction of coupling beams to dissipate energy during extreme seismic events: a) position of the coupling beams in the building structure connecting the two opposite rigid core halfs, b) image of the pre-fabricated coupling beams and c) image of the Glorio Poppongi residential high-rise building where the coupling beams have been applied.

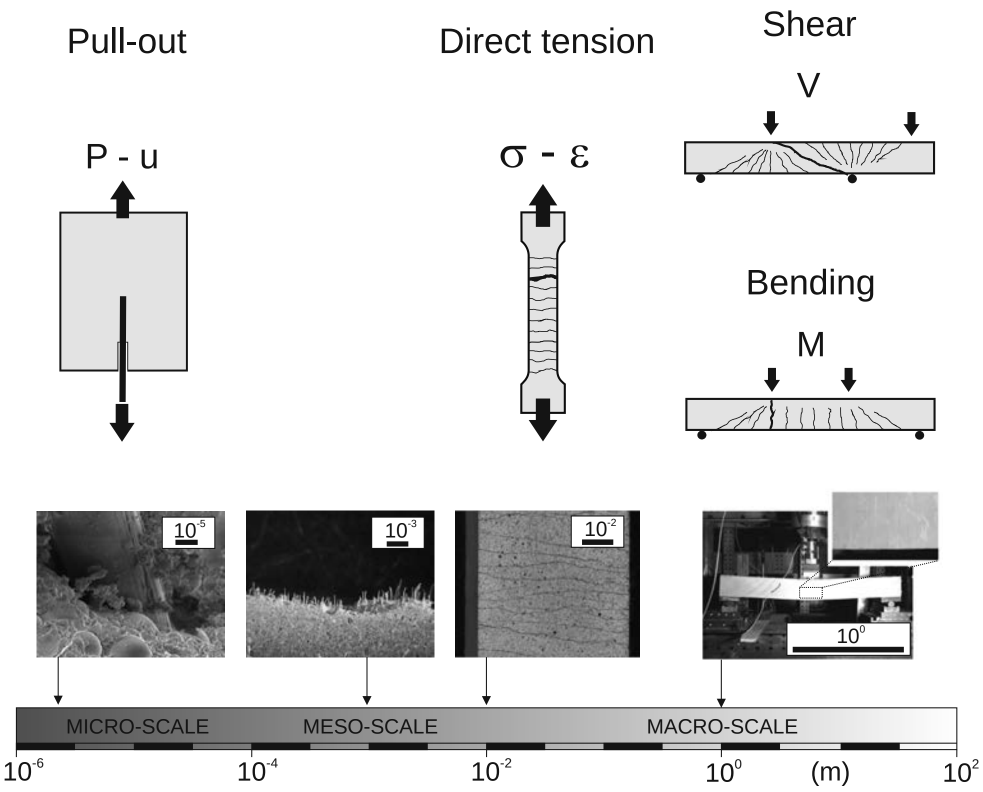

Figure 1.6: Material multi-scale nature of SHCC and significant tests used to characterize the mechanical behavior.

energetic. These concepts will be further explored in the next chapter, but essentially the mechanical criterion is met if the material is able to withstand increasing tensile stresses after cracking, meaning that the admissible traction at the fibers bridging the cracks formed must exceed the matrix cracking stress. The energetic criterion is met if, in a broad sense, the complimentary energy available as a result of fiber bridging at steady state propagating crack exceeds the energy required to propagate the crack in the matrix, that is to say, the matrix fracture toughness [Li, 2003]. The design of SHCC and the attainment of pseudo-strain hardening in tension are therefore significantly dependent on the properties of the fibers, of the cementitious matrix, of the fiber-matrix interaction and of the optimal combination of all these properties. Furthermore, assuming that short discontinuous fibers are used, fiber distribution and orientation also contribute considerably to the tensile responses obtained.

The fiber bridging stress-crack opening curve is a central element of information in the composite design process toward pseudo-strain hardening in tension [Kanda and Li, 1999; Yang et al., 2008]. The composite material parameters that are more important to the definition of the optimal combination of fiber types and of the cementitious matrix compositions are revealed in a particularly objective way by the tensile stress-crack opening curve. The most significant information required to define the potential of a certain composite to develop pseudo-strain hardening in tension can be found at the fiber bridging stress-crack opening behavior, by verifying the mechanical and the energetic criteria, as previously referred. Because SHCC materials are designed to develop multiple cracks in tension, the characterization of the fiber bridging stress-crack opening behavior is typically carried out indirectly. At the micro-scale level, the pull-out behavior of single fibers at different angles is carried out to construct and calibrate micro-mechanical models that describe the fiber bridging stress-crack opening behavior[Betterman et al., 1995; Naaman et al., 1991; Leung and Li, 1992; Lin and Li, 1997; Yang et al., 2008]. The analytical description of the fiber-matrix interaction, mainly of the distribution of shear stresses originated in the fiber due to the matrix-fiber load transfer at cracking, is a requirement to the analytical study of the multiple cracking process in fiber reinforced cementitious composites[Li and Leung, 1992; Kanda and Li, 2006]. At the macro-scale level, the mechanical behavior of the composite in direct tension is typically characterized, as well as its ability to withstand an increasing tensile load while multiple cracks develop. Different micro-mechanical models have been proposed over time and, provided that the correct parameters are adopted, these models have been showing satisfactory correlation with the results obtained from the direct tension tests [Yang et al., 2008]. Nevertheless, there is a significant separation between the two scales involved in this process, at the level of which the composite behavior is typically characterized. The alternative mechanical characterization of SHCC materials at the meso-scale level can contribute with additional information about the micro-mechanics and the fracture process. In particular, the material characteristics at the meso-scale level are essential to evaluate the efficient utilization of the new types of fibers, binders and admixtures that are developed every day, as well as to broaden the quantity and quality of the information about the mechanical behavior of these composites.

The main objective of this research is to explore the mechanical features of the tensile behavior of SHCC materials at the level of the meso-scale, particularly those related with the initiation and propagation of cracks. The macro-scale tensile behavior of SHCC is intimately related to the micro-mechanisms of the cracking process in the composite, in particular to the interaction between the tension-weak and brittle cement-based matrix, and the discrete deformable and tensile-strong linear thin reinforcement elements, the fibers. The typical approach adopted in the analysis and design of SHCC materials is focused on the study of the material properties both at the micro-scale and at the macro-scale. The effective conceptual linkage of these two scales has resulted in the successful design of composite mixtures exhibiting high tensile deformability, when the departing quasi-brittle behavior of the conventional cement-based composites is considered. However, this process may be enriched by incorporating additional information about the cracking process, when analyzed at the meso-scale level. In addition, the central role occupied by the tensile stress-crack opening behavior of fiber reinforced cementitious composites in the entire design process motivates the development of an appropriate experimental procedure to characterize objectively the tensile stress-crack opening behavior of the composite. In this study, the conditions necessary for assessment of the tensile stress-crack opening behavior at the level of a single crack in direct tension were studied, with the simultaneous documentation of the initiation and propagation of the formed cracks in the composite. Furthermore, considering the permanent evolution of the fiber technology, the rapid development of new binders and admixtures, and the increasing demand for economically and environmentally efficient concretes, the present research also explores the possibility of using alternative types of fibers and the combination of different fibers to improve the tensile performance. The influence of each type of fiber on the mechanisms of cracking is investigated at the meso-scale level, and the possible synergistic effects resulting of the combination of different fiber types is explored. The influence of altering the cementitious matrix composition is also investigated. Eventually, the approach suggested in this research aims at contributing to the design of cementitious matrix composites by providing an objective framework to assess the most important material properties that influence its proneness to developing pseudo-strain hardening in tension. The procedure followed also tries to partially avoid the complex weighing of all the material parameters and redundancy typically involved in the SHCC design process. The information about the tensile behavior of SHCC is explored further, while the research is directed especially towards the meso-scale, and therefore positioning at the interval existing between the typical micro-scale and macro-scale analysis of SHCC materials. At the macro-scale level, the present research also tries to contribute to the development of numerical tools and procedures directed to a better usage of the important tensile properties of SHCC materials. Considering the specific material properties of SHCC, in this research the approach adopted focuses mainly on the utilization of numerical plasticity principles in the simulation of the 3D behavior. Although the advantages and weaknesses of numerical plasticity models are well known, the present research aims at verifying the extent to which these models can contribute to the effective analysis of structures conceived with SHCC, and as such, to contribute to an integrated material and structural design with SHCC materials.

1.3 Thesis outline

Chapter 1: Introduction:

Fiber reinforced cementitious composites exhibiting pseudo-strain hardening in tension are a relatively recent type of cement-based composite. However, the research carried out over the past 40 years towards the development of affordable and sustainable mixtures is extensive. Although the intention is not to produce a thorough compilation and review of all the research carried out, in the past half of a century, related to the characterization and design of fiber reinforced cementitious composites, *chapter one* was dedicated to the necessary general overview of the development of fiber reinforced cements and concretes. The mechanical characterization of cement-based composites, mainly of their mechanical properties in tension was particularly emphasized. Since the development of cement-based composites took many different directions and led to different material design philosophies, the approach followed gradually focused on the aspects related to the type of materials studied in the present research. Therefore the introduction presented in *chapter one* is intended to locate the research of SHCC materials in the context of the vast world of concrete, and to contextualize the objective of the present research.

Chapter 2: Characterization of tensile behavior:

The process of designing Strain Hardening Cementitious Composites (SHCC) is mainly driven by the need to achieve a certain performance in tension. The formation and further development of cracking under tensile loading strongly influences the mechanical behavior of SHCC in tension. Consequently, the assessment of the tensile stress-crack opening behavior of these materials is of great significance. The characterization of the tensile response of SHCC is typically based on the direct tension testing of coupon, dog bone or dumbbell-shaped specimens. The experimental procedure mostly consists of characterizing the tensile stress-strain response of these types of specimens under an imposed constant displacement rate. The results reported by several researchers mainly focus on the typical tensile stress-strain responses, together with the identification of the number of cracks, crack spacing and crack width distributions until failure is reached. Alternative experimental procedures are based in bending tests and inverse analysis to derive indirectly the significant material constitutive parameters. Although the information collected with these experiments approaches well the main features of the tensile behavior of SHCC, these procedures seem to lack sensitivity to a group of composite parameters that play a major role in the composite mechanical behavior. As mentioned earlier, the typical experimental and analytical description of SHCC seems to rely on two distinct material scales, which are the micro-scale and the macro-scale. *Chapter two* addresses the characterization of the tensile behavior of SHCC by investigating an alternative procedure to characterize the tensile response of SHCC in terms of the tensile stress-crack opening behavior. The particular details of the experimental procedure and test setup used to evaluate the tensile stress-crack opening behavior for these materials are discussed, considering that they are designed to prevent the formation and localization of a single crack. In the experimental program, specimens of fiber reinforced cementitious composites are notched and loaded in direct tension, with the purpose of inducing the formation of a single crack during the entire loading sequence. While deriving the crack behavior in terms of stress-crack opening, the procedure allows the quantitative and objective evaluation of different aspects of the composite behavior, including the matrix fracture properties and the fiber-matrix interaction mechanisms. The deformations occurring during tensile loading are also examined using a digital image analysis technique to gain detailed insight into the crack formation, propagation and opening stages. With this image analysis technique the achievement of a single crack over the entire loading sequence is confirmed. The derived tensile stress-crack opening relationships of different types of SHCC are utilized to analyze and compare the effect of various relevant composite parameters, including the type and nature of the fiber reinforcement, the properties of the cementitious matrix and the influence of fiber-matrix interactions on the resulting tensile behavior. The characterization of the tensile behavior of SHCC in terms of the tensile stress-crack opening behavior contributes to bridge the information typically collected at the micro-scale and at the macro-scale levels, with the characterization of cracking processes at the meso-scale level.

Chapter 3: Fracture properties and crack propagation in cementitious composites:

The initiation and propagation of cracking in concrete and other cementitious materials is a governing mechanism for many physical and mechanical material properties of these materials. The observation of these cracking processes in concrete is typically carried out at discrete locations and often using destructive methods, after the cracking process has occurred. The alternative non-destructive methods are often either not precise enough or experimentally too demanding. In the literature different methods are proposed to characterize the cracking process occurring in cementitious composites and other brittle or quasi-brittle materials. Special attention is often dedicated to the region of the material located ahead of the tip of the propagating crack, which establishes the transition between the fully open crack and the intact bulk material. In *chapter 3*, the use of an image analysis procedure to capture the crack initiation and propagation process is described, which utilizes digital images of the concrete surface while undergoing the cracking process. The results obtained with this method have shown that it is possible to monitor relatively small displacements on the specimen surface, independently of the scale of the representative area of interest. The formed cracks are visible at relatively small crack openings, allowing the thorough investigation and analysis of the cracking processes in concrete. The fracture process zone encloses relevant mechanisms that explain the quasi-brittle behavior of cementitious composites. It is an important concept in non-linear fracture mechanics and in the simulation of cracking processes. The use of fibers as reinforcement may alter the crack initiation and propagation processes. In particular, the use of fibers as reinforcement may alter the cracking process at the level of the micro-cracked region that establishes the transition between the tip of the fully open crack and the intact bulk material ahead of the crack tip. A better understanding of the micro-cracking mechanisms taking place at the level of the micro-cracked region of the fracture process zone is therefore relevant for the optimized design of these materials, as well as for the simulation of their mechanical behavior. In this chapter, the use of an image analysis procedure to capture the crack initiation and propagation process in concrete and other cementitious composites is described. The procedure utilizes high resolution digital images of the surface of the specimens, while undergoing the cracking process, to determine the continuous development of the displacement fields at the surface of the specimen. Furthermore, the tensile stress-crack opening curves obtained in chapter two are utilized to simulate the mechanical results determined in this chapter with a different test setup. To this purpose, a finite element model is constructed and the likely crack plane is simulated using interface elements. The traction-separation laws assigned to the interface elements are derived from the tensile stress-crack opening curves obtained in chapter two. Eventually, the documented crack patterns were essential to explain the results obtained. The utilization of the tensile stress-crack opening relationships to derive the traction-separation laws of the interface elements has led to satisfactory approximations of the experimentally obtained results. However, the numerical model was unable to simulate fully the complex cracking processes observed. Nevertheless, the single crack tensile stress-crack opening results obtained in chapter 2 were shown to be relevant to the numerical modeling and simulation of SHCC structural behavior.

Chapter 4: Single and hybrid fiber-type reinforcement:

The simultaneous use of different types of fibers as reinforcement in cementitious composites is typically motivated by the underlying principle of a multi-scale nature of the cracking process in fiber reinforced cementitious composites. It is hypothesized that, while undergoing tensile deformations in the composite, the fibers with different geometric and mechanical properties restrain the propagation and further development of cracking at different scales, from the micro- to the macro- scale. Although the beneficial outcome and the micro-mechanics of a multi-scale fiber reinforcement may be intuitively understood and favored, the explicit evidence of the synergistic mechanisms established in fiber reinforced cementitious composites when hybrid fiber reinforcements are used is still searched. The optimized design of the fiber reinforcing systems requires the objective assessment of the contribution of each type of fiber to the overall tensile response. Possible synergistic effects resulting from particular combinations of fibers need to be clearly identified. In *chapter four*, the response of different fiber reinforced cementitious composites is evaluated by assessing directly their tensile stress-crack opening behavior. The efficiency of hybrid fiber reinforcements and the multi-scale nature of cracking processes are discussed based on the experimental results obtained. The micro-mechanisms underlying the contribution of different fibers to restrain cracking at different scales are investigated using the single crack tension test. The benefit of adopting fibers with different geometries and of different natures is discussed, based on the analysis of the tensile response at different scales of the cracking process.

Chapter 5: Plasticity-based constitutive modeling:

The improvement of the tensile performance of SHCC has been, over time, motivated by the frequent and unwelcome secondary effects originated by the typical quasi-brittle behavior of conventional concrete. Crack width was assumed by several standard codes and design norms as the main parameter governing the proneness of reinforced concrete to several degradation mechanisms. The development of SHCC has achieved outstanding levels of material performance in tension, as well as of other important functional properties. This new mechanical behavior within the family of cement-based composites has recently motivated the development of new constitutive and structural modeling techniques, aiming at taking full advantage of the special material properties demonstrated by SHCC materials in structural applications. In *chapter five* this thematic is approached within the framework of FEM-based elasto-plasticity. In general, the material behavior of concrete and other granular materials is highly nonlinear and greatly dependent on the confining stresses. The CEB-FIP Model Code [Comite Euro-international du Beton, 1993] recommends the use of a four-parameter failure criterion to estimate the strength of concrete under multi-axial states of stress. This failure criterion is also known as the Ottosen failure criterion, and it captures with considerable accuracy the failure of these materials, as experimentally demonstrated by several researchers. The estimation of concrete strength takes into account the effect of the increase in the confining stresses, which is thought to be of significant importance in this type of materials. In order to simulate the monotonic quasi-static multi-axial behaviour of concrete, one possible strategy is to integrate hardening parameters and the corresponding evolution laws in this failure criterion, assuming isotropic behavior. In chapter five, the CEB-FIP Model Code [Comite Euro-international du Beton, 1993] law proposed to describe the uni-axial nonlinear behavior of concrete is utilized to derive the hardening function. In this particular case the loading surface is not explicitly defined as a function of the hardening parameter, in contrast to other common isotropic models. The formulation of the model is presented, including the implementation of the implicit backward Euler algorithm and the derivation of the algorithmic and the consistent tangent elasto-plastic matrices. The general behavior of this model is investigated by simulating the monotonic multi-axial loading of concrete elements. Finally, some conclusions are drawn concerning the applicability of plasticity-based constitutive modeling to support the analysis of the structural behavior of SHCC applications.

Chapter 6: Concluding remarks:

In this last chapter the main findings of this research are summarized. The unfinished nature of this research also leaves open issues for further developments, and some suggestions are left for future research in the topic.

Bibliography

Aveston, J., Cooper, G., and A., K. (1972). Single and multiple cracking. In *The properties of fibre composites*, pages 15–24, Guilford UK. National Physical Laboratory, IPC Scinece and Technology Press.

Benson, S. and Karihaloo, B. (2005). Cardifrc® - development and mechanical properties. part iii: Uniaxial tensile response and other mechanical properties. *Mag Concr Res*, 57(8):433–443.

Bentur, A. and Mindess, S. (2006). *Fibre reinforced cementitious composites*. Modern concrete technology series. Taylor & Francis.

Betterman, L., Ouyang, C., and Shah, S. (1995). Fiber-matrix interaction in microfiber-reinforced mortar. *Advanced Cement Based Materials*, 2(2):53–61.

Boulay, C., Rossi, P., and Tailhan, J.-L. (2004). Uniaxial tensile test on a new cement composite having a hardening behaviour. In Prisco, M., Felicetti, R., and Plizzari, G., editors, *PRO 39: 6th International RILEM Symposium on Fibre-Reinforced Concretes (FRC) - BEFIB 2004*, volume 1 of *Fibre-reinforced Concretes: Proceedings of the Sixth International RILEM Symposium*, pages 61–68, Varenna, Italy. RILEM.

Comite Euro-international du Beton (1993). *CEB-FIP model code 1990: design code*. Number 213-214. T. Telford.

Fischer, G. and Li, V. C. (2003a). Deformation behavior of fiber-reinforced polymer reinforced engineered cementitious composite (ecc) flexural members under reversed cyclic loading conditions. *ACI Struct J*, 100(1):25–35.

Fischer, G. and Li, V. C. (2003b). Intrinsic response control of moment-resisting frames utilizing advanced composite materials and structural elements. *ACI Struct J*, 100(2):166–176.

Fischer, G. and Li, V. C. (2007). Effect of fiber reinforcement on the response of structural members. *Eng Frac Mech*, 74(1-2):258–272.

Idorn, G. M. (1997). *Concrete Progress - from antiquity to the third millenium*. Thomas Telford.

Kanda, T. and Li, V. C. (1999). New micromechanics design theory for pseudostrain hardening cementitious composite. *ASCE Journal of Engineering Mechanics*, 125(4):373–381.

Kanda, T. and Li, V. C. (2006). Practical design criteria for saturated pseudo strain hardening behavior in ecc. *J Adv Conc Tech*, 4(1):59–72.

Karihaloo, B., Carpinteri, A., and Elices, M. (1993). Fracture mechanics of cement mortar and plain concrete. *Advanced Cement Based Materials*, 1(2):92–105.

Krstulovic-Opara, N. and Malak, S. (1997). Tensile behavior of slurry infiltrated mat concrete (simcon). *ACI Materials Journal*, 94(1):39–46.

Kunieda, M. and Rokugo, K. (2006). Required performance and applications. *Journal of Advanced Concrete Technology*, 4(1):19–33.

Landis, E. N. and Shah, S. P. (1995). The influence of microcracking on the mechanical behavior of cement based materials. *Advanced Cement Based Materials*, 2(3):105–118.

Lankard, D. R. (1984). Slurry infiltrated fiber concrete (sifcon). *Concrete International*, 6(12):44–47.

Lepech, M. D. and Li, V. C. (2009). Application of ecc for bridge deck link slabs. *Mater Struct*, 42(9):1185–1195.

Leung, C. K., Cheung, Y. N., and Zhang, J. (2007). Fatigue enhancement of concrete beam with ecc layer. *Cement and Concrete Research*, 37(5):743–750.

Leung, C. K. Y. and Li, V. C. (1992). Effect of fiber inclination on crack bridging stress in brittle fiber reinforced brittle matrix composites. *Journal of the Mechanics and Physics of Solids*, 40(6):1333–1362.

Li, V. C. (2002). Large volume, high-performance applications of fibers in civil engineering. *Journal of Applied Polymer Science*, 83(3):660–686.

Li, V. C. (2003). On engineered cementitious composites (ecc). *J Adv Conc Tech*, 1(3):215–230.

Li, V. C. (2011). High-ductility concrete for resilient infrastructures. *Journal of Advanced and High-Performance Materials*, pages 16–21.

Li, V. C. and Leung, C. K. (1992). Steady-state and multiple cracking of short random fiber composites. *Journal of Engineering Mechanics - ASCE*, 118(11):2246–2264.

Li, V. C., Wang, S., Ogawa, A., Saito, T., and Wu, C. (2002). Interface tailoring for strain-hardening polyvinyl alcohol-engineered cementitious composite (pva-ecc). *ACI Materials Journal*, 99(5):463–472.

Li, V. C., Wang, S., and Wu, C. (2001). Tensile strain-hardening behavior or polyvinyl alcohol engineered cementitious composite (pva-ecc). *ACI Mater J*, 98(6):483–492.

Lin, Z. and Li, V. C. (1997). Crack bridging in fiber reinforced cementitious composites with slip-hardening interfaces. *Journal of the Mechanics and Physics of Solids*, 45(5):763–787.

Làrusson, L. and Fischer, G. (2011). Flexible concrete link slabs used as expansion joints in bridge decks. *Proceedings of the 9th International Symposium on High Performance Concrete - Design, Verification & Utilization*, pages –.

Maeder, U., Lallemant-Gamboa, I., Chaignon, J., and Lombard, J. (2004). Ceracem, a new high performance concrete: characterisations and applications. . no. 3 ed. In Schmidt, M., Fehling, E., and Geisenhansluke, C., editors, *International Symposium on Ultra High Performance Concrete*, number 3, pages 59–68, Kassel, Germany. Kassel University Press GmbH.

Marković, I. (2006). *High-performance hybrid-fibre concrete: development and utilisation.* IOS Press.

Mehta, P. and Monteiro, P. (2006). *Concrete: microstructure, properties, and materials.* McGraw Hill professional. McGraw-Hill.

Naaman, A. (1992). Sifcon: tailored properties for structural performance. In Reinhardt, H. and Naaman, A., editors, *High Performance Fiber-Reinforced Cement Composites: Proceedings of the International Rilem-ACI Workshop*, RILEM Reports, pages 18–38, Mainz, Germany. Spon.

Naaman, A. (2008). *High Performance Fiber Reinforced Cement Composites*, volume 1 of *Engineering Materials for Technological Needs*, chapter 3, pages 91–154. World Scientific Publishing Co.

Naaman, A. E., Namur, G. G., Alwan, J. M., and Najm, H. S. (1991). Fiber pullout and bond slip. i. analytical study. *Journal of Structural Engineering*, 117(9):2769–2790.

Neville, A. (1996). *Properties of concrete.* John Wiley & Sons.

Orange, G., Acker, P., and Vernet, C. (1999). A new generation of uhp concrete: Ductal - damage resistance and micromechanical analysis. In Reinhardt, H. and Naaman, A., editors, *PRO 6: 3rd International RILEM Workshop on High Performance Fiber Reinforced Cement Composites (HPFRCC 3)*, RILEM proceedings, pages 101–111. RILEM Publications.

Parra-Montesinos (2005). High-performance fiber-reinforced cement composites an alternative for seismic design of structures. *ACI Structural Journal*, 102(5):668–675.

Parra-Montesinos, G. and Wight, J. K. (2000). Seismic response of exterior rc column-to-steel beam connections. *Journal of Structural Engineering*, 126(10):1113–1121.

Reinhardt, H. and Naaman, A. (1992). *High Performance Fiber-Reinforced Cement Composites: Proceedings of the International Rilem-ACI Workshop*. RILEM Reports. Spon.

Rokugo, K., Kanda, T., Yokota, H., and Sakata, N. (2009). Applications and recommendations of high performance fiber reinforced cement composites with multiple fine cracking (hpfrcc) in japan. *Materials and Structures*, 42(9):1197–1208.

Rossi, P. (1997). High performance multimodal fiber reinforced cement composites (hpmfrcc): the lcpc experience. *ACI Mater J*, 94(6):478–483.

Stang, H. and Li, V. C. (1999). Extrusion of ecc-material. In Reinhardt, H. and Naaman, A., editors, *Third International RILEM Workshop on High Performance Fiber Reinforced Cement Composites*, pages 203–212. RILEM Publications SARL.

van Mier, J. (1997). *Fracture processes of concrete: assesment of material parameters for fracture models*. New directions in civil engineering. CRC Press.

Wille, K., Kim, D. J., and Naaman, A. E. (2011). Strain-hardening uhp-frc with low fiber contents. *Mater Struct*, 44(3):583–598.

Wu, H.-C. and Li, V. C. (1994). Trade-off between strength and ductility of random discontinuous fiber reinforced cementitious composites. *Cement and Concrete Composites*, 16(1):23–29.

Yang, E. H., Wang, S., Yang, Y., and Li, V. C. (2008). Fiber-bridging constitutive law of engineered cementitious composites. *Journal of Advanced Concrete Technology*, 6(1):181–193.

CHAPTER 2

Characterization of tensile behavior

2.1 Introduction

The recent technological development of a wide variety of fibers has been creating new opportunities for the development of fiber reinforced cementitious composites as structural materials. The behavior of the composites containing these distinct fibers, which are dispersed in the cementitious matrix, can be very diverse, allowing the development of numerous functional properties in these materials. In particular, the designing of fiber reinforced cementitious composites focusing the development of tensile strain hardening property leads, when successfully accomplished, to the so-called Strain Hardening Cementitious Composites (SHCC). From the viewpoint of structural design, strain-hardening ability in tension is often referred to as the most relevant feature of SHCC, although many other functional properties are found in this special class of fiber reinforced cementitious composites (FRCC).

Pseudo-strain hardening in tension exhibited by SHCC is the consequence of the development of multiple cracks under tensile loading. Tensile hardening at the level of a single crack is the main prerequisite to the multiple crack formation and the effective capability of withstanding tensile hardening at considerable imposed deformations. This material property represents a dual advantage in engineering applications: while considerably more cracks develop at the same tensile deformation level, the individual crack openings are significantly smaller. The result of this multiple cracking behavior is enhanced durability and better preservation of functional properties in the structural elements. Conversely, higher energy dissipation ability exists at the level of a single crack, which is amplified by the large number of cracks typically developed. These materials are therefore designed to exhibit high toughness and significant tolerance to damage in tension.

Over the past few decades, the research carried out in the field of SHCC materials has followed different development directions and design approaches [Li, 2002, 2003; Brandt, 2008; Naaman, 2008]. As discussed previously in Chapter 1, in the vast field of different FRCC the special class of High Performance Fiber Reinforced Cement-based Composites (HPFRCC) encloses a few different versions of FRCC exhibiting tensile strain-hardening ability. Although HPFRCC materials are a restrict group of FRCC, a significant diversity of tensile behaviors of different composites can be found in the literature.

SHCC materials research has been mostly based on the characterization of their tensile stress-strain behavior, particularly dealing with their unique characteristic, the pseudo-strain hardening ability in tension [Li, 2003; Naaman and Reinhardt, 2006]. The type of test mostly used is the direct tension test using dog bone-shaped (dumbell-shaped) or coupon specimens [Kanda and Li, 2006; Naaman, 2008; Rokugo et al., 2009]. The material tensile stress-strain behavior is thereby assessed as well as the potential of the material to develop multiple cracks. The direct tension tests are experimentally demanding, therefore inverse analysis is also alternatively used to derive indirectly the stress-strain or the stress-separation law from bending tests [Quian and Li, 2008]. Other test setups used are inspired by common test methods adopted to extract the fracture parameters of concrete and other tension softening FRCC. These test methods include the Compact Tension test (CTT), the Wedge Splitting test (WST), the Split Cylinder Tensile Strength Test and the Three Point Bending Test (see for example [Cotterell and Mai, 1996; Karihaloo, 1995; Shah et al., 1995; Lofgren et al., 2008; RILEM-TC162-TDF, 2002]). However, the initiation of multiple cracks and the individual particular testing conditions interfere with the explicit and objective characterization of SHCC constitutive properties.

2.1.1 SHCC design and multiple cracking conditions

The design of FRCC toward the achievement of multiple cracking and strain hardening in tension essentially deals with the different aspects of the mechanical properties of the fibers, of the matrix, and of the fiber-matrix interaction. The composite ingredients need to be properly selected in order to promote the synergistic interaction between the strong, deformable fibers and the tension weak, brittle matrix. Due to the multi-scale nature of SHCC, this adjustment has to consider the relevant mechanisms occurring at each material scale, and link them in a systematic procedure.

Single fiber pull-out behavior:

At the micro-scale level, the fiber-matrix interaction properties have been systematically studied and the main aspects of these properties were condensed in micro-mechanical models. In the case of ECC materials, micro-mechanical models were established in early 90's [Li and Leung, 1992; Leung and Li, 1992; Li and Wu, 1992]. The description of the behavior of the single fiber embedded on the matrix while subjected to a pull-out force is the starting point to the construction of these micro-mechanical models. Considering that ECC materials are typically reinforced with short, randomly distributed micro-fibers (with a diameter of 10 to 50 μm and length of 6 mm to 12 mm), the global bridging stress-crack opening relationship of a single crack can be obtained by averaging the contribution of the fibers crossing the crack with different embedment lengths and orientations. The study of these micro-mechanical models is out of the scope of the present research. However, due to their importance, the micro-mechanisms that govern the overall pull-out behavior of a fiber are briefly addressed and discussed.

In general two distinct mechanical regimes may be distinguished in the pull-out response of a single straight fiber (Figure 2.1): bonded (elastic behavior) and debonded (frictional behavior). Initially, while the fiber is fully bonded, the single fiber pull-out response is dictated by the elastic fiber-matrix shear stress transfer. After the full debonding of the fiber, the shear stress is transmitted from the fiber to the matrix by interfacial friction [Geng and Leung, 1996]. While debonding occurs, both regimes may coexist. If the fiber-matrix interfacial bonding, also known as the chemical bonding, is significant, the elastic regime has an important influence on the entire single fiber pull-out response. When the debonding process is initiated, the tunel crack propagates from the fiber exit into the embedded portion. This process may occur in a stable or unstable manner, and is controlled by a fracture criterion, for example if the chemical bonding is high, or by a strength criterion [Stang and Shah, 1986; Leung and Li, 1990].

The pull-out behavior of a single fiber embedded on the matrix may be assumed to depend on three distinct types of strengthening mechanisms: the ones deriving from fiber deformation, from interfacial transition zone modification and from fiber surface modification [Li and Stang, 1997].

At a larger scale, the fiber deformation includes all the aspects related to the fiber geometry changes, either during the processing of the fiber or while the fiber is being pulled out of the matrix. During the processing of the fiber, different techniques are typically applied to increase the surface area of contact with the matrix per unit fiber length. Mechanical anchorage is also affected by most of these pro-

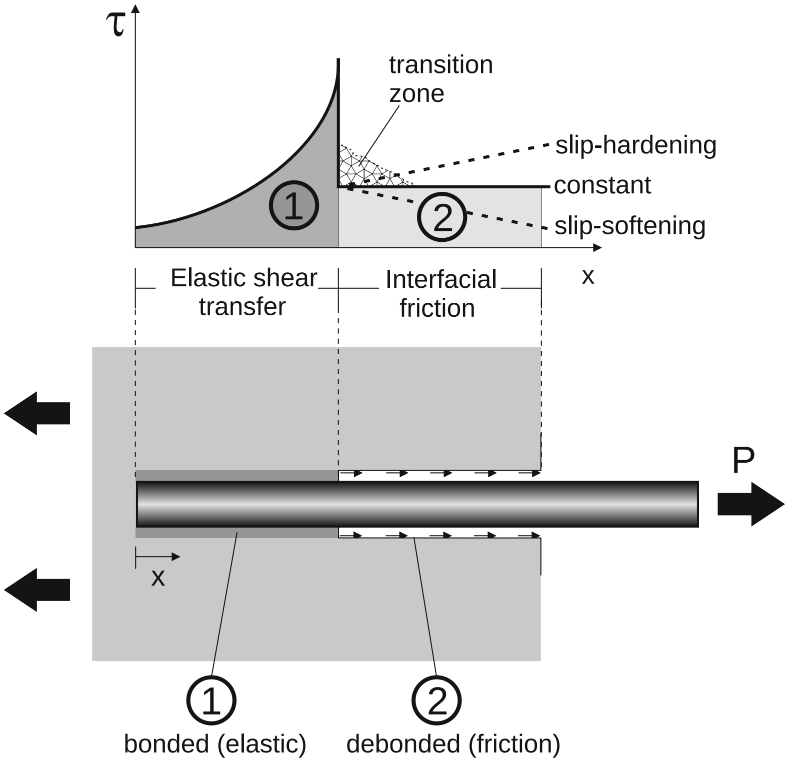

Figure 2.1: Debonding and pull-out behavior of a single, straight fiber from the cementitious matrix.

cesses. Examples are fibrillation [Krenchel and Shah, 1985], fiber twisting [Naaman and Shah, 1976], fiber crimping [Banthia and Trottier, 1995] or other types of fiber geometry alteration including the introduction of hooked ends (Figure 2.2). While the fiber is being pulled out of the matrix, the deformation of the fiber between the two crack flanks may be the consequence of the inclination of the fiber with respect to the crack plane, which alters the pull-out behavior of the single fiber [Leung and Li, 1992]. Also when the fiber is not perpendicular to the crack plane, it is subjected to an additional frictional stress due to the interaction with the matrix in the region where the fiber exits the matrix, known as the loaded end zone, and at the same time the fiber nominal tensile strength is reduced. The proximity of neighbor fibers being pulled out simultaneously and the matrix spalling close to the exit of inclined fibers are also factors which influence considerably the pull-out response of the single fiber [Li et al., 1990; Cunha et al., 2010]. An important aspect of fiber deformation while considering polymeric fibers is the alteration of the fiber surface during pull-out. Due to the relatively low hardness of the polymeric fibers, surface abrasion may occur while the fibers slip against the hard rough embedding matrix. Fiber debris and stripped fibrils may accumulate at the debonding interface and create a clogging effect that increases the interface shear stress and hinders slipping [Lin and Li, 1997]. As a result, slip-hardening pull-out behavior is obtained (see Figure 2.1).

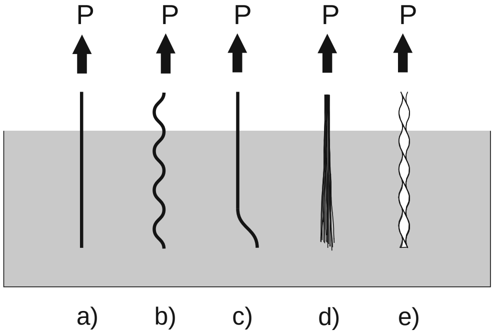

Figure 2.2: Types of fiber geometry alteration to change the fiber-matrix interaction properties: a) straight, b)crimped, c) hooked end, d) fibrillated and e) twisted.

The interfacial transition zone (ITZ) in cementitious matrix composites consists of a porous and weak layer of cementitious matrix that surrounds the larger inclusions dispersed, whether fibers or aggregates. It is the result of several factors, among which the wall effect plays an important role as the main cause for bleeding around inclusions and inefficient packing of fine particles around the fiber surface. As a consequence, during hydration advancement the development of the microstructure is affected, and the initially water-filled spaces in the transition zone do not develop the high density of the microstructure found in the bulk matrix. ITZ also contains a considerable volume of CH crystals, which tend to accumulate in larger pores [Bentur and Mindess, 2006]. The ITZ is therefore assumed as the weakest link among the constituents that govern the composite properties. The effect of the ITZ densification on the improvement of the bond strength between fibers and the cementitious matrix was studied by several researchers (see Li and Stang [1997]), and in general the fiber-matrix interfacial bonding can be altered by changing the water to cement ratio, the local packing density of the fine particles and by adding other admixtures, like polymers.

The modification of the fiber surface is adopted mostly on polymeric fibers, when there is a mismatch between the fiber strength and the fiber-matrix interfacial bonding requirements. In general, an excessive fiber-matrix bonding leads to early fiber rupture, and on the contrary, if fiber-matrix interfacial bonding is too low the strengthening mechanisms previously discussed cannot be fully mobilized. In both cases, the performance of the fiber is not optimal. Plasma surface treatment has been utilized to alter the fiber-matrix interfacial bond, for example with polypropylene and polyethylene fibers. The typical hydrophobic nature of these polymers was altered, increasing their reactivity and wettability [Li et al., 1996; Wei et al., 2002]. As such, the contact and bonding of the fiber with the surrounding matrix was increased. Experimental results have shown that the untreated slip-softening pull-out behavior was altered to a slip-hardening response [Lin and Li, 1997]. In contrast, the application of oil coating to the surface of Polyvinyl alcohol (PVA) fibers has been used to reduce the fiber-matrix interface bonding [Li et al., 2002]. The strong chemical bonding of PVA fibers with the cement matrix was found to be excessive, and the reduction of the fiber-matrix interfacial bonding led to improved tensile behavior of ECC.

Conditions for multiple cracking:

The tensile hardening behavior and multiple crack formation observed in SHCC materials at the macro-scale level derive from the convenient adjustment of the fiber-matrix interaction mechanisms, established at the composite micro-scale level. The above discussed micro-mechanisms that influence the single fiber pull-out response can be summarized in the form of analytical expressions. For example, general formulations can be found in Lin and Li [1997]; Redon et al. [2001]; Yang et al. [2008], where the fiber pull-out load (P) versus the displacement at the loaded end of the fiber (δ) is derived considering the effect of both the debonding and the pull-out processes on the entire fiber pull-out response, and the general slip hardening/softening constitutive relationship is considered. As previously discussed, the slip-hardening consideration is necessary in the case of polymeric fibers, which are softer than the matrix and consequently experience abrasion during slip. This is the case when PP, PE or PVA fibers are used. The complete general formulation of the $P - \delta$ response is obtained by considering the additional effects of considering the two-sided fiber pull-out [Wang et al., 1988; Yang et al., 2008], the matrix micro-spalling at the fiber exit [Kanda and Li, 1998], and the effect of fiber inclination with respect to the crack plane on the additional frictional stress and on the reduction of the in-situ fiber strength [Morton and Groves, 1976; Li, 1992; Lin et al., 1999; Kanda and Li, 1998] (see Figure 2.3).

Considering that the single fiber $P - \delta$ response is completely defined, it is described as dependent of the matrix and fiber properties, position and inclination angle with respect to the crack plane (see Figure 2.3). The randomness of fiber orientation and location can be accounted for by adopting the probability density functions of fiber orientation and position with respect to the crack plane [Wang et al., 1989].

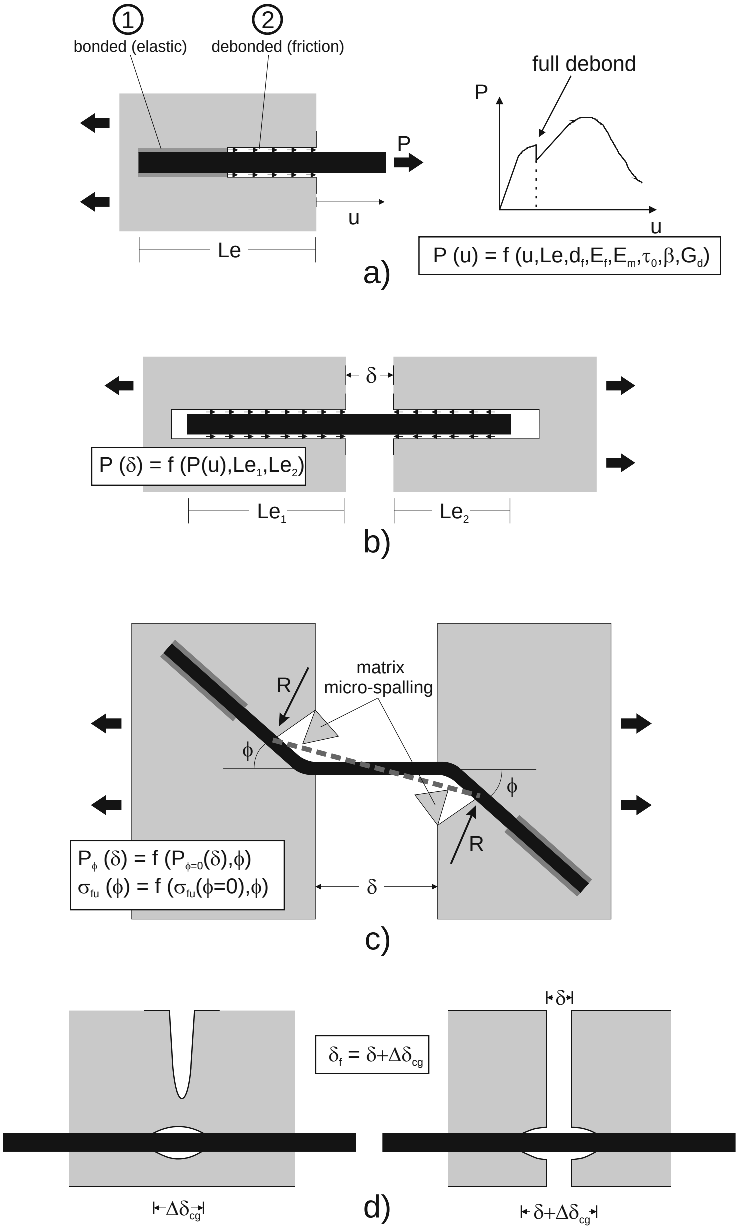

Figure 2.3: Schematic description of the main fiber-matrix interaction mechanisms during matrix crack propagation: a) single fiber pull-out, b) two-way fiber pull-out, c) pull-out of inclined fibers and d) Cook-Gordon effect.

Eventually, the averaged fiber bridging stress, σ_b, versus the crack opening, δ, for the particular composite in consideration is obtained (equation 2.1):

$$\sigma_B(\delta) = \frac{V_f}{A_f} \int_{\phi_0}^{\phi_1} \int_{z=0}^{z=(L_f/2)cos\phi} P_\phi(\delta)p(\phi)p(z)dzd\phi \tag{2.1}$$

The early fiber-matrix interface debonding due to the Cook-Gordon effect and the corresponding additional displacement due to fiber stretching can also be considered [Li et al., 1993], assuming that this phenomenon applies to all fibers regardless of their orientation (Figure 2.3).

The description of the fiber bridging $\sigma_b - \delta$ response of a given composite is essential to the analysis of the composite tensile behavior at the macro-scale. The $\sigma_b - \delta$ behavior is needed to link the fiber-matrix interaction mechanisms at the micro-scale level and the structural response, at the macro-scale.

In a broad sense, the composite tensile behavior of SHCC may be seen as the assemblage of two types of spring elements in series, one having the properties of the uncracked composite and another simulating the equivalent stiffness of the open crack that is bridged by the fibers [Yang and Fischer, 2006]. In this sense, it becomes reasonable to assume that the tensile load capacity of the fibers bridging the cracks formed must exceed the tensile load at which the first crack is formed. This is a simplistic approach to the description of the tensile behavior of SHCC, but clear on establishing a necessary but not sufficient condition for multiple cracking and tensile hardening attainment in the fiber reinforced cementitious composite in tension. The investigation of Aveston et al. [1972] was pioneering on the establishment of the theoretical framework to analyze the conditions for single and multiple fracture on tensioned brittle matrix fiber reinforced composites. Important concepts were introduced in his research, including the determination of crack spacing in the saturated state, the stress transfer length, the composite mechanical properties and the conditions under which multiple fracture occurs. This investigation was followed later by the work of Marshall and Cox [1988], where the J-integral method was used to calculate the steady-state matrix cracking stress in brittle matrix composites. According to Marshall and Cox [1988], if the crack is large compared with the dimensions of the material structure features and bridging ligaments, the composite can be approximated to a continuum with the average elastic properties of the composite and a continuous traction acting over the crack surfaces $\sigma(\delta)$, where δ represents the average local crack opening displacement. The crack opening displacement and the crack surface pressure increase monotonically with the distance behind the crack tip and, for sufficiently long cracks, approach asymptotic limits equal to δ_a and σ_a at the mouth of the crack. The stresses and the strains near the crack tip can be calculated by determining the opening pressures acting over the crack surfaces, σ_o, by subtracting the traction due to the ligament bridging, $\sigma(\delta)$, to the remotely applied ambient stress, σ_a (Figure 2.4).

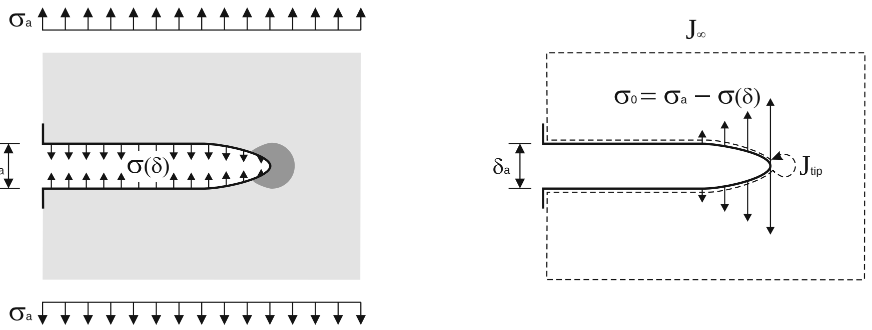

Figure 2.4: Crack propagation mechanics and energetics [Marshall and Cox, 1988].

The opening pressure σ_o is maximum at the crack tip, and approaches zero far from the crack tip. By evaluating the J-integral [Rice, 1968] using this crack configuration the following expression is obtained (equation 2.2):

$$\sigma_a \delta_a - \int_0^{\delta_a} \sigma(\delta) d\delta = J_{tip} \tag{2.2}$$

In equation 2.2, the first term on the left hand side may be interpreted as the net energy input by the external loading, and the second term represents the energy consumed by the bridging ligaments while opening from zero to δ_a. The term on the right hand side of the expression is the crack tip toughness, which may be expressed as a function of the crack tip stress intensity factor and the matrix Young's modulus, considering that the fiber volume fraction is small. As such, the left hand side of the equation may be interpreted as the net energy available to drive the crack tip propagation, which must equal the crack tip toughness. The net energy available to drive the crack tip propagation is therefore independent of crack length. This simple and insightful interpretation of the steady state crack propagation proposed by Marshall and Cox [1988] (see Figure 2.5 b)) is very useful in the design of SHCC, where the optimal design of the composite toward the formation of multiple cracking and tensile hardening is pursued [Kanda and Li, 2006]. One critical design requirement to achieve multiple cracking in the composite is, therefore, to guarantee that the critical complimentary energy of the bridging stress-crack opening relationship, J'_c, exceeds the crack tip toughness, J_{tip}, that is equal to the steady state complimentary energy, J'_a (see Figure 2.5 b)).

As discussed by Marshall and Cox [1988], it is interesting to contrast the steady state crack propagation with the steady state toughness, the later occurring when the matrix cracking strength, σ_c, exceeds the peak value of $\sigma(\delta)$ and fibers break at the onset of cracking (see Figure 2.5 a)). In this case the traction in the bridging zone that remains over a limited region behind the crack tip only contributes to increase the material toughness in a steady state regime, consequently classified as steady state toughness. Essentially the Griffith-type of crack propagation regime is preserved, as well as the typical tensile softening of the remote stresses behind the crack, although the fibers contribute to increase the material toughness and the bridging stresses. Therefore, in these cases the flat crack propagation at constant ambient stress in the composite is not possible.

According to the above exposed, the fundamental requirements for multiple crack formation and hardening in tension may be expressed by the following two expressions:

- $J'_a = \sigma_a \delta_a - \int_{\delta_a}^{0} \sigma(\delta) d\delta \geq J_{tip}$;

- $\sigma_0 \geq \sigma_c$.

where the first expression states that the complimentary energy calculated from the bridging stress-crack opening curve, $\sigma - \delta$, which represents the energy available to drive the crack tip extension, must exceed the crack tip toughness; the second expression states that the peak bridging stress, σ_u, must exceed matrix tensile strength, σ_c. The first is the energy-based criterion, that governs the crack propagation mode, and the second is the strength-based criterion, that determines the initiation of cracks and the ability of the composite to withstand increasing loading after cracking. Both criteria are typically used in the design of ECC [Li and Wu, 1992; Kanda and Li, 2006]. The fiber bridging stress-crack opening behavior is, therefore, an essential key element in the design procedure of SHCC materials [Yang et al., 2008].

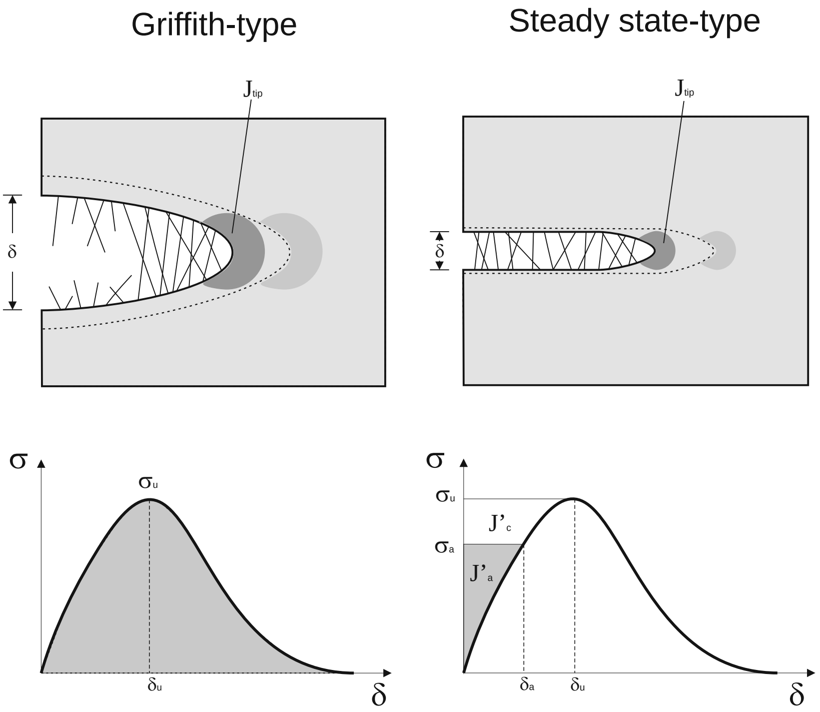

(a) (b)

Figure 2.5: Schematic distinction of the (a) Griffith and the (b) steady state types of crack propagation, including energetic considerations supporting each type of crack propagation.

2.2 Tensile stress-strain behavior of SHCC

The mechanical behavior in tension of SHCC, as a result of the synergistic interaction between the fibers and the cementitious matrix, is highly sensitive to the multiplicity of factors discussed earlier. The characterization of this intricate composite behavior may focus on many different aspects of this composite behavior, and the definition of the most apropriate type of test that summarizes the essential properties of these composites is not simple. In practice, the tensile behavior of SHCC is typically assessed by characterizing the tensile stress-strain behavior, which emphasizes SHCC unique characteristic, that is, the pseudo-strain hardening ability in tension. The direct tension test using dog bone-shaped (dumbell-shaped) or coupon specimens [Kanda and Li, 2006; Naaman et al., 2007; Rokugo et al., 2009] is the type of test

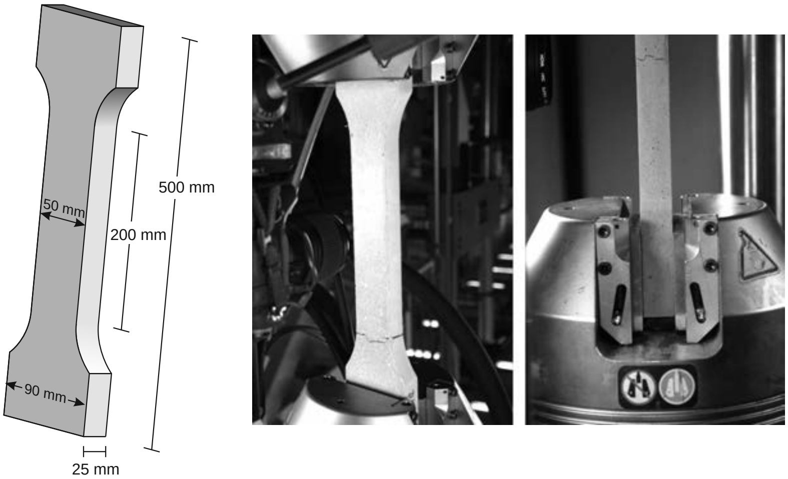

Figure 2.6: Specimen geometry used in the assessment of the tensile stress-strain behavior.

that is most frequently used. Important parameters extracted with this type of test are the peak tensile stress, the strain at peak stress and the average crack width evolution, as well as the overall shape of the tensile stress-strain behavior.

In Figure 2.6 the specimen geometry and test setup are shown. Other types of specimens and test setups used for direct tension testing may be found in the literature [Naaman et al., 2007].In Figure 2.7 the tensile stress-strain behavior obtained from three specimens of ECC is shown [Làrusson et al., 2010, 2011]. The appropriate design of the composite ingredients led to the typical tensile ultimate strain of 4% at a peak stress of 4 MPa. Also important is the tracing of the crack opening, or alternatively the crack spacing at the surface of the specimen, which indicate that the formation of cracks occurs steadily until crack saturation is achieved. The steady state crack propagation mode and the ability of the composite to withstand increasing tensile loading after cracking are determinant in the achievement of the so-called pseudo-strain hardening behavior typical of ECC. These two concepts embody the fundamental criteria for multiple crack formation and tensile hardening behavior.

In the previous section, the essential role of the micro-mechanical models on the design of SHCC materials was evidenced. The information collected at the material micro-scale level summarizes all the parameters and mechanisms that affect the stiffening mechanisms provided by the short, straight and randomly dispersed fibers during cracking. The micro-mechanical models establish the necessary background

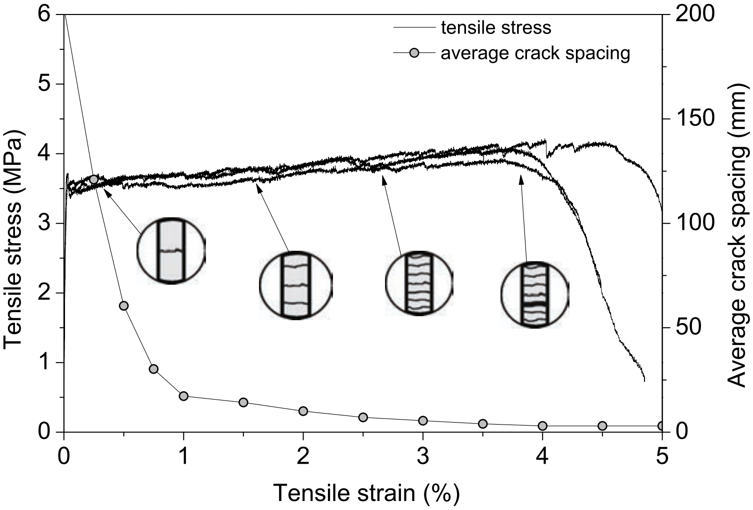

Figure 2.7: Tensile stress-strain response and average crack spacing evolution obtained from ECC dogbone specimens in direct tension.

to derive the fiber bridging stress-crack opening curve from the composite micro-mechanical parameters. The fiber bridging stress-crack opening curve is essential to model the mechanical behavior of SHCC observed at the macro-scale level, as well as to verify the fundamental requirements of the material design and to achieve multiple cracking. It becomes clear that, in this procedure, the estimation of the macro-scale behavior of SHCC is based on the mechanical characterization of the material at a much smaller scale, by evaluating the micro-mechanical parameters. Besides the great distance between the two scales involved in this description of SHCC materials, the additional difficulty associated with the experimental evaluation of most of the micro-mechanical parameters involved are clear. These observations suggest that complimentary strategies to characterize the material behavior at other length scales are welcomed, namely at the level of the meso-scale.

2.2.1 Tensile stress-crack opening behavior of SHCC

Considering the characterization of the mechanical behavior of SHCC materials at the meso-scale, in this study an alternative approach to the assessment of the tensile behavior of SHCC materials is investigated. This approach is based on the characterization of the tensile stress-crack opening behavior of SHCC at the level of a single crack. The main obstacle to this strategy is the difficulty associated with obtaining a single crack when the material is especially designed to develop multiple cracks. To produce adequate mechanical conditions for the initiation and evolution of a single crack, the stress fields generated in test specimens under tension may be locally intensified using geometrical constrictions or notches. This procedure is well known from the characterization of the tensile stress-crack opening behavior of tension softening FRCC. Research has been carried out in this field, using different test methods to assess the post-cracking behavior of FRCC in direct tension (see for example [Li et al., 1993; RILEM-TC162-TDF, 2001; Stang and Aarre, 1992]). However, when pseudo-strain hardening materials are considered this strategy shows difficulties in keeping the crack single throughout the entire loading sequence [Shah et al., 1996]. Nevertheless, previous work has shown that if the geometry of the specimen is modified, a single crack may be obtained and mechanically characterized [Fischer et al., 2007; Yang et al., 2008]. In this study the geometry of the specimen was investigated and special attention was dedicated to the minimizing of the thickness of the notches created in the specimens. The motivation supporting this procedure is the possibility to assess directly and objectively important features of the composite behavior in tension, also when the material shows pseudo-strain hardening in tension. The benefits extend beyond the material design process. The tensile stress-crack opening relationship is of major importance to the constitutive modeling of the material behavior, which is a central element in the numerical simulation of structures. Seeking optimal usage of SHCC material properties, research has been carried out to develop numerical modeling strategies especially suited to simulate the behavior of SHCC structures [Kabele, 2007]. In particular, the single crack cohesive law was adopted by [Kabele, 2009] to characterize the tensile behavior of SHCC in numerical models. Typically, the performance and accuracy of these models depend on the objective assessment of the SHCC material behavior, which motivates the exploration of experimental procedures that consistently lead to an explicit tensile stress-crack opening characterization of FRCC using notched specimens [RILEM-TC162-TDF, 2001; Naaman et al., 2007].

The verification that a single crack is indeed obtained during the entire testing sequence is important for the unique characterization of the tensile stress-crack opening behavior of SHCC. To help with the identification of the various crack initiation and propagation stages, an image-based monitoring system has been used to document the generated deformations at the surface of the specimens during testing. The so-called Digital Image Correlation (DIC) technique involves the comparison of two digital images of the surface of an object before and after deformation using an appropriate correlation technique [Chu et al., 1985]. The accuracy of the correlation between the recorded images depends mainly on the quality of the image speckle pattern (including light conditions) and the resolution of the imaging system [Berfield et al., 2007]. By using DIC, the crack initiation and propagation stages in direct tension in notched SHCC specimens have been monitored and characterized. This is particularly important during the early stages of the testing sequence, when the crack is developing and while the tensile stresses gradually transfer from the matrix to the fibers bridging the crack.

2.3 Materials

In this study the tensile behavior of seven different FRCC was assessed. The materials used in the composition of the cementitious matrix were essentially the same for all composites, and the type and volume fraction of fiber reinforcement was varied. The matrix composition in terms of the weight of each ingredient for a total volume of 1 dm^3 is presented in Table 2.1.

Table 2.1: Weight of the materials used for 1 dm^3 of cementitious matrix.

Cement	Fly ash	Fine sand (0.17 mm)	Quartz powder	Water
428 g	856 g	150 g	150 g	320 cm^3

Fibers of three different natures were used: PVA (polyvinyl alcohol), PAN (polyacrylnitrile) and PP (polypropylene). The main geometric and mechanical properties of these fibers are presented in Table 2.2

The fiber volume fraction was 2% in the case of the composites containing PP or PAN fibers, while the percentages of 1% and 2% by volume were used in the case of the composites containing PVA fibers.

Table 2.2: Main properties of the fibers used.

Fiber	Tensile strength (MPa)	Length (mm)	Diameter (μm)
PVA	1600	8	40.0
PP	900	12	40.0
PAN 1.5	826	6	12.7
PAN 3.0	767	6	18.0
PAN 6.7	413	6	26.8
PAN 30	295	6	57.0

2.4 The Single Crack Tension Test (SCTT)

The main pre-requisite to the direct and objective characterization of the tensile stress-crack opening behavior during the initiation and propagation stages is the obtaining of a single crack during the entire loading sequence. SHCC materials are designed to develop multiple cracks in tension, consequently the formation of a single crack is naturally prevented by the material. To meet this requirement, different geometries of notched specimens were previously investigated, and their ability to promote the initiation and propagation of a single crack was verified. Special attention was dedicated to the minimization of the thickness of the created notches.

In general terms, cracking saturation in SHCC materials is achieved when, while new cracks form, the decreasing crack spacing reaches a critical value that is equal the load transfer length required to induce new cracking. This load transfer length, determined by the fiber properties, the matrix fracture parameters and the fiber-matrix interaction properties, is a lower bound limit to the crack spacing in the composite. The notch thickness adopted in this investigation, 0.5 mm, is well below the typical crack spacings found in the literature and observed in un-notched SHCC specimens tested in direct tension (see for example [Li et al., 2001]). These crack spacings can reach values as low as 5 mm, but seldom below 2 mm. The notch thickness and specimen geometry selected in this study are aimed at preventing the possibility of additional cracking to occur in the immediate vicinity of the primary induced crack.

The specimen dimensions and final geometry are presented in Figure 2.8. The length of the specimen was 120 mm and the free distance between the fixed ends during testing was 70 mm. To produce six specimens of each composite, plates of $600\times125\times20$ mm^3 (length×width×thickness) were cast, sealed and left to cure for 28 days. The casting surface of the plates was then ground to a thickness of 12 mm and a matrix of six specimens was cut from the central part of the plate (see Figure

2.8. After curing, the 0.5 mm thick notches were cut in the coupon specimens using a small diamond cutting disc. The high rotation speed of the disc and a delicate setup were used to avoid causing damage in the specimens.

The testing sequence consisted of applying a displacement controlled constant axial displacement rate of 5 μm/s, transmitted by the hydraulic actuator to the specimen by means of two hydraulic grips providing fixed support to both ends of the specimen (rotations and transverse displacements were restrained). During testing, the opening of the notch was evaluated by means of two clip gauges positioned in opposite sides as shown in Figure 2.9.

The example of one specimen adopting the final geometry proposed in this study is presented in Figure 2.10 where a single crack was formed and characterized in tension. After adopting this geometry the formation of a single crack was consistently obtained in tests conducted subsequently.

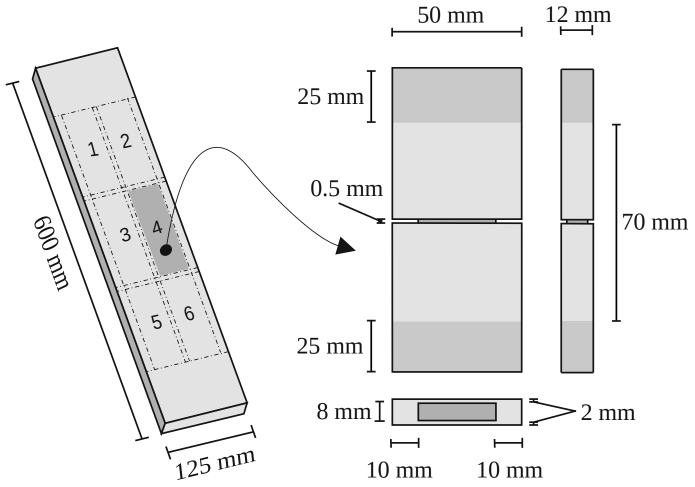

Figure 2.8: Specimen geometry used in the assessment of the tensile stress-crack opening behavior.

2.4.1 Tensile stress-crack opening behavior results

The results obtained after testing the specimens in direct tension are presented in Figure 2.11. The tensile stress values (nominal tensile stress) presented were obtained by computing the ratio between the experimental tensile load and the net area of the

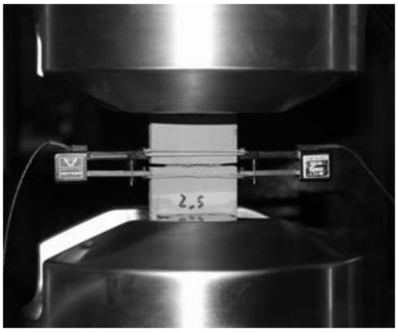

Figure 2.9: Tensile test setup including supports and clip gauges.

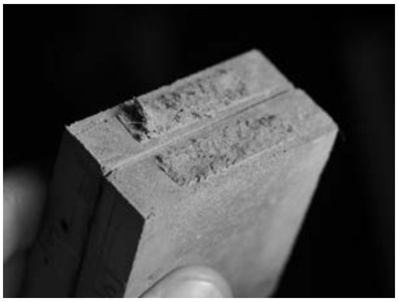

Figure 2.10: Single crack obtained after testing.

notched cross-section (8×30 mm^2). The crack mouth opening displacements (CMOD) were obtained by averaging the displacements measured in the two opposite clip gauges, although these were later verified to be practically similar. The adoption of the fixed supports contributed to this requirement of minimizing the difference between the displacements observed in the opposite clip gauges. The distance between the two sampling points of each clip gauge was 25 mm.

For each composite, the results of three of the six specimens tested are shown. The upper and lower limit results are presented to show an envelope of the obtained behavior.

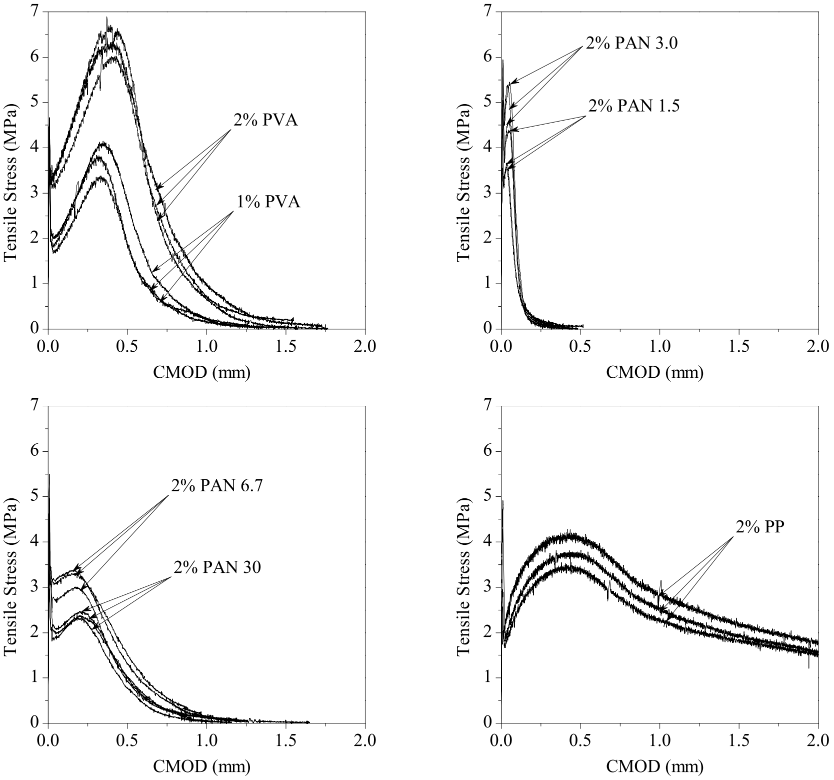

Figure 2.11: Tensile stress-CMOD of the tested composites.

2.5 Numerical study of crack initiation

2.5.1 Numerical model

The notches inserted at the middle section of the specimens produce a local intensification of the stress field. This intensification is desirable, regarding the intention of inducing the formation of a single crack during tensile loading. The initiation of the crack at the corners of the notched cross-section and its subsequent propagation occur rapidly, while the opening of the crack tip is still small. At this stage, the fracture micro-mechanisms depend almost exclusively on the properties of the matrix. In order to estimate the effect of the local intensification of the stress field induced by the notch on the generation of the crack plane, a 3D finite element model was constructed.

Considering the very small deformations at which the formation of the crack occurs, the numerical model represents a valuable contribution to understand the dominant micro-mechanisms occurring at this stage of the cracking process. Assuming that the specimen is composed of the cementitious matrix only, the contribution of the adopted geometry and of the notches to the initiation and propagation of a single crack plane was studied. The geometry of the left half of the modeled portion of the specimen and the adopted finite element mesh are shown in Figure 2.12 and Figure 2.13, respectively.

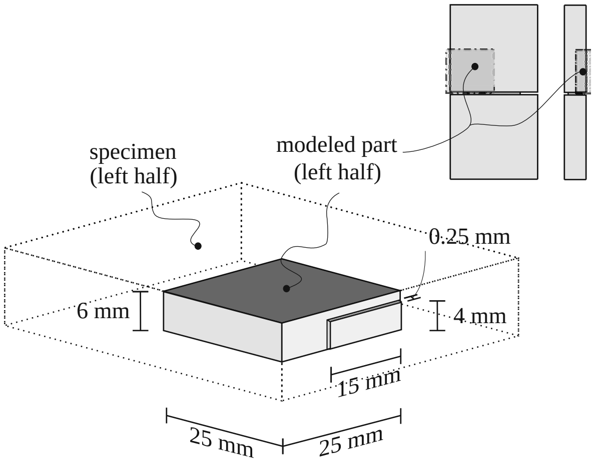

Figure 2.12: Geometry of the left half of the modeled portion of the specimen.

In Figure 2.14 the mesh near the lateral notch tip and at the mid-plane of the specimen ($x_3 = 0$) is shown. In Figure 2.15 the mesh near the lateral notch tip is shown, when looking from the top ($x_3 = 6$ mm).

One quarter of the specimen was modeled. In Figure 2.12 and Figure 2.13 only the left half of the modeled portion is displayed. In Figure 2.14 and Figure 2.15 both left and right parts of the modeled portion are shown, in a close view of the notch tip region. This simplification was possible due to the symmetry of the loading and the boundary conditions. Loading and structural bisymmetry with respect to the longitudinal axis (x_2, Figure 2.13) of the specimen have been assumed. The boundary conditions adopted in the simulation are presented in Figure 2.13, where δ_u represents the prescribed displacement increment at each step of the numerical simulation.

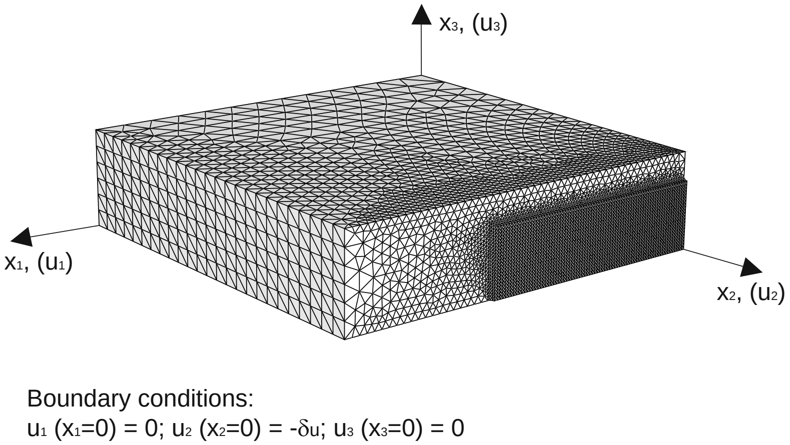

Figure 2.13: 3D finite element mesh used to model the specimen, boundary conditions and prescribed displacement increment.

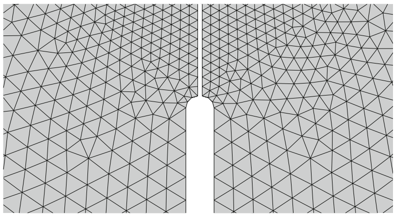

Figure 2.14: Mesh in the region of the notch tip, plane $x_3 = 0$.

The model was constructed using elastic 4-noded linear tetrahedral volume elements. The high geometrical gradients close to the notches were modeled with a significant increase of the number of elements in these regions, as represented in Figure 2.13, Figure 2.14 and Figure 2.15. The blunted shape of the notch tip, with a radius of 250 μm, was discretized with sufficient smoothness, relevant for the satisfactory approximation of the real stress intensity at the tip of the notches. The young modulus assigned to the elements was 20 GPa and the Poisson coefficient was 0.2. One layer of interface elements was added in the notched section between the left and the right parts of the modeled quarter ($x_2 = 25$ mm in Figure 2.13; Figure 2.16). These interface elements were assigned with a linear softening stress-separation law, typical of cement-based materials exhibiting quasi-brittle behavior in tension (Figure 2.16). The local tensile strength, σ_{cr}, was assumed equal to 5.0 MPa, and the ultimate crack opening, w_u, equal to 10.0 μm (Figure 2.16), which correspond to the matrix fracture energy, G_f, of 25 J/m^2. The local tensile strength, σ_{cr}, was approximately

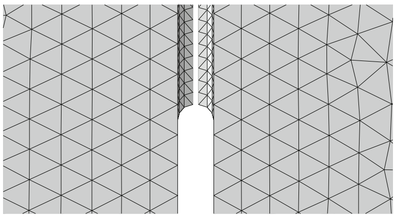

Figure 2.15: Mesh in the region of the notch tip, plane $x_3 = 6$mm.

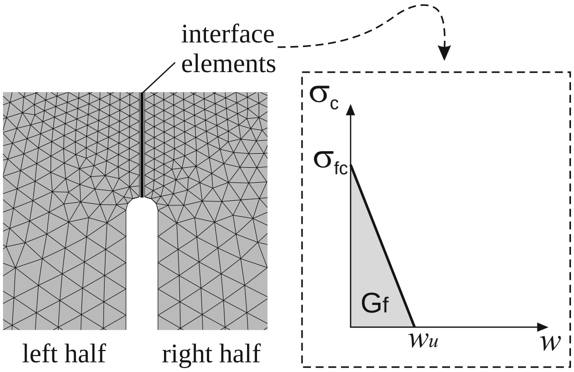

Figure 2.16: Detail of the 3D mesh close to the notch tip (plane $x_3 = 0$) and stress-crack opening law adopted for the interface elements.

estimated based on the average compressive strength results obtained for the composite reinforced with 2% of PVA fibers [Làrusson et al., 2011] and on the compressive strength-tensile strength relationships proposed by [Comite Euro-international du Beton, 1993]. The ultimate crack opening, w_u and the fracture energy, G_f, were approximately estimated considering the experimental results obtained by other researchers dealing with the fracture properties of mortar and concrete [Bazant and Pfeiffer, 1987; Bazant and Kazemi, 1990; Lange et al., 1993; Li et al., 1993; Stang and Aarre, 1992]. These parameters were not obtained by previous trial and error, or fitting to any specific group of the experimental results obtained. The estimated fracture parameters were directly used to analyze and explain the overall behavior and early conditions of crack initiation and propagation in the notched specimens.

2.5.2 Numerical results

In Figure 2.17 the general load-displacement curve obtained with the numerical model is presented. Increments 2, 10 and 36 of the increment-iterative algorithm are highlighted for three distinct load levels.

The effect of the notches and specimen geometry are best understood by visualizing the major principal stress fields produced at the longitudinal mid-plane of the specimen ($x_3 = 0$, Figure 2.13). In Figure 2.18 these stress fields are represented for the two of the distinct load levels previously identified in Figure 2.17.

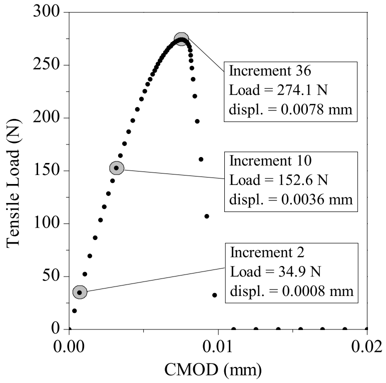

Figure 2.17: Axial load-displacement curve obtained with the numerical model of one quarter of the specimen.

The stress fields generated at the outer surface of the specimen ($x_3 = 6$ mm, Figure 2.13) are also displayed in Figure 2.19. These allow the visualization of the effect produced by the longitudinal notches, which seem to help with keeping the path of the crack progression confined inside the notched section.

The numerical results presented in Figure 2.17 to Figure 2.19 show that the initiation and complete formation of the crack is greatly conditioned by the geometry of the specimen and the notched section. In Figure 2.17 the load-displacement curve shows a deviation from the linear elastic behavior starting almost from the onset of the tensile test. The presence of the slender notches creates high stress intensity at the corners of the rectangular notched cross-section, as shown in Figure 2.18 and Figure 2.19 for two distinct load levels. The major principal stress reaches the local tensile strength, σ_{cr}, (5.0 MPa) at the referred corners when the tensile load reaches 13% of the tensile peak load (load increment 2, see Figure 2.17). Therefore cracking

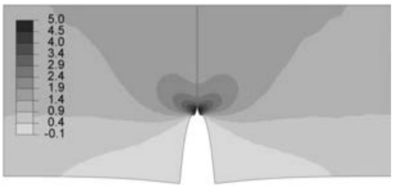

Load increment = 10

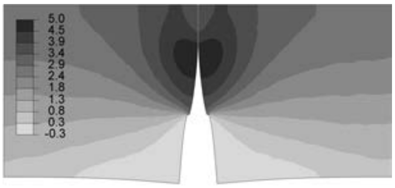

Load increment = 36

Figure 2.18: Major principal stress field (MPa) at the longitudinal mid-plane ($x_3 = 0$).

Load increment = 10

Load increment = 36

Figure 2.19: Major principal stress field (MPa) at the outer surface of the specimen ($x_3 = 6$ mm).

process starts early.

The results obtained allow establishing a relation between the local tensile strength, σ_{cr}, and the numerical peak nominal stress. Observing the results obtained with the numerical model, the peak load reaches the maximum value of 274.1 N (one quarter of the specimen). Dividing the peak load by the net area of the notched cross-section, the numerical peak nominal stress of 4.57 MPa is obtained. The ratio between the numerical peak nominal stress and the local tensile strength, σ_{cr}, is 91%, as a result of the local stress intensification produced by the notches and the geometry of the specimen. Disregarding the contribution of the fibers, this means that the local composite tensile cracking stress should be approximately 9% higher than the nominal peak cracking stress. This information can be used later on to estimate the cracking tensile stress for design purposes, based on the experimental results obtained with the SCTT.

When the local tensile strength, σ_{cr}, is reached at the corners of the notched section, the numerical nominal stress is 0.58 MPa. The necessary single crack plane is initiated at the corners, propagating afterwards rapidly to the middle of the notched section. The major principal stress fields in Figure 2.19 reveal that the stress intensification produced inside the notches is significant, while the stress levels outside the notches remain low. This effect produces the shielding of the crack plane, keeping the crack progression confined to the plane of the notched section. For the better understanding of the resulting 3D shielding effect of crack propagation, the major principal stress fields are displayed at three different load levels in Figure 2.20. As shown, the crack front is shaped and guided by the lateral long notches. The geometry of the specimen effectively contributes to the initiation and propagation of a single crack plane.

After the full development of the crack surface, the migration of the tensile stresses from the matrix to the fibers produces the rapid decrease of the tensile stiffness. Together with the simultaneous increase of the crack opening displacement, these contribute to keep the crack plane single. Nevertheless, if the bridging stresses reach very high levels in a later stage, secondary parallel crack planes may subsequently form. This event would affect the experimental tensile stress-crack opening curves obtained. The formation of secondary parallel cracks would result in visible abrupt load drops during the post-cracking tensile hardening stage. In this case, the attainment of a single crack could be recovered by increasing the ratio between the net area of the un-notched and the notched cross-sections. The notch slenderness could be increased as well for the enhancement of the stress intensification at the tip of the notches, but in this case a different cutting technique would be necessary.

Observing again the major principal stress fields in Figure 2.18, these show that an envelope of high stresses surrounding the crack tip exists. This envelope of high stresses follows the crack tip while it propagates from its onset at the corners of the

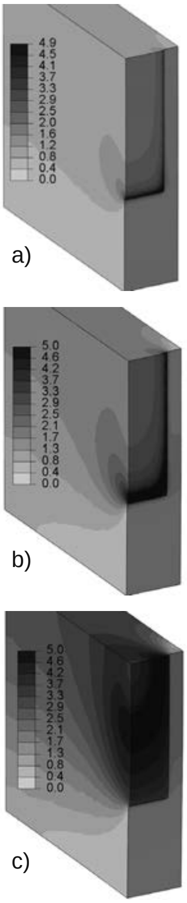

Figure 2.20: Major principal stresses (MPa) at the notched section for: a) load increment 2, b) load increment 10 and c) load increment 36.

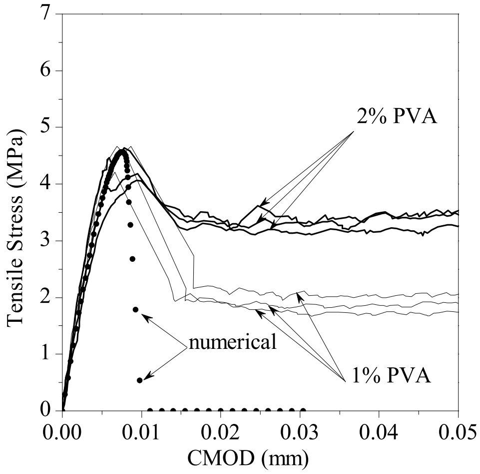

Figure 2.21: Numerical and experimental tensile stress-crack opening results for 1% PVA and 2% PVA fiber reinforced composites.

notched section to the middle. The maximum size of the 90% stress envelope (the curve limiting the area where the stresses are equal or greater than 90% of the local tensile strength, σ_{cr}, see Figure 2.18) is approximately 2.5 mm at the peak load (load increment 36, see Figure 2.17). The high stress in this region may cause initial damage in the matrix. In a later stage, with the increase of the crack bridging stress, these previously damaged areas may induce the formation of secondary cracks. In the present case, regarding the length and diameter of the fibers used, the size of this high stress envelope seems small enough to be considered insignificant, remaining the crack plane single. Nevertheless this should be reconsidered, if different material scales are involved, including the size of the fibers or the aggregates.

Before the full development of the crack surface, the resulting tensile behavior is mainly determined by the fracture properties of the matrix. The experimental and the numerical results at this stage are compared in Figure 2.21, Figure 2.22 and Figure 2.23. Considering the numerical results, the nominal stress was computed by multiplying the numerical load (see Figure 2.17) by 4 (due to the symmetry conditions) and dividing it by the net area of the notched cross-section. The nominal stress values were plotted for each CMOD, that is the relative displacement in x_2 direction between two points placed in opposite sides of the notch. In the numerical model, these two points were placed in the same positions as the ones adopted by the clip gauges in the experimental test-setup (see Figure 2.9).

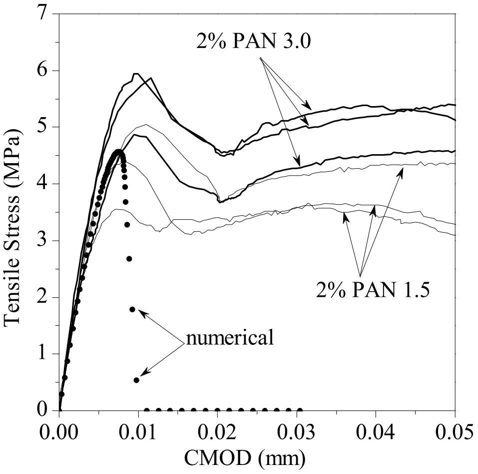

Figure 2.22: Numerical and experimental tensile stress-crack opening results for PAN 1.5 and PAN 3.0 fiber reinforced composites.

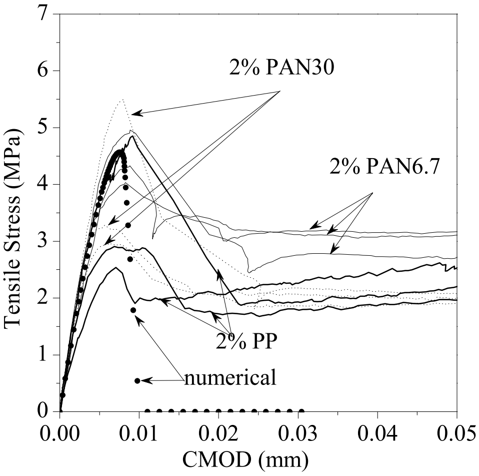

Figure 2.23: Numerical and experimental tensile stress-crack opening results for PAN 6.7, PAN 30 and PP fiber reinforced composites.

In general, Figures 2.21, 2.22 and 2.23 show a good correlation between the experimental and the numerical results during the initial stage of cracking. The higher scatter of results obtained with PAN1.5 and PAN3.0 may be explained by the reduced diameter of these fibers. While in the fresh state, the thinner PAN1.5 and PAN3.0 fibers showed to be more difficult to mixture and disperse, due to their considerably greater specific surface. Since the matrix used was the same for all fibers and not adapted to perform better with the thinner ones, the adverse fresh mixture properties obtained with the PAN1.5 and PAN3.0 have resulted in decreased homogeneity after hardening. Nevertheless, a substantial difference between the pre-peak behaviors obtained with the different fibers is observed. This suggests that the thinner fibers, due to their greater specific surface and the resulting enhanced bond with the matrix, contribute to the increase of the peak load at this stage. Their earlier mobilization in tension may explain this result. PAN3.0 fibers start contributing to resisting the tensile stresses at much smaller crack openings, delivering a superior contribution to the tensile hardening mechanisms in the early stage of the crack formation and propagation. This effect was not so visible for the PAN1.5 fibers, due to the adverse fresh mixture properties and the resulting loss of homogeneity caused by the very small diameter of the fibers. In the case of the composites reinforced with PAN 30 and PP fibers (Figure 2.23), the higher scatter of results may be the consequence of a weaker fiber-matrix interfacial bonding. The weak activation of these fibers at this stage results in a less controlled process of the crack initiation and propagation, as shown by the frequent snap-back effects in the tensile stress-CMOD curves.

In the region of the tensile stress-crack opening behavior where cracking occurs, for most of the composites the post-cracking tensile softening occurs smoothly, with a gradual decrease of the tensile stress at increasing CMOD. For the PAN fiber reinforced composites, although the specimens reach higher stresses during cracking, the post-peak load decay is still smooth, due to the improved mobilization of the thinner fibers at this stage. This indicates that the fibers contribute to restrain the abrupt release of energy during the brittle failure of the matrix. It has been previously shown that the crack initiates and propagates in the matrix at a very limited period. During this period, depending on the geometry of the fibers and their interaction with the matrix, their activation in tension occurs earlier or later and more or less effectively. For the 1% PVA fiber reinforced composite a small post-cracking jump of the CMOD seems to occur. The fiber reinforcement ratio in this case may be insufficient to restrain crack propagation in a controlled manner for a limited period. The abrupt energy release associated with the matrix fracture seems to be larger than the energy dissipation ability provided by only 1% of PVA fiber reinforcement.

The displacements observed when the cracking peak load is reached are very small. This stage of the single crack behavior seems to contain very relevant information for the characterization and design of the composite mechanics. The convenient characterization of the stage where the transfer of the tensile stresses from the matrix to the fibers occurs is essential for the successful design of the composite toward pseudo-strain hardening in tension and multiple cracking ability.

2.6 Image analysis of crack propagation

2.6.1 Procedure and method

The formation and propagation of the tensile crack was monitored at the surface of the specimens using a digital image-based system. The setup comprised two high resolution cameras, positioned 270 mm away from the specimen and 130 mm apart from each other (see Figure 2.24). Two lenses with focal length of 50 mm were used, allowing the observation of a 50 mm by 50 mm area in the surface of the specimen at a working distance of 270 mm. Photos with a resolution of 4 megapixel were captured during testing with time intervals of 0.20 seconds. These photos were subsequently used for the continuous interpolation of the displacements and the derivation of the strain fields occurring at the surface of the inspected specimen.

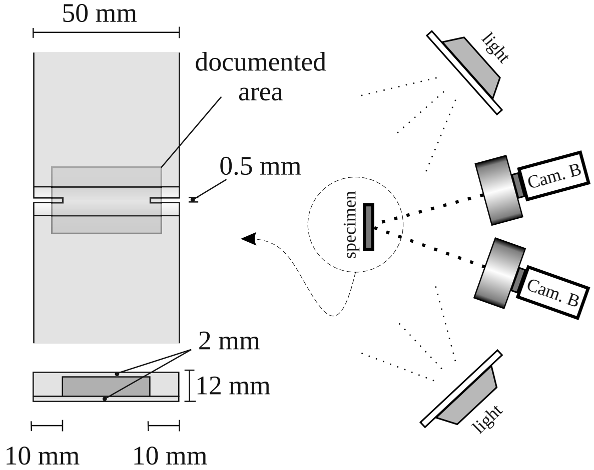

Figure 2.24: Geometry of the specimen and setup of the imaging system for the monitoring of surface deformations.

In order to allow the optical inspection of the crack, the geometry of the specimen near the notched section was altered. The original geometry (see Figure 2.8) was not viable because the intersection of the crack plane with the surface of the specimen was not visually accessible. The rounded shape and cylindrical surface at the notched area were adopted to approximate better the stress conditions of the original specimen in the notched section, as well as to allow the visual access to the intersection of the crack with the surface of the specimen (see Figures 2.24 and 2.25). Although the geometry of the specimen in the region of the notched cross section is different, the attainment of a single crack was verified visually. The crack surface obtained with one of the composites reinforced with 2% of PVA fibers is shown in Figure 2.25.

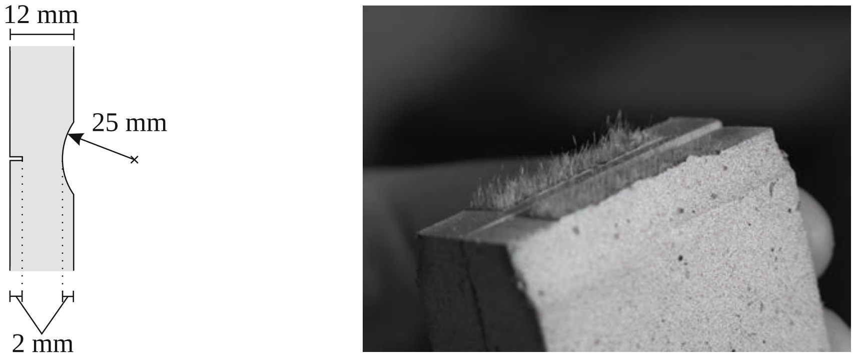

a)

b)

Figure 2.25: Single crack obtained with specimen used for the image analysis of cracking: a) schematic detail of transverse cut of the specimen in the rounded shape region and b) photograph sowing half of the specimen after testing.

The optimal conditions of image correlation were met with the application of a speckle pattern at the surface of the specimen. Sufficient randomness and high contrast of the pattern captured from the surface is important for the continuous recognition and tracing of the shape and position of each facet. In the present case, each facet was composed of 10×10 pixels. Each pixel covered a real area of 25×25 μm^2. The total area of 50×50 mm^2 was covered by a facet mesh overlay of 200×200 facets.

2.6.2 Image analysis results

Specimens with the geometry presented in Figure 2.24 were tested and a single crack was obtained and confirmed visually. The typical tensile stress-CMOD behavior obtained is presented in Figure 2.26. A few relevant stages of the image-based monitoring procedure are identified, consisting of representative generic stages of the material single crack tensile behavior.

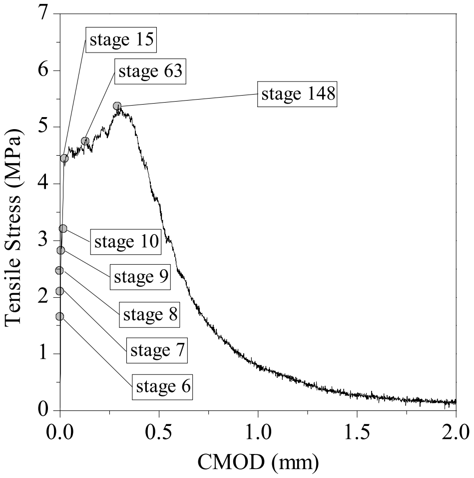

Figure 2.26: Tensile Stress-CMOD obtained during imaging and identification of relevant image-based monitoring stages.

The strain fields were derived from the displacements computed at each facet adopting the digital correlation procedure. Each facet is treated as a continuum and strains are derived from displacements according to the principles of continuum mechanics [Chu et al., 1985]. Cracks are, however, intuitively identified by visualizing the the major principal strain fields. The small facet size contributes to the high resolution with which the appearing cracks are identified and represented. The results in terms of major principal strains at the facet overlay are represented in Figure 2.27. The stages highlighted previously (see Figure 2.26) are identified in each frame.

The image-based monitoring of the cracking process near the notched area allowed the detailed tracing of the crack initiation and propagation stages. The initiation of the tensile crack is already visible in stage 9, near the two opposite corners of the

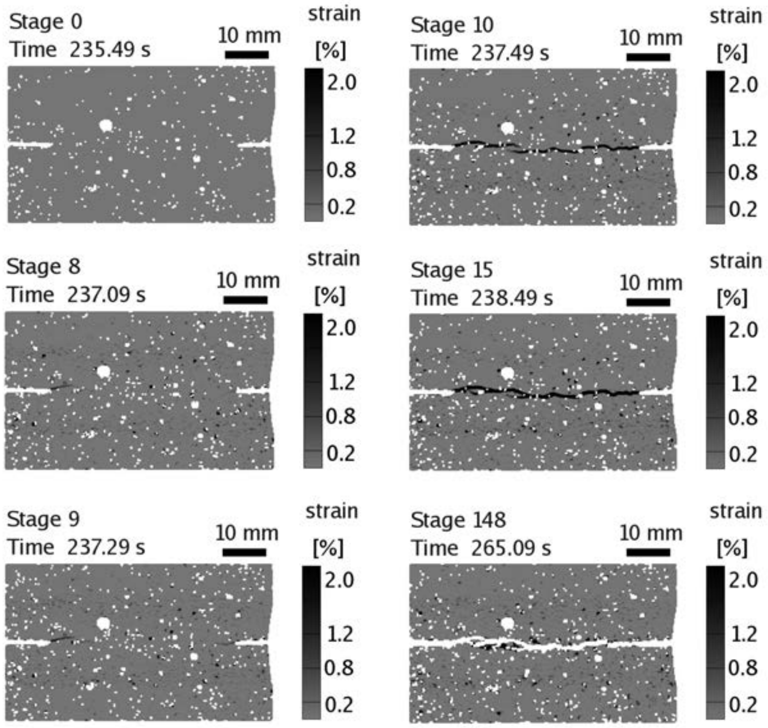

Figure 2.27: Major principal strains in the facets overlay based on the sequence of images of the specimen. The time step between stages is 200 ms.

notched cross-section. 200 ms later the crack had propagated to the center of the notched section, as shown in stage 10 (see Figure 2.27). A straight and localized crack plane has formed. From stage 15 onwards, the crack seems to remain single and fully developed. The fiber bridging mechanisms assure the necessary stress transfer ability for the specimen to keep withstanding an increasing tensile load.

To further analyze these results, the captured stages are presented in a closer view in Figure 2.28. For each stage, on the left hand side the original photo taken from the surface of the specimen is zoomed. On the right hand side the interpolated major principal strains are shown, together with a virtual clip gauge showing the interpolated crack opening near the tip of the notch. The word *virtual* is herein utilized to distinguish the results obtained with the image-based deformation analysis from the results obtained experimentally with *physical* clip gauges. In both cases, the result refers to the displacement difference between two points. The main advantage of this image-based monitoring technique is that it allows the simple and straightforward tracing of the evolution of the principal strains throughout the sequence of stages represented. The cracking processes are accurately revealed, from their onset.

The concept of an open discrete crack is rather unclear. The distinction between a preliminary diffuse micro-cracking region ahead of the crack tip and the subsequent coalesced crack is conceptually difficult to define. Nevertheless, the cracking topology was captured and identified with good resolution, much before it became visible. The observed thin and elongated shape of a hypothetical fracture processing zone ahead of the crack tip, typical of cementitious matrices, agrees with the observations of other researchers [Bolander and Hirosaka, 1995; Otsuka and Date, 2000].

As shown in Figure 2.28, the notch creates the necessary local stress or deformation conditions to the initiation of a single crack. After initiation, the crack propagates to the center of the specimen, remaining single and straight. After the full development of the crack throughout the entire specimen, the two opposite crack faces remain interconnected only by the fibers bridging them, which seems to occur at stage 15. The mechanical characteristics of the subsequent hardening and softening stages are determined by the fiber reinforcement parameters only, including the number, geometry, mechanical properties, orientation and interfacial bonding established between the fibers and the surrounding matrix.

2.6.3 Simulation of the post-cracking behavior

Considering that a single crack was consistently obtained while performing the SCTT, the numerical model previously presented can adequately simulate the entire tensile

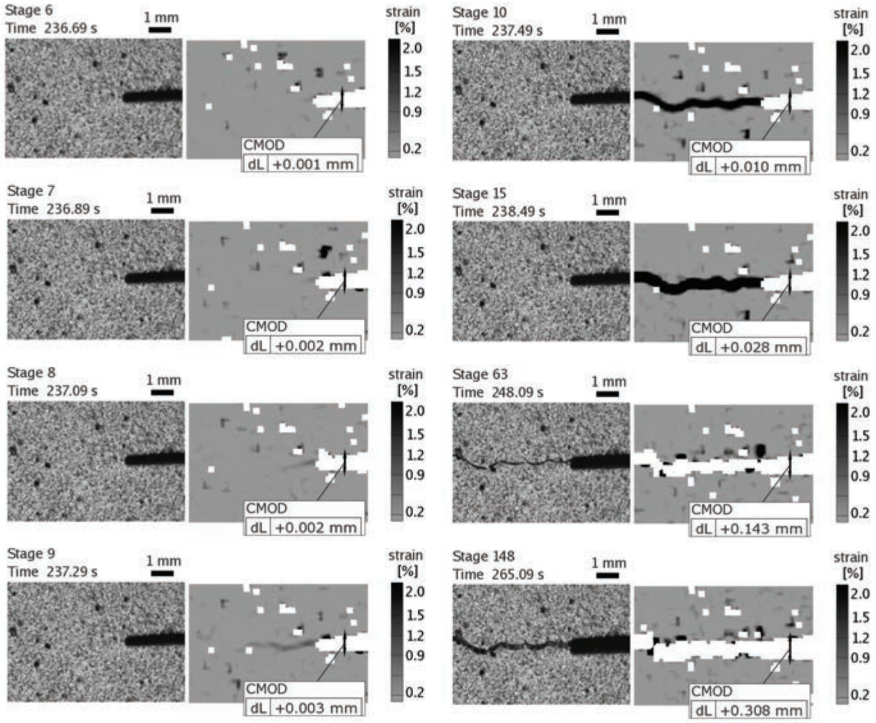

Figure 2.28: Detailed image-based deformation analysis near the notch tip, showing cracking initiation and propagation.

response of the specimen if one layer of interface elements is positioned at the expected crack plane in the numerical model. For comparison, the traction-separation law assigned to the interface elements was derived from the SCTT tensile stress-crack opening response experimentally obtained for the 2.0% PVA fiber reinforced cementitious composite. The traction-separation law was derived by extracting the post-cracking portion of the average experimental tensile stress-CMOD curve. The post-cracking portion of the tensile stress-CMOD curves starts at the point where the first cracking stress is reached. The first cracking stress corresponds to the peak stress reached during the first hardening sequence and before the subsequent abrupt load decay, which determines the conclusion of the crack propagation process. Further description of the most important parameters of the tensile stress-CMOD response will be presented in a subsequent section. Typically, the first cracking stress was reached for CMOD values between 8 μm and 12 μm (see Figures 2.21 to 2.23). All experimental measurements (10 per second) were used to define the traction-separation law. The numerical results obtained are presented in Figure 2.29 and compared to the experimental average curve previously shown.

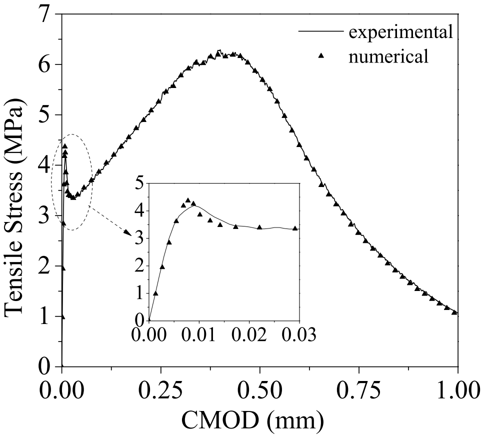

Figure 2.29: Numerical simulation of the entire tensile stress-CMOD response obtained for the 2% PVA FRCC.

The numerical response obtained is mostly identical to the experimental, with slight differences observed at the initial stage. During the initiation and propagation of the crack, the geometry of the specimen and of the notches influence somewhat the shape of the tensile stress-CMOD response. In contrast, this influence may be neglected after the crack is fully formed, while the opposite crack flanks become bridged by the fibers exclusively. The influence of the specimen geometry on the initial stages of the tensile responses is, in part, revealed by the slight discrepancy between the crack opening when observed at the notch mouth or at the tip of the notch. As shown in Figure 2.30, although the tensile stresses in the region of the notch mouth remain low, the crack tip opening displacement (δ) is slightly overestimated when evaluated outside the notch, that is, when the crack mouth opening displacement (w) is evaluated and used as approximation. This effect tends to be insignificant after the crack is fully formed. Therefore, when the traction-separation law adopted in the numerical model is derived utilizing the experimental tensile stress-crack opening curve, the described effect may justify the small difference observed at the initial part of the response, during the crack initiation and propagation stages.

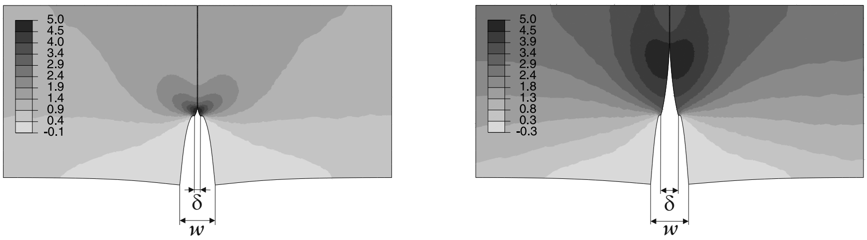

a)

b)

Figure 2.30: Difference between the crack tip opening displacement (δ) and the crack mouth opening displacement (w) at two different stages of the crack initiation and propagation: a) load increment 10, and b) load increment 36 (see Figure 2.17).

To compare the crack profiles obtained with the image-based analysis and the numerical simulation, two distinct loading stages were selected. The crack profiles measured with the image-based analysis system at stages 9 and 15 (see Figure 2.26) are compared with the crack profiles obtained in the numerical model at the load increments where the same CMOD was measured (Figure 2.31). In the image-based analysis, the crack opening displacement (δ) was measured in 30 equally spaced points along the crack path, using virtual clip gauges with a length of 5 mm. The crack opening displacements measured are compared with the crack profiles obtained in the numerical model for one half of the ligament, with coordinate x_1 starting at the center of the ligament and ending at the tip of the notch ($x_1 = 15$ mm, see Figure 2.13).

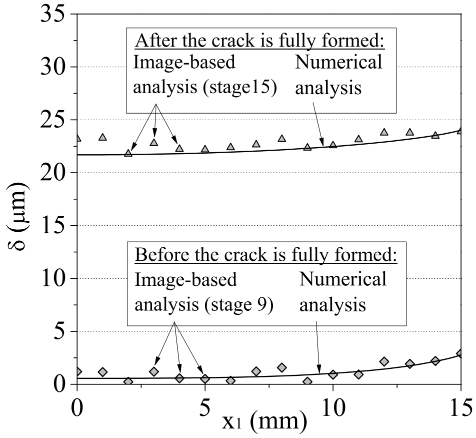

Figure 2.31: Crack profiles obtained in two stages of the cracking process, before and after the crack is fully formed.

2.7 Tensile stress-crack opening behavior in dogbone-shaped specimens

The tensile stress-strain behavior typically observed in SHCC specimens under direct tension is characterized as a tensile pseudo-strain hardening behavior. The overall tensile hardening experienced by SHCC specimens in tension occurs while the deformation in the loading direction significantly increases due to the formation of multiple parallel cracks perpendicular to the loading direction. This pseudo-strain hardening behavior in tension and the formation of multiple parallel cracks are possible because individual cracks in the SHCC material are designed to develop fiber bridging stresses that exceed the first cracking strength. Furthermore, the fracture energy involved in the formation of an individual crack must meet an additional criterion for multiple cracking criterion to occur [Kanda and Li, 2006]. SHCC materials are micromechanically designed to withstand increasing tensile stresses after the formation of cracks. Although the cement-based matrix is brittle, the fiber bridging stresses at a crack exceed the cracking stress of the cement-based matrix, therefore allowing the formation of additional parallel cracks before ultimate failure. As a result of this multiple cracking in tension, SHCC materials exhibit high toughness and ductile behavior in tension.

The importance of the fiber bridging mechanisms to the pseudo-strain hardening behavior is the motivation in the investigation of the tensile behavior of SHCC at

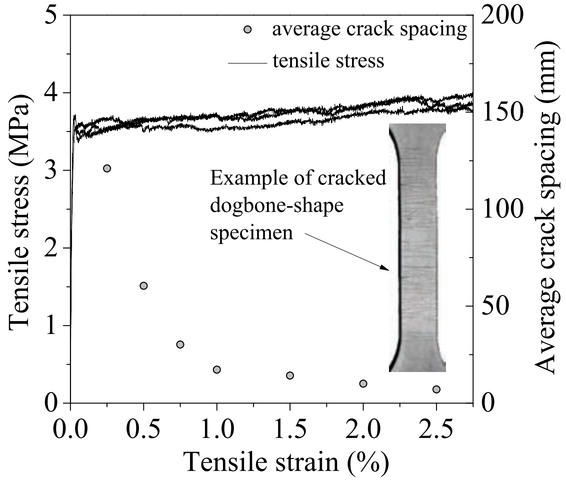

Figure 2.32: Tensile stress-strain curves and average crack spacing obtained from three dogbone-shaped specimens of 2% PVA FRCC [Làrusson et al., 2011].

the level of a single crack. In a previous section, the procedure utilized to characterize the tensile stress-crack opening behavior of various FRCC was described. To evaluate how these results compare with experimentally obtained data of the tensile stress-crack opening behavior in dogbone specimens with multiple crack formation, in Figure 2.32 the tensile stress-strain behavior obtained for the composite containing 2.0% of PVA fibers is shown [Làrusson et al., 2011]. Dogbone specimens with fixed rotation boundary conditions were subjected to a constant tensile displacement rate of 1.0 mm/min. The specimens reached a tensile strength of 4.2 MPa at a tensile strain of 4.5%. In a closer view of the results obtained up to a tensile strain of 2.5%, tensile hardening is observed while the tensile deformation significantly increases. The formation of several parallel cracks was verified during testing until tensile failure of the specimens occurred with the localization of the deformations at one crack, after cracking saturation.

The image-based analysis described in previous section was utilized to interpolate the displacements at the surface of the specimens during the entire loading sequence. Using the results of the image-based deformation analysis, it was possible to trace the evolution of the tensile stress-crack opening displacement at each crack during testing. The nominal tensile stress was obtained by dividing the tensile load by the net area of the specimen cross section, 25×50 mm^2. The tensile stress-crack opening behavior was characterized at 30 cracks. In Figure 2.33 the setup used to measure the

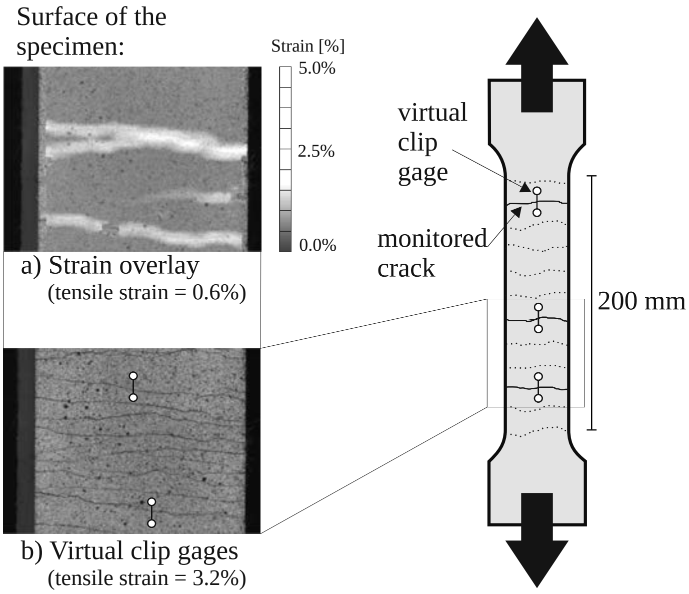

Figure 2.33: Schematic of the cracked dogbone specimen and results obtained with the image-based deformation analysis: a) cracked surface and strain overlay at 0.6% of tensile strain and b) cracked surface at 3.2% of tensile strain and positioning of two virtual clip gauges used to monitor the crack opening displacements.

deformations at the surface of the dogbone-shaped specimen is explained. The strain overlay, resulting from the image-based deformation analysis, reveals the formation of cracks at the early stage of the tensile loading, as shown at a tensile strain of 0.6%. At increasing tensile strain the cracks become clearly visible, as shown at a tensile strain of 3.2%. The crack opening at three representative cracks was traced during the entire loading sequence using the virtual clip gauges, as exemplified. In Figure 2.34 the tensile stress-crack opening obtained for these three representative cracks is shown.

Due to the typical scatter of sectional properties in cement-based composites, the first cracking strength and the density of fiber distribution are different at each location of the specimen, therefore a range of tensile stress-crack opening behaviors are expected at the observed crack locations. Within this range, a general trend can be observed as initial crack widening at almost constant tensile stress, followed by tensile hardening identical to the observed in the SCTT. As a result of the interaction between the cracks during the formation and propagation phase in the dogbone-shaped specimen, a full interpretation of the mechanisms governing the overall behavior ob-

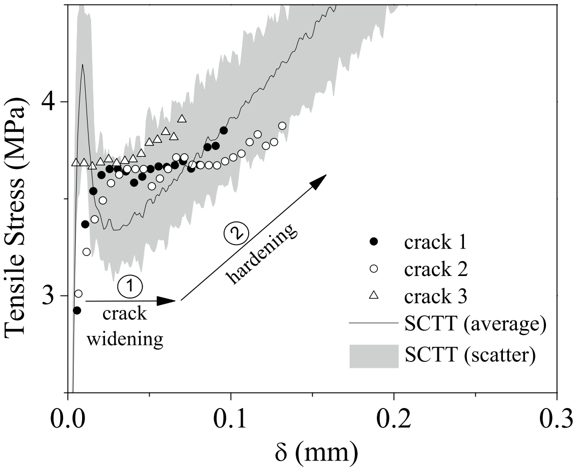

Figure 2.34: Tensile stress-crack opening (δ) curves obtained at three representative cracks and comparison with the SCTT results.

served is complex and out of the scope of the present investigation. In general, the results suggest that once the cracks have propagated through the specimen cross-section and the deformations have reached a steady state, the tensile stress-crack opening behaviors observed in the dogbone-shaped specimen are found within the range predicted by the SCTT. The tensile strength observed in the SCTT is not reached because the crack that determines the rupture of the dogbone-shaped specimen is the weakest in terms of bridging tensile strength. Therefore, for simulation or design purposes, a probabilistic description of the tensile stress-crack opening behavior characterized with the SCTT is necessary.

2.8 Composite behavior at the level of a single crack

The results obtained with the seven different composites showed, in general, a good agreement between different tests for each composite. As shown in Figure 2.11, the results are consistent, revealing the intrinsic mechanics of each composite system. The influence of the geometric and mechanical parameters of each fiber reinforcing system can be identified and studied. The activation of fibers with different diameters has been shown to occur at different stages of the cracking process. The PAN fibers, with a smaller diameter, were activated even before the first cracking strength was reached, and contributed effectively to the increase of the cracking peak stress. Their premature activation was followed by an also premature exhaustion of their contribution to the post-cracking tensile behavior. The contribution of PVA and PP fibers to the increase of the first cracking strength was negligible. Instead their full mobilization occurs after cracking, with significant tensile hardening ramps developing after cracking in both cases. The main difference between the SCTT results observed for PVA and PP fiber reinforced composites located in the region of the tensile stress-crack opening curves where the peak bridging stress is reached. While for the PVA fiber reinforced composites the experimental curves exhibited a sharp transition between the tensile hardening and the tensile softening stages, with the PP reinforced composites this transition occurs gradually and smoothly. The well known superior interfacial bonding of the PVA fibers with the matrix may justify these results, as opposed to the poorer bonding of the PP fibers due to their hydrophobic nature [Li et al., 2002; Wei et al., 2002]. Therefore, the gradual increase of the tensile stress in the fibers, during the composite tensile hardening stage after cracking, causes the premature debonding of a gradually increasing number of PP fibers, resulting in the also gradual decrease of the tensile hardening stiffness for increasing CMOD and the observed smooth transition to softening. The superior bonding of the PVA fibers with the matrix results in a constant tensile hardening stiffness after cracking, with most of the fibers being fully mobilized. Once the applied tensile stress in the composite approaches the peak bridging stress, the great majority of active fibers start rupturing. Therefore the tensile softening occurs more rapidly with the PVA fiber reinforced composite than with the PP fiber one, exhibiting the tensile stress-crack opening curve a sharp transition from the tensile hardening to the tensile softening stages. In addition, the composites reinforced with PP fibers maintain higher residual tensile strengths for relatively large CMOD, as a result of the reduced interfacial bonding and the preservation of a higher number of active fibers for greater CMOD.

The obtained results suggest that a group of generic stages of a typical tensile stress-crack opening behavior can be distinguished. At the onset of tensile testing, the mechanical response starts with what is usually assumed as the predominantly elastic behavior, with a steep increase in the applied load while tensile deformation increases. This first stage ends when the nominal matrix cracking strength is achieved, with the rapid transfer of the tensile stresses from the cracked matrix to the fibers and the subsequent rapid tensile load decay. Preliminary stages of micro-cracking and micro-defects propagation may affect the shape of this transition stage, governed by fracture mechanisms and dependent on the shape and size of pores and micro-defects. The micro-mechanisms taking place at this stage were systematically discussed in the previous section, supported by the numerical model and the image-based monitoring results. Fibers may also play a role at this stage as crack inducers, but the extension of the experimental data available is not detailed enough to allow a thorough analy-

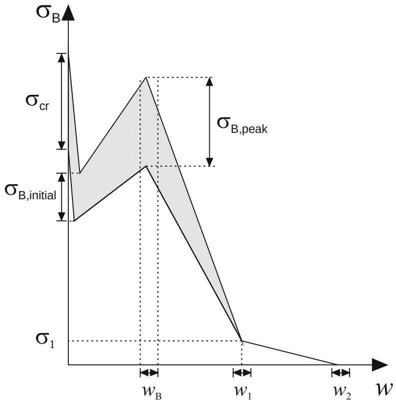

Figure 2.35: Tensile stress-crack opening design law for SHCC [Yang and Fischer, 2006].

sis of this mechanism. Packing density of the solid skeleton is also influenced by the presence of the fibers and their geometry, which in turn affect the matrix fracture properties.

After the rapid load decay caused by the transfer of the tensile stresses from the matrix to the fibers, a new hardening stage supported by the full mobilization of the fiber-matrix bonding mechanisms is initiated. While the fibers stretch, hardening occurs until the peak bridging stress is reached. In this third stage the stiffening effect of the fiber reinforcement is exhausted either due to fiber debonding and slip-softening pull out mechanisms or fiber rupture. The result is, respectively, a smooth or sharp transition between the tensile hardening and softening stages.

The fourth stage consists of the post-peak softening stage observed in all curves. It coincides with the gradual neutralization of the remaining links between opposite crack faces. This stage may be divided into two different branches with different inclinations, one steeper and other mostly horizontal, influenced by the geometry and the mechanical properties of the aggregates and the fibers.

The sequence of stages previously described consists of an interpretation of complex mechanisms taking place at the level of a single crack in the bulk composite, which summarize and condense in a rational way the tensile behaviors observed, useful from a design perspective. In Figure 2.35, this systematic approach of the tensile stress-crack opening behavior is summarized in the shape of a constitutive design law [Yang and Fischer, 2006].

The identification of the parameters defining the shape of the bridging stress,

σ_B, versus the crack opening, w, relationship may be carried out experimentally using the SCTT. For that purpose the test setup conditions suggested above can be adopted. The first cracking strength,σ_{cr}, the initial bridging stress, $\sigma_{B,initial}$, the peak bridging stress, $\sigma_{B,peak}$, and the corresponding crack opening at peak bridging stress, w_B , represent the most significant parameters to be identified. Subsequently the residual bridging stress, σ_1, the corresponding crack opening, w_1, and finally the ultimate cohesive crack opening, w_2, represent also important design parameters. All this data, and the scatter associated to each of these parameters, may be used to support the structural design and to define safety factors for each mechanical parameter. Alternatively, the material requirements may be imposed by the structural concept. These requirements may assume the shape of a predefined bridging stress-crack opening curve, which will guide the material design with a fiber reinforced cementitious composite based solution. Material and structural design may be integrated with this approach.

The sequence of distinctive stages above mentioned is clearly identifiable in all tested composites. The adopted fiber reinforcements show different mechanical performances in tension, however these stages remain clearly distinctive and keep the same formal details. This suggests that a rational design approach can be based on the assumption that the tensile stress-crack opening behavior of FRCC follows a standard sequence of stages assuming the shape of a generic tensile stress-crack opening design curve (see Figure 2.35).

2.9 Conclusions

The objective of characterizing the tensile behavior of SHCC at the level of a single crack described in this study was approached by performing the proposed single crack tension test (SCTT). The formation of a single, localized crack was consistently confirmed on tension softening and pseudo-strain hardening materials. With the purpose of understanding the nature and topology of the cracks generated when using the proposed SCTT setup, the crack formation and propagation stages during testing were documented using an image-based deformation analysis system. This procedure allowed the visualization of the displacements at the surface of the specimen with reasonable accuracy. The initiation and propagation of a single crack during the pre- and post-cracking stages were observed and the measured crack profiles during testing showed good correlation with the crack profiles obtained at the same CMOD using the numerical simulation. The experimental tensile stress-crack opening responses were also utilized to derive the cohesive law of the interface elements adopted in the numerical model of the SCTT. The numerical responses obtained were in good agreement with the experimental tensile stress-CMOD responses, supporting the assumption that a single crack is forming during the loading sequence in the SCTT. In particular, the geometry and reduced thickness of the adopted notches were demonstrated to have an important influence on the formation of a single crack during the entire loading process.

The activation of fibers with different diameters occurred at different stages of the cracking process of SCTT. The fibers of smaller diameter showed significant contribution even before the first cracking strength was reached, collaborating effectively to the increase of the first cracking strength. The fibers with larger diameter have demonstrated an effect on the tensile responses only after crack formation, contributing to the development of considerable post-cracking tensile hardening stages. The main difference between the tensile stress-crack opening behaviors observed with PVA and PP fibers was located at the region where the peak bridging stress is reached. While the PVA reinforced composites exhibited a sharp transition between the tensile hardening and softening stages, in the PP reinforced composites this transition was smooth and the peak bridging stress reached was lower. The SCTT showed high sensitivity to important composite properties, such as the different interfacial bonding characteristics, fiber properties and pull-out conditions established between the fibers and the matrix, which makes SCTT very attractive to support the design process of these materials.

The assessment of the tensile stress-crack opening behavior is important to the material constitutive modeling and the design of structures based on the finite element method. The response obtained can be summarized into a group of relevant fracture parameters, depending on the precision required in the design process. In terms of the material properties of SHCC, the design procedure may be based on a set of requirements established with respect to the main parameters characterizing the tensile stress-crack opening behavior, including the first cracking strength, the fiber bridging stiffness, the ultimate bridging strength and the crack opening at reaching the fiber bridging strength. The SCTT setup allows the explicit characterization of the stress-crack opening behavior and may therefore guide the process of designing and optimizing SHCC materials, as well as aid with the integration of material selection in the structural design process.

Bibliography

Aveston, J., Cooper, G., and A., K. (1972). Single and multiple cracking. In *The properties of fibre composites*, pages 15–24, Guilford UK. National Physical Laboratory, IPC Scinece and Technology Press.

Banthia, N. and Trottier, J.-F. (1995). Concrete reinforced with deformed steel fibers part ii: toughness characterization. *ACI Mater J*, 92(2):146–154.

Bazant, Z. and Kazemi, M. (1990). Determination of fracture energy, process zone length and brittleness number from size effect, with application to rock and concrete. *Int J Fract*, 44(2):111–131.

Bazant, Z. P. and Pfeiffer, P. A. (1987). Determination of fracture energy from size effect and brittleness number. *ACI Materials Journal*, 84(6):463–480.

Bentur, A. and Mindess, S. (2006). *Fibre reinforced cementitious composites*. Modern concrete technology series. Taylor & Francis.

Berfield, T., Patel, J., Shimmin, R., Braun, P., Lambros, J., and Sottos, N. (2007). Micro-and nanoscale deformation measurement of surface and internal planes via digital image correlation. *Exp Mech*, 47(1):51–62.

Bolander, J., J. and Hirosaka, H. (1995). Simulation of fracture in cement-based composites. *Cem Conc Comp*, 17(2):135–145.

Brandt, A. M. (2008). Fibre reinforced cement-based (frc) composites after over 40 years of development in building and civil engineering. *Compos Struct*, 86(1-3):3–9.

Chu, T. C., Ranson, W. F., and Sutton, M. A. (1985). Applications of digital-image-correlation techniques to experimental mechanics. *Exp Mech*, 25(3):232–244.

Comite Euro-international du Beton (1993). *CEB-FIP model code 1990: design code*. Number 213-214. T. Telford.

Cotterell, B. and Mai, Y.-W. (1996). *Fracture mechanics of cementitious materials*. Blackie, London.

Cunha, V., Barros, J., and Sena-Cruz, J. (2010). Pullout behavior of steel fibers in self-compacting concrete. *J. Mater. Civ. Eng.*, 22(1):1–9.

Fischer, G. and Li, V. C. (2007). Effect of fiber reinforcement on the response of structural members. *Eng Frac Mech*, 74(1-2):258–272.

Fischer, G., Stang, H., and Dick-Nielsen, L. (2007). Initiation and development of cracking in ecc materials: Experimental observations and modeling. In G.F.A., C. and Gambarova, P., editors, *High Performance Concrete, Brick- Masonry and Environmental Aspects.*, volume 3, pages 1517–1522. FraMCos, Taylor & Francis.

Geng, Y. and Leung, C. K. Y. (1996). A microstructural study of fibre/mortar interfaces during fibre debonding and pull-out. *Journal of Materials Science*, 31(5):1285–1294.

Kabele, P. (2007). Multiscale framework for modeling of fracture in high performance fiber reinforced cementitious composites. *Engineering Fracture Mechanics*, 74(1-2):194–209.

Kabele, P. (2009). Finite element fracture analysis of reinforced shcc members. In van Zijl, G. and Boshoff, W., editors, *Advances in Cement-Based Materials*, volume International Conference on Advanced Concrete Materials, pages 237–244, Stellenbosch, South Africa.

Kanda, T. and Li, V. (1998). Interface property and apparent strength of high-strength hydrophilic fiber in cement matrix. *ASCE Journal of Materials in Civil Engineering*, 10(1):5–13.

Kanda, T. and Li, V. C. (2006). Practical design criteria for saturated pseudo strain hardening behavior in ecc. *J Adv Conc Tech*, 4(1):59–72.

Karihaloo, B. (1995). *Fracture mechanics and structural concrete*. Longman Scientific and Technical, Harlow.

Krenchel, H. and Shah, S. (1985). Applications of polypropylene fibers in scandinavia. *Concr Int Concrete international*, 7(3):32–34.

Lange, D. A., Jennings, H. M., and Shah, S. P. (1993). Relationship between fracture surface roughness and fracture behavior of cement paste and mortar. *J Am Ceram Soc*, 76(3):589–597.

Leung, C. and Li, V. (1990). Strength-based and fracture-based approaches in the analysis of fiber debonding. *J. Mater. Sci. Lett.*, 9(10):1140–1142.

Leung, C. K. Y. and Li, V. C. (1992). Effect of fiber inclination on crack bridging stress in brittle fiber reinforced brittle matrix composites. *Journal of the Mechanics and Physics of Solids*, 40(6):1333–1362.

Li, Wu, H.-C., and Chan, Y.-W. (1996). Effect of plasma treatment of polyethylene fibers on interface and cementitious composite properties. *J. Am. Ceram. Soc. (USA)*, 79(3):700–704.

Li, V., Wang, Y., and Backer, S. (1990). Effect of inclining angle, bundling and surface treatment on synthetic fibre pull-out from a cement matrix. *Composites*, 21(2):132–140.

Li, V. and Wu, H. (1992). Conditions for pseudo strain-hardening in fiber reinforced brittle matrix composites. *Journal of Applied Mechanics Review*, 45(8):390–398.

Li, V. C. (1992). Postcrack scaling relations for fiber reinforced cementitious composites. *ASCE Journal of Materials in Civil Engineering*, 4(1):41–57.

Li, V. C. (2002). Large volume, high-performance applications of fibers in civil engineering. *Journal of Applied Polymer Science*, 83(3):660–686.

Li, V. C. (2003). On engineered cementitious composites (ecc). *J Adv Conc Tech*, 1(3):215–230.

Li, V. C. and Leung, C. K. (1992). Steady-state and multiple cracking of short random fiber composites. *Journal of Engineering Mechanics - ASCE*, 118(11):2246–2264.

Li, V. C. and Stang, H. (1997). Interface property characterization and strengthening mechanisms in fiber reinforced cement based composites. *Advanced Cement Based Materials*, 6(1):1–20.

Li, V. C., Stang, H., and Krenchel, H. (1993). Micromechanics of crack bridging in fibre-reinforced concrete. *Mater Struct*, 26(8):486–494.

Li, V. C., Wang, S., Ogawa, A., Saito, T., and Wu, C. (2002). Interface tailoring for strain-hardening polyvinyl alcohol-engineered cementitious composite (pva-ecc). *ACI Materials Journal*, 99(5):463–472.

Li, V. C., Wang, S., and Wu, C. (2001). Tensile strain-hardening behavior or polyvinyl alcohol engineered cementitious composite (pva-ecc). *ACI Mater J*, 98(6):483–492.

Lin, Z., Kanda, T., and Li, V. (1999). On interface property characterization and performance of fiber-reinforced centitious composites. *Concrete Science and Engineering*, 1:173–184.

Lin, Z. and Li, V. C. (1997). Crack bridging in fiber reinforced cementitious composites with slip-hardening interfaces. *Journal of the Mechanics and Physics of Solids*, 45(5):763–787.

Lofgren, I., Stang, H., and Olesen, J. F. (2008). The wst method, a fracture mechanics test method for frc. *Mater Struct*, 41(1):197–211.

Làrusson, L., Fischer, G., and Jonsson, J. (2010). Mechanical interaction of engineered cementitious composite (ecc) reinforced with fiber reinforced polymer (frp) rebar in tensile loading. In van Zijl, G. and Boshoff, W., editors, *Advances in Cement-based Materials*, pages 83–90, Stellenbosch, South Africa. Tailor & Francis.

Làrusson, L., Fischer, G., and Jonsson, J. (2011). Mechanical interaction between concrete and structural reinforcement in the tension stiffening process. In Parra-Montesinos, G., Reinhardt, H., and Naaman, A., editors, *High performance fiber reinforced cementitious compoistes 6*, volume 2, pages 247–254, Ann Arbor, USA. Springer.

Marshall, D. and Cox, B. (1988). A j-integral method for calculating steady-state matrix cracking stresses in composites. *Mechanics of Materials*, 7(2):127–133.

Morton, J. and Groves, G. W. (1976). The effect of metal wires on the fracture of a brittle-matrix composite. *Journal of Materials Science*, 11(4):617–622.

Naaman, A. (2008). *High Performance Fiber Reinforced Cement Composites*, volume 1 of *Engineering Materials for Technological Needs*, chapter 3, pages 91–154. World Scientific Publishing Co.

Naaman, A. E., Fischer, G., and Krustulovic-Opara, N. (2007). Measurement of tensile properties of fiber reinforced concrete: draft submitted to aci committee 544. In Reinhardt, H. W. and Naaman, A. E., editors, *Rilem International Workshop on High Performance Fiber Reinforced Cement Composites*, number Pro. 53 in RILEM Proceedings, pages 3–12. RILEM, RILEM S.A.R.L.

Naaman, A. E. and Reinhardt, H. W. (2006). Proposed classification of hpfrc composites based on their tensile response. *Mater Struct*, 39(5):547–555.

Naaman, A. E. and Shah, S. P. (1976). Pull-out mechanism in steel fiber-reinforced concrete. *ASCE Journal of the Structural Division*, 102(8):1537–1548.

Otsuka, K. and Date, H. (2000). Fracture process zone in concrete tension specimen. *Eng Frac Mech*, 65(2-3):111–131.

Quian, S. and Li, V. C. (2008). Simplified inverse method for determining the tensile properties of strain hardening cementitious composites (shcc). *Journal of Advanced Concrete Technology*, 6(2):353–363.

Redon, C., Li, V., Wu, C., Hoshiro, H., Saito, T., and Ogawa, A. (2001). Measuring and modifying interface properties of pva fibers in ecc matrix. *ASCE Journal of Materials in Civil Engineering*, 13(6):399–406.

Rice, J. (1968). A path independent integral and approximate analysis of strain concentration by notches and cracks. *Journal of Applied Mechanics*, 35(2):379–386.

RILEM-TC162-TDF (2001). Rilem tc 162-tdf: Uni-axial tension test for steel fibre reinforced concrete. *Materials and Structures*, 34:3–6. 10.1007/BF02482193.

RILEM-TC162-TDF (2002). Rilem tc 162-tdf: Bending test. *Materials and Structures*, 35:579–582. 10.1007/BF02483127.

Rokugo, K., Kanda, T., Yokota, H., and Sakata, N. (2009). Applications and recommendations of high performance fiber reinforced cement composites with multiple fine cracking (hpfrcc) in japan. *Materials and Structures*, 42(9):1197–1208.

Shah, S., Brandt, A., Ouyang, C., Baggott, R., Eibl, J., Glinicki, M., Krenchel, H., Lambrechts, A., Li, V., Mobasher, B., and Taerwe, L. (1996). Toughness characterization and toughening mechanisms. In Naaman, A. and Reinhardt, H., editors, *High performance fiber reinforced cement composites 2*, volume 31 of *RILEM Proceedings*, pages 194–224. E & FN Spon.

Shah, S., Swartz, S., and Ouyang, C. (1995). *Fracture mechanics of concrete - Applications of fracture mechanics to concrete, rock, and other quasi-brittle materials.* Wiley, New York,N.Y.

Stang, H. and Aarre, T. (1992). Evaluation of crack width in frc with conventional reinforcement. *Cem Conc Comp*, 14(2):143–154.

Stang, H. and Shah, S. P. (1986). Failure of fibre-reinforced composites by pull-out fracture. *Journal of Materials Science*, 21(3):953–957.

Wang, Y., Backer, S., and Li, V. (1989). A statistical tensile model of fibre reinforced cementitious composites. *Composites*, 20(3):265–274.

Wang, Y., Backer, S., and Li, V. C. (1988). A special technique for determining the critical length of fibre pull-out from a cement matrix. *J Mater Sci Lett*, 7(8):842–844.

Wei, Q. F., Mather, R. R., Fotheringham, A. F., and Yang, R. D. (2002). Esem study of wetting of untreated and plasma treated polypropylene fibers. *J Ind Text*, 32(1):59–66.

Yang, E. H., Wang, S., Yang, Y., and Li, V. C. (2008). Fiber-bridging constitutive law of engineered cementitious composites. *Journal of Advanced Concrete Technology*, 6(1):181–193.

Yang, J. and Fischer, G. (2006). Implications of the fiber bridging stress - crack opening relationship on properties of fiber reinforced cementitious composites in uniaxial tension. In *International Workshop on High Performance Fiber Reinforced Cementitious Composites in Structural Applications*, volume RILEM Proceedings PRO 49, pages –.

CHAPTER 3

Fracture properties and crack propagation in cementitious composites

3.1 Introduction

The mechanical properties of concrete are intimately related to the formation of cracks. The macroscopic aspects of the mechanical and physical behavior of concrete are the result of its intrinsic cracking mechanisms. Due to their importance, the initiation and the propagation of cracks in concrete and other cement based composites have been studied extensively in the past few decades.

The quasi-brittle mechanical behavior that is typical of concrete is characterized by the moderate tensile hardening prior to the attainment of the ultimate tensile capacity and the subsequent rapid tensile softening. Classic linear elastic fracture mechanics (LEFM) is known to be insufficient to completely describe such mechanical response. The so-called cohesive crack concept has been developed as an extension to LEFM, which relies on the existence of a diffusely micro-cracked region ahead of the macro-crack tip [Hillerborg et al., 1976]. This transition zone between the intact material and the fully developed macro-crack possesses residual stress transfer ability. All the relevant micro-cracking mechanisms, which lead to the typical quasi-brittle mechanical behavior exhibited by concrete, seem to be located in this region, also known as the fracture process zone (FPZ) [Karihaloo et al., 1993; Landis and Shah, 1995; Wittmann and Hu, 1991]. The great attention that the scientific community devotes to the fracture process zone derives from its importance to the non-linear fracture mechanics discipline and to the simulation of cracking processes in cementitious composites.

When fibers are used to restrain crack propagation, the immediate outcome is the additional bridging stresses that develop in the region of the macro-crack immediately behind the tip of the propagating crack. The contribution of the fibers to restrain crack propagation in fiber reinforced cementitious composites (FRCC) is generally assumed to be restricted to the region where fibers are bridging the fully formed crack, also called the macro-crack region. However, the presence of the fibers may also have an effect in the region of the fracture process zone ahead of the crack tip, and therefore affect the mechanics of crack initiation and propagation. A better understanding of the micro-cracking mechanisms taking place at the level of the fracture process zone is therefore important to the development of improved FRCC and to the optimal design of the fiber reinforcement composition. The importance of the cracking processes on the mechanical performance of these composites motivates the better understanding of the micro-mechanisms that govern cracking dynamics at the level of the fracture processing zone.

The research described in the literature towards a better understanding of the fracture process zone led to the development of special techniques of analysis of cracking. The particularly complex nature of the cracking processes in cementititous matrix composites demands for special techniques of analysis. The small deformations and very fine cracks to be detected require high resolution equipments [Hornain et al., 1996; Otsuka and Date, 2000]. In addition, most of the intrusive characterization techniques used in other materials potentially induce early cracks in concrete, either due to direct mechanical action or to the alteration of other physical variables important for the delicate balance of the micro-structure of concrete, like induced drying or thermal variations. Many different techniques have been especially developed to analyze the fracture process zone and cracking, in concrete and other cement based materials. Radiography (x-rays, neutrons, or others), dye impregnation, acoustic emission, ultrasound, laser holography and interferometry represent some of the techniques that have successfully revealed quantitative information about the fracture process zone [He et al., 1997; Knab et al., 1984; Landis et al., 2007; Otsuka and Date, 2000; Regnault and Bruhwiler, 1990; Shah, 1990]. Although most of the macroscopic features of cracking processes in concrete are well understood, the micro-mechanisms that govern cracking and the essence of the fracture process zone are still object of abundant discussion. More qualitative and quantitative information about the fracture process zone is welcomed, as it can contribute to improve the design of cement based materials and in particular the design of more efficient FRCC.

Recent developments in digital photography technology have reached significant improvements in the quality of digital acquisition of images for scientific research.

The new charged couple devices (CCD) of high resolution and quality allow the image-based deformation analysis and documentation of cracking processes at small scales. In the previous chapter, the observation of the surface displacements in concrete specimens under controlled tensile loading conditions was carried out using this technique, from the initiation to the fully open state of the crack. This was possible at crack stages where the crack was still far from becoming visible or detectable by conventional means. In this chapter the same technique will be explored, but at a more demanding level from a technical point of view. Since the nature of the cracking processes to be documented require high resolution and detail, more attention will be dedicated to the basic principles and concepts of the technique. The objective is to document and characterize relevant information about toughening mechanisms and phase interaction in cement based materials, while contributing to the understanding of the tensile micro-mechanisms taking place during cracking in cementitious matrix composites.

3.1.1 Fracture mechanisms and fracture process zone

Micro-structure of the cementitious matrix:

It is well understood that the complexity of the mechanical behavior of cement-based composites derives from the great diversity of physical properties of its constituents. Hardened concrete can be defined as a three-phase material, where the cement-based matrix phase, composed of particles of smaller size ($D_n < 125\ \mu m$) and cement, binds the constituents of the aggregates and other inclusions phase. The third phase is the Interfacial Transition Zone (ITZ), which has special properties as consequence of its increased porosity and poor packing of particles. The stiffness and strength of cementitious composites matrix result from the combination of the behavior of these three distinct phases. Different structural features can be found in the material at different scales of observation, from the smallest atomic scale to the largest civil construction scale size [van Mier, 1984]. As mentioned in the previous chapter, the study of cementitious matrix composites has been focusing mainly tree distinct material scale levels:

- Micro-scale: at this level, physical and chemical processes that affect mostly the cement paste hardening, or after hardening its deformational behaviour and ultimate strength, are observed. The underlying mechanisms of creep and shrinkage are evidenced, since they are related to the pore-structure of the hardened cement and its hydration processes. Also at this scale level the behavior of interfacial transition zone between the inclusions (aggregates, fibers) and the cementitious matrix are described;

- Meso-scale: the interaction between the inclusions and the cementitious matrix (or between inclusions itself), large pores and other imperfections, in the solid skeleton, originate stress concentrations that are described at this scale. The underlying mechanisms of crack formation and fracture processes are described at the level of the meso-scale. The highly non-linear and quasi-brittle behavior of cementitious matrix composites are largely influenced and explained by the phenomena occurring at this scale;
- Macro-scale: The level at which structural design is performed. At this scale the material is considered as a homogeneous material, without considering the micro- and meso- scale inhomogeneities. The mechanical charaterization is carried out by averaging the non-linear stress-strain behavior, which is furhter utilized in structural analysis models.

Cementitious materials are generally classified in three different categories, depending on the main components used. If the mixture is mainly composed of cement and water, it is generally classified as paste. If fine aggregates are also present in the mix, it may be classified as mortar. Finally, the mix is in general classified as concrete when cement, water, fine and coarse aggregates are used. The properties of cementitious materials are typically improved by including admixtures, additives and fibres in the mixture. Superplasticizers are one important class of admixtures often used. The properties of the cementitious materials are known to be greatly dependent on the paste properties. Although the chemical dynamics of cement setting and hardening is quite complex and not within the main scope of this investigation, it is important at this stage to address briefly the micro-scale architecture of the hardened paste to establish the elementary structure-property relationships.

Hardened cement paste is a composite material whose properties depend on the characteristics of its components and on the way they interact and arrange themselves, forming its micro-structure. These components include mainly the principal products of hydration of cement: calcium silicate hydrates (C-S-H), calcium hydroxide (CH), and calcium sulfoaluminate hydrates (AFt and AFm phases) [Shah et al., 1995]. Calcium silicate hydrates (C-S-H) appear with different morphologies during hydration, but they can be mainly distinguished in two phases, one referring to the amorphous or quasi-crystaline phase, and the other referring to the assemblage of

C-S-H in a colloidal scale intermixed with other cryptocristaline phases, called C-S-H gel. It constitutes about one half to two thirds of the volume of hydrated paste, and particle sizes are approximately 0.1 μm [Gartner et al., 2002]. Calcium hydroxide (CH) appears in the form of large hexagonal prismatic crystals (0.01 to 0.1 mm), and occupies about one fourth of the paste volume. These crystals grow within the water filled capillary pores, surrounding partially hydrated grains, eventually forming percolating networks. Hydration temperature may affect their size and shape. Calcium sulfoaluminates may present themselves in two distinct phases, the AFt and the AFm. The AFt phase consists mainly of what is more commonly known as ettringite, forming prisms of hexagonal cross-section and long slender shape, like needles, commonly $10 \times 1\mu\ m$. AFt formation is accompanied by an increase in volume, being the basis of shrinkage-compensating cements when expansion due to its formation is controlled, or the justification to some common forms of sulphate attack. The AFm phase is formed by a group of compounds that have a layer structure, being calcium monosulphoaluminate one example [Gartner et al., 2002].

Pore structure is an important feature of hardened cement paste, which affects every major properties of concrete. Hardened cement paste contains a wide range of pores of different nature and size. These may be classified in micro, meso, and macro-pores. Micro-pores have very small dimensions (less than 2.5 nm), and they are considered as an intrinsic part of C-S-H Gel, representing narrow spaces between layers and surfaces. Meso-pores are present in a range of dimensions between 50 nm and 2.5 nm, but they are manly composed by medium capillaries that lead to the development of internal pressures due to the variation of moisture. Macro-pores range in dimension between 10 μm and 50 μm, and consist on large capillaries and interfacial pores remnant from water filled spaces that exist between the partially hydrated cement grains. They form an interconnected network, providing pathways for easy penetration of aggressive agents, and depend mainly on the w/c ratio and the degree of hydration [Mehta and Monteiro, 2006; Gartner et al., 2002].

Interfacial Transition Zones:

The micro-structure of the cementitious paste shows great variation with the distance from the surface of the inclusions. Observations by quantitative analysis of back-scattered electron images reveal that the level of porosity steadily increases from a certain level, at 20 μm from the physical contact surface, to nearly twice this level [Scrivener and Pratt, 1996].Concrete strength, and other mechanical properties, are largely influenced by the heterogeneity of the ITZ, therefore it is considered as a third phase in cementitious composite material models [Chandra, 2002; Scrivener and Pratt, 1996]. Two main micro-structural regions exist in the transition zone (see figure 3.1). First, a thin layer of products are formed directly on the inclusion surface, with a thickness of approximately 1 μm, resulting from the reaction that may exist between the inclusion (aggregate, fibers or others) and the cement paste. This first thin layer is characterized as a 'duplex film' [Barnes et al., 1978], consisting of a layer of Calcium Hydroxide (CH) on the inclusion side, and a layer of short needles of Calcium Silicate Hydrate Gel (C-S-H Gel), on the bulk cement paste side. Second, a region of the paste that extends up to 50 μm from the first contact surface exists. The lower packing density of the binder grains due to the wall-effect produced by the surface of the inclusions determine the distinct features of the paste micro-structure in this region. This transition zone between the 'duplex film' and the bulk cement paste is mainly composed by Calcium Hydroxide (CH) long hexagonal crystals, which develop perpendicularly to the inclusion surface, as well as clusters of ettringite needles filling the remnant empty spaces [Chandra, 2002]. ITZ typically possesses a lower concentration of unhydrated cement particles, larger contents of ettringite (AFt) and significantly lower strength and stiffness [Diamond and Huang, 2001]. ITZ properties are greatly affected by ultra-fine mineral additions and the roughness of the surface of the inclusions, as well as by the w/c ratio and the utilization of superplasticizers.

Among the three phases which are present in the cementitious matrix micro-structure, the ITZ is usually regarded as the weakest, typically of poorer quality and more prone to faults and defects. The bond between the inclusions and the

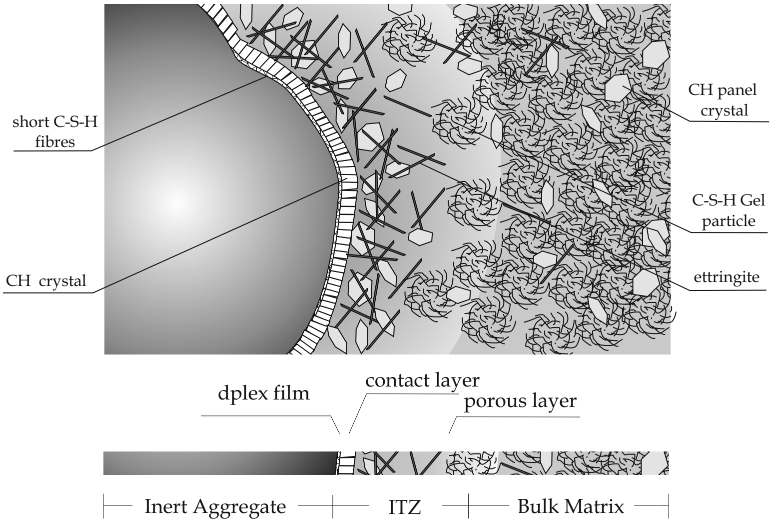

Figure 3.1: Schematic representation of the ITZ in concrete.

cementicious matrix depends upon different mechanisms (Zimbelman [1985], Yuan and Guo [1987]): the mechanical keying of the hydration products of cement with the rough surface of the aggregate or other inclusions; the ordered growth of the new compounds, as they form and deposit on substrates of hydration products and at the surface of the inclusions (known as Epitaxial growth); the physical-chemical bond between the hydrating cement paste and the inclusions. The surface properties of aggregates have great influence on bonding quality. The roughness, hardness, stiffness and chemistry are the most important properties of the inclusions. The overall mechanical behavior and failure of cementitious matrix composites is the result of the micro-mechanical interaction of these different phases in the composite.

Cracking processes and Fracture Process Zone:

Concrete is known to be a tension-weak material, with a much lower tensile strength than the compressive strength (around 10%). Cracks and internal flaws exist even prior to loading, and the mechanical behavior of concrete under distinct loading conditions is mainly governed by the way these initial cracks and flaws propagate. Placing and hardening of concrete is accompanied by different phenomena that induce the formation of these initial cracks. As discussed previously, factors like bleeding, segregation and wall effects create strong micro-structure gradients at the interface between cement matrix and aggregates or other inclusions, increasing the probability of the formation of cracks in these regions. Also, the great differences between the physical and mechanical properties of aggregates and the cementitious matrix (distinct thermal dilactancy coefficients, modulus of elasticity and shrinkage response to changes in moisture content) induce strong stress/strain gradients at the weaker zone in concrete matrix, that is the interfacial transition zone. Since different mechanical responses of concrete structures can be explained by the fracture processes at distinct loading conditions, it is important to understand how internal cracks initiate and propagate while load is increased.

Typically, three different types of structural materials can be identified: elastic-brittle materials (like ceramics and glass), elasto-plastic ductile materials (like steel and other metals) and quasi-brittle materials (like concrete and other cementitious composites). Fracture behavior of all three cannot be explained simply by adopting the strength criterion, otherwise the infinite stresses appearing at a flaw or sharp edge would imply the occurence of failure at any load level. Instead, a small inelastic zone around the crack tip must exist, where material softening occurs. In steel, this inelastic zone is typically classified as the yielding zone. In contrast to linear elastic fracture mechanics, the nonlinear zone is large for both types of nonlinear fracture mechanics. For ductile elasto-plastic materials, most of the nonlinear zone undergoes plastic hardening or perfect plasticity, and the fracture process zone is still a very small part of the nonlinear zone (Figure 3.2-b). In contrast, for quasi-brittle materials, which is the case for concrete, the fracture process zone is large and occupies nearly the entire nonlinear zone [446, 1999] (Figure 3.2-c).

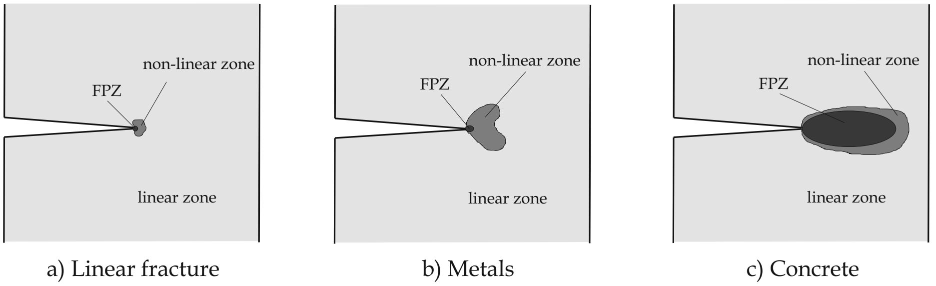

a) Linear fracture b) Metals c) Concrete

Figure 3.2: Alteration of the linear stress field at the vicinity of a crack tip, non-linear zones and FPZ in (a) elastic-brittle, (b) ductile and (c) quasi-brittle materials [446, 1999].

Essentially as a result of micro-cracking, the region of material ahead of the crack tip softens after the peak stress is locally reached. The tension softening zone ahead of the crack tip is responsible for the continuous dissipation of energy while the crack tip advances (see Figure 3.3).

As mentioned in Chapter 2, two basic criteria govern the fracture of materials, and these are the stress and the energy criteria. The stress criterion involves the need to overcome, at a flaw or sharp tip, the cohesive strength of the material, so that a crack can be formed. The energy criterion determines that the energy available to extend the crack tip must exceed the energy that is dissipated during the propagation of the crack at the level of the FPZ. The most common toughening mechanisms that take place at the FPZ, which influence the fracture processes in concrete, are represented in figure 3.4. The nature of these mechanisms is directly related to the porous and heterogeneous nature of cementitious composites [Shah et al., 1995].

During fracture, the high stresses near the crack tip trigger the formation of randomly dispersed and oriented micro-cracks in flaws and porosities ahead of the crack tip. These diffusely micro-cracked areas dissipate much of the energy available to propagate the crack, therefore the crack tip propagation becomes more difficult. This phenomenon is therefore known as micro-crack shielding (see figure 3.4-a).

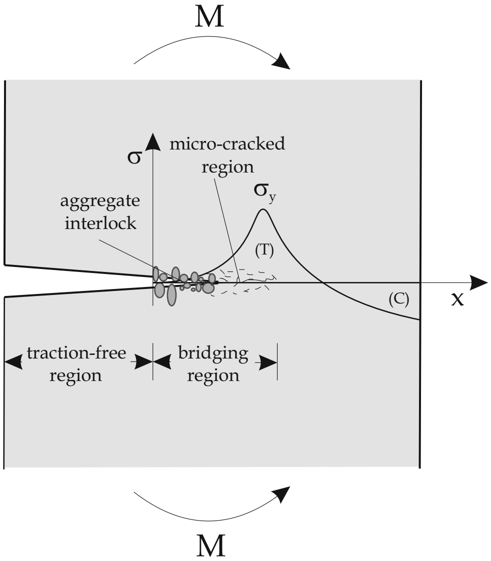

Figure 3.3: Fracture process zone and the different regions of tensile softening in the transition from the macro-crack tip to the bulk intact material ahead of the propagating crack.

When the crack intersects a large hard aggregate and the least resistance path is found by circumventing the obstacle along the weak interface, the increase of energy needed to propagate the crack also contributes to increase toughness (see figure 3.4-b). When the crack intersects the aggregates without fracturing them, and stresses continue to be transmitted across the crack until they are pulled out or fail (figure 3.4-c), aggregate bridging occurs. Also, interlock mechanisms and friction (see figure 3.4-d) are responsible for energy dissipation during fracture, due to the tortuous paths that cracks typically adopt. Crack branching is another frequent phenomenon at the FPZ (see figure 3.4-f). The heterogeneity of concrete favors the propagation of the crack into several branches, and each new branch that is formed requires more energy dissipation to extend further. In some cases, internal voids also tend to act as obstacles to crack extension, when the crack intersects one void and it produces a blunt tip (see figure 3.4-e), and additional energy to propagate the crack beyond that void is required. This mechanism is called tip blunting [Shah et al., 1993].

The desired enhancement of the fracture toughness of cementitious composites can be achieved either by adding other energy dissipating elements to the mixture or by altering the existing toughening mechanisms, considering the properties of the three phases above discussed. The addition of fibers to the mixture is one of the most common procedures used to increase the fracture toughness of cementitious compos-

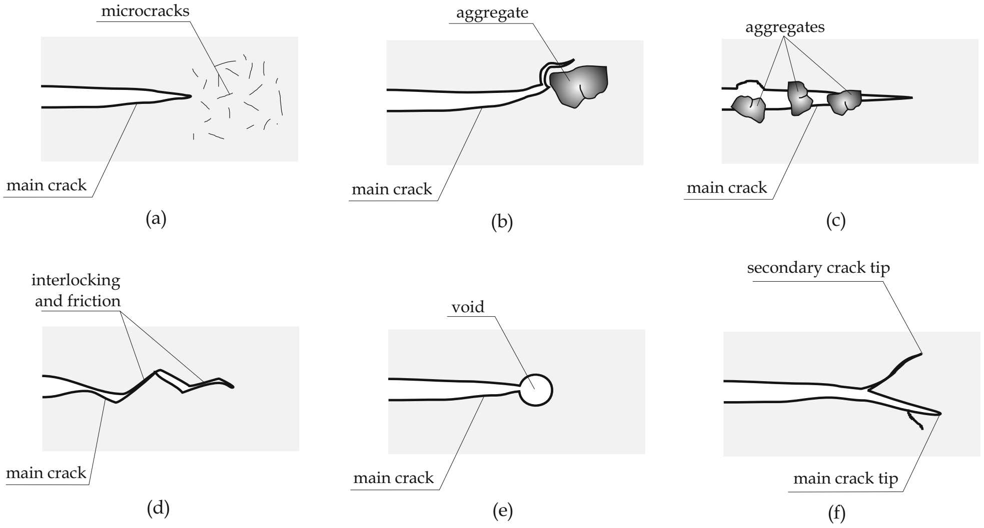

Figure 3.4: Toughening mechanisms at fracture process zone and crack propagation mechanisms: (a) crack shielding, (b) crack deflection, (c) aggregate bridging, (d) crack interlock and friction due to roughness, (e) crack tip blunting and (f) crack branching [Shah et al., 1995].

ites.

Experimental characterization of the FPZ:

In the past few decades, a variety of experimental techniques have been developed to measure the extent and characterize the FPZ. There is general agreement that a zone of discontinuous micro-cracking does exist ahead of the propagating tip of the continuous crack. The highly porous and heterogeneous nature of cementitious composites, as well as its intrinsic pre-microcracked condition, naturally suggest that the introduction of a macro-crack into the matrix leads to the initiation of microcracks at the nearby flaws or inclusions. Similarly, as with other fracture mechanics measurements, in cementitious composites the responses obtained under testing depend upon the size and geometry of the specimen or structure. The interpretation of the existence of a fracture process zone as a material property is very convenient to explain the scale-size effects of structural response. There is still, however, the need for a conclusive agreement on the details about the extent and nature of this zone. Although most of the macroscopic features of cracking processes in concrete are well understood, the micro-mechanisms that govern cracking and the essence of the fracture process zone are still object of discussion.

The size of the FPZ is apparently related to a few important material parameters [Hillerborg et al., 1976; Karihaloo, 1995]. The parameter more frequently considered when discussing the size of the FPZ of different materials is the characteristic length, l_{ch}. Approximately, the characteristic length can be calculated from the tensile strength of the material, f_t, the material fracture energy, G_f, and the Young's modulus, E_t (equation 3.1):

$$l_{ch} \approx \frac{E_t G_f}{f_t^2} \tag{3.1}$$

The estimation of l_{ch} for typical cementitious materials is compared with glass (Gettu and Shah [1992] *in* Karihaloo [1995]) in Table 3.1.

Table 3.1: Comparison of FPZ length.

Material	$l_{ch}(mm)$	Reference
Glass	10^{-6}	Bache [1986]
Cement paste densified by silica fume	1	Bache [1986]
Hardened cement paste	$5-15$	Hillerborg [1983]
Mortar	$100-200$	Hillerborg [1983]
High-strength concrete (50-100 MPa)	$150-300$	Hilsdorf and Brameshuber [1991]
Conventional concrete	$200-500$	Hillerborg [1983]
Dam concrete ($D_{max} = 38mm$)	700	Bruhwiler et al. [1991]

The particularly complex nature of the cracking processes at the FPZ and the importance of the detailed understanding of its entire structure has motivated the development of special techniques for its visualization and analysis. The small deformations and the very fine cracks to be detected require high resolution equipments [Hornain et al., 1996; Otsuka and Date, 2000]. The susceptibility of the cementitious matrix to damage induced by hygro, thermal or mechanical actions requires for particularly delicate measurement techniques, whereas the conventional intrusive characterization techniques used with other materials may potentially induce premature cracks. Many different techniques have been developed to analyze the fracture process zone and cracking in concrete and other cement based materials. Discrete micro-cracking at the tip of extending cracks was observed in epoxy impregnated specimens using scanning electron microscopy, as well as an overall heterogeneous micro-structure of cracking at a micrometer scale [Struble et al., 1989]. Laser holographic interferometry was also successfully utilized to characterize the small deformations observed near the tip of propagating cracks at the surface of concrete specimens [Jacquot and Rastogi, 1983; Cedolin et al., 1983, 1987; Maji and Shah, 1990; Regnault and Bruhwiler, 1990; He et al., 1997]. Although the resolution achieved with laser holography in the description of the surface strain fields near the crack tip is high, the technique cannot give any information about the deformations along the specimen thickness. The acoustic emission (AE) technique contributed to extend the information about the micro-cracking formation at the FPZ, considering also the micro-cracking events taking place along the specimen thickness. AE detection apparatuses were also used to detect the location, size, orientation and even the nature of the micro-cracks generated during the fracture process [Miller et al., 1988; Maji and Shah, 1988; Maji et al., 1990; Shah, 1990]. Fluorescent dye impregnation was one of the first techniques employed in the investigation of the cracking processes at the FPZ [Knab et al., 1984]. While relevant information about the topology and mechanics of crack propagation was obtained with this technique, it may be difficult to distinguish the newly formed micro-cracks from previously existing mechanical or shrinkage induced micro-cracking [Hornain et al., 1996; van Mier, 1997]. The continuous propagation of the crack cannot be studied as well. Radiography (x-ray, neutron, or others), ultrasound and other techniques have also been successful in revealing quantitative information about the fracture process zone [Landis et al., 2007; Otsuka and Date, 2000]. A review of the various and most important techniques used to detect and analyze the FPZ, as well as their advantages and disadvantages may be found in the work of Mindess [1991]. The micro-mechanisms that govern cracking and the essence of the fracture process zone are still object of discussion, mainly the aspects related to the propagation of cracking. Additional research and information about the FPZ is still regarded as an important contribute to the improvement of the design of cement based materials, and in particular the design of more efficient and durable FRCC.

3.1.2 Digital image-based deformation analysis

Deformation analysis based on the digital image processing has assumed increasing importance in the last decade, mostly as a result of the significant development of the digital imaging technology. The quality and resolution of the CCDs produced nowadays, still in rapid development, have reached sufficient sophistication to allow the documentation and examination of the cracking processes, at small scales and with significant detail.

The technique is based on the utilization of sequential digital images of an object to determine the displacements and displacement gradient fields at surface of the object, using digital image correlation [Chu et al., 1985; Bruck et al., 1989]. The digital images acquired are stored in the form of matrix sets of numbers representing the image. Each number represents the intensity of light captured by each small portion of the digital sensor, which is referred to as a pixel. The output of each pixel is an eight-bit number, ranging from 0 to 255. The lowest value represents black, the highest value white, and the values in between represent different shades of gray. Digital image correlation can then be summarized to the identification of the position and deformation of pixel subsets between two digital images. The accuracy of the correlation between recorded images depends on the quality and contrast of the image speckle pattern (including light conditions) and the resolution of the imaging system [Berfield et al., 2007]. Each subset of the image needs to be statistically different from any other subset [Chu et al., 1985].

The comparison of the subsets of numbers between two digitized images is carried out by evaluating the correlation (S, equation 3.2) between subsets and finding the location of each subset of the first image on the second image (equation 3.2):

$$S\left(x, y, u, v, \frac{\partial u}{\partial x}, \frac{\partial u}{\partial y}, \frac{\partial v}{\partial x}, \frac{\partial v}{\partial y}\right) = \frac{\sum \left(I_u(x,y) - I_d(x^*, y^*)\right)^2}{\sum I_u(x,y)^2} \tag{3.2}$$

The cross-correlation coefficient is also typically evaluated to determine how well the subsets match (equation 3.3):

$$S\left(x, y, u, v, \frac{\partial u}{\partial x}, \frac{\partial u}{\partial y}, \frac{\partial v}{\partial x}, \frac{\partial v}{\partial y}\right) = 1 - \frac{\sum I_u(x,y) I_d(x^*, y^*)}{\sqrt{\sum I_u(x,y)^2 \sum I_d(x^*, y^*)^2}} \tag{3.3}$$

where u and v are the displacement components of the subset center in the x and y direction respectively, I_u and I_d represent the gray level values at the undeformed (u) and deformed (d) images, respectively, and (x, y) and (x^*, y^*) are the coordinates of a point in the subset before and after the deformation, respectively. If the displacements occurring at the object surface relative to the camera are parallel to the image plane, the coordinates (x^*, y^*) after deformation may be described as a function of the coordinates (x, y) before deformation considering the first order gradients of the displacement field (equation 3.4):

$$\begin{aligned} x^* &= x + u + \frac{\partial u}{\partial x}\Delta x + \frac{\partial u}{\partial y}\Delta y \\ y^* &= y + v + \frac{\partial v}{\partial x}\Delta x + \frac{\partial v}{\partial y}\Delta y \end{aligned} \tag{3.4}$$

where the terms Δx and Δy are the distances from the subset center to the point (x, y). In Figure 3.5 the procedure is schematically presented, where a subset is shown before and after the deformation (image before and image after deformation). The subset center point P and generic point Q on the undeformed subset translate to points P^* and Q^* respectively, on the deformed subset. The image correlation process is performed by determining the values of u, v, $\partial u/\partial x$, $\partial u/\partial y$, $\partial v/\partial x$ and $\partial v/\partial y$ which minimize the correlation coefficient S. The numerical algorithm utilized to find the combination of variables which minimize the correlation coefficient was, in the early applications of the technique, the coarse-fine search. The Newton-Raphson method was later suggested as a faster converging alternative, with the ability to correct the initial guesses of all variables simultaneously [Bruck et al., 1989].

The discrete nature of the information collected as a representation of the real surface of the specimen requires for sub-pixel interpolation methods. Different al-

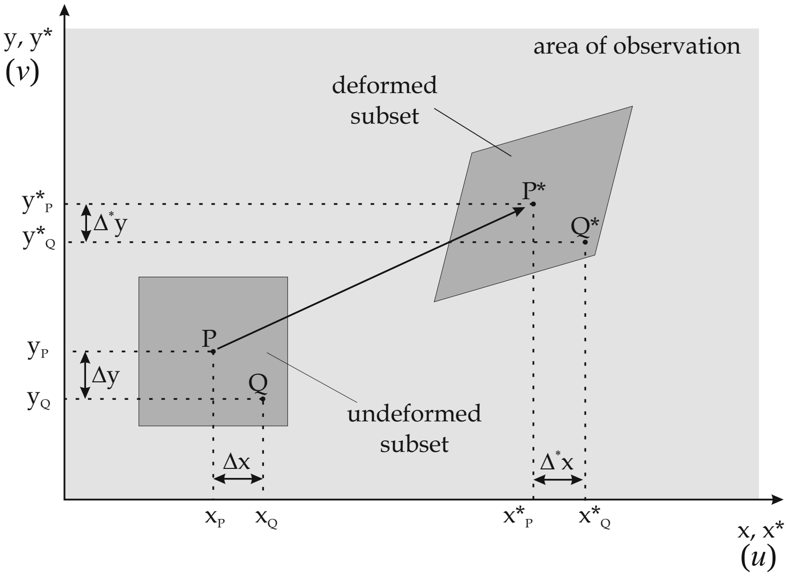

Figure 3.5: Schematic description of the displacement field and deformation of a generic subset in the area of observation.

ternative methods exist to smooth and reduce noise of the acquired gray level in all pixels of each subset. As a result, an approximation of gray level values between pixels can be obtained, which is necessary to determine the full-field displacements and deformations [Vendroux and Knauss, 1998; Bruck et al., 1989].

In the literature some examples can be found of applications of digital image correlation to the description of the deformations at the surface of specimens of distinct materials and at different scales. In most cases the technique is used to study the fracture behavior of materials, with the documentation of the early processes of crack propagation in notched specimens of wood, metals and metal alloys, polymers and polymeric foams, biological tissues and also cementitious materials [Abanto-Bueno and Lambros, 2005; Corr et al., 2007; Savic et al., 2010; Yoneyama et al., 2006; Lawler et al., 2003], both for quasi-static loading conditions and for impact loading and fatigue behavior characterization [Guo et al., 2008; Tiwari et al., 2009].

3.2 The Compact Tension Test (CTT)

The large number and variety of specimen sizes, geometries and test setups proposed by different authors and standardization institutions to characterize the fracture behavior of materials is the consequence of the complexity associated with the fracture failure mechanisms. Among all the alternatives proposed, the Compact Tension specimen assumed special relevance and widespread use. It is mostly used to characterize the fatigue crack growth rates in materials, as described by ASTM Standard E647 [ASTM-E647, 2005]. Although it has been mainly utilized for testing metallic specimens, ASTM E647 inspired many other test setups developed to characterize the fracture behavior of other types of materials. The establishment of compact tension specimen as one of the most common fracture test specimens, and the large quantity of test results and studies available with other types of materials justify its use in the present research. The work by Chona et al. [1983] was particularly interesting to the purpose of the present research, in the sense that a complete characterization of the stress fields generated at the modified compact tension specimen during crack propagation was carried out, using the near-field equations suggested by Irwin [1958] and the photo-elastic method to visualize the stresses. In conjunction with a collocation procedure [Chona et al., 1983; Sanford, 2003], they were able to accurately represent the regions around the crack tip where the singular term in the series solution of the near-tip stress fields was sufficient to obtain an almost accurate solution. The geometry and size of these regions are dependent of the crack length, as shown in Figure 3.6. It is of general agreement that the fracture process zone is located entirely ahead of the crack, therefore Chona et al. [1983] have suggested that a meaningful measure of the singularity dominated zone would be largest circle lying within the shaded regions presented in Figure 3.6. Furthermore, Chona et al. [1983] observed that the governing parameter was not the length of the crack, but rather the distance to the nearest boundary. This singularity dominated zone is precisely the area where the attention of present research is focused, while trying to document the fracture processes occurring in this region during crack initiation and propagation.

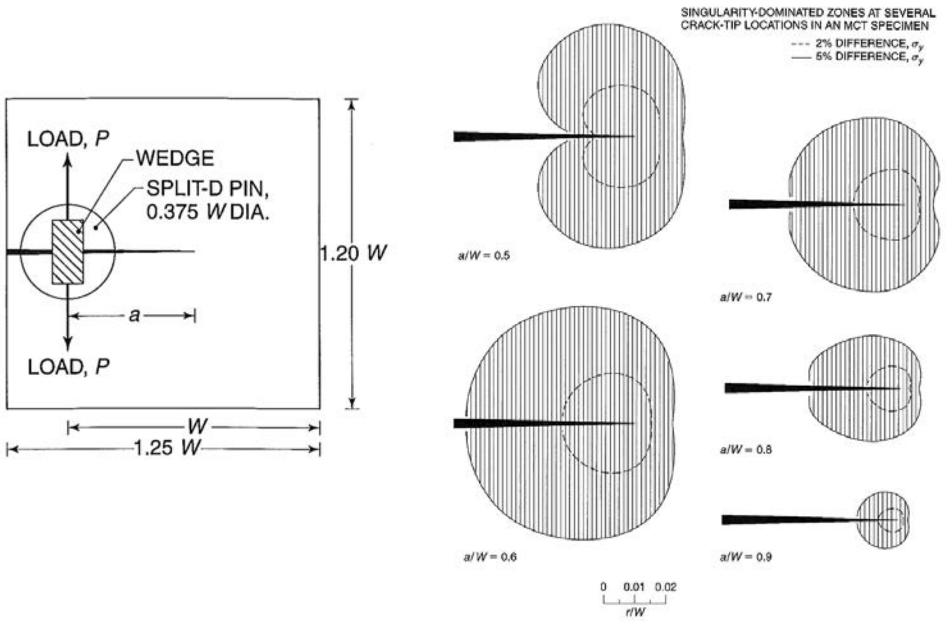

Figure 3.6: Size and geometry of the singularity dominated zones at the notch tip of the modified compact tension specimen, for different notch depths [Sanford, 2003].

3.2.1 Experimental procedure

The testing procedure consisted of applying a tensile load to a single-edge notched specimen at a constant displacement rate of 5 μm/s, inducing the formation of a single crack and its subsequent propagation in a controlled manner. The specimen shape adopted resembles the one used for the evaluation of the crack growth behavior [ASTM-E647, 2005], the so-called Compact Tension (CT) specimen. The unobstructed access to the surface where the crack progression becomes visible is the most relevant requirement of the present experimental procedure. With the purpose of maximizing the stress intensity at the tip of the notch, the notch thickness was minimized to 0.5 mm using a diamond cutting disc. The thickness of the specimen was also minimized (12 mm) to obtain, as close as possible, the plain stress state in the specimen. The geometry and dimensions adopted for the specimens are presented in Figure 3.7. Two rods with a diameter of 22 mm were used to apply the load to the specimens, providing free rotation (Figure 3.8).

The initial phase of this study included four specimens with different compositions: cement paste, mortar, concrete and a fiber reinforced cementitious composite (FRCC). The composition of the cement paste consisted of cement and water only. The concrete composition consisted of the addition of aggregates with a maximum size of 4 mm to the cement and water paste. The composition of the mortar and the FRCC consisted of cement, fly ash, fine sand (0.170 mm) water and admixtures, and Polyvinyl Alcohol (PVA) fibers as reinforcement in the case of the FRCC.

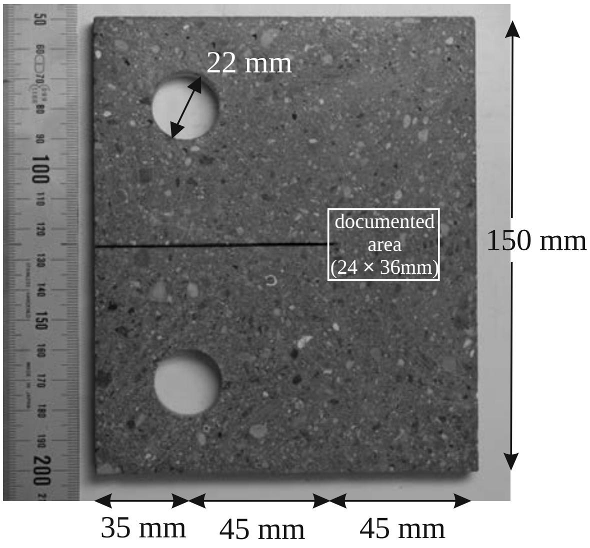

Figure 3.7: Specimen geometry used for the CT test.

The formation and propagation of the crack was traced on the surface of the specimens using a high resolution digital camera, positioned 90 mm away from the specimen. The 60 mm focal length lens allowed the observation of a 24 mm by 36 mm area of the surface of the specimen (see Figure 3.7). Images with resolution of 24 megapixel were captured during testing with time intervals of one second. These images were subsequently used for the continuous interpolation of the strain fields at

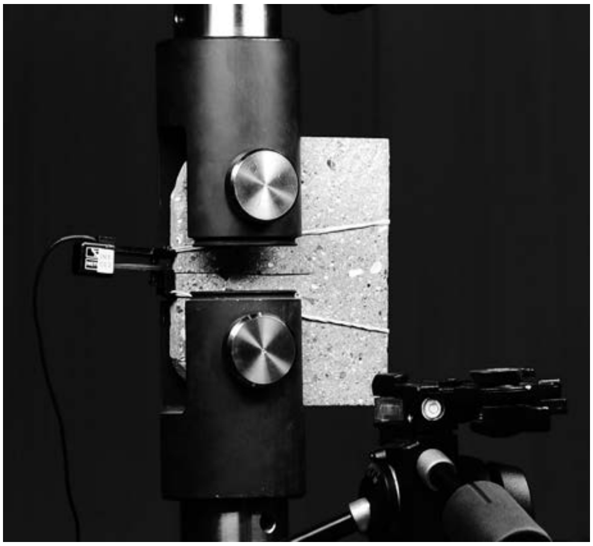

Figure 3.8: CT test setup, position of the specimen and of the camera stage.

the inspected surface of the specimen.

Sufficient randomness and high contrast of the stochastic patterns captured from the surface of the specimen are important for the effective analysis of the captured images [Berfield et al., 2007]. In the present study, the natural features observed at the surface of the specimens were found to be sufficient for a satisfactory image correlation (Figures 3.9 and 3.10). Each facet was composed of 15×15 pixels. Each pixel covered an approximate area of $6\times6\ \mu\text{m}^2$. The total area of $24\times36\ \text{mm}^2$ was modeled by a facet mesh overlay composed of approximately 267×400 facets.

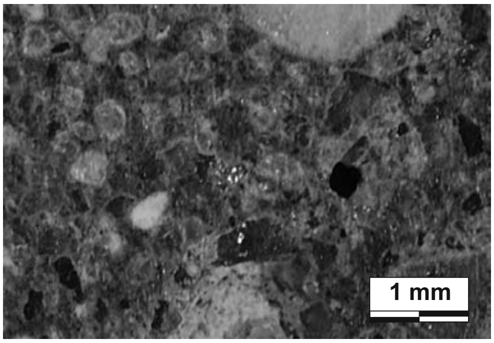

Figure 3.9: Amplified image captured from the surface of the concrete specimen.

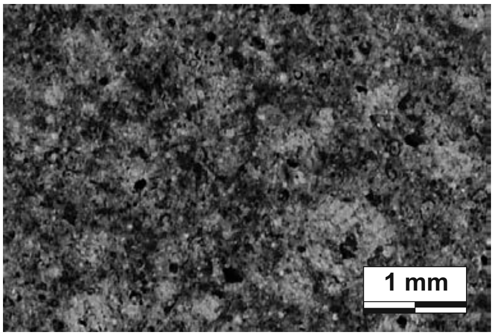

Figure 3.10: Amplified image captured from the surface of the mortar specimen.

3.2.2 Mechanical responses

The results obtained in terms of load *versus* crack mouth opening displacement (CMOD) during testing are presented in Figure 3.11. The CMOD was measured using a clip gauge with 25 mm of distance between sampling points, positioned at the edge of the notch (Figure 3.8). The results are presented for CMOD values of up to 1.6 mm.

In general, the load-CMOD curves obtained for the three non-reinforced cementitious matrices present a similar shape. The registered behavior is quasi-brittle, showing the typical moderate tensile hardening before reaching the peak load, and the subsequent rapid strain softening. The cement paste reached the lowest tensile load (86 N), and the concrete the highest (192 N). The post-peak softening branch in the concrete specimen was smoother than in the other two unreinforced cementitious matrices. The presence of aggregates seemed to help with the development of a more controlled fracture process, minimizing the sudden energy release events and the abrupt load drops during softening. These results are in agreement with the conceptual discussion about the toughening mechanisms in cementitious composites, at Section . In particular, the presence of the aggregates increases the energy that is dissipated during crack propagation due to both crack deflection and aggregate bridging (see Figure 3.4). This observation will be further discussed in the following sections, with the support of the image-based deformation analysis resulots to document the crack propagation. The existence of the PVA fibers in the FRCC specimen resulted in a pronounced tensile strain hardening stage after the first peak load (ini-

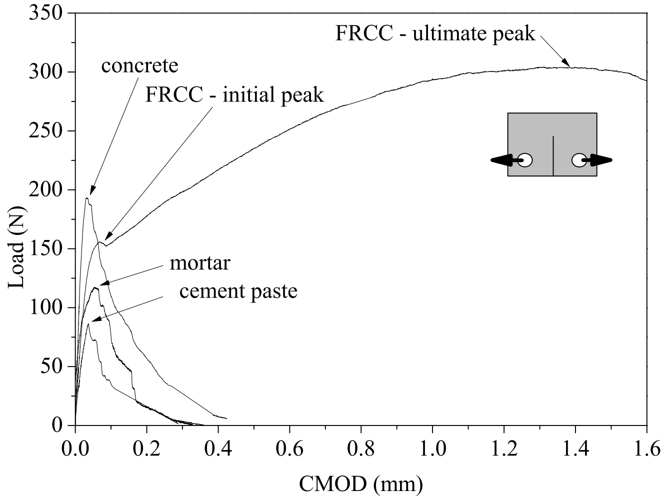

Figure 3.11: Load-CMOD curves measured during testing. The peak loads are identified in all specimens with the arrow.

tial peak). In the FRCC specimen, the maximum tensile load of 304 N (global peak) was reached at a CMOD of 1.46 mm.

The shape of the crack obtained in each specimen during testing is shown in Figure 3.12. These cracks are generally straight and show no evident signs of smearing or branching. They initiate at the tip of the notch and propagate to the edge of the specimen by following the shortest path.

3.3 Observation of crack initiation and propagation

In Table 3.2, the results obtained with the image-based monitoring system are shown. The maximum principal strains derived from the interpolated displacement fields at the facets overlay are presented. The color gradients evolve from dark gray (zero strain) to white (maximum strain of 5%). These strain values refer to the displacement gradients derived at the facets overlay, according to the principles of continuum mechanics, as discussed previously [Chu et al., 1985]. A discrete displacement jump between the two opposite crack faces is revealed by a strong strain gradient registered in the facets traversed by the crack. These strains are physically not realistic, in the

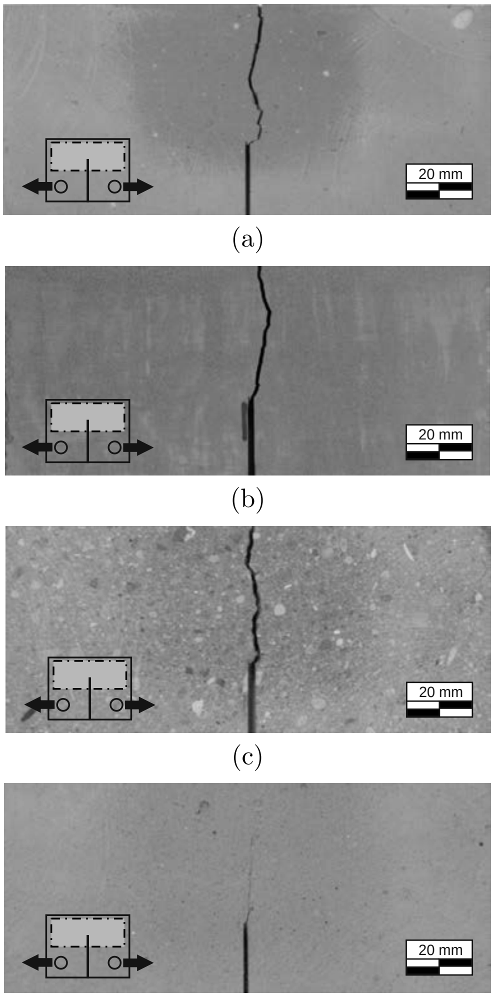

(a)

(b)

(c)

(d)

Figure 3.12: Images of the cracks formed in each specimen, after testing: (a) cement paste, (b) concrete, (c) mortar and (d) FRCC.

sense that they result from the smearing of the local displacement jump occurring between the crack flanks by the traversed facets assuming continuum displacement fields [Chu et al., 1985]. Despite this unusual representation of a crack opening with strain, the graphical results represent well the extent of cracking.

Table 3.2: Maximum principal strains in the facet overlay for three load levels: before peak load (90% of the peak load); when peak load is reached; after peak load (50% of the peak load).

	90% of peak load (before peak)	peak load	50% of peak load (after peak)	
Cement paste				
Concrete	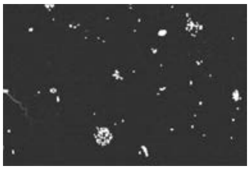	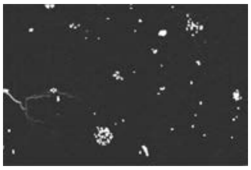		
Mortar	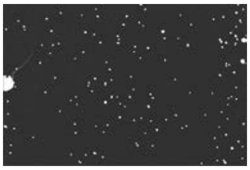	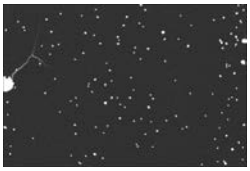	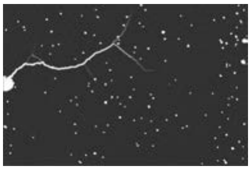	
FRCC				

The sequence of pictures taken with a time interval of one second allowed the reconstruction and tracing of the full field displacements and strains during the entire testing sequence. To illustrate the obtained results, three representative stages were selected: before the peak load was reached (90% of the peak value), when the peak load was reached and after the peak load (50% of the peak value). In the case of the FRCC specimen, the peak load refers to the first peak load. The strong geometrical gradients found in larger pores and defects located at the imaged surface of the specimens influence the pattern correlation. As a consequence, some of the facets in the overlay show the white color, corresponding to areas where the image correlation was not possible.

The images in Table 3.2 allow the observation of how the cracks initiate and propagate in each specimen. The cracks become clearly visible for very small openings. When 90% of the peak load is reached the opening at the tip of the notch is 4 μm for the cement paste specimen, 4 μm for the mortar, 5 μm for the concrete and 4 μm for the FRCC. For all specimens the measured deformations reveal the early initiation of the cracks at the tip of the notch well before the peak load has been reached. The propagation of these cracks was subsequently followed with high precision at the subsequent stages. The images presented in Table 3.2 are amplified for all specimens near the notch tip at this stage (Figure 3.13). The technique showed an interesting potential to detect very small cracks in a consistent manner. When compared to alternative methods, the high accuracy and resolution found on the description of the cracking processes was achieved with a simple test setup, and the control of the environment conditions did not require any special attention or complicated preparations, in contrast to other equivalent methods, like for example laser holography.

The effect of crack branching is visible in all the specimens tested, although they are assuming different features in a closer view. In the mortar specimen, the crack branches developed are fewer, longer and more discrete. In the concrete specimen the crack branching occurs more frequently and the branches of the main crack are less visible and more diffuse. A small area of diffuse micro-cracking ahead of the principal crack is also visible in some stages. The increase in the number of aggregates and their size contributed to the increase of crack smearing near the propagating tip. At the same time, the smaller and more frequent crack branches formed suggest that the smearing of the crack tip contributes to the gradual dissipation of the energy associated with the fracture process. In the FRCC specimen, branching and crack smearing are less visible probably due to the contribution of the fibers to arrest the propagation of micro-cracks. Observing the results obtained with the cement paste specimen (Table 3.2), secondary cracks become visible right from the onset of the testing sequence. These secondary cracks were not connected to the principal crack initiating at the tip of the notch, suggesting that these are probably shrinkage cracks that become active when the specimen is loaded and the crack propagation alters the ambient stress in the vicinity. The crack path seems to be greatly influenced by these pre-existing shrinkage cracks, which divert the principal crack originated at the notch tip from its natural path. Considering that the cement paste specimen is made of cement and water only, significant autogenous shrinkage can be expected. This explains the tortuous shape of the final crack and may also explain the lower initial stiffness observed in the load-CMOD diagram of the cement specimen. In addition, the length of the cracks observed in Figure 3.13 is mostly identical in all cases, ex-

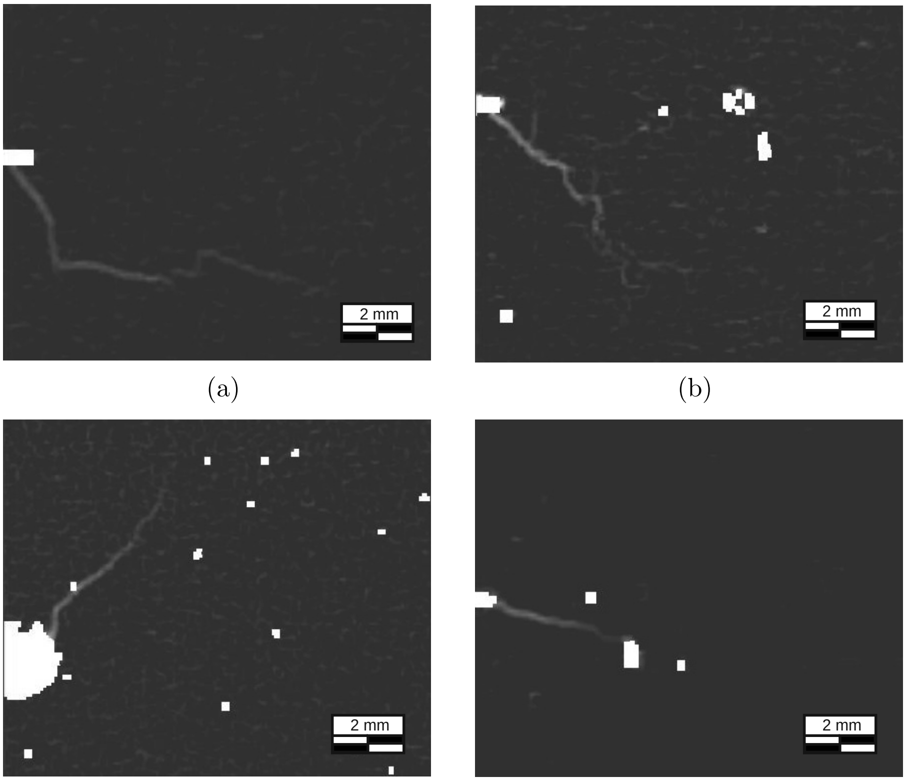

(a) (b)

(c) (d)

Figure 3.13: Amplified images of the deformations measured at the surface of the specimens, at a load level of 90% of the peak load, before the peak load has been reached: (a) cement paste, (b) concrete, (c) mortar and (d) FRCC.

cept the one observed at the cement paste specimen. The much greater crack length observed in the case of the cement paste specimen may again be justified by the pre-existing shrinkage cracks, which create easier paths for crack propagation once the tip of the main crack reaches them. It could even be assumed that the crack observed in Figure 3.13.a may be the result of the coalescence of different pre-existing shrinkage cracks with somewhat similar angles, eventually connected by the main crack once it runs through the specimen.

In general, the initiation of the cracks at the tip of the notch is revealed at very early stages. The tracing of the subsequent progression of these cracks was possible with considerable resolution. In some cases, the initiated main crack diverted from its main horizontal path, to which it returned later on leaving behind a crack branch.

This behavior was particularly visible in the mortar specimen, where long branches of the main crack were detected. These branches were untraceable in the final cracked specimens. The apparently single crack observed in the final cracked specimens was in fact the final path that prevailed among a number of cracking branches and crack path diversions.

3.4 Influence of the presence of fibers on the cracking processes

The presence of the fibers in the matrix is known to influence the the fracture processes and crack propagation. In this research the influence of the fibers on the fracture processes was evaluated by investigating the crack profiles obtained in the mortar and the FRCC specimens. The morphology of the principal crack formed in the mortar specimen is depicted in Figure 3.14 at five distinct loading stages: before the first peak load when 90% of the load is reached (P-10%), when the peak load is reached (P), and after the peak load is reached for 90% of the peak load (P-10%), 80% of the peak load (P-20%) and 50% of the peak load (P-50%). The crack profiles were obtained by computing the evolution of the distance difference between two points placed in opposite sides of the observed principal crack. Thirty of these virtual clip gauges were evenly spaced (1 mm) and positioned vertically along an initial portion of the macro-crack measuring 30 mm, starting from the tip of the notch.

In general, the results presented in Figure 3.14 show that the displacements measured in the virtual clip gauges follow approximately the shape of a third order polynomial trend line. Significant differences between the general shapes in the mortar and in the FRCC specimens can although be observed. In the case of the mortar specimen, when using the 2 mm virtual clip gauges the open crack portion of the displacement profiles seems to gradually change from a single curvature shape to double curvature, with the increase of the CMOD ($\delta(x = 0)$). When these crack profiles are compared with the ones obtained with the FRCC specimen, the gradual transition from a single to the slight double curvature shape is no longer observed. For comparison, the five stages selected for the FRCC were the ones for which the crack opening at the tip of the notch (x = 0) was approximately identical to the respective ones observed in the five load stages selected for the mortar specimen, while using the 2 mm virtual clip gauges. This comparison allows also to observe that cracks with the same opening at the tip of the notch (x = 0) show a much smaller length in the case of the FRCC than in the mortar specimens. Additionally, in the case of the FRCC

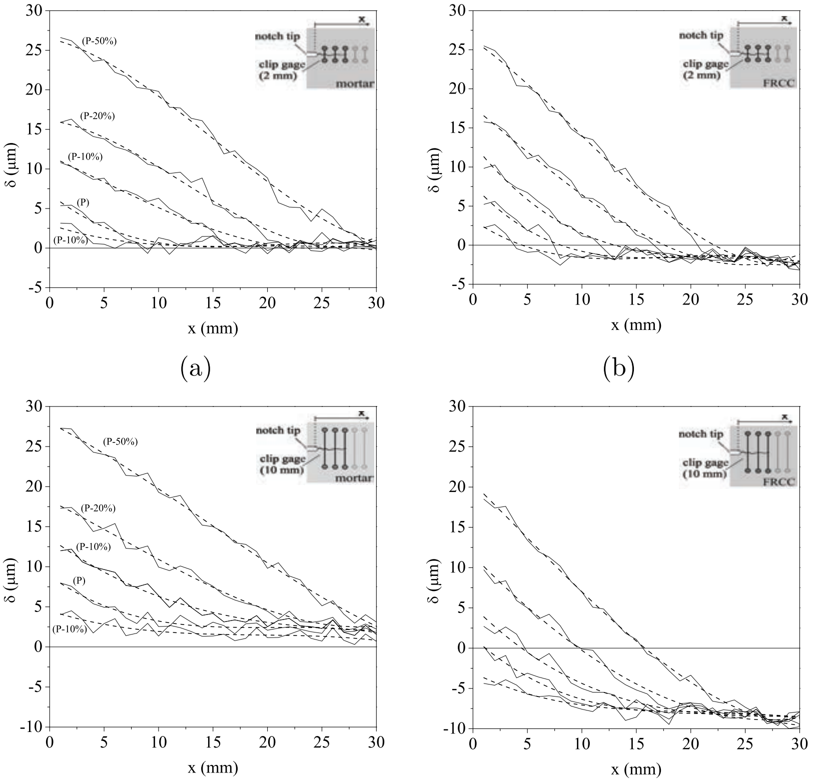

(a) (b) (c) (d)

Figure 3.14: Crack profiles obtained for different loading stages using virtual clip gauges with a length of 2 mm for mortar (a) and for FRCC (b), and using virtual clip gauges with a length of 10 mm for mortar (c) and FRCC (d).

specimen, the relative displacements in the region ahead of the tip of the crack are negative, which may be the consequence of the bridging stresses originated by the fibers in the region of the open crack. These additional compression strains/stresses in the region ahead of the crack tip affect the propagation of the crack by promoting the rapid transition from the undamaged bulk material to the fully open crack.

The use of the virtual clip gauges with a length of 10 mm instead of the 2 mm aimed at helping to distinguish the area around the crack which was predominantly affected by the crack propagation. Figure 3.14 shows that the differences observed previously considering the curvature of the displacement profile in the region of the open cracks are similar but less evident. The compression strains observed ahead of the crack tip become more pronounced in the case of FRCC, contrarily to the mortar specimen where small tensile strains are observed through the entire monitored length, even at the early stages of the cracking process. This suggests that the contribution of the fibers in the case of the FRCC results in the overall increase of the ambient compression stresses in the vicinity of the crack tip and the fracture process zone, which in turn contribute to the reduction of the crack length at the same CMOD, and to the reduction of the size of the transition region between the open crack and the intact bulk material. Due to the reduced post-peak residual tensile stresses in the mortar, the ambient stresses surrounding the crack tip region are tensile and develop along the full monitored length even at the early crack stages. As a consequence, the stabilization of the cracking processes and crack propagation resulting from the adoption of the fibers was not only a direct consequence of the fiber contribution to the macro-crack bridging but also a result of the alteration of the stress and strain fields in the vicinity of the crack tip. Not only the shape but also the length of the transition zone between the fully open crack and the intact bulk material were changed or affected by the presence of the fibers.

3.5 Effect of different fiber types on the cracking processes

The observation of the propagation of a crack initiated at the tip of a sharp notch in cementitious composites reinforced with different types of fibers is the next step of this research.The previous exploratory tests have showed that the digital imaging analysis technique formerly presented has satisfactory resolution to capture the features of the cracking process, which are relevant for this investigation. The detail and resolution required to capture these events are high, considering that the mechanical response is brittle and the cementitious composite materials have a multi-scale nature [Hornain et al., 1996; Otsuka and Date, 2000].

In this section the propagation of cracks in cementitious composites reinforced with PVA, PAN and PP fibers is investigated. The surface properties, the geometry and the mechanical properties of these fibers are very different, therefore the procedure is aimed at understanding how these different properties can affect the fracture processes and crack propagation. The design of advanced FRCC is nowadays based on the use of a multiplicity of different types of fibers with various geometries. The fast developing fiber technology is everyday widening the spectrum of available types of fibers, with significant developments in the production processes and synthetic materials, making available new fibers of improved mechanical and physical properties.

The design of FRCC can effectively take advantage of these opportunities if the crack propagation and fracture mechanisms in these materials are thoroughly understood. In particular, the influence of the fiber reinforcing mechanisms on the fracture process can be further clarified, which is important in the design of the fiber reinforcement for specific applications as well as to guide the development of new fibers and new production technologies.

3.5.1 Materials

In this study the tensile behavior of three different FRCC was investigated. Both the type of fiber reinforcement and the composition of the matrix were different in the composites tested. Fibers of three different natures were used: PVA (polyvinyl alcohol), PAN (polyacrylnitrile) and PP (polypropylene). The main properties of the fibers used are recalled in Table 3.3.

The composition of each FRCC is represented in Table 3.4. As shown two different types of cementitious matrices were used. The volume fraction of fiber reinforcement employed was 2% in the case of the PVA (PVAcc) and the PAN (PANcc) FRCC, and 2.5% in the case of the PP FRCC (PPcc). The higher volume fraction in the case of the PPcc aimed at compensating the lower tensile strength of PP fibers when compared to the PVA ones. In the case of the PANcc this compensation was not considered due to the significant influence of the fiber volume increase in the flow properties of the fresh mixture.

Table 3.3: Main properties of the fibers.

Fiber	Tensile strength	Length	Diameter
PVA	1600	8	40.0
PP	900	12	40.0
PAN 1.5	826	6	12.7

3.5.2 Experimental procedure

As before, the CTT testing procedure consisted on applying an eccentric tensile load to a single-edge notched specimen, at a constant displacement rate of 5 $\mu m/s$, to in-

Table 3.4: Weight proportions of the materials used in each composite.

Composite	Fiber reinforcement	Cement	Fly ash	Fine sand (0.17 mm)	Quartz powder	Water
PVAcc	2% PVA	1	2	0.35	0.35	0.75
PPcc	2.5% PP	1	2	0.35	0.35	0.75
PANcc	2% PAN	1	6	0	0	1.40

duce the initiation of a single crack and allow its propagation in a controlled manner. The dimensions and geometry of the specimen were slightly adapted with respect to the ones adopted in the previous section, as presented in Figure 3.15. The length of the notch was altered and the final a/W was approximately 0.6, maximizing this way the size of the singularity dominated zone (see Figure 3.6). In addition, the altered geometry allowed the full coverage of the region ahead of the notch tip by the camera sensor field, from the notch tip to the opposite specimen edge.

The formation and propagation of the tensile crack was traced on the surface of the specimens using a high resolution digital camera, positioned 90 mm away from the specimen. The 60 mm focal length lens allowed the observation of a 24 mm by 36 mm area of the surface of the specimen (see Figure 3.15). In Figure 3.16 the image of the specimen reinforced with PP fibers after testing is shown. Images with 24 megapixel of resolution were captured during testing with time intervals of one second. These images were subsequently used to continuously interpolate the strain fields at the inspected surface of the specimen.

As before, the optimal conditions to the strain field interpolation were met without the need of applying a speckle pattern on the surface of the specimen, in contrast to the typical procedure. The main advantage is that, because the surface of the specimen is directly observed, the possible influence of conditioning overlays on the results obtained is minimized. This is particularly important when trying to measure very small displacements, of the order of the micrometer. The images of the surface of the specimens were analyzed prior to testing and sufficient image correlation was obtained. Each facet was composed of 15×15 pixels. Each pixel covered a real area of 6×6 μm^2. The total area of 24×36 mm^2 was modeled by a facet mesh overlay composed of approximately 267×400 facets.

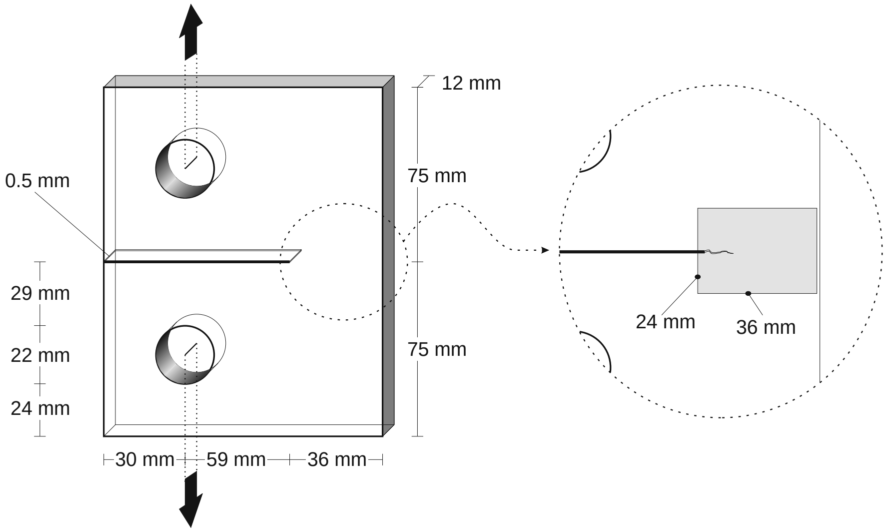

Figure 3.15: Adjusted geometry and dimensions of the CTT specimen.

3.5.3 Load-displacement results

The experimental responses obtained for the three composites in terms of the tensile load versus the displacement are presented in Figure 3.17. In this case the displacements measured correspond to the total displacement between the loading points. For comparison, in Figure 3.17.d the average responses of each composite are presented. The average responses were obtained by averaging the tensile load measured for the three specimens of each composite at every displacement level.

In general, the CTT tensile load-displacement responses obtained show that the different types of fibers have resulted essentially in different deformational behaviors. Although the peak load reached in all composites was approximately the same (350 N), the displacement at which the peak load is reached was clearly distinct, of approximately 0.5 mm in the case of the PANcc and 2 mm in the case of the PVAcc and the PPcc. The thorough analysis of the results obtained with the image-based analysis showed that cracking starts early, at tensile load values of around 150 N, as discussed subsequently. When observing the measured tensile load-displacement responses of the three composites, the overall behavior and shape of the curves obtained reflect the different nature of the fiber reinforcements used. This relation will be further explored in the next section, where the influence of the composite parameters (fiber and matrix properties) on the mechanical responses obtained is clarified.

Figure 3.16: Image of test-setup and size of the documented area.

3.6 Simulation of CTT tensile load-displacement response

The finite element method-based simulation of the load-displacement, or alternatively, the moment-curvature response of FRCC is typically performed considering that the crack path is localized at the mid-section of the specimen. This assumption is reasonable when tensile-softening FRCC are considered. The expected crack path at the mid-section is simulated by adopting a layer of interface elements, which are assigned with a traction-separation law that is derived from the mechanical characterization of the tensile behavior of the cementitious composite. The cohesive elements for the simulation of interfaces, with the traction-separation law defined in terms of damage evolution of Abaqus® [Aba, 2011]. In this research, although one may not be dealing with tensile softening materials, the same strategy will be adopted to simulate the tensile load-displacement response of the CTT specimens. The results are discussed in conjunction with the fracture processes identified when using the image-based deformation analysis previously presented. The characterization of the traction-separation law of the interface elements will be based on the tensile responses obtained with the SCTT

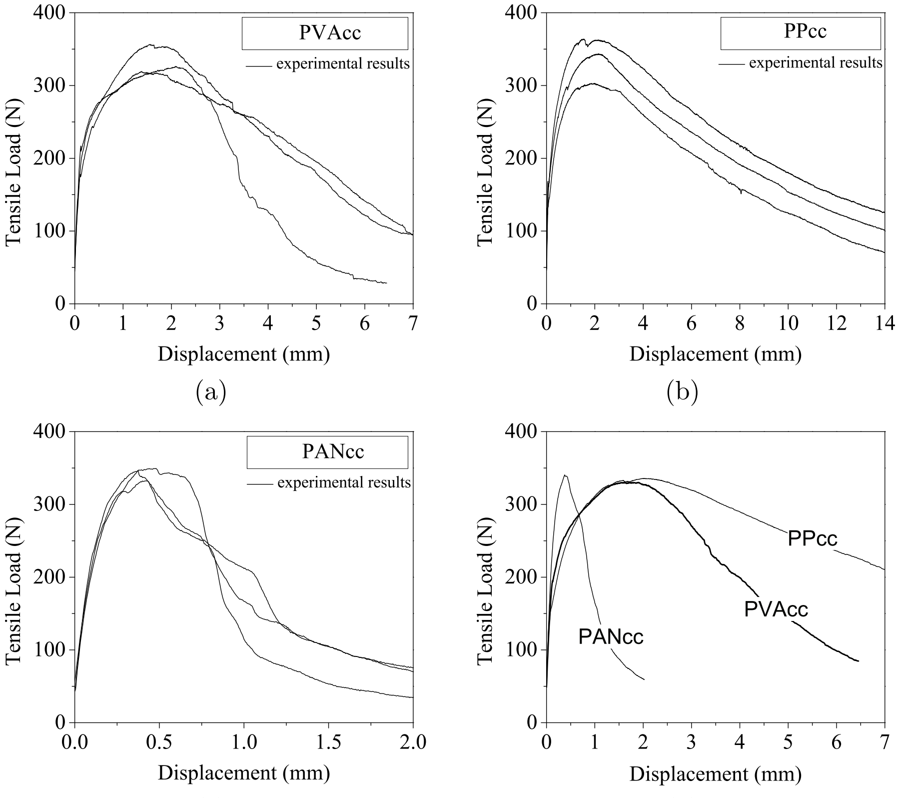

(a) (b)

(c) (d)

Figure 3.17: Tensile load-displacement curves for the composites reinforced with PVA fibers(a), PP fibers (b), and PAN fibers (c). Average load-displacement curves for the three composites (d).

3.6.1 Characterization of the tensile responses using the SCTT

The SCTT provides information about the composite tensile behavior when a single crack is considered. The initiation of the crack is somewhat determined by the geometry of the specimen and the shape of the notched section. The slender notches and the strong section reduction adopted contribute to locally alter the stress fields and increase substantially the stress intensity. Before the crack is fully formed the tensile responses obtained are influenced by the specimen geometry. However, after the brief stage of crack formation, the fibers remain as the final links between the opposite flanks of the crack. It may then be assumed that the measured tensile bridging stress-CMOD responses are evaluated objectively and are essentially independent of specimen geometry. Consequently, this information can be used to describe the constitutive behavior of the material in tension in terms of the tensile stress,σ_t, as a function of the crack width, δ. The constructed finite element model of the CTT will help to verify this possibility.

The results obtained after testing six specimens of each composite in direct tension are presented in Figure 3.18. The values of the tensile stress (nominal tensile stress) were obtained by computing the ratio between the experimental tensile load and the net area of the notched cross-section ($8\times$ 30 mm^2). The crack mouth opening displacements (CMOD) were obtained by averaging the displacements measured in the two opposite clip gauges.

As shown in Figure 3.18, the activation of fibers with different diameters and of different natures occurs at different stages of the cracking process. The PAN fibers, with a smaller diameter, were activated even before the first cracking stress was reached, and have contributed effectively to increase the cracking peak stress. Their early effective activation was followed by an also premature exhaustion of their contribution to the post-cracking tensile behavior. The contribution of PVA and PP fibers to increase the first cracking strength was insignificant. In contrast, their full mobilization became apparent in the post-cracking stage, with the pronounced post-cracking increase of the tensile bridging stress. The main difference between the SCTT results observed for PVA and PP fibers locates at the region of the tensile stress-CMOD curves where the peak bridging stress is reached. While for the PVA reinforced composites the experimental curves exhibited a sharp transition from the tensile hardening to the tensile softening stage of the tensile bridging stress, for the PP reinforced composites this transition was smooth and gradual. The well known superior interfacial bonding of the PVA fibers with the matrix may justify these results, as opposed to the poorer bonding of the PP fibers due to their hydrophobic nature [Li et al., 2002; Wei et al., 2002]. Further discussion regarding the significance of each stage of the tensile stress-CMOD responses obtained with the SCTT can be found in Chapter 2 and in previous work [Pereira et al., 2010, 2012].

3.6.2 FEM model of the CTT

As shown in Figure 3.19, the geometry of the specimen and testing boundary conditions were modeled assuming plane stress conditions. The two transverse steel rods

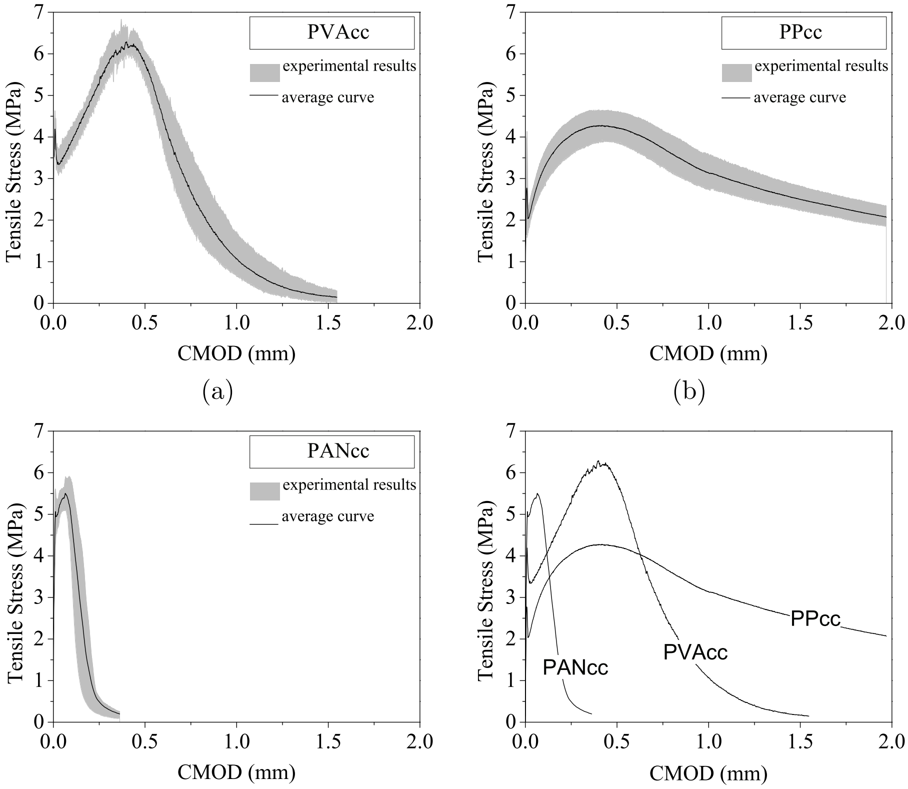

(a) (b)

(c) (d)

Figure 3.18: Tensile stress-CMOD for the composites reinforced with PVA fibers(a), with PP fibers (b), and with PAN fibers (c). Average tensile stress-crack opening curves obtained for the three composites (d).

transmitting the load were placed in the two circular openings presented. The model was constructed using elastic 3-node linear triangular elements. The high geometrical gradients close to the notch tip were overcome with the considerable increase of the number of elements in these regions. The blunted shape of the notch tip, with a radius of 250 μm, was discretized with increased number of finite elements. The young modulus, E, assigned to the elements was 20 GPa and the Poisson coefficient, ν, was 0.2. One layer of interface elements was added in the notched section between the left and the right portions of the specimen (x = 75 mm, Figure 13). The interface elements were assigned with a traction-separation law, $\sigma_t = f(\delta)$, directly derived from the results obtained with the SCTT of each composite. These laws correspond to the responses shown in Figure 3.18, when the portion of the response prior to the attainment of the first cracking stress is excluded. In this case the average tensile stress-crack opening responses obtained with the SCTT of each composite were utilized (Figure 3.18.d).

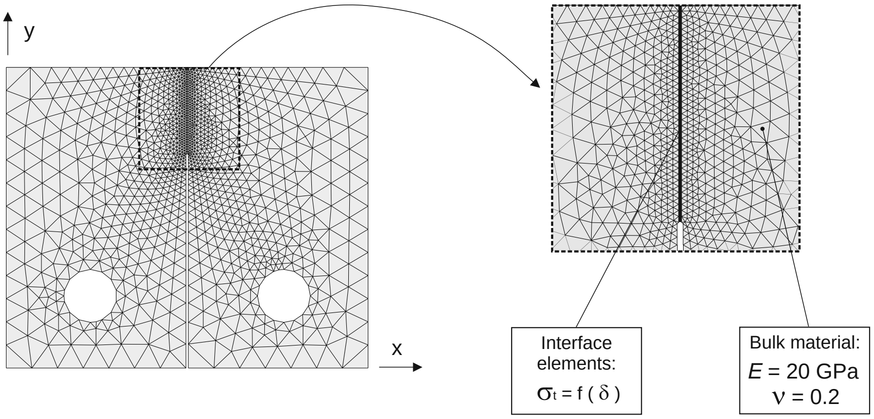

Figure 3.19: Geometry of the specimen and finite element mesh adopted in the simulation.

The tensile load-displacement responses obtained for each composite are represented in Figure 3.20.a. The displacement was evaluated by calculating the displacement difference between the center of the two opposite loading rods. For each composite the computed tensile load-displacement response was compared to the experimental results (Figure 3.20.b to Figure 3.20.d). In addition, four different stages of the CTT response obtained from one specimen of each composite were highlighted.

The simulated CTT responses are, in general, similar to the experimental ones. The peak load is generally overestimated by the simulations, and in contrast the displacements are in general somewhat underestimated. The formation of multiple cracks may justify this result. In the finite element model the formation of a single crack is assumed during the entire loading sequence, and if more than one crack is formed the resulting displacements are increased at the same load levels. In addition, when more than one crack is formed, the rupture of the tested specimen will be eventually determined by the crack where the lowest bridging stresses are generated, among all cracks formed (the weakest link principle). The peak load overestimation is therefore the result of both the assumption of a single crack forming in the numerical model and the adoption of the average tensile stress-CMOD behavior to derive the stress-separation law of the interface elements.

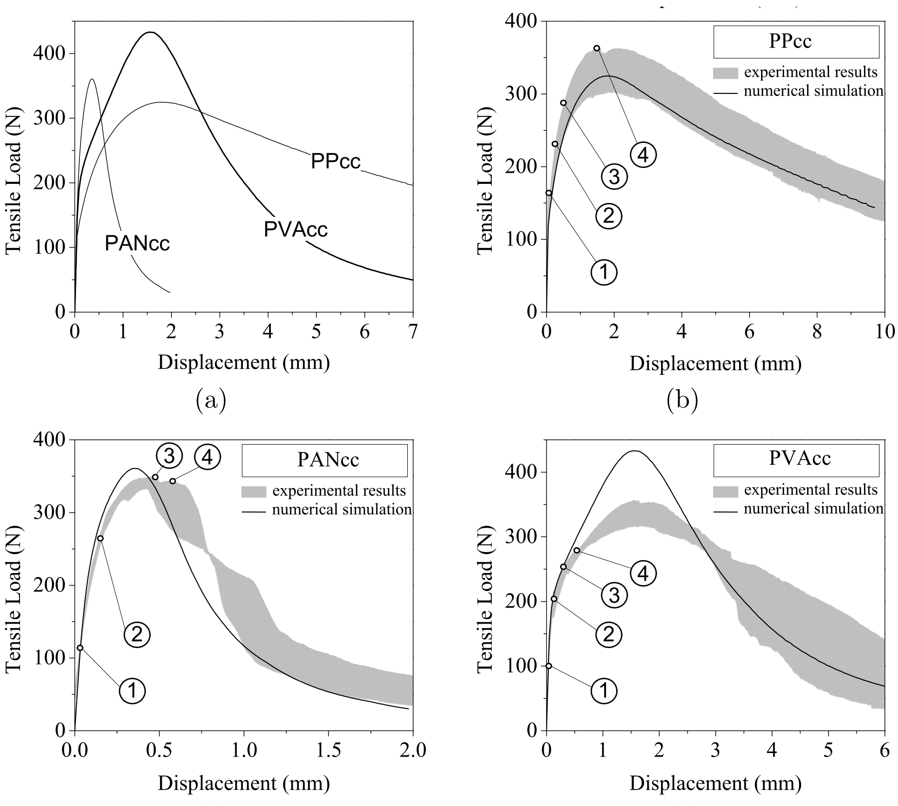

(a) (b)

(c) (d)

Figure 3.20: Tensile load-displacement response for the three composites tested (a). Tensile load-displacement response of the composites reinforced with PP fibers (b), with PAN fibers (c) and with PVA fibers (d).

The detailed analysis of the crack patterns generated at the surface of the specimens confirm that more than one crack was formed in the tested specimens (Table 3.5). The stage number one was selected in all specimens to show the last stage at which no cracks were detected. All stages are identified for all specimens in Figure 3.20. Considering the PPcc specimen, the stage two was selected as the last stage where only one major crack was detectable. Considering the PANcc and the PVAcc specimens a single major crack was never observed, at least two diagonal cracks were forming simultaneously. In the case of the PVAcc results, stages 2 and 3 correspond to the points of the tensile response where the numerical results start diverging more clearly from the experimental ones. As shown in Table 3.5, the cracks forming in the PVAcc specimen indicate that the behavior experimentally obtained is different from the one assumed in the finite element model. The main crack diverts from its horizontal path earlier than in the other two composites, bifurcating at a considerable distance from the right border of the specimen and partly justifying the divergence between the experimental and the numerical results from stage 3 onwards. The considerable alteration of the structural behavior caused by this early crack bifurcation in the experimental test, in opposition to the assumed single crack in the numerical model, explains partly the underestimation of the experimental displacements and the overestimation of the peak tensile load by the numerical model. The profuse cracking observed in the PANcc specimen (stage 4, Table 3.5) also caused a substantial alteration of the structural behavior assumed in the numerical model, however the divergence between the numerical and the experimental results is not so pronounced. Although the main crack also diverts clearly from its original path, the crack branches reach longer distances in the direction of the right border of the specimen. Also, since the tensile response in the case of the PANcc is occurring at clearly smaller tensile displacement, meaning that the cracking processes are involved at a much smaller scale, the overestimation of the peak tensile load and the underestimation of the tensile deformation do not become as pronounced as in the case of the PVAcc. In the case of the PPcc the predicted tensile response is almost identical to the experimental, and this result is supported by the observed crack pattern that is mostly identical to the one assumed by the numerical model. The displacements are, as before, somewhat underestimated by the numerical model, due to the absence of the possibility to consider and simulate crack branching in the numerical model.

3.7 Conclusions

An intuitive analysis of the micro-cracking mechanisms occurring in cementitious composites was carried out using the image-based monitoring technique presented in this study. The full-field displacements interpolation and measurement at the surface of the specimens allowed the immediate and intuitive interpretation of the micro-mechanical events taking place during the initiation and the propagation of the cracks. The effect of pre-existing cracks or other micro-defects, of fibers or aggregates, could be evaluated in a meticulous and efficient manner with the aid of the present technique.

The revealed cracking features contributed to the supported interpretation of the mechanical test results. The influence of shrinkage induced pre-existing cracks on the final path of the principal crack was revealed in the images of the deformations

Table 3.5: Image-based analysis of crack patterns on the surface of the specimens at stages 1 to 4.

	PPcc	PVAcc	PANcc	
1				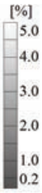
2				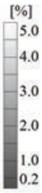
3	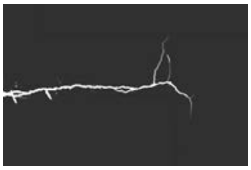	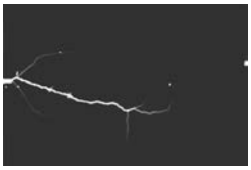	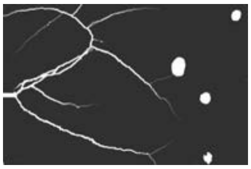	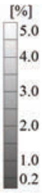
4	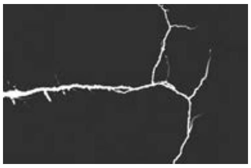	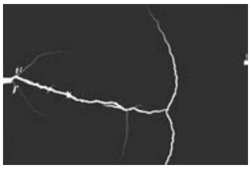	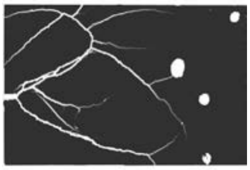	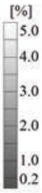

derived to the cement paste specimen. The secondary cracks detected with the increase of the load have influenced the crack path, diverting and shaping the primary crack originated at the tip of the notch. In addition, the presence of these pre-existing cracks contributed to explain the smaller initial stiffness registered for the cement past specimen. Similarly, the presence of different quantities of aggregates and with different sizes has influenced the morphology of the propagating cracks in the remaining specimens, especially near the crack tip. The cracks propagating in the cementitious composites containing more and larger aggregates have shown shorter and more smeared crack branches. In contrast, in the FRCC specimen the crack branches were less visible, suggesting that the fibers have contributed effectively to arrest micro-cracking.

The investigation of the displacement profiles along the cracks formed in the mortar and in the FRCC specimens has shown that the shape of the crack was altered by the presence of the fibers in the cementitious composite. Also the crack lengths observed at different loading stages for the same crack tip opening displacements (CTOD) were shown to be reduced by the contribution of the fibers in the case of the FRCC. The presence of the fibers in the FRCC affected the mechanical behavior of the composite not only by contributing to the crack bridging in the region of the macro-crack but also by altering the ambient stresses/strains surrounding the crack tip region, and in particular by modifying the geometry and boundary conditions of the fracture process zone.

The investigation of the initiation and propagation of cracks in cementitious materials using the compact tension test (CTT) was also extended to the study of specimens reinforced with different types of fibers. The tensile load-displacement responses measured have shown different characteristic tensile behaviors, as a result of the different geometry and nature of the fibers used. Although the geometry of the specimen and the test setup configuration were delineated to create the necessary conditions to the initiation of a single crack, the results obtained with the image-based analysis have shown that this was not the case. The original pictures taken from the surface of the specimen, although with high amplifications, did not allow the detection of more than one crack. However, the post-processing of these pictures revealed disordered crack patterns substantially different from the ones assumed after a simple visual inspection, and also different from the ones initially expected. These results should be taken into consideration when extracting the stress-separation law by inverse analysis. The precise and explicit characterization of the stress-separation behavior by inverse analysis is only possible if the exact crack pattern formed is known in advance, and the model used to simulate the experimental response is able to accommodate these complex crack patterns which are typically formed in SHCC materials.

The characterization of the tensile stress-CMOD behavior of the three different FRCC using the single crack tension test (SCTT) has shown high sensitivity to the main parameters of each cementitious composite. The post-cracking behaviors obtained have shown that different fibers have an optimal contribution to the tensile bridging stresses at clearly distinct scale sizes of the cracking process. The tensile stress-CMOD responses obtained with the SCTT were used to predict the tensile load-displacement behaviors obtained with the CTT of the corresponding composites. In the numerical model the typical formation of a single crack with the direction of the notch plane was assumed. Although a good general agreement between the numerical and experimental results were obtained, the peak load was somehow overestimated in some cases and the deformations underestimated by the numerical model. The results obtained with the image-based analysis explain the deviation between the numerical and the experimental results by showing the formation of cracking patterns distinct from the one assumed in the numerical model.

Bibliography

(2011). *Abaqus/CAE User's Manual.* DSimulia, 6.10 edition.

446, A. C. (1999). Fracture mechanics of concrete: concepts, models and determination of material properties. ACI Committee Report ACI 446.1R-91 (Reapproved 1999), American Concrete Institute.

Abanto-Bueno, J. and Lambros, J. (2005). Experimental determination of cohesive failure properties of a photodegradable copolymer. *Exp. Mech.*, 45(2):144–152.

ASTM-E647 (2005). Standard test method for measurement of fatigue crack growth rates.

Bache, H. (1986). Fracture mechanics in design of concrete and concrete structures. In Whittmann, F., editor, *Fracture toughness and fracture energy of concrete*, pages 577–586, Lausanne, Switzerland. Elsevier.

Barnes, B. D., Diamond, S., and Dolch, W. L. (1978). The contact zone between portland cement paste and glass 'aggregate' surfaces. *Cement and Concrete Research*, 8:233–43.

Berfield, T., Patel, J., Shimmin, R., Braun, P., Lambros, J., and Sottos, N. (2007). Micro-and nanoscale deformation measurement of surface and internal planes via digital image correlation. *Exp Mech*, 47(1):51–62.

Bruck, H., McNeill, S., Sutton, M., and Peters, W. (1989). Digital image correlation using newton-raphson method of partial differential correction [displacement measurement]. *Experimental Mechanics*, 29(3):261–267.

Bruhwiler, E., Broz, J. J., and Saouma, V. (1991). Fracture model evaluation of dam concrete. *ASCE Journal of Materials in Civil Engineering*, 3(3):235–251.

Cedolin, L., Dei Poli, S., and Iori, I. (1983). Experimental determination of the fracture process zone in concrete. *Cement and Concrete Research*, 13(4):557–567.

Cedolin, L., Dei Poli, S., and Iori, I. (1987). Tensile behavior of concrete. *ASCE Journal of Engineering Mechanics*, 113(3):431–449.

Chandra, S. (2002). *Chapter five - Properties of concrete with mineral and chemical admixtures*, pages 140–85. Spon Press.

Chona, R., Irwin, G. R., and Sanford, R. J. (1983). Influence of specimen size and shape on the singularity-dominated zone. *American Society for Testing and Materials, Special Technical Publications 791.*, pages 3–23.

Chu, T. C., Ranson, W. F., and Sutton, M. A. (1985). Applications of digital-image-correlation techniques to experimental mechanics. *Exp Mech*, 25(3):232–244.

Corr, D., Accardi, M., Graham-Brady, L., and Shah, S. (2007). Digital image correlation analysis of interfacial debonding properties and fracture behavior in concrete. *Engineering Fracture Mechanics*, 74(1-2):109–121.

Diamond, S. and Huang, J. (2001). The itz in concrete - a different view based on image analysis and sem observations. *Cement and Concrete Composites*, 23(2-3):179–88.

Gartner, E. M., Young, J. F., Damidot, D. A., and Jawed, I. (2002). *Chapter three - Hydration of Portland Cement*, pages 57–113. Spon Press.

Gettu, R. and Shah, S. (1992). Fracture mechanics and high strength concrete. In Shah, S. and Ahmad, S., editors, *High performance concrete and applications*, pages 1–75, Seven Oaks, UK.

Guo, L.-P., Sun, W., He, X.-Y., and Xu, Z.-B. (2008). Application of dscm in prediction of potential fatigue crack path on concrete surface. *Engineering Fracture Mechanics*, 75(3-4):643–651.

He, S., Feng, Z., and Rowlands, R. (1997). Fracture process zone analysis of concrete using moire interferometry. *Exp Mech*, 37(3):367–373.

Hillerborg, A. (1983). Analysis of one single crack. *Developments in Civil Engineering*, pages 223–249.

Hillerborg, A., Modéer, M., and Petersson, P. (1976). Analysis of crack formation and crack growth in concrete by means of fracture mechanics and finite elements. *Cement and Concrete Research*, 6(6):773–781.

Hilsdorf, H. K. and Brameshuber, W. (1991). Code-type formulation of fracture mechanics concepts for concrete. *International Journal of Fracture*, 51(1):61–72.

Hornain, H., Marchand, J., Ammouche, A., Commeìne, J., and Moranville, M. (1996). Microscopic observation of cracks in concrete – a new sample preparation technique using dye impregnation. *Cement and Concrete Research*, 26(4):573–583.

Irwin, G. R. (1958). *Fracture*, volume 6 of *Handbuch der Physik*, pages 551–590. Springer-Verlag.

Jacquot, P. and Rastogi, P. K. (1983). Speckle metrology and holographic interferometry applied to the study of cracks in concrete. *Developments in Civil Engineering*, pages 113–155.

Karihaloo, B. (1995). *Fracture mechanics and structural concrete*. Longman Scientific and Technical, Harlow.

Karihaloo, B., Carpinteri, A., and Elices, M. (1993). Fracture mechanics of cement mortar and plain concrete. *Advanced Cement Based Materials*, 1(2):92–105.

Knab, L., Walker, H., Clifton, J., and Fuller Jr., E. (1984). Fluorescent thin sections to observe the fracture zone in mortar. *Cement and Concrete Research*, 14(3):339–344.

Landis, E. N. and Shah, S. P. (1995). The influence of microcracking on the mechanical behavior of cement based materials. *Advanced Cement Based Materials*, 2(3):105–118.

Landis, E. N., Zhang, T., Nagy, E. N., Nagy, G., and Franklin, W. R. (2007). Cracking, damage and fracture in four dimensions. *Mater Struct*, 40(4):357–364.

Lawler, J., Wilhelm, T., Zampini, D., and Shah, S. (2003). Fracture processes of hybrid fiber-reinforced mortar. *Mater Struct Materials and structures*, 36(257):197–208.

Li, V. C., Wang, S., Ogawa, A., Saito, T., and Wu, C. (2002). Interface tailoring for strain-hardening polyvinyl alcohol-engineered cementitious composite (pva-ecc). *ACI Materials Journal*, 99(5):463–472.

Maji, A., Ouyang, C., and Shah, S. (1990). Fracture mechanisms of quasi-brittle materials based on acoustic emission. *Journal of Materials Research*, 5(1):206–217.

Maji, A. and Shah, S. P. (1988). Process zone and acoustic-emission measurements in concrete. *Experimental Mechanics*, 28(1):27–33.

Maji, A. K. and Shah, S. P. (1990). Measurement of mixed-mode crack profiles by holographic interferometry. *Experimental Mechanics*, 30(2):201–207.

Mehta, P. and Monteiro, P. (2006). *Concrete: microstructure, properties, and materials*. McGraw Hill professional. McGraw-Hill.

Miller, R. A., Shah, S. P., and Bjelkhagen, H. I. (1988). Crack profiles in mortar measured by holographic interferometry. *Experimental Mechanics*, 28(4):388–394.

Mindess, S. (1991). *Fracture mechanics test methods for concrete*, chapter Fracture process zone detection, pages 231–255. Report of RILEM FMT-89. Chapman & Hall, London.

Otsuka, K. and Date, H. (2000). Fracture process zone in concrete tension specimen. *Eng Frac Mech*, 65(2-3):111–131.

Pereira, E., Fischer, G., and Barros, J. (2012). Direct assessment of tensile stress-crack opening behavior of strain hardening cementitious composites (shcc). *Cement and Concrete Research.*

Pereira, E. B., Fischer, G., Barros, J. A., and Lepech, M. (2010). Crack formation and tensile stress-crack opening behavior of fiber reinforced cementitious composites (frcc). *7th International Conference on Fracture Mechanics of Concrete and Concrete Structures (FraMCoS 7).*

Regnault, P. and Bruhwiler, E. (1990). Holographic interferometry for the determination of fracture process zone in concrete. *Engineering Fracture Mechanics*, 35(1-3):29–38.

Sanford, R. (2003). *Principles of fracture mechanics.* Prentice Hall.

Savic, V., Hector Jr, L. G., and Fekete, J. R. (2010). Digital image correlation study of plastic deformation and fracture in fully martensitic steels. *Exp Mech*, 50(1):99–110.

Scrivener, K. L. and Pratt, P. L. (1996). Characterization of interfacial microstructure. In Maso, J. C., editor, *Interfacial Transition Zone in Concrete*, pages 3–17. RILEM Technical Committee 108-ICC, E & FN Spon.

Shah, S., , and Ouyang, C. (1993). Toughening mechanisms in quasi-brittle materials. *Journal of Engineering Materials and Technology*, 115(3):300–307.

Shah, S. (1990). Experimental methods for determining fracture process zone and fracture parameters. *Engineering Fracture Mechanics*, 35(1-3):3–14.

Shah, S., Swartz, S., and Ouyang, C. (1995). *Fracture mechanics of concrete - Applications of fracture mechanics to concrete, rock, and other quasi-brittle materials.* Wiley, New York,N.Y.

Struble, Stutzman, and Fuller, J. (1989). Microstructural aspects of the fracture of hardened cement paste. *Journal of American Ceramic Society*, 72(12):2295–2299.

Tiwari, V., Sutton, M. A., McNeill, S., Xu, S., Deng, X., Fourney, W. L., and Bretall, D. (2009). Application of 3d image correlation for full-field transient plate deformation measurements during blast loading. *International Journal of Impact Engineering*, 36(6):862–874.

van Mier, J. (1984). *Strain Softening of Concrete under Multiaxial loading conditions.* PhD thesis, Delft Technical University.

van Mier, J. (1997). *Fracture processes of concrete: assesment of material parameters for fracture models.* New directions in civil engineering. CRC Press.

Vendroux, G. and Knauss, W. (1998). Submicron deformation field measurements: Part 2. improved digital image correlation. *Experimental Mechanics*, 38(2):85–92.

Wei, Q. F., Mather, R. R., Fotheringham, A. F., and Yang, R. D. (2002). Esem study of wetting of untreated and plasma treated polypropylene fibers. *J Ind Text*, 32(1):59–66.

Wittmann, F. H. and Hu, X. (1991). Fracture process zone in cementitious materials. *Int J Fract*, 51(1):3–18.

Yoneyama, S., Morimoto, Y., and Takashi, M. (2006). Automatic evaluation of mixed-mode stress intensity factors utilizing digital image correlation. *Strain*, 42(1):21–29.

Yuan, C. Z. and Guo, W. J. (1987). Bond between marble and cement paste. *Cement and Concrete Research*, 17:544–52.

Zimbelman, R. (1985). A contribution to the problem of cement aggregate bond. *Cement and Concrete Research*, 15:801–8.

CHAPTER 4

Single and hybrid fiber-type reinforcement

4.1 Introduction

Fiber technology is nowadays evolving rapidly. New types of fibers are becoming available everyday, with remarkable physical and mechanical properties. While showing improved surface properties and enhanced tolerance to aggressive agents or extreme temperature exposure, the new fibers, under permanent development and rapid evolution, are creating new opportunities to the improvement of composite materials that can efficiently utilize the advanced material properties exhibited by the fibers. The addition of more than one type of fiber onto a ceramic, metallic or polymeric matrix is not uncommon, and is regarded as a strategy that promotes the cooperative contribution of all fiber types while leading to an overall improved mechanical behavior. Eventually the type and number of different fibers used in the composite are additional parameterr in the optimization process of hybrid fiber reinforced composites, as well as each fiber length, geometry and mechanical properties.

The use of fiber reinforcements containing multiple types of fibers is also not uncommon in cementitious matrix composites. Whether discrete short or long, in the form of mats, yarns or rods, the fibers of different shapes and forms used in hybrid fiber reinforcements introduce different mechanical properties in the cementitious composites that they integrate. In the context of the present research, hybrid fiber reinforcements will be restricted to the case of fiber reinforcements containing discrete short fibers of different natures. In the case of fiber reinforced cementitious composites, the addition of these short discrete fibers may have important effects on distinct properties of the composite. The re-design of the surface properties of the newly developed fibers is particularly important when considering the fiber applications as reinforcement on cementitious materials. For example, the presence of smaller fibers in the cementitious matrix is known to have significant effect on the fresh properties of the mixture and on the micro-structural packing of fine particles. Additionally, the ordered growth of cement products during hydration and setting can be greatly influenced by the presence of the small fibers and their surface properties. Larger fibers also have an important effect on the fresh properties of cementitious composites, although not as relevant at the smaller material scale. When designing fiber reinforced cementitious matrices, all the aspects of the mixture fresh behavior and micro-structure formation must be taken into careful consideration, as discussed in the previous chapters. Two options to deal with this at the composite design level may include the re-design of the fiber surface properties, or the adoption of a combination of different fiber types with a balanced trade-off between the requirements in terms of fresh mixture properties and the hardened mechanical behavior.

Although the most successful examples of cementitious composites exhibiting tensile hardening and multiple cracking properties are typically reinforced with a single fiber type (see Chapter 1), the utilization of fibers of different types and sizes in the same composite has also been extensively explored. In principle, the adoption of fibers of different natures simultaneously in the same mixture aims at achieving improved tensile properties in the cementitious composite, by taking advantage of the superposition of the contributions of each fiber type to the overall tensile performance. Furthermore, the multi-scale nature of the cementitious composites material structure suggests that the use of different fibers to restrain cracking at the level of each distinct material scale should result in a synergistic effect, that is, on the cooperation between distinct fiber types to restrain crack progression at the level of distinct material scales.

The use of fibers of different natures and with distinct geometrical and material properties in hybrid fiber reinforced cementitious composites has been reported to improve the material properties of fiber reinforced cementitious composites. Examples of recently developed high performance fiber reinforced cementitious composites using hybrid fiber reinforcements may be found in the literature. High Performance Multimodal Fiber Reinforced Cementitious Composites have been developed at LCPC using two different types of steel fibers (1200 MPa of yield strength) in a cementitious matrix [Rossi, 1997]. The fiber volume fractions used were 5% of 5 mm long and 0.25 mm of diameter cylindrical straight fibers, plus 2% of 25 mm long and 0.3 mm of diameter cylindrical hooked end fibers. Average compressive strengths of 193.3 MPa and flexural tensile strengths of 41.4 MPa have been reported, as well as average tensile strength of 15 MPa obtained from direct tension tests in notched specimens

[Rossi, 1997]. Studies conducted in hybrid fiber reinforced concretes containing two or three distinct types of fibers (macro and micro fibers) at less than 1.3 total fiber volume fractions have shown some improvement on the flexural toughness, when compared with the corresponding single fiber type composites [Banthia and Gupta, 2004]. Similar conclusions have been reported by Qian and Stroeven [2000] using the four-point bending test to characterize cementitious composites containing hybrid reinforcements of two and three different types of steel and polypropylene fibers. The documentation of the cracking mechanisms on single and hybrid fiber-type reinforced composites containing up to 1% of fiber volume percentage revealed essentially different cracking mechanisms when micro and macro fibers were used, as well as in the situations where hybrid reinforcements were adopted [Lawler et al., 2003]. The improvement of the flexural behavior with hybrid fiber reinforcements containing steel, polyvinyl alcohol and polyethylene fibers at less than 2.5% fiber dosages was evaluated under different perspectives by Ahmed et al. [2007]. Different fiber combinations were shown to produce optimal flexural behavior if different flexural properties were considered: the composite containing 0.5% of steel and 2.0% of polyethylene fiber volumes exhibited the highest deflection and energy absorption capacities, while the composite containing 1.5% steel and 1.0% polyvinyl alcohol fiber volumes exhibited the best performance in terms of flexural strength. Marković [2006] also reported improved tensile performances obtained with newly developed mixtures of Hybrid-Fiber Concrete (HFC). Short and long steel fibers were combined together in one concrete mixture with the goal of improving tensile strength by the action of the short fibers and enhance ductility by the action of long fibers. Straight and hooked end steel fibers were combined at a total fiber percentage of 2% and tensile strengths of up to 15 MPa were obtained in direct tension.

The analysis of the mechanical behavior of hybrid fiber reinforced cementitious composites is typically carried out considering the results of flexural tests, with few exceptions. In fact, few research studies include the characterization of the tensile behavior of these composites in direct tension. Also, few studies are successful on clearly distinguishing the beneficial effect of adopting multiple fiber-type reinforcements, as opposed to the single fiber-type reinforcement case. Additionally, even when direct tension tests are performed it is seldom possible to distinguish from the experimental results the intrinsic material behavior, and to isolate it from the structural response and the influence of the specimen geometry and testing boundary conditions. The evaluation of the possible synergistic cooperation between different fibers dispersed in the same cementitious matrix to restrain cracking in tension is seldom objective, in part due to the several dimensions at which the tensile performance of hybrid fiber reinforced cementitious composites may be evaluated.

4.1.1 Hybrid fiber-type reinforcement and the multi-scale nature of the cracking processes

As discussed in Chapter 3, cementitious matrix composites may be regarded as materials with a pronounced multi-scale structure. The cementitious paste, the agregates (and other inclusions like, for example, the fibers), and the interfacial transition zone (ITZ) are regarded as the three distinct phases present in the material structure. The consideration of these three main phases, with different mechanical, physical and micro-strucutral properties, is important to describe entirely the cracking process and to establish the relation between the heterogeneous material structure and the composite mechanical and physical properties. In addition,it is possible to distinguish different material scales and sub-phases at the level of each of the three main phases, increasing even further the complexity of the composite behavior.

The main advantage often attributed to the utilization of hybrid fiber reinforcement in FRCC is the possibility to restrain cracking at the level of each of these different scales [Mobasher and Li, 1996; Brandt, 2008]. It is generally recognized and assumed that the micro-mechanics of the cementitious composites is determined by the multi-scale nature of these materials, which in turn is reflected into a multi-scale structure of the cracking processes [van Mier, 1997]. In a simplistic perspective, it is assumed that the micro-cracks generated during the cracking process may be bridged by smaller fibers, while the propagation of macro-cracks is restrained by the larger fibers at later stages of the cracking processes [Betterman et al., 1995]. According to this multi-scale conception of the cracking processes, a visible crack can be assumed as the result of the coalescence of randomly oriented and diffusely distributed micro-cracks previously formed in the cementitious matrix (Figure 4.1). In turn, these diffusely distributed micro-cracks may be the result of the extension of damage at pre-existing micro-defects and pores. These micro-defects are originated during setting and curing of the mixture, and depend on numerous factors related to the placing and curing conditions. The different properties of the mixture constituents and inclusions may also, reciprocally, have significant influence on the initiation of the micro-cracking and initial damage propagation. In this context, it is believed that the design of the combination of fibers for reinforcement is optimal when the multi-scale nature of the cracking process is taken into account. Further research concerning this mechanism is required though, as the explicit evidence of the true crack restraining micro-mechanics of multiple fiber-type reinforced cementitious composites is not fully established, as discussed previously.

The relation between the hierarchized cracking process in a composite, the differ-

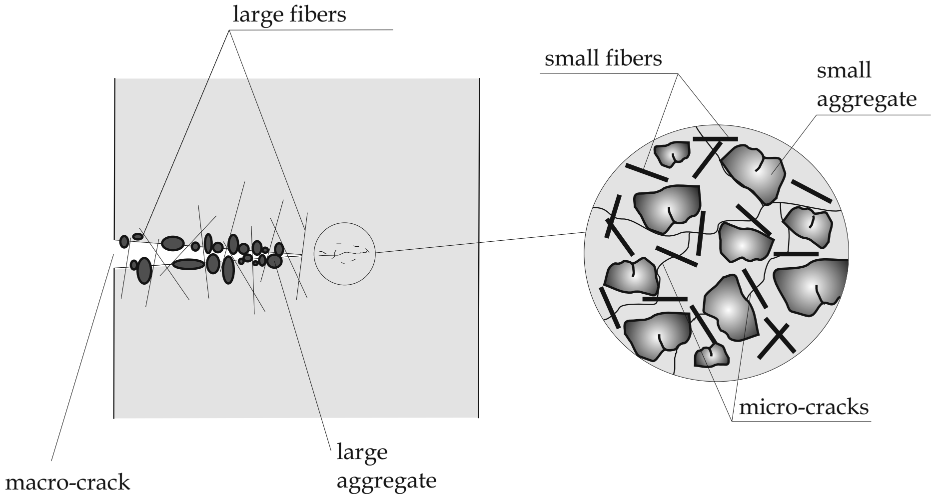

Figure 4.1: Multi-scale nature of the cracking processes in cementitious matrix composites and the multiple fiber-type reinforcement concept.

ent material scales and the mechanics of crack restraining by the different types of fiber reinforcements at different scales is not clearly and unequivocally understood. It is the objective of the research presented in this chapter to investigate how fibers of different types and sizes are affecting the crack bridging behavior, and to verify if a synergistic effect resulting of the cooperation of different fibers to the crack bridging mechanisms in the composite can be established. The strategy adopted in the assessment of the tensile performance of the fiber reinforced cementitious composites was directed to the explicit assessment of the importance and role of the micro-mechanisms of each composite phase in the overall composite response. In particular, when multiple fiber-type reinforcements are used, further clarification of the contribution of each type of fiber and of the interaction between different types of fiber reinforcements and different matrices to the overall composite mechanics was searched.

4.1.2 Assessment of the tensile performance of hybrid fiber-type reinforced cementitious composites

The tensile performance of fiber reinforced cementitious composites is often characterized by the fracture parameters and the load-deformation behavior derived with different standard test setups [Cotterell and Mai, 1996; Karihaloo, 1995; Shah et al., 1995]. For conventional types of fiber reinforcement, the three point bending test and the wedge splitting test setups are the most frequently used, mainly because the experimental procedure is considered simple and allows the characterization of the composite post-cracking behavior in a replicable and stable fashion [Barros et al., 2005; Chanvillard, 1999a; Lofgren et al., 2008; Zhang et al., 2010]. Inverse analysis is often utilized to derive the tensile stress-crack opening behavior from these experimental load-deformation results. Although satisfactory correlations are typically obtained, the uniqueness and universality of the solution independently of the test setup, of the boundary conditions and of the stress fields generated at the ligament region are not guaranteed [Chanvillard, 1999b]. In addition, when SHCC materials are considered, the probable formation of an unknown number of cracks during testing compromises the explicit characterization of the tensile material constitutive behavior.

For practical reasons, the three and four point bending tests in notched and unnotched specimens are the most frequently used to characterize the flexural and tensile behavior of hybrid fiber reinforced cementitious composites. The direct assessment of the tensile stress-crack opening behavior, while experimentally more demanding, may be regarded as a more effective approach to characterize objectively the tensile performance of fiber reinforced cementitious composites. In particular, when multiple types of fibers are used as reinforcement, this procedure may also allow the clear distinction of the contribution of each type of fiber to the overall composite behavior. Furthermore, the assessment of the tensile stress-crack opening behavior has clear advantages to the numerical modeling and structural design procedures, when advanced fiber reinforced cementitious composites are utilized. The post-cracking tensile stress-crack opening responses obtained when multiple types of fibers are used simultaneously are expected to be more complex than usual, due to the presence of different fibers in the composite. The numerical modeling of the mechanical behavior of SHCC at the meso-scale level may alternatively be based on the micro-mechanical parameters of the composite, including the mechanical properties of the fibers and of the matrix, and the properties of the fiber-matrix interface [Bolander and Saito, 1997; Cunha et al., 2012]. However, the explicit characterization of all these micromechanical parameters is challenging. The explicit characterization of the material behavior in terms of the stress-crack opening behavior is therefore important to the consistent and objective definition of the constitutive model for structural analysis [Stang et al., 1995; Kabele, 2007, 2009]. In a different perspective, the material design process also becomes more efficient when the direct assessment of the tensile stress-crack opening behavior is considered.

In this chapter the single crack tension test (SCTT) setup is used to quantify the contribution of different fibers to the overall tensile response of hybrid fiber-type reinforced cementitious composites. As discussed in Chapter 2, this procedure allows the direct and objective assessment of the tensile stress-crack opening behavior of SHCC [Pereira et al., 2010, 2012a], following previous research carried out in tensile-softening and tensile-hardening cementitious composites [Yang and Fischer, 2006; Fischer et al., 2007]. The contribution of the single crack tension test to understand the fracture micro-mechanisms and their influence on the tensile performance of fiber reinforced cementitious composites is addressed, as well as its importance to support the design process of cementitious composites reinforced with multiple types of fibers. Subsequently, the CTT procedure described in Chapter 3 is also utilized to characterize the load-displacement behavior of the cementitious composites reinforced with multiple fibers. The influence of the type of fiber, of the presence of multiple fiber types in the matrix, and of the type of the cohesive law utilized to simulate the structural behavior of cementitious composites reinforced with multiple fiber types are addressed as well.

4.2 Materials

Although most of the materials utilized in this chapter are similar to the ones previously referred, for the sake of clarity they are summarized subsequently. The present study is mostly focused on investigating the influence of each type of fiber on the tensile behavior of SHCC when single or multiple types of fibers are used as reinforcement. Therefore a similar composition of the cementitious matrix was used in all the tested composites, with a few exceptions that are identified throughout the text of this chapter. The cementitious matrix was mainly composed of cement (CEM 52.5 N type I), fly ash (type S), fine sand (0.17 mm), quartz powder and water, with the weight proportions presented in Table 4.1.

Table 4.1: Weight of the materials used for 1 dm^3 of cementitious matrix.

Cement	Fly ash	Fine sand (0.17 mm)	Quartz powder	Water
428 g	856 g	150 g	150 g	320 cm^3

Fibers of three different natures were used: PVA (polyvinyl alcohol), PAN (polyacrylnitrile) and PP (polypropylene). The main geometrical and mechanical properties of these fibers are presented in Table 4.2.

Table 4.2: Main properties of the fibers used.

Fiber	Tensile strength (MPa)	Length (mm)	Diameter (μm)
PVA 15	1600	8	40.0
PP	900	12	40.0
PAN 1.5	826	6	12.7

Considering the extensive experience available with PVA fibers in the design of SHCC [Li, 2003], the composite formulations containing 1% and 2% of PVA fibers were characterized and considered as performance references, regarding the objective of accomplishing strain hardening ability in tension. The volumetric percentages of the six composites tested are presented in Table 4.3.

Table 4.3: Fiber reinforcement volumetric percentages of the developed fiber reinforced cementitious composites.

Composite	PVA 15 % vol.	PAN 1.5 % vol.	PP % vol.
1PVA	1	0	0
2PVA	2	0	0
HybPAN	1	1	0
2PAN	0	2	0
HybPP	1	0	1.25
2.5PP	0	0	2.5

The adoption of 2.5% fiber volume in the case of the PP fiber reinforced composite aimed at partly compensating the lower strength of PP fibers when compared to the PVA fibers. The specific composite tensile strength obtained with the PP fibers would be equivalent to the 2% of PVA fiber reinforcement if 3.56% volume of PP fibers was used. This would correspond to the equivalent volume fraction of PP fibers if the composite specific tensile strength is considered, but the fiber dispersion during the mixing process was found to be unsatisfactory for PP fiber contents exceeding 2.5%. The redesign of the matrix composition to achieve satisfactory fiber dispersion for greater fiber volumetric percentages was not considered in this study, whereas the adoption of the same matrix composition in all composites was necessary to allow the direct comparison of the performance of each fiber in each composite. The lower tensile strength of PAN fibers would also imply the need to increase the volumetric percentage of PAN fiber reinforcement used. However, due to their high specific surface PAN fibers also showed strong interaction with the fresh matrix. Satisfactory fiber dispersion using the same matrix composition was observed only for fiber volume percentages not exceeding 2%.

4.3 Characterization of the tensile stress-crack opening behavior

4.3.1 Single Crack Tension Test (SCTT)

The mechanical characterization of a crack during the initiation and propagation stages of SHCC materials was carried out and discussed in Chapter 2. In the present section the Single Crack Tension Test (SCTT) will be utilized to characterize the tensile stress-crack opening behavior of cementitious composites reinforced with multiple fiber-type reinforcement. The geometry of the specimen, test setup and other testing procedure details may be found in Section 2.4. The specimens were loaded at a tensile displacement rate of 5 μm/s. The formation of a single crack was confirmed by inspecting the tensile stress-crack opening responses and the crack surface of the specimens, as shown in Figure 4.2(a) and Figure 4.2(b).

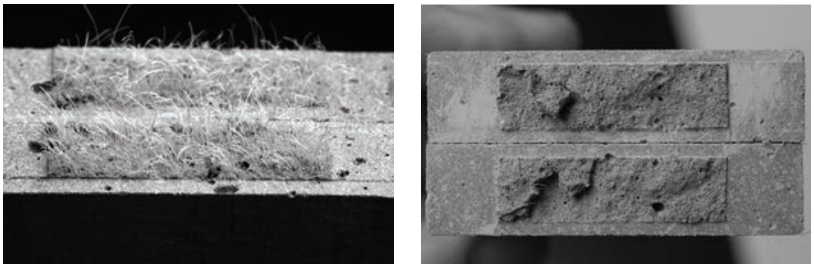

(a) Composite containing 1% PVA + 1.25% PP fibers.

(b) Composite containing 1% PVA + 1% PAN fibers

Figure 4.2: Crack surface of specimens.

4.3.2 Compression test

When investigating the tensile performance of conventional fiber reinforced cementitious composites, the information obtained from compression testing is also considered, and typically regarded as predominantly associated with the mechanical properties of the matrix exclusively. The influence of fiber reinforcement on the composite compressive strength is commonly assumed as negligible, although it contributes to increase the post-cracking energy dissipation ability (see for example Pereira et al. [2008]). The fibers used in the present study are, however, substantially smaller than the ones typically observed in conventional fiber reinforced cementitious composites.

The compactness of the solid skeleton is known to have significant influence on the composite compressive strength. In particular, at the material scale of the paste, the microscopic arrangement of the particles of cement, fly ash and other fine additions affects the mechanical properties of the matrix [de Larrard, 1999]. Considering that the diameters of the fibers studied are of the same order of magnitude as the fine particles which compose the cementitious paste, fibers will have an effect on the micro-structural arrangement of the fine particles in the solid skeleton at the material scale of the cementitious paste. The chemical composition and surface properties of the small particles, fine additions and admixtures also affect the balance of the interaction forces between the fine particles in suspension composing the fresh paste. Therefore the different diameters and surface properties of the fibers studied will likely have a differentiated effect on the fresh properties and on the micro-structure of the hardened composite. As generally accepted, the ordered phase growth and chemical dynamics during hardening and setting stages are affected by the presence of micro-fibers ([Mehta and Monteiro, 2006; Bentur and Mindess, 2006; de Larrard, 1999; Neville, 1996]. The compressive strength may consequently differ in all composites, although the composition of the matrix is the same. The compressive strength was therefore assessed in all composites, aiming at identifying different micro-structural characteristics in the composites emanating from the cementitious matrix properties. These different micro-structural characteristics are mostly the result of different fiber-matrix interaction mechanisms in the fresh mixture and their consequences on the fresh properties and on the interaction between the particles in suspension.

The experimental procedure consisted on loading the specimens at a compressive displacement rate of 0.1 mm/s. For each composite three cubes (40×40×40 mm^3) were tested.

4.3.3 Experimental results

For each composite, the tensile stress-crack opening behavior was evaluated using six specimens. The tensile stress was computed by dividing the tensile load by the net area of the notched cross-section. The crack opening was computed by averaging the displacements registered by the clip gauges measuring the notch opening. Considering the results obtained in the previous chapters, and that the SCTT has revealed high sensitivity to the contribution of different fibers for crack restraining during fracture, the tensile characteristics of each composite are, in this research, described by a multi-linear tensile stress-crack opening relationship, as presented in Figure 4.3.

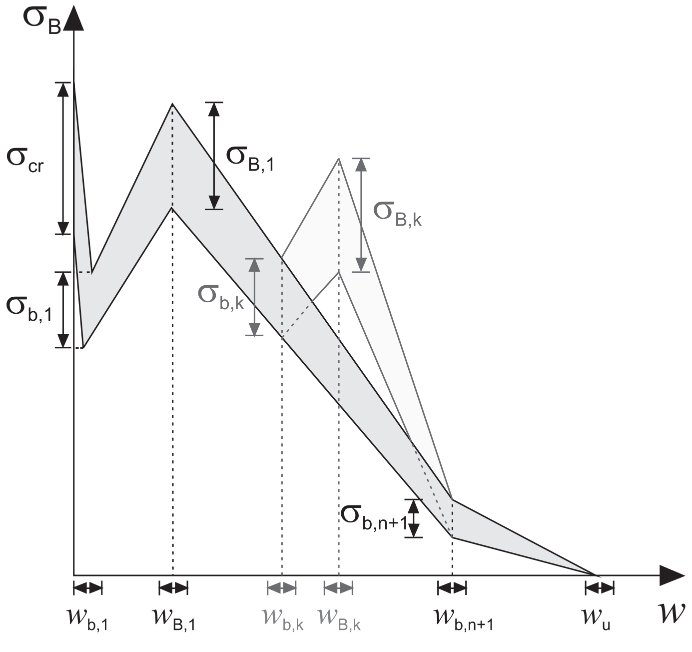

Figure 4.3: Schematic of tensile stress-crack opening response of cementitious composites reinforced with multiple fiber types.

The overall shape of the bridging stress, σ_B, versus the crack opening, w, curve is expected to be sensitive to the simultaneous use of different types of fibers as reinforcement, causing the formation of multiple bridging stress peaks [Pereira et al., 2012b]. The main parameters defining the schematic of bridging stress, σ_B, versus the crack opening, w, relationship are the first cracking stress, σ_{cr}, the initial bridging stress, $\sigma_{b,1}$, the peak bridging stress, $\sigma_{B,1}$, and the corresponding crack opening at peak bridging stress, $w_{B,1}$. When multiple bridging stress peaks develop, multiple tensile hardening-softening sequences can be distinguished. In each of these tensile hardening-softening sequences, the local initial minimum and peak bridging stresses are distinguished by using the lower-case b or the capital B as subscripts, respectively. The tensile hardening-softening sequence k will have as main parameters the local initial bridging stress $\sigma_{b,k}$, the local peak bridging stress $\sigma_{B,k}$ and the corresponding crack openings $w_{b,k}$ and $w_{B,k}$. The index k can adopt the integer value from 2 to n, being n the total number of tensile hardening-softening sequences. Finally, the residual bridging stress, $\sigma_{b,n+1}$, the corresponding crack opening, $w_{b,n+1}$, and the ultimate cohesive crack opening, w_u, characterize the last portion of the tensile bridging stress-crack opening curve, where the exhaustion of the remaining links between the two opposite crack surfaces occurs. The scatter of results associated with each parameter is also relevant in the modeling and up-scaling of the mechanical parameters derived with the SCTT to the structural level, as represented in Figure 4.3 by the shaded area. The micro-mechanisms involved in each of these fracture parameters was extensively discussed in Chapter 2 for the case of single fiber-type reinforced cementitious composites. Further discussion about the micro-mechanisms underlying each of these mechanical parameters may be found in previous research ([Pereira et al., 2010, 2011, 2012a]).

The experimental results obtained for a few representative parameters of the aforementioned are presented in Table 4.4. The compressive strength, σ_{fc}, and the first cracking stress, σ_{cr}, were selected due to their relation with the mechanical properties of the cementitious matrix. The peak bridging stress, $\sigma_{B,1}$, and the ultimate cohesive crack opening, w_u, were selected due to their sensitivity to the type of fiber reinforcement used. During testing, the achievement of the absolute zero load at the softening portion of the tensile responses is not viable. For simplicity, in the present case w_u was assumed as the crack opening observed at a residual tensile strength of 0.5 MPa. The average (*avg*), the standard deviation (*std*) and the coefficient of variation (*cv*) statistical dispersion measures were computed for each parameter in Table 4.4.

As shown in Table 4.4, the scatter of the experimental results was relatively low. The *cv* derived for all parameters was below 15%, with the exception of σ_{cr}. For both the composites reinforced with PP fibers the value of w_u was not determined, since the test sequence was terminated at a CMOD of 2.0 mm for all specimens. In the case of the PP fiber reinforced composites the tensile stresses measured at this point still remain higher than 0.5 MPa.

In Figure 4.4 the experimental tensile stress-crack opening curves are presented. For clarity, the experimental average curves were obtained by averaging the tensile

Table 4.4: Main parameters and scatter of results obtained from compression and tension tests.

Composite		σ_{fc} MPa (%)	σ_{cr} MPa (%)	$\sigma_{B,1}$ MPa (%)	w_u mm (%)
1PVA	*avg*	68.17	3.98	3.77	0.87
	std	5.16	0.70	0.25	0.12
	cv	(7.6)	(17.2)	(6.6)	(13.4)
2PVA	*avg*	70.51	4.36	6.64	1.20
	std	6.56	0.44	0.43	0.13
	cv	(9.3)	(10.0)	(6.4)	(11.0)
HybPAN	*avg*	89.53	5.25	4.64	0.64
	std	5.60	0.84	0.48	0.07
	cv	(6.3)	(16.0)	(10.2)	(11.4)
2PAN	*avg*	54.02	4.99	5.03	0.15
	std	6.17	0.77	0.42	0.01
	cv	(11.4)	(15.5)	(8.4)	(5.9)
HybPP	*avg*	52.37	2.95	4.05	> 2.0
	std	2.80	0.69	0.54	-
	cv	(5.3)	(23.2)	(13.4)	-
2.5PP	*avg*	70.48	2.99	4.33	> 2.0
	std	3.12	0.96	0.35	-
	cv	(4.4)	(32.2)	(8.1)	-

stresses measured at each crack opening observed in all the tested specimens of every composite. Additionally, the envelope of all experimental results is represented with the shaded area.

The results presented in Table 4.4 summarize the essential mechanical parameters characterizing the tensile response of the fiber reinforced cementitious composites tested. The robustness of the results is supported by the overall low statistical scatter obtained, with the exception of the results obtained for the first cracking stress.

Although all composites possessed the same matrix composition, the compressive strengths were clearly different. The average compressive strength results ranged between a minimum of 52 MPa and a maximum of 90 MPa. The maximum *cv* was 11.4%, suggesting that the computed average compressive strengths are satisfactorily robust. The clearly different results obtained show that the compressive strength of the composite is not exclusively determined by the composition of the matrix. Con-

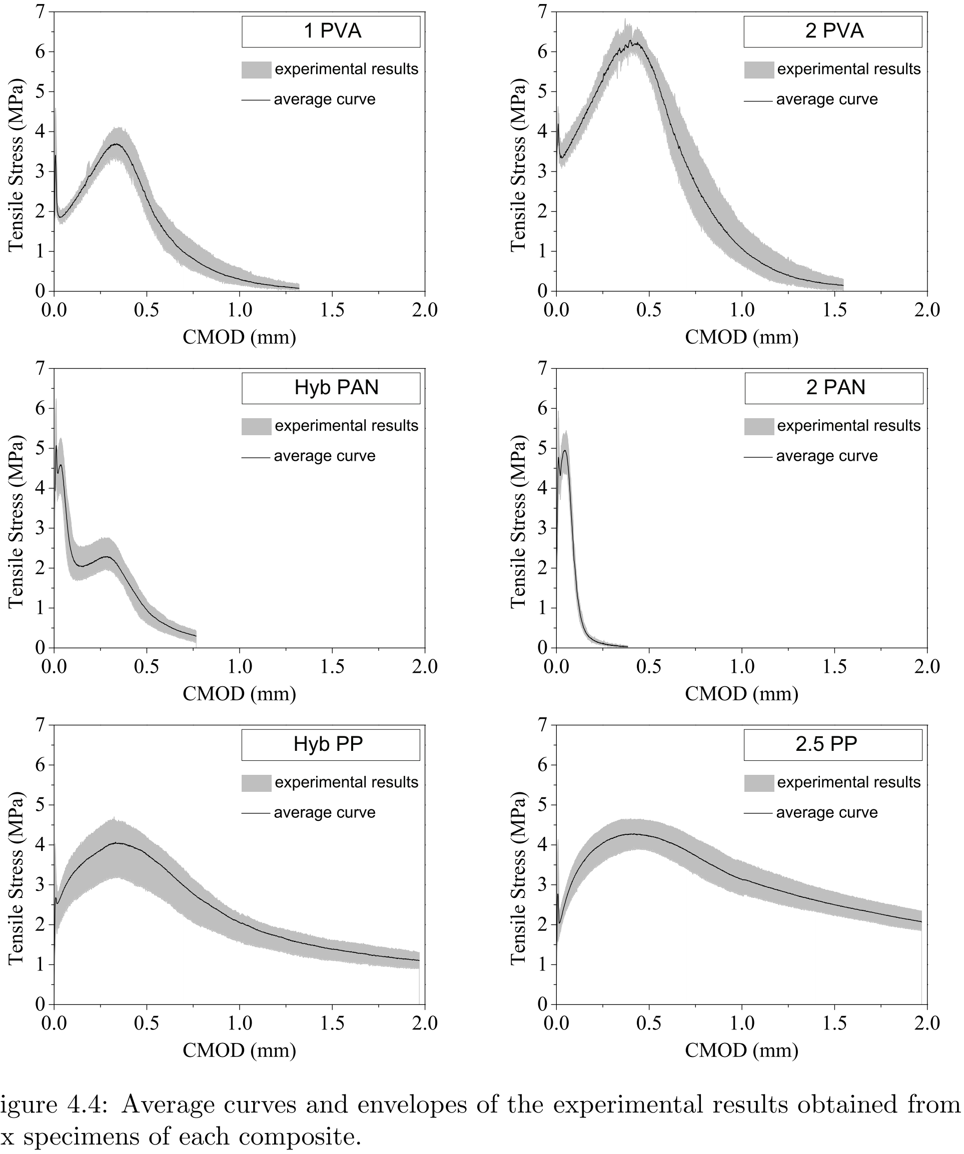

Figure 4.4: Average curves and envelopes of the experimental results obtained from six specimens of each composite.

sequently, either in a direct or indirect fashion, the fibers have an important influence on the compressive behavior of the composite. When designing the mixture composition for a specific compressive strength class, the consideration of the contribution of different fiber types and volumes is therefore of great importance.

The results of the average first cracking stresses also showed a clear influence of the fiber reinforcement type. Either due to the direct contribution of fibers to restrain crack propagation or due to their interference with the micro-structural arrangement of the fine particles, the hardened composite solid skeleton and flaw size distribution, these results show that the first cracking stress is not exclusively influenced by the matrix composition. The *cv* values derived were in this case noticeably higher, probably due to the greater influence of brittle fracture mechanisms and the associated typical scatter. While the *cv* clearly differs when comparing the different composites tested, the *std* is, however, of the same order of magnitude, suggesting that the reason for this scatter is an underlying mechanism that is common to all tested composites, such as the consequence of an identical flaw size distribution in the matrix to the fracture process in the composites.

The peak bridging stress may be considered as the mechanical parameter that is more closely related to the characteristics of the fiber reinforcement adopted in each composite. The lower *cv* values obtained for the peak bridging stresses may be justified by the greater influence of the properties of the fiber reinforcement. In general these have low scatter as a result of quality control associated with the production of the fibers.

When comparing the experimental results of all composites, no clear correlation between the average peak bridging stresses and the average compressive strengths is perceptible. Given that the matrix composition is identical in the tested composites, each type of fiber reinforcement seems to influence differently the compressive and the tensile properties of each composite. Similarly, no correlation is perceptible between the first cracking stress and the compressive strength or the peak bridging stress. These results find explanation at the level of the composite micro-mechanics, which are of great complexity as discussed previously. Their complete understanding may be circumvented if a robust procedure is employed to describe the fundamental mechanical parameters of the tensile composite behavior, both in the material design and in constitutive modeling viewpoints. This procedure should be sensitive to the main composite parameters, like the nature and geometry of fiber reinforcements used, the matrix mechanical properties and the fiber-matrix interaction in the composite.

Using the SCTT setup previously described, in this research six distinctive tensile stress-crack opening behaviors were identified. The experimental results shown in Figure 4.4 demonstrate that the tensile stress-crack opening curve is very sensitive to the characteristics of the fiber reinforcements used.

As shown in Figure 4.4, the effective contribution of the fibers to the tensile-hardening mechanisms occurred at clearly different CMOD in the tensile stress-crack opening behavior. The different orders of magnitude of the CMOD at which the diverse fibers showed greater efficiency may be one motivation supporting the typically idealized multi-scale nature of the mechanics of cementitious composites in tension, when these contain multiple types of fibers. In general, the composites showed singular tensile bridging stress hardening-softening sequences (n=1, see Figure 4.3). The exception was the composite containing 1%PVA + 1%PAN fibers, where two distinct tensile hardening-softening sequences were identified ($n = 2$, see Figure 4.3). Hence, in this case the tensile response in terms of the tensile stress-crack opening behavior clearly revealed the use of two distinct types of fibers in the composite.

4.4 Identification of multiple scales on the cracking process

The results presented in Figure 4.4 show that the effective mobilization of the different types of fibers during the SCTT sequence occurs at very different CMOD ranges. With regards to the cementitious matrix, the different CMOD ranges at which the different fibers are more effective have impact at different scales of the material structure. As discussed in the previous chapters, the heterogeneous nature of the cementitious matrix composites can be structured at different material scale levels, from the micro- to the macro-scale. Micro-cracking can therefore be explained considering the material heterogeneity at the material micro-scale, as well as macro-cracking can be described in the context of the material meso- and macro-scale. The PAN fibers are effective at restraining crack opening at small crack widths, the peak bridging stress being reached at CMOD of approximately 50 μm. This is in the order of magnitude of the size of the cement or fly ash particles, the diameter of the fibers and other fine constituents of the composite. Therefore, PAN fibers may be considered to have an effective contribution to crack restraining at the level of the composite material micro-scale. In contrast, the composites reinforced with PP fibers show little contribution to crack restraint at smaller CMOD. Instead PP fibers show a more extended CMOD range of activity, maintaining a high level of residual tensile strength in the composite up to the maximum CMOD adopted in the experimental program (2 mm). The peak bridging stress in the PP fiber reinforced composite is reached at a CMOD of approximately 500 μm, one order of magnitude above the CMOD at peak bridging stress observed in the PAN fiber reinforced composite, and almost three times larger than the size of the sand particles.

In the subsequent sections the cracking processes will be analyzed considering the different CMOD ranges, related to the different composite material size scales. The smallest scale will comprise the CMOD range up to 50 μm. One order of magnitude above, the tensile stress-crack opening behaviors will also be analyzed in the CMOD range of up to 0.5 mm. The global tensile responses obtained will be finally analyzed up to the maximum CMOD obtained of 2.0 mm. As subsequently shown, the analysis of the tensile responses obtained at these different size-scales differentiates particular aspects of the multi-scale nature of the cracking processes, and of the contribution of the different fibers to restrain cracking.

4.4.1 Tensile response up to 50 μm

In Figure 4.5, the tensile stress-crack opening behavior of all composites is presented up to a CMOD of 50 μm. At this range of CMOD, it may be assumed that the cracking process involves the composite material micro-scale.

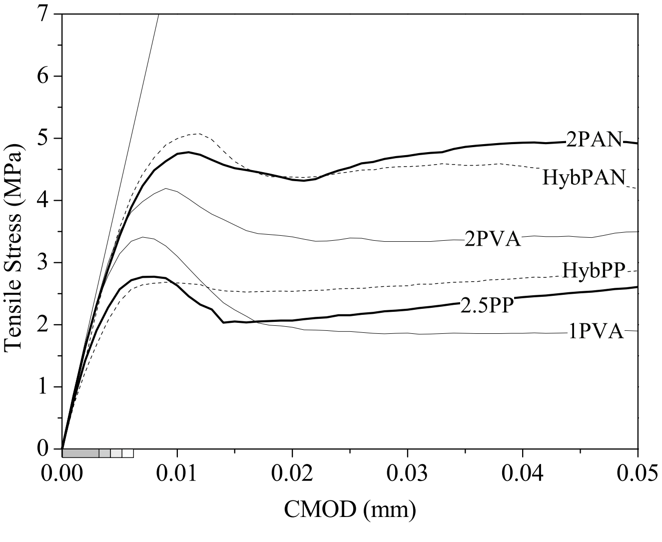

Figure 4.5: Tensile responses up to a CMOD of 50 μm.

The tensile stress-crack opening curves presented in Figure 4.5 show that the contributions provided by the different fiber reinforcements up to a CMOD of 50 μm are clearly differentiated. The tensile responses diverge from the linear elastic behavior almost right from the onset of the testing sequence. The high stress concentrations created at the tip of the notch in the SCTT specimens lead to the early initiation and propagation of the crack surface. Therefore, some fibers crossing the notched cross-section plane near the tip may become active before the conventionalized first cracking stress (σ_{cr}, see Figure 4.3) is reached. In general all types of fibers contribute to the first cracking stress, although the significance of this contribution depends of the nature and geometry of the fiber. The conventionalized σ_{cr} represents the the peak stress reached up to a CMOD of 10 μm. The early crack initiation obtained in a controlled manner with the SCTT setup allows to distinguish the different contributions provided by different fibers at very small crack widths.

Within the same matrix, PAN fibers showed a more effective contribution to crack restraint at very small CMOD, followed by the PVA fibers and by the PP fibers. The average value of σ_{cr} ranges from 2.95 MPa for the composites containing PP fibers to 5.25 MPa for the composites containing PAN fibers. The load decay subsequent to reaching σ_{cr} is smoother in the case of the composites reinforced with the PAN fibers. Although the transfer of the tensile stresses from the matrix to the fibers occurs at a higher tensile load, the effective mobilization of PAN fibers at this stage contributes to the smoother load decay observed. In contrast, even at lower tensile stresses the post-peak load decay observed in the PP fiber reinforced composites occurs rapidly, probably due to the poorer fiber-matrix interface properties. In the remaining parts of the observed tensile responses in Figure 4.5, PAN fibers show a superior contribution to crack restraining at CMOD up to 50 μm. Therefore, when considering crack formation and propagation mechanisms at the micro-scale, PAN fibers are more effective on restraining these mechanisms. At this scale of the cracking processes, the hybrid formulations did not show any substantial performance difference when compared to the single fiber-type reinforced composites, but this aspect will be further discussed at Section 4.5.

4.4.2 Tensile response up to 0.5 mm

In Figure 4.6 the tensile behavior obtained for all composites is presented for a CMOD up to 0.50 mm. At this scale of the cracking process the more effective contribution to crack restraining of the PVA fibers becomes evident. The composites reinforced with 2%PVA reached the highest peak bridging stress at a CMOD of approximately 0.40 mm. The PP fibers also showed an important crack restraining effect at this scale, but the poorer fiber-matrix interface properties led to the gradual loss of fiber bridging contribution at increasing CMOD. These properties were also reflected in the low initial bridging stress reached ($\sigma_{b,1}$, see Figure 4.3) and the previous abrupt load decay. In the hybrid composite containing PP and PVA fibers the same abrupt load decay after first cracking stress and the subsequent load recovery are observed, although they are slightly attenuated due to the presence of the PVA fibers. The enhanced efficiency at crack restraining by the PAN fibers at smaller CMOD becomes more evident. In the 2PAN composite, the load decay that follows the reaching of the first cracking stress is subtle, despite it occurs at higher tensile loads. This shows that PAN fibers are clearly more efficient at crack restraining up to a CMOD of approximately 0.1 mm. The HybPAN composite also shows some of this superior capacity to restrain cracking at small CMOD, but not as vigorously as in the case of the 2PAN composite. Some of the crack restraining capacity at smaller CMOD was traded for additional crack restraining capacity at grater CMOD in the HybPAN composite. Also when half of the PAN fiber reinforcement is replaced by PVA, a second tensile hardening sequence builds up ($n = 2$, see Figure 4.3) at higher CMOD values. While combining the features observed in each of the single fiber composites, the hybrids always seem to underperform the corresponding single fiber-type reinforced composites, as it will be further discussed in Section 4.5.

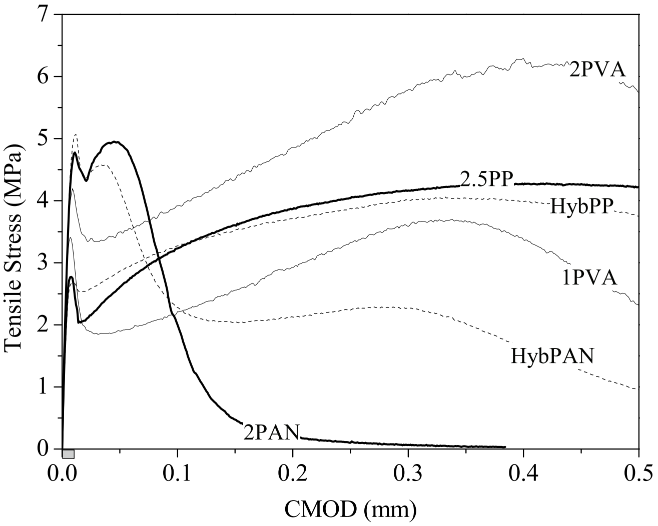

Figure 4.6: Tensile responses up to a CMOD of 0.50 mm.

4.4.3 Tensile response up to 2.0 mm

At this scale of observation the cementitious matrix material structure may be considered as homogenenous. While the overall contributions of the PVA and the PP fibers for crack restraining become fully described and understood, the contribution of the PAN fibers becomes almost indistinguishable. In a simplistic perspective, with this approach it is stated that the reinforcement effect provided by the PAN fibers at this scale is insignificant.

The use of the PP fibers resulted in a delayed mobilization of the fiber reinforcement, when compared to the other composites. As shown in Figure 4.7, the tensile stress-crack opening curve of the composite reinforced with 2.5% PP fibers presented a long tail of relatively high tensile bridging stresses remaining for the entire range of measured CMOD, after the peak bridging stress was reached. Due to the poorer fiber-matrix interface properties, pull-out is the prevailing mechanism of PP fibers. During the early stage of cracking, the contribution of the PP fibers to the first cracking stress was weaker than the one observed in the PVA fiber reinforced composites. After cracking, the load decay observed in the PP fiber reinforced composites was more pronounced and the first bridging stress ($\sigma_{b,1}$, see Figure 4.3) was lower, as observed in the previous section. This is the consequence of the rapid debonding of a longer portion of the PP fibers during cracking, with the rapid transfer of the tensile stresses form the matrix to the fibers and the fast propagation of the tunnel crack initiated with the matrix fracture. The subsequent fiber bridging stress recovery was also steeper in the PP reinforced composites, as a consequence of the low stress ($\sigma_{b,1}$) at which the high fiber reinforcement fraction is being mobilized. With the increase of the CMOD the initial stiffness observed in the tensile hardening stage gradually decreases, as a result of the prevailing fiber debonding and pull-out mechanisms.

The main difference between the SCTT results observed in PVA and PP fiber reinforced composites is located at the region where the peak bridging stress is reached ($\sigma_{B,1}$, see Figure 4.3). In fact, while in the PVA fiber reinforced composites the experimental curves exhibited a sharp transition from the tensile hardening to the tensile softening stages, in the PP fiber reinforced composites the same transition is smooth and gradual (Figure 4.7). The well known superior interfacial bonding of the PVA fibers with the matrix may justify these results, as opposed to the lower bonding of the PP fibers due to their hydrophobic nature [Li et al., 2002; Wei et al., 2002]. In the PP fiber reinforced composites the gradual increase of the stress transferred to the fibers during the post-cracking tensile hardening stage results in the early debonding of a gradually increasing number of PP fibers. Therefore the initial tensile hardening

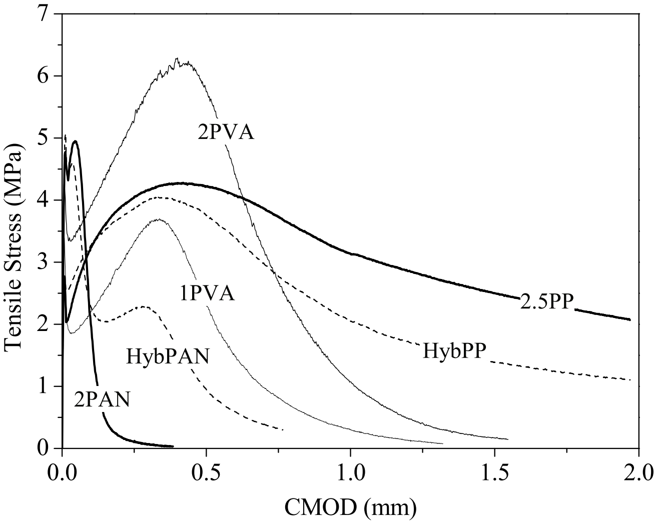

Figure 4.7: Tensile responses up to a CMOD of 2.0 mm.

stiffness steadily decreases at increasing CMOD and the transition to the softening phase occurs gradually, generating the typical smoothly curved shape of the tensile response in the vicinity of the peak bridging stress. The superior bonding of the PVA fibers with the matrix results in a constant tensile hardening stiffness during most of the post-cracking tensile hardening stage. This improved bond behavior is also responsible for the rupture of most of the fibers once the tensile load approaches the bridging peak. Therefore, after the peak bridging stress is reached, tensile softening occurs more rapidly in the PVA than in the PP fiber reinforced composites. Additionally, this differentiated bond behavior also explains the preservation of a higher residual tensile strength in the composites reinforced with PP fibers. The HybPP showed essentially a combined behavior of the two corresponding single fiber-type reinforced composites (2PVA and 2.5PP). As before, the hybrid composite apparently underperformed the respective composites reinforced with single types of fibers. In particular, the peak bridging stress reached in the HybPP was smaller than both the peak bridging stresses obtained in the corresponding single fiber-type reinforced composites. This result seems to suggest that the combination of fibers in the hybrid composite is deleterious to the composite tensile performance, and this observation will be further discussed in Section 4.5.

4.4.4 Energy dissipated during the fracture process

An important indicator of the overall tensile performance of the tested composites is the energy dissipated in the fracture process. For the better understanding of the role of each type of fiber in each of the scales of the cracking processes previously defined, the energy dissipated during the fracture process was computed at three distinct CMOD: 50 μm, 0.50 mm and 2.0 mm. In Figure 4.8, the results are presented for the six composites tested. These results were based on the average experimental tensile stress-crack opening curves of each composite.

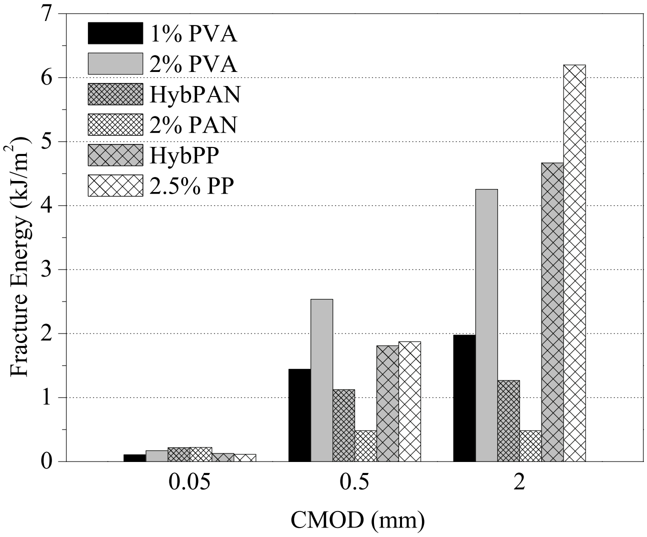

Figure 4.8: Energy dissipated during fracture computed for a maximum CMOD of 50 μm, 0.50 mm and 2.0 mm, based on the average tensile stress-crack opening curves.

In general, the results show that the most effective type of fiber is not the same at each of the represented scales of the cracking process. Up to a CMOD of 50 μm, both in the single fiber and in the hybrid fiber reinforced composites, the PAN fibers exhibit higher effectiveness, showing the highest cumulative dissipated energies in the fracture process. The PVA fibers are more effective at the intermediate scale, showing the highest cumulative dissipated energies at a CMOD of 0.50 mm. PP fibers have significant effect at larger crack openings, showing both the composites containing PP fibers the highest cumulative dissipated energy at a CMOD of 2.0 mm. Considering the potential synergistic effect of having multiple fiber-type reinforcements, the hybrid composites would be expected to outperform the superposition of the corresponding single fiber reinforced composites. Nevertheless the results obtained did not clearly show a positive synergistic effect. In the special case of the hybrid composite reinforced with PVA and PAN fibers, the hybrid even underperformed the 1% PVA fiber reinforced composite at CMOD between 0.1 and 0.5 mm. One explanation for this result may be the unfavorable effect of PAN fibers on the fresh properties of the composite. As discussed previously, the fresh properties of the composites significantly influence the cementitious matrix and the overall mechanical properties of the composite.

4.5 Effectiveness of hybrid fiber reinforcements

The effectiveness of the hybrid fiber reinforcements may be quantified by estimating the tensile behavior of the hybrid fiber reinforced composites based on the tensile behaviors obtained with the single fiber-type reinforced composites. These estimated tensile behaviors may be compared with the experimentally obtained responses.

The tensile response of the hybrid fiber reinforced composites were estimated considering the superposition of the tensile responses obtained with the single fiber-type reinforced cementitious composites. For this purpose, the expected tensile stress-crack opening curves of the hybrid fiber reinforced composites were obtained by essentially superposing the contribution of each fiber fraction in the composite. Since the hybrid fiber reinforced composites contain 50% of the amount of fiber reinforcement used in the corresponding single fiber reinforced composites, it is reasonable to assume a contribution of each type of fiber in the hybrid composites as 50% of the tensile stress measured at each CMOD in the corresponding single fiber-type reinforced composites. The total volume of fiber reinforcement in the single fiber and in the hybrid fiber reinforced composites is thus nearly identical to the total volume of fiber reinforcement assumed in the estimated tensile responses. This is essential to have reasonably comparable micro-structural arrangements of the solid particles and fibers dispersed in the composite, both to the experimental and to the estimated tensile responses.

4.5.1 Hybrid fiber reinforcement with PVA and PAN fibers

In Figure 4.9, the estimated tensile stress-crack opening response is compared to the experimental, for the composite reinforced with 1%PVA + 1%PAN fibers (HybPAN). Additionally the experimental responses of the corresponding single fiber reinforced composites (2PVA and 2PAN) are shown. The gray shaded area represents the envelope of the expected tensile responses to the hybrid fiber reinforced composite, when assuming that this tensile response is the synthesis of the tensile responses obtained for the corresponding single fiber reinforced composites. Exemplifying, one boundary of this gray shaded area is obtained when the estimated hybrid fiber composite tensile response is the result of adopting a ratio of 100% of the 2PVA tensile response and 0% of the 2PAN tensile response, which coincides with the experimental tensile response obtained for the 2PVA composite. The other boundary of this gray shaded area is obtained when the ratios of 0% of participation of the 2PVA tensile response and of 100% of participation of the 2PAN tensile response are considered, and the expected tensile response for the hybrid coincides with the 2PAN composite. The estimated tensile response obtained when 50% of participation of the 2PVA tensile response and 50% of participation of the 2PAN tensile response are considered corresponds to the expected tensile response for the HybPAN composite. The estimated response of the hybrid composite is therefore a weighted average of the corresponding single fiber composite tensile responses in terms of tensile stress. This estimated tensile response can thus be compared to the experimentally obtained tensile response for the HybPAN and the HybPP composites, with the purpose of investigating possible synergistic effects emerging from the simultaneous use of two different types of fibers in the same cementitious composite. This analysis is presented in Figure 4.9 for the case of the HypPAN composite.

The experimental tensile stress-crack opening curve of the HybPAN never surpasses the upper limit of the gray shaded area, as shown Figure 4.9. Therefore, the HybPAN composite is not performing better than the corresponding single fiber reinforced composites in the regions of the tensile response where the latter perform better individually. Comparing the expected and the experimental tensile responses obtained for the HybPAN, only at very small CMOD the experimental curve outperforms the expected one. Only at this small region of the tensile response a probable positive synergy may be assumed. This leads to the conclusion that the presence of different types of fibers in the same composite does not necessarily lead to better tensile performance. In fact the achievement of a better performance is unlikely, since the regions of the tensile response where the optimal mobilization of each fiber

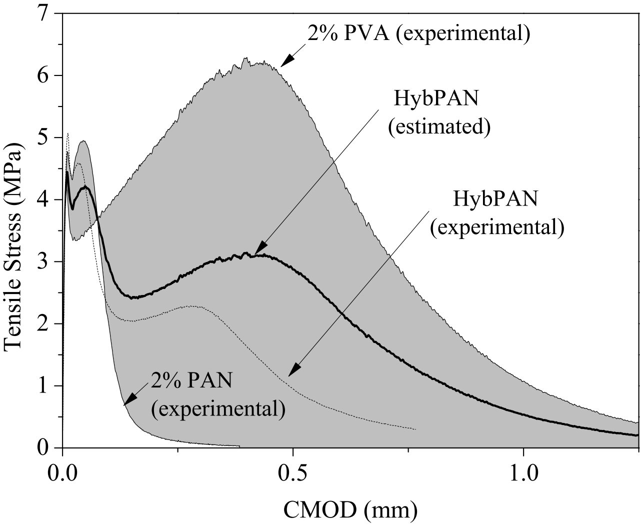

Figure 4.9: Expected tensile response of the hybrid fiber reinforced composite (PVA, PAN) based on the weighted average of the corresponding single fiber reinforced composites.

type occurs are different. As a consequence, the activation of the fibers during the fracture process is not synchronized, which results in a reduction of the overall tensile performance. In addition, fiber reinforcement mechanisms of individual fibers are not optimized when several types of fibers are used in the same composite, as it is unlikely that the optimal matrix considering one type of fiber is simultaneously optimal for the other types of fibers which are present in the same composite.

The multi-scale nature of the cracking process, and the adoption of different fiber reinforcement types for crack restraining at the level of these different scales of the cracking process, are generally recognized as two fundamental principles leading to optimized fiber reinforcement design with regards to tensile performance. The length and diameter of the PVA and PAN fibers used in this study were clearly different, and the experimental results showed that the crack restraining effect provided by these two fibers was occurring at clearly distinct scales of the cracking process. However, a positive synergy between these two different fibers in the hybrid composite was not observed. Only for very small CMOD the experimental curve surpassed the expected response, suggesting that in the early stage of crack formation a synergistic collaboration of the fibers to crack restraining has occurred. This may, however, be insufficient to support the general use of hybrid fiber formulations, if optimal tensile performance is pursued. Nevertheless, the double-peak nature of the tensile stress-crack opening response was a unique feature demonstrated by the HybPAN composite, which may be of interest for particular applications.

4.5.2 Hybrid fiber reinforcement with PVA and PP fibers

In Figure 4.10 the expected tensile stress-crack opening curve is compared to the tensile response experimentally obtained for the HYbPP composite, considering the definition previously given for expected hybrid tensile response (see Section 4.5.1). The tensile responses experimentally obtained for the corresponding single fiber reinforced composites (2%PVA and 2.5%PP) are also shown. As in the previous section, the envelope of the gray shaded area is established by the tensile responses experimentally obtained for the composites reinforced with 2%PVA and with 2.5%PP, which are the hypothetical limits of the expected HybPP tensile response.

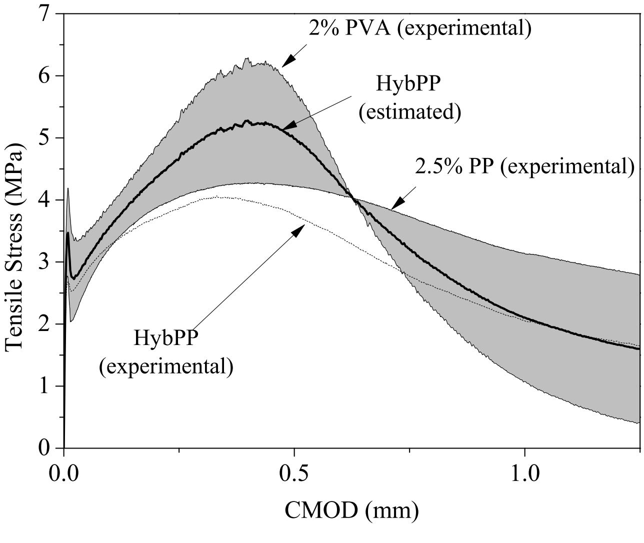

Figure 4.10: Expected tensile response of the hybrid fiber reinforced composite (PVA, PP) based on the weighted average of the corresponding single fiber reinforced composites.

As shown in Figure 4.10, the tensile response of the HybPP composite never surpasses the upper limit of the gray area. Therefore, also when using PVA and PP fibers as reinforcement, the hybrid composite is unable to perform better than the corresponding single fiber reinforced composites in the regions of the tensile response where the latter perform better individually. Comparing the predicted and the experimental tensile responses obtained for the HybPP composite, the experimental response also under-performs the predicted response in the entire range of CMOD measured. The discrepancy between the predicted and the experimental responses is higher in the vicinity of the peak bridging stress, that is, in the region of the tensile response where the optimal mobilization of the fibers should occur. Although the overall shape of the tensile responses obtained with the single fiber reinforced composites (2%PVA and 2.5%PP) are substantially different, mainly as a result of the different properties of the fiber-matrix interface, the region of the tensile response where optimal mobilization of the fibers occurs is essentially identical, being the CMOD at which the peak bridging stress is reached nearly the same. This would lead to the conclusion that a synchronized mobilization of the fibers is occurring in the hybrid composite, but the experimentally obtained tensile response of the hybrid composite clearly under-performs the estimated tensile response. Therefore an absence of synchronization in the full mobilization of the PVA and the PP fibers may be hypothesized, not because their full mobilization occurs at different CMOD, but in this case because the micro-mechanisms of fiber mobilization are essentially distinct for PVA and for PP fibers. In particular, as a result of the poorer fiber-matrix properties in the case of the PP fibers, the fiber length required to transfer the tensile stresses from the matrix to the fibers is considerably larger in PP fibers. The different mechanics of interaction between the matrix and the PVA or the PP fibers result in considerable differences in the micro-mechanisms of crack restraining provided by the PVA or the PP fibers. The result is the formation of substantially different stress fields in the transition zone between the fiber bridged crack surface and the intact bulk material, depending on the type of fiber. This discrepancy may have caused the loss of performance observed in the hybrid composite, and may be interpreted as a lack of synchronization of the crack restraining micro-mechanisms between PVA and PP fibers. Additionally, the different type of interaction of the different fibers with the fresh mixture probably led to poorer fiber dispersion during mixing, influencing negatively the tensile performance of the hardened composite.

4.6 Effect of matrix properties on tensile response

The influence of the matrix properties on the composite tensile performance is significant. In the previous chapters this influence was discussed in the context of the cracking processes and fiber-matrix interaction mechanisms in the composite. In this section this influence is briefly addressed by considering two composite formulations with two different matrix compositions and one hybrid fiber reinforcement. Although identical matrix compositions were utilized in most of the previous experiments, the same matrix composition leads to different matrix hardened properties, as previously shown and discussed. Nevertheless, in this section the direct consequence of adopting a substantially different matrix composition was investigated. The compositions of the two hybrid fiber reinforced cementitious composites tested are represented in Table 4.5. The volume fractions of the two types of fibers used are similar to the ones adopted in the HypPAN composite (see Table 4.3).

Table 4.5: Weight proportions of the materials used in each composite.

Composite	Cement	Fly ash	Fine sand (0.17 mm)	Quartz powder	Water	Compressive strength (MPa)
HybPAN2	1	2	0.35	0.35	0.75	89.5[5.6]
HybPAN6	1	6	0	0	1.40	49.6[2.0]

The results obtained from six specimens of each composite are presented in Figure 4.11. As before, the SCTT setup was used to evaluate the tensile behavior of each composite. In addition, the compressive strength of the two composites was evaluated using three cubes ($40 \times 40 \times 40 mm^3$) that were loaded at an axial displacement rate of 0.1 mm/s (Table 4.5). The corresponding standard deviations are presented between brackets.

The average tensile response of each composite was computed by averaging the tensile stress obtained from the six specimens at each CMOD. The average responses are compared with the experimental results of all specimens in Figure 4.11. The average responses summarize well the results obtained for each composite. The scatter of results is generally low and the overall shape of the average curve represents with reasonable detail the main features found in all the experimental responses of each composite. The experimental results are compared in Figure 4.12 considering the two calculated average responses.

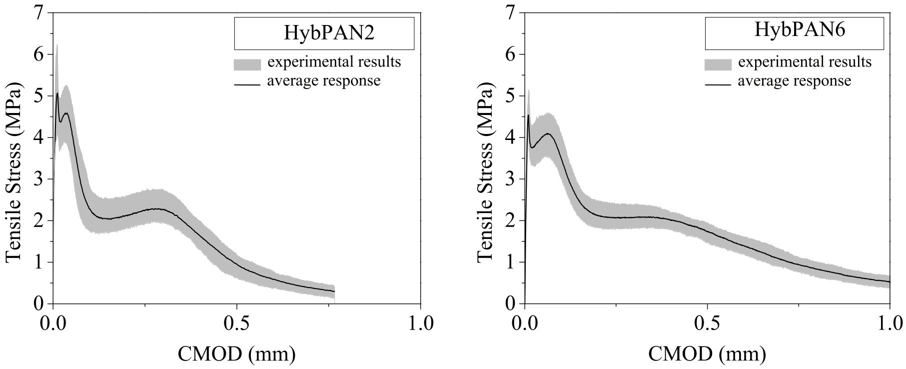

(a) (b)

Figure 4.11: Average responses and experimental scatters obtained for the HybPAN2 (a) and HybPAN6 (b) composites.

The tensile responses obtained show that the tensile behavior of a hybrid fiber reinforced cementitious composite is significantly influenced by the properties of the matrix. This influence is not restricted to the stage of crack formation, and the first cracking strength is not the only parameter reflecting the change of the matrix composition. The entire response is somewhat altered by the adoption of matrices with different properties.

The higher first cracking stress reached with the HybPAN2 composite is in agreement with the also higher compressive strength obtained for the same composite. However, the average compressive strength of the HybPAN2 is approximately twice as high as the HybPAN6 one, while the difference in the first cracking stress, σ_{cr}, is only about 20%. This result may be the consequence of the considerable contribution that the fibers used in this study have on the early stages of the cracking process. In general, the contribution of the fibers to the compressive strength is not significant, and the relation between compressive and tensile properties can be established mostly indirectly, as a result of the fiber effect on the composite properties while in the fresh state. As discussed in Capter 2, the rheological properties of the composite fresh mixture affect the micro-structural arrangement of the fine solid particles in suspension in the paste, as well as the fiber-matrix interface properties. The fiber debonding process occurring during the early stages of crack initiation and propagation is influenced by both the fiber-matrix interface properties and the energy involved in the matrix fracture process. Following the discussion in Chapter 2, different combinations of these two fracture properties can result in clearly differentiated composite tensile be-

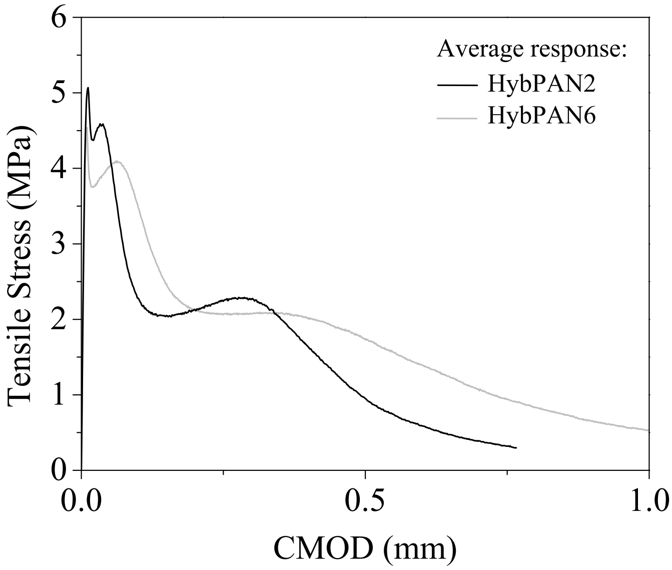

Figure 4.12: Comparison of HybPAN2 and HybPAN6 average tensile responses.

haviors. In the present case, the results indicate that the composite with the higher matrix tensile strength, which combines both a higher matrix fracture energy and a higher bonding / frictional fiber-matrix interaction, exhibits higher first cracking stress. The number of fibers rupturing during this stage is, though, probably higher, and the debond lengths of the fibers crossed by the failure crack are smaller. This stage of the cracking process has great influence on the remaining tensile response. Apparently there exists a general effect of tensile load reduction (effect 1, see Figure 4.13) and of increase of the tensile deformation at the same tensile load (effect 2, see Figure4.13). These two effects are the direct consequence of the micro-mechanical alterations produced at the level of the matrix and of the fiber-matrix interface, as a result of the modification of the cementitious matrix composition and properties. In general, the final change in the composite tensile behavior resulting of the alteration of the matrix properties may be considered as the superposition of effects 1 and 2 (see Figure 4.13).

In general, two tensile hardening-softening sequences can be clearly identified in the results obtained of both composites (see Figure 4.3). These can be attributed to the predominance of the contribution of each fiber type at each stage of the composite tensile response, as observed in the previous sections. Both the first and the

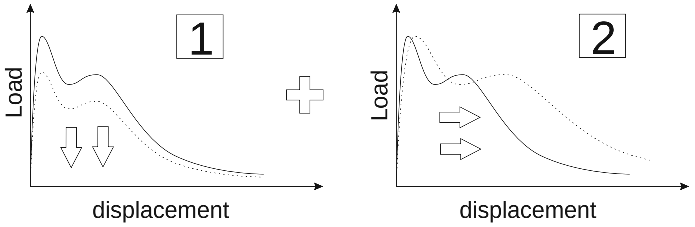

Figure 4.13: Schematic representation of the two independent shape alteration modes of the tensile stress-crack opening response, observed when the matrix properties of HybPAN2 were altered and HybPAN6 composite was obtained.

second hardening-softening sequences are somewhat more pronounced in the case of the HybPAN2. The alteration of the matrix properties, essentially resulting in a lower matrix strength, as well as the decreased bonding/frictional fiber-matrix interaction, have resulted in a generally smoother tensile response curve, with milder peaks and smoothed transitions between different hardening-softening stages (HybPAN6, Figure 4.3). The superposition of effects 1 and 2 (Figure 4.13) in different proportions may be understood as the result of the two main causes on the alteration of the hybrid composite behavior when the cementitious matrix is changed: the first cause, and apparently the most important, is the alteration of the fiber-matrix interface properties, with the reduction of the fiber bonding and friction during pull-out; the second cause is the decrease of the matrix fracture energy during crack initiation, which may lead to the reduction of the number of fibers rupturing at the fracture stage, while the rapid tensile stress transition from the matrix to the fibers bridging the crack occurs.

4.7 Characterization of the mechanical behavior using the CTT

In Chapter 3 the CTT setup was used to characterize the initiation and propagation of a crack in cementitious composites reinforced with a single fiber type, considering both the obtained mechanical responses and the observation of the propagation of the crack initiated at the sharp notch tip. The mechanical responses were also simulated using a FE model, considering that the cohesive law could be directly obtained from the tensile stess-crack opening behaviors obtained with the SCTT.

In this section the study presented in Chapter 3 is extended to the case of the composites containing hybrid fiber reinforcements. The utilization of the CTT setup can further extend the understanding of how the application of fibers of different natures within the same composite as reinforcement can alter the mechanical behavior of hybrid fiber reinforced cementitious composites, by considering the different loading configuration and boundary conditions of the CTT. Additionally, the procedure applied in Chapter 3 to simulate the CTT responses using a FE model and applying the results obtained with the SCTT to extract the tensile bridging stress-crack opening behavior will be extended to the case of the cementitious composites containing hybrid fiber reinforcements. With this procedure, the possibility of utilizing the tensile stress-crack opening behavior obtained using the SCTT to simulate the CTT response is further confirmed, aiming at the generalization of this procedure to other types of testing configurations or loading conditions.

For clarity, the composition and nomenclature of the hybrid cementitious composites tested in this section are summarized in Table 4.6. HybPP composition is the previously described at Tables 4.1 and 4.2.

Table 4.6: Weight proportions of the materials used in the hybrid fiber reinforced cementitious composites tested.

Composite	Cement	Fly ash	Fine sand (0.17 mm)	Quartz powder	Water	Fiber (%)		
						PVA	PP	PAN
HybPP	1	2	0.35	0.35	0.75	1	1.25	0
HybPAN2	1	2	0.35	0.35	0.75	1	0	1
HybPAN6	1	6	0	0	1.40	1	0	1

4.7.1 Experimental results

In Figures 4.14 to 4.16 the experimental load-displacement responses of the composites HybPP, HybPAN2 and HybPAN6 are presented. The measured displacement corresponds to the displacement difference between the center points of the opposite loading rods. Additionally, the images of the surface of specimen nr.1 of each composite are shown, as obtained after testing. The results obtained for specimen 1 of all composites will be further examined in the following sections, where the digital images taken from the surface of the specimens are utilized to trace the surface deformations and analyze the cracking processes during testing.

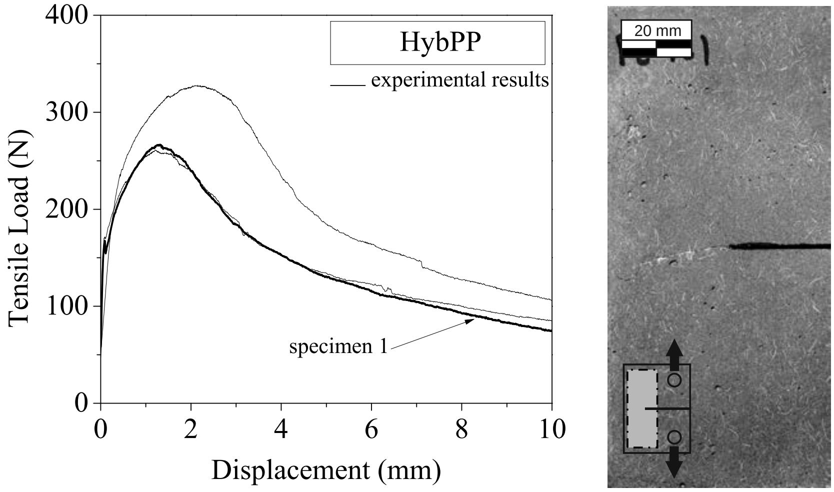

(a) (b)

Figure 4.14: CTT experimental results of HybPP composite (a), and image of specimen 1 after testing (b).

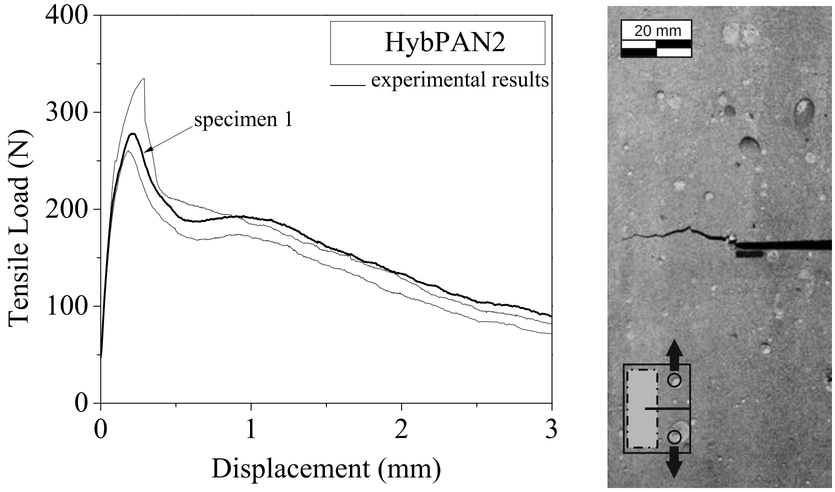

(a) (b)

Figure 4.15: CTT experimental results of HybPAN2 composite (a), and image of specimen 1 after testing (b)

4.7.2 Discussion of results

The average curves of the CTT tensile load-displacement responses were obtained by averaging the tensile load obtained at each displacement in the three specimens tested

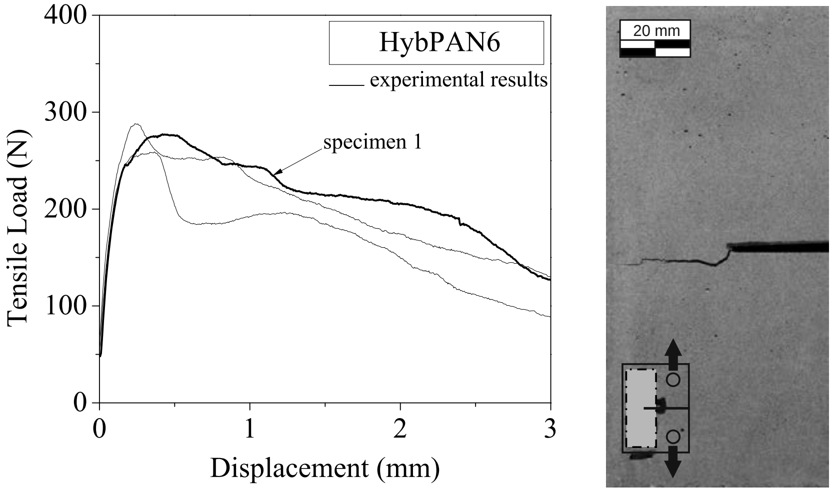

(a) (b)

Figure 4.16: CTT experimental results of HybPAN6 composite (a), and image of specimen 1 after testing (b)

of each composite. These average responses are shown in Figure 4.17. In general, the experimental results are reasonably well represented by the corresponding average curves. The scatter of results is essentially low and the average curves exhibit the same typical mechanical behavior features as each of the individual specimens. For clarity, the three average responses are compared in Figure 4.17.d).

In general, the peak load was reached after the cracking process had already initiated, as it will be further discussed subsequently. The peak load was roughly similar in all composites, but the displacement at peak load was clearly different. As expected, the composite containing PP fibers has sustained higher tensile loads up to significantly higher displacements. In addition, the existence of fibers of different natures in the hybrid composites was not evidenced as clearly in the case of the HybPP as in the case of the HybPAN2 and HybPAN6 composites. The multiple load peaks resulting from the contribution of different fibers for crack restraining observed in the composites containing PAN fibers were not visible in the case of the composite containing PP fibers. Similar results were observed previously, while using the SCTT.

In Figures 4.18 and 4.19 the tensile load-displacement behavior of the hybrid composites are compared with the corresponding composites containing single fiber-type reinforcements. The effect of having multiple fiber types as reinforcement on

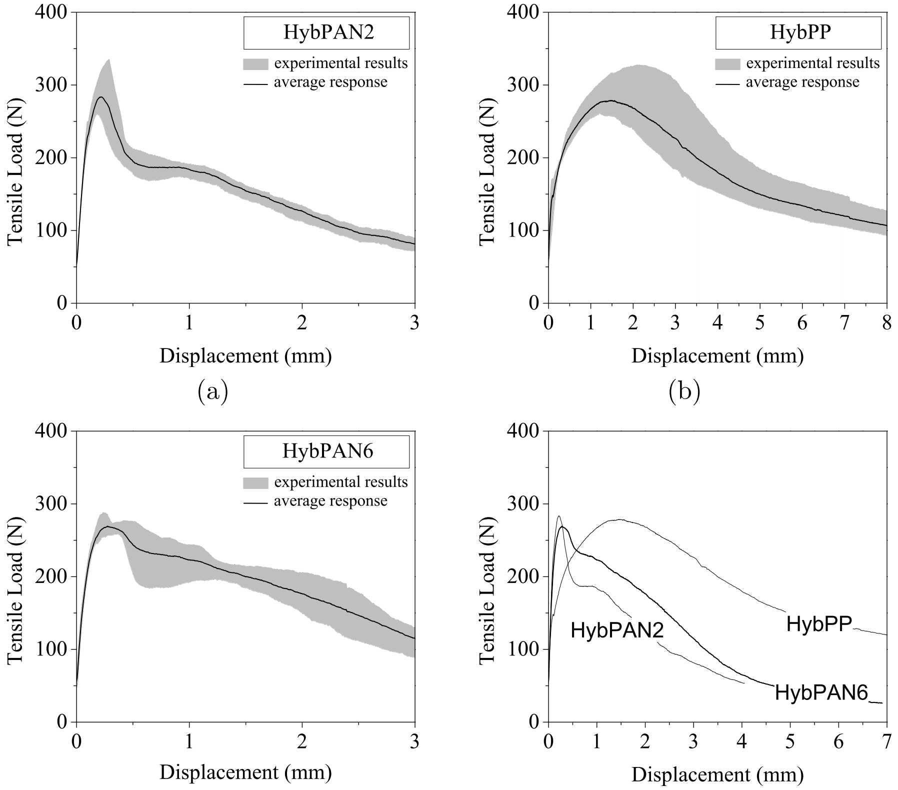

(a) (b)

(c) (d)

Figure 4.17: Average CTT responses and scatter of experimental results obtained for the HybPAN2 (a), HybPP (b) and HybPAN6 (c), and comparison of all average responses obtained (d)

the tensile load-displacement behavior of the hybrid composites can be evaluated by comparing the responses obtained.

In the case of the composites reinforced with PVA and PP fibers, the shape of the average tensile load-displacement curves is essentially similar (see Figure 4.14). The peak load obtained with the hybrid fiber reinforced composite is considerably lower than the one obtained with the single fiber-type reinforced composites. Although the hybrid composite sustains higher tensile loads than the PVA fiber reinforced composite for displacements larger than 5 mm, for smaller displacements there seems to be

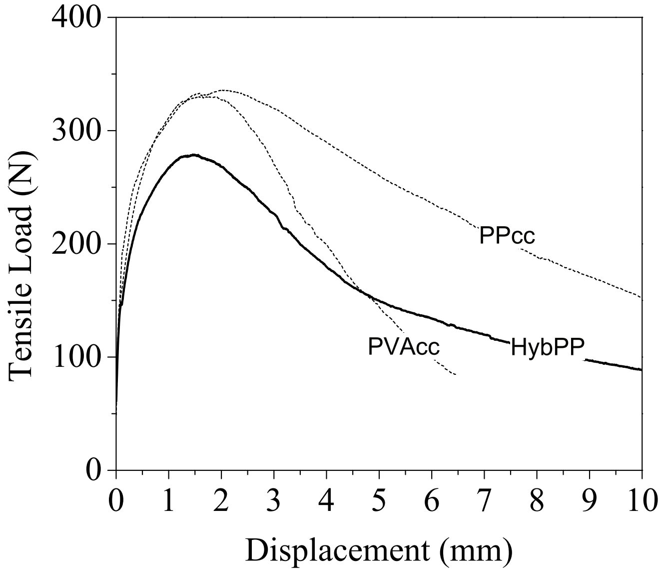

Figure 4.18: Comparison of the average CTT responses obtained with all composites containing PP fibers.

no advantage deriving from the adoption of the hybrid fiber reinforcement.

Considering the composites reinforced with PVA and PAN fibers, the shape of the average tensile load-displacement curves of the hybrid composites is significantly different, when compared to the shape of the average curves of the single fiber-type reinforced composites. In this case, the range of displacements at which the obtained responses are compared is lower. Both shapes of the HybPAN2 and the HybPAN6 curves reveal the existence of fibers of different natures in their compositions, with the alteration of the main trend of the mechanical behavior at a certain point.

Two different stages can be distinguished in the softening branch of the tensile load-displacement behaviors obtained with the hybrid formulations. These different parts of the response evidence the two different stages at which each fiber type is contributing more efficiently to restrain crack propagation in the composites. In agreement with the results obtained previously with the SCTT, the peak load obtained with the HybPAN2 composite is higher than the HybPAN6 one. Additionally, the residual tensile load remains higher in the case of the HybPAN6 composite when compared with the HybPAN2 composite. In both cases, the alteration of the matrix properties between the HybPAN2 and the HybPAN6 composite seems to have led

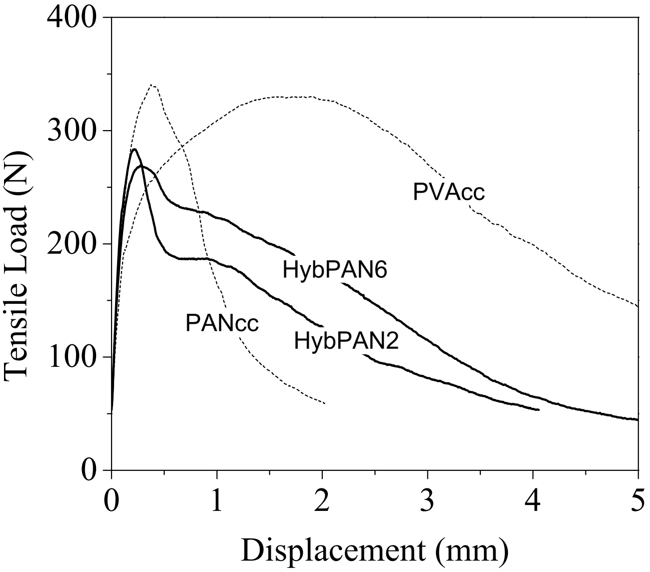

Figure 4.19: Comparison of the average CTT responses obtained with all composites containing PAN fibers.

to the reduction of the fiber-matrix bond and fiber pull-out friction properties. As discussed previously, this may have led to the simultaneous reduction of the tensile load transferred to the fibers during fracture, as well as a reduction of the number of ruptured fibers during crack formation. These may justify the observed simultaneous reduction of the peak load and the increase of the residual tensile load for considerably larger displacements.

The overall tensile responses of the hybrid composites are, as before, underperforming the single fiber-type reinforced composites under the tensile performance viewpoint. The single fiber-type reinforced composites consistently outperform the corresponding hybrid fiber reinforced composites at all stages of the loading sequence in which they are individually more efficient. Therefore, the occurrence of a synergistic collaboration between the different fibers in the composite to restrain crack propagation is not evidenced in any of the hybrid composites tested. Although the features observed in the tensile behavior of the hybrid fiber reinforced composites are unique and quite distinct from the ones observed in the single fiber ones, the immediate interpretation of the observed results suggests that the effect of crack restraining produced by the fibers is better utilized when single fiber-type reinforcements are adopted, and that in general the combination of different fiber types in the same composite does not lead to a better usage of the potential of a certain type of fiber to contribute to the improvement of the tensile response.

4.7.3 Numerical modeling of the CTT mechanical responses

In Chapter 3 the tensile bridging stress-crack opening relationships of the single fiber reinforced cementitious composites were used to simulate the CTT tensile load-displacement responses of the respective composites. The tensile bridging stress-crack opening relationships obtained using the SCTT were adopted to define the traction-separation law of the interface elements that were used to simulate the ligament region of the CTT specimens (see Section 3.6). The numerical results showed good correlation with the experimental responses, therefore supporting the adoption of the SCTT to objectively evaluate the tensile stress-crack opening behavior of strain hardening cementitious composites.

In this section the study formerly described is extended to the case of cementitious composites containing multiple fiber-type reinforcements. The multiple-peak typology of the tensile behaviors observed in the hybrid fiber reinforced composites will be used to describe the traction-separation law of the ligament zone of the CCT specimens. The utilization of the SCTT and the resulting tensile-stress crack opening behaviors to simulate the mechanical behavior of hybrid fiber reinforced cementitious composites will be discussed, to further verify the validity of the use of SCTT to assess the tensile stress-crack opening behavior and to simulate the mechanical behavior of different types of fiber reinforced cementitious composites. The description of the numerical model, geometry and other details may be found in Section 3.6.

The average tensile stress-crack opening curves presented in Figures 4.4 and 4.11 were utilized to derive the traction-separation law assigned to the interface elements placed in the ligament region of the CTT specimen finite element model. The pre-cracking portion of the responses were excluded and all the experimentally recorded points (10 per second) were used to define the traction-separation laws adopted for the HybPP, HybPAN2 and HybPAN6 composites. The numerical and the experimental results are compared, and the average responses are represented in Figures 4.20 to 4.22.

In the case of the HybPP composite, the comparison of results is carried out in the range of displacements between 0 and 8 mm, at which most of the important features of the tensile load-displacement responses are visible. The numerical and the average experimental responses are essentially identical, with a small discrepancy occurring

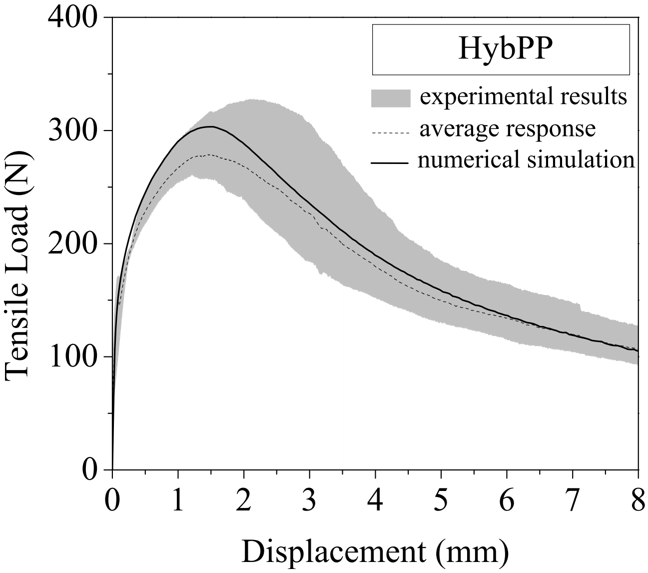

Figure 4.20: Average experimental *versus* numerical response obtained for the HybPP composite.

near the peak load region of the responses. The number of specimens used to characterize the SCTT response was six, while only three specimens were considered in the case of the CTT. Probably the numerical and the average experimental responses would show greater resemblance if a higher number of CTT specimens was considered.

For both the HybPAN2 and the HybPAN6 composites the comparison of results is carried out in the range of displacements between 0 and 3 mm, up to which most of the tensile load bearing capacity is exhausted. The results show that the numerical simulations approximate well the experimental average responses obtained. Up to the peak load the experimental average and the numerical curves are essentially identical. After the peak load there is a slight divergence in the case of the HybPAN2, most likely due to the insufficient characterization of the tensile stress-crack opening response for greater CMOD (probably the SCTT tensile stress-crack opening curve tail is not described up to sufficiently large CMOD). Nevertheless, the numerical curves and the corresponding experimental responses are essentially similar, considering that only three specimens were utilized to characterize the CTT tensile load-displacement behavior. In the case of the HybPAN6, the slight divergence between experimental and numerical curves that starts right after the peak load is

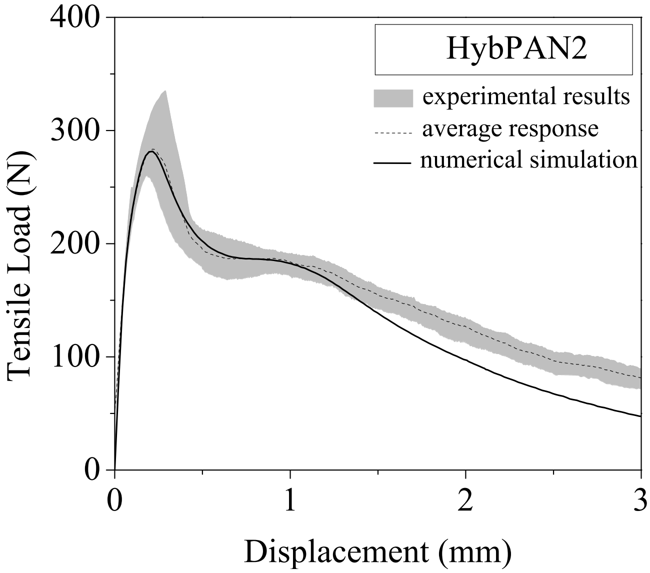

Figure 4.21: Average experimental *versus* numerical response obtained for the HybPAN2 composite.

reached, may be considered as within the expected scatter of results, considering the reduced number of specimens used in the CTT experiments. Additionally, the various hardening-softening stages that are easily identified in the experimental responses of the individual specimens (see Figures 4.14 to 4.16) are out of phase and, therefore, a cancellation effect of these stages may have occurred when the individual tensile responses were averaged.

In the following section, the observation of the crack patterns at the surface of the specimens may allow to further explain the particular details of the obtained CTT tensile responses, particularly the regions of the obtained responses at which slight divergence between the numerical simulations and the experimental results were observed. The numerical model assumes that a single crack is generated at the tip of the notch, and that this is the only crack appearing and propagating through the ligament region during the entire loading sequence. Using the same procedure as before (see Section 3.5.2) the image-based deformation analysis procedure will be utilized to interpret the overall failure mechanisms obtained in the specimens.

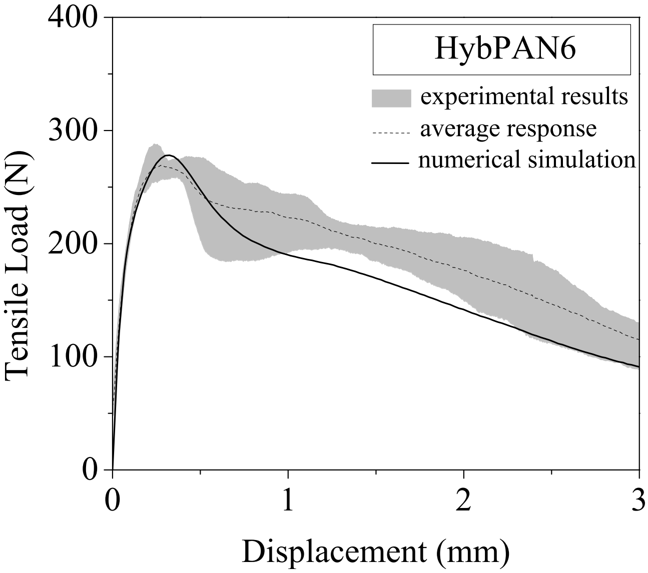

Figure 4.22: Average experimental *versus* numerical response obtained for the HybPAN6 composite.

4.7.4 Image-based deformation analysis of the CCT specimens

The deformations at the surface of one specimen of each hybrid fiber reinforced cementitious composite were analyzed adopting the procedure previously described (see Section 3.5.2). During testing, images of the surface of the first specimen of each composite were taken with time intervals of 1 sec. The crack initiation and propagation processes occurring during testing were subsequently reconstructed by compiling and processing all the images. A few particular stages of the entire process were selected for each composite. The selected stages are presented in Figure 4.23.

The results obtained at each of the selected stages, after image processing, are presented in Table 4.7. Stage 1 represents the last stage obtained before any crack was traceable at the facet overlay. Stages 2 to 4 correspond to noticeable alterations of the overall cracking mechanisms and the crack pattern. In Table 4.7, the major principal strains obtained at the facet overlay are presented (see Section 3.1.2 for a description of the concept of *facet overlay*). As shown, the cracking process starts at load values between 80 N and 160 N. Therefore most of the hardening-softening

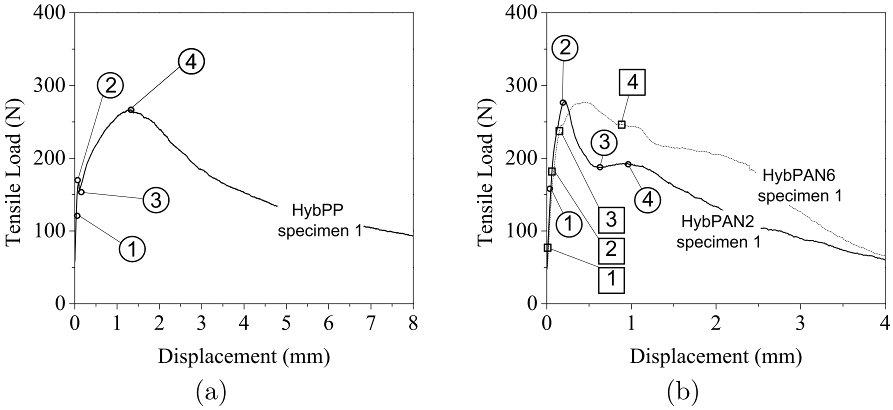

Figure 4.23: Identification of the selected stages from the image-based deformation analysis for the HybPP (a) and the HybPAN2 and HybPAN6 (b) composites.

tensile load-displacement behaviors observed previously occur with at least one crack already formed.

Considering the results obtained for the HybPAN6 composite, the initial formation of two diverging cracks at the tip of the notch was observed. One of these cracks propagates faster, apparently attracted by another pre-existing crack that is most likely a shrinkage-induced crack. At stage 2 the propagated crack after being attracted by the pre-existing shrinkage crack can be observed (see Table 4.7). The second crack is still barely visible, and does not propagate any further up to this point. At stage 3 the first crack had propagated further, as well as the second crack, demonstrating that the bridging stresses transferred across the first crack are large enough to cause the further increase of the local tensile stresses and the further opening of the second crack. Subsequently, the tensile bridging stresses in the region of the notch tip increase even further, as revealed by the formation of a third horizontal crack in the region of the notch tip and other crack branches initiated at the first and the second cracks. At stage 4, the crack branching near the notch tip seems to have stabilized, while new crack branches are forming in the region of the ligament which is closer to the specimen edge. Eventually, the further propagation of these crack branches also stabilizes, and localization at one of these branches leads to the rupture of the ligament region in two different parts. The gradual advancement of the region at which the new crack branches are forming during crack propagation is especially noticeable: initially, crack branches are forming at the left region of the documented area, and this region gradually advances to the right, with the increase

Table 4.7: Image-based analysis of crack patterns on the surface of the specimens at stages 1 to 4.

	HybPP	HybPAN2	HybPAN6	
1				 [%] 5.0 4.0 3.0 2.0 1.0 0.2
2				 [%] 5.0 4.0 3.0 2.0 1.0 0.2
3				 [%] 5.0 4.0 3.0 2.0 1.0 0.2
4		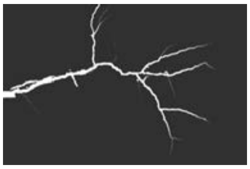	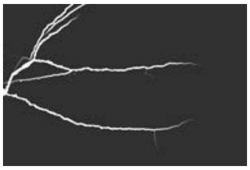	 [%] 5.0 4.0 3.0 2.0 1.0 0.2

of the displacement.

The sequence of cracking processes observed at the surface of HybPAN2 specimen was distinct. As shown in Table 4.7 the initiation and propagation of a single crack prevailed, essentially until the crack reached half of the ligament length (stage 2). Crack branching starts at this point, with the increase of the displacement. In contrast to HybPAN6 specimen, crack branches form mostly at later stages of the loading sequence, and on the last half of the total crack length. The absence of crack branches forming in the region of the notch tip at early stages of the cracking process suggests that the bridging stresses originated at the main crack, while leading to the increase of the local tensile stresses, do not produce a large enough increase of the local tensile stresses to exceed the local tensile strength of the cementitious matrix.

Considering that the same fiber reinforcement was used in the HybPAN6 composite, the increase of the tensile strength of the cementitious matrix, which is indirectly revealed by the significantly higher compressive strength obtained for the HybPAN2 specimens (see 4.5) was the main reason to this result. Eventually, the tensile load-displacement response of the HybPAN6 composite shows higher displacements than the HybPAN2 composite, at identical load levels. Additionally, the higher fracture toughness of the HybPAN2 composite matrix may have led to the rupture of an increased number of fibers during crack initiation.

The selected stages of the HybPP specimen show that the formation of a single principal crack is prevailing. Stage 2 shows that in the early stage of the loading sequence two cracks initiated at the tip of the notch. These two cracks initiating from the tip of the notch were also observed in the other specimens. Nevertheles, only the principal crack further propagates during testing, becoming clearly visible. The formation of small bifurcations and crack branches is minimal, until the crack tip reaches the last third of the ligament length. As shown at stage 4, when the peak load is reached, crack branching is almost confined to the last third of the ligament length. From this point onwards, the observation of the subsequent images shows that no other crack branches form. Further extension of these crack branches occurs during the descending part of the load-displacement curve, until one of these branches reaches the right edge of the specimen and the specimen becomes completely divided into two pieces. In the case of the HybPP the contribution of the PP fibers to restrain crack propagation, which was observed to take place at much larger crack openings in previous sections, is not as significant as in the other two previous cases. Therefore, less crack branches are produced at smaller crack openings. When larger displacements are reached the contribution of the PP fibers becomes more important, and the load observed for larger displacements becomes much higher than in the previous cases.

Comparing the cracking processes observed with the image-based deformation analysis, the differences between the results obtained for different hybrid composites are more subtle than the differences observed in Chapter 3 for different single fiber-type composites. This is probably due to the existence of a common fraction of PVA fibers in all hybrid composites. However, the general trend towards an increase in the number of parallel horizontal cracks forming in the case of the composites reinforced with smaller fibers, or alternativelly for the composites containing 'weaker' cementitious matrices, seems to remain. The multiple horizontal cracks, which are frequently formed in some composites, are most likely the result of the increase of the local tensile stresses even after the formation of cracks, as a result of a tensile bridging stresses build-up that exceeds the matrix tensile strength. In contrast, the vertical crack branches become more visible if the fiber reinforcement is not sufficient to restrain the further propagation of these crack branches, when they initiate at the principal crack. These two different types of secondary cracking should be distinguished, as they emerge from two opposite conceptions of the cracking mechanisms and the composite mechanical behavior.

The results obtained are obviously influenced by the scale at which the tests were conducted. As discussed in Section 4.4, the different fibers used in this study are more efficient at clearly different length scales of the cracking process, therefore the CTT results obtained are influenced by the size of the specimen. Considering the specimen size used and the associated length scale, the PAN fibers have revealed greater potential to generate multiple parallel cracks, despite the significant stress intensity created at the tip of the long sharp notch. Similar crack patterns could be expected with the other types of fibers if the size of the CT specimens was changed to the appropriate length scale relative to each type of fiber.

4.8 Conclusions

The use of the single crack tension test (SCTT) to assess the tensile performance of six fiber reinforced cementitious composites showed significantly distinct tensile stress-crack opening behaviors. The tensile responses obtained showed high sensitivity to the parameters of the different cementitious composites tested and particularly to the different fiber reinforcements used, allowing the detailed understanding of the fiber-matrix interactions and of the composite micro-mechanisms occurring during crack initiation and propagation. Furthermore, the experimental results obtained showed considerable robustness, with reasonably low variability of results. The type of information extracted from SCTT contributed to the comprehensive characterization of the tensile behavior of the tested composites and showed significant advantages when compared to conventional testing methods. Additionally, the effect of adopting significantly different cementitious matrices on the tensile response of hybrid fiber reinforced cementitious composites was directly evaluated using the SCTT. The SCTT procedure has showed desirable characteristics to support the optimal selection and usage of fibers in the design process of the cementitious composite for a specific application, while allowing to characterize explicitly their tensile performance. Additionally, the constitutive tensile stress-crack opening behaviors derived with the SCTT can be used as an input parameter to the description of the material constitutive relationship in the simulation of the structural behavior of SHCC elements.

The experimentally obtained tensile stress-crack opening responses showed that the different fibers used are activated at different length scales of the cracking process. The small diameter fibers (PAN) showed to be more effective in the range of very small crack openings, almost ten times smaller than the one observed for the large diameter fibers (PVA, PP). This contribution of the fibers to crack restraining at different length scales of the cracking process was also revealed by the tensile response of one of the hybrid fiber reinforced composites, the HybPAN, where two distinct tensile hardening-softening sequences were observed. The simultaneous use of multiple types of fibers in the same composite resulted in tensile responses that were somewhat related to the superposition of the corresponding single fiber-type reinforced composites. However, in general the hybrid composites showed poorer tensile behaviors than the corresponding composites reinforced with single fiber types.

The multi-scale nature of cracking mechanisms in cementitious matrix composites is often assumed as the reason to support a hybrid fiber reinforcement. Although the experimental results have shown that these different scales of the cracking process exist, and that the activation of different fibers occurs at different scales of the cracking process, the synergistic effect of having different types of fibers in the same composite was not observed. The hybrid formulations underperformed the respective single fiber reinforced composites in the CMOD ranges where the latter showed to be more effective. In addition, the hybrid formulations also underperformed the estimated tensile performances based on the direct superposition of the tensile responses of the corresponding single fiber reinforced composites, by showing poorer tensile bridging stresses than expected by superposition. The multiple peaks of the tensile bridging stress reached in composite containing two geometrically distinct types of fibers may be of interest for further investigation. However, with respect to optimizing the tensile performance, the synchronized activation of the fibers intersecting a crack in the hybrid composites is in general desirable, and may be incompatible with the hybridization of the fiber reinforcement.

The design of a hybrid fiber reinforced cementitious composite will eventually consist of selecting the scale or scales of the cracking process at which the fiber crack restraining effect is more important. This multi-scale design of the combinations of fibers for reinforcement can be assumed as mostly related to the material size-scales in which the cementitious composite material structure is organized. A multiplicity of different applications may pose diverse requirements concerning the tensile stress-crack opening response of the cementitious composite, which for various reasons may justify the adoption of fiber reinforcements composed of two or more different types of fibers. However, the design of the optimal composition of the fiber reinforcement towards optimized tensile performance must consider the need to preserve synchronism in the activation of the different types of fibers, which is less likely when multiple types of fibers are used simultaneously in the cementitious composite.

Bibliography

Ahmed, S. F. U., Maalej, M., and Paramasivam, P. (2007). Flexural responses of hybrid steel-polyethylene fiber reinforced cement composites containing high volume fly ash. *Construction & building materials*, 21(5):1088–1097.

Banthia, N. and Gupta, R. (2004). Hybrid fiber reinforced concrete (hyfrc): Fiber synergy in high strength matrices. *Mater Struct Materials and structures*, 37(274):707–716.

Barros, J., Cunha, V., Ribeiro, A., and Antunes, J. (2005). Post-cracking behaviour of steel fibre reinforced concrete. *Materials and Structures*, 38(275):47–56.

Bentur, A. and Mindess, S. (2006). *Fibre reinforced cementitious composites.* Modern concrete technology series. Taylor & Francis.

Betterman, L., Ouyang, C., and Shah, S. (1995). Fiber-matrix interaction in microfiber-reinforced mortar. *Advanced Cement Based Materials*, 2(2):53–61.

Bolander, J. and Saito, S. (1997). Discrete modeling of short-fiber reinforcement in cementitious composites. *Advanced Cement Based Materials*, 6(3-4):76–86.

Brandt, A. M. (2008). Fibre reinforced cement-based (frc) composites after over 40 years of development in building and civil engineering. *Compos Struct*, 86(1-3):3–9.

Chanvillard, G. (1999a). Characterization of fibre reinforced concrete's performance after a flexular test - part 2: Identification of an intrinsic behaviour relationship in tension caracterisation des performances d'un beton renforce de fibres a partir d'un essai de flexion. partie 2: Identification d'une loi de comportement intrinseque en traction. *Mater Struct Materials and structures*, 32(222):601–605.

Chanvillard, G. (1999b). Characterization of fibre reinforced concrete's performance after a flexural test - on subjectivity of toughness indices caracterisation des performances d'un beton renforce de fibres a partir d'un essai de flexion. partie 1: De la subjectivite des indices de tenacite. *Mater Struct Materials and structures*, 32(220):418–426.

Cotterell, B. and Mai, Y.-W. (1996). *Fracture mechanics of cementitious materials.* Blackie, London.

Cunha, V., Barros, J., and Sena-Cruz, J. (2012). A finite element model with discrete embedded elements for fibre reinforced composites. *Computers & structures*, 94-95:22–33.

de Larrard, F. (1999). *Concrete mixture proportioning: a scientific approach*. Modern concrete technology series. E & FN Spon.

Fischer, G., Stang, H., and Dick-Nielsen, L. (2007). Initiation and development of cracking in ecc materials: Experimental observations and modeling. In G.F.A., C. and Gambarova, P., editors, *High Performance Concrete, Brick- Masonry and Environmental Aspects.*, volume 3, pages 1517–1522. FraMCos, Taylor & Francis.

Kabele, P. (2007). Multiscale framework for modeling of fracture in high performance fiber reinforced cementitious composites. *Engineering Fracture Mechanics*, 74(1-2):194–209.

Kabele, P. (2009). Finite element fracture analysis of reinforced shcc members. In van Zijl, G. and Boshoff, W., editors, *Advances in Cement-Based Materials*, volume International Conference on Advanced Concrete Materials, pages 237–244, Stellenbosch, South Africa.

Karihaloo, B. (1995). *Fracture mechanics and structural concrete*. Longman Scientific and Technical, Harlow.

Lawler, J., Wilhelm, T., Zampini, D., and Shah, S. (2003). Fracture processes of hybrid fiber-reinforced mortar. *Mater Struct Materials and structures*, 36(257):197–208.

Li, V. C. (2003). On engineered cementitious composites (ecc). *J Adv Conc Tech*, 1(3):215–230.

Li, V. C., Wang, S., Ogawa, A., Saito, T., and Wu, C. (2002). Interface tailoring for strain-hardening polyvinyl alcohol-engineered cementitious composite (pva-ecc). *ACI Materials Journal*, 99(5):463–472.

Lofgren, I., Stang, H., and Olesen, J. F. (2008). The wst method, a fracture mechanics test method for frc. *Mater Struct*, 41(1):197–211.

Marković, I. (2006). *High-performance hybrid-fibre concrete: development and utilisation*. IOS Press.

Mehta, P. and Monteiro, P. (2006). *Concrete: microstructure, properties, and materials*. McGraw Hill professional. McGraw-Hill.

Mobasher, B. and Li, C. Y. (1996). Mechanical properties of hybrid cement-based composites. *ACI Mater J*, 93(3):284–292.

Neville, A. (1996). *Properties of concrete*. John Wiley & Sons.

Pereira, E., Fischer, G., and Barros, J. (2011). Hybrid fiber reinforcement and crack formation in cementitious composite materials. In Parra-Montesinos, G., Reinhardt, H., and Naaman, A., editors, *High Performance Fiber Reinforced Cement Composites 6 - HPFRCC 6*, volume 2 of *RILEM state of the art reports*, pages 535–542, Ann Arbor, Michigan, USA. Springer.

Pereira, E., Fischer, G., and Barros, J. (2012a). Direct assessment of tensile stress-crack opening behavior of strain hardening cementitious composites (shcc). *Cement and Concrete Research*.

Pereira, E., Fischer, G., and Barros, J. (2012b). Effect of hybrid fiber reinforcement on the cracking process in fiber reinforced cementitious composites cement and concrete composites. *Cement and Concrete Composites*, (Accepted for publishing.).

Pereira, E. B., Fischer, G., Barros, J. A., and Lepech, M. (2010). Crack formation and tensile stress-crack opening behavior of fiber reinforced cementitious composites (frcc). *7th International Conference on Fracture Mechanics of Concrete and Concrete Structures (FraMCoS 7)*.

Pereira, E. N. B., Barros, J. A. O., and Camoes, A. (2008). Steel fiber-reinforced self-compacting concrete: Experimental research and numerical simulation. *ASCE Journal of Structural Engineering*, 134(8):1310–1321.

Qian, C. and Stroeven, P. (2000). Fracture properties of concrete reinforced with steel-polypropylene hybrid fibres. *Cement and Concrete Composites*, 22(5):343–351.

Rossi, P. (1997). High performance multimodal fiber reinforced cement composites (hpmfrcc): the lcpc experience. *ACI Mater J*, 94(6):478–483.

Shah, S., Swartz, S., and Ouyang, C. (1995). *Fracture mechanics of concrete - Applications of fracture mechanics to concrete, rock, and other quasi-brittle materials.* Wiley, New York,N.Y.

Stang, H., Li, V. C., and Krenchel, H. (1995). Design and structural applications of stress-crack width relations in fibre reinforced concrete. *Materials and Structures*, 28(4):210–219.

van Mier, J. (1997). *Fracture processes of concrete: assesment of material parameters for fracture models.* New directions in civil engineering. CRC Press.

Wei, Q. F., Mather, R. R., Fotheringham, A. F., and Yang, R. D. (2002). Esem study of wetting of untreated and plasma treated polypropylene fibers. *J Ind Text*, 32(1):59–66.

Yang, J. and Fischer, G. (2006). Implications of the fiber bridging stress - crack opening relationship on properties of fiber reinforced cementitious composites in uniaxial tension. In *International Workshop on High Performance Fiber Reinforced Cementitious Composites in Structural Applications*, volume RILEM Proceedings PRO 49, pages –.

Zhang, J., Leung, C. K. Y., and Xu, S. (2010). Evaluation of fracture parameters of concrete from bending test using inverse analysis approach. *Mater Struct*, 43(6):857–874.

CHAPTER 5

Plasticity-based constitutive modeling

5.1 Introduction

The development of ultra high performance fiber reinforced cement composites (UHPFRCC), and in particular of the strain hardening cementitious composites (SHCC), has undergone significant improvements and achievements in recent years. These novel materials, as described in the previous chapters, are still in a process of rapid development and discovery. The characterization of the mechanical behavior of SHCC materials is following closely the process of their development, and the necessary design guidelines and standard tests are currently in a process of consolidation.

The multi-scale nature of such composite materials is complex, and the need of a thorough knowledge about the nature of the different phases and their interaction in the composite, at the distinct material size-scales, is critical. As a result, this aspect of the composite material behavior and numerical modeling attracts great attention, mostly because all the macroscopic material properties are a direct consequence of the composite material properties at the different material size-scales, and of the interaction between these different scales. Although the field is still undergoing rapid evolution, there is already a substantially well consolidated knowledge about the micro-mechanics of these materials, as discussed in Chapter 1 and 2.

Aside from the innovations in the material design and material micro-mechanical characterization, advanced numerical strategies have been also developed, aiming at simulating the composite behavior of SHCC. The main focus is often directed to the description of the inter-relations between different composite constituents at the micro-scale level. Considering the different material size-scales, the mechanical properties at the meso- or macro- scale are derived departing from micro-mechanical composite parameters. Multi-scale numerical strategies based on the homogenization of the composite micro-scale properties at the level of the representative element volume (RVE) [Kabele, 2007], and the consideration of the fracture mechanisms of micro-cracking propagation [Karihaloo and Wang, 2000] have been proposed to link the micro-and macro-scale behavior of SHCC. Probably due to the great complexity and high degree of disorder encountered in cementitious composites material structure, although some of these models are quite broad at considering most of the relevant micro-mechanical composite parameters, they become less practical when dealing with the simulation of the macro-scale behavior of SHCC structures. Alternatively, other widely used approaches essentially adapt models originally developed for concrete. The smeared crack model is one example, where the meso-scale tensile stress-crack opening / sliding behaviors considering a multiple-cracked RVE can be used to derive the post-cracking constitutive relationships [Kabele, 2009]. Of similar nature, the total strain rotating crack model is adopted by Han et al. [2003] to simulate the behavior of ductile fiber reinforced cement-based composite (DFRCC) members subjected to cyclic and seismic loading. Other models consider the simulation of the matrix as a continuum [Cunha et al., 2012] or with discrete elements [Bolander and Hirosaka, 1995; Bolander and Saito, 1997; Schlangen et al., 2009; Kunieda et al., 2011], and dispersed short fibers are embedded in the matrix, often using interface elements to simulate the fiber-matrix frictional interaction. The results obtained with these models correlate well with the experiments and the cracking patterns obtained are often intuitive, however the available applications are mostly restricted to the simulation of tensile tests.

Besides the smeared cracking approaches, examples exist of the adoption of the phenomenological approaches based on the plasticity theory. The failure surfaces typically used to simulate the non-linear behavior of concrete were adapted to the simulation of SHCC, such as the Rankine failure criterion, mostly to members subjected to uni-axial and bi-axial stress conditions, and in some cases combined with the smeared cracking concept [van Zijl, 2009; Vorel and Boshoff, 2009]. In most of these models, the post-cracking tensile behavior of SHCC is based on the tensile stress-strain relationship. Individual cracks are not explicitly described by these models, instead the behavior of an RVE that is assumed to contain a large number of cracks is considered. Although this approach has proven itself as computationally effective in most situations, in the particular case of structural elements failing in shear-tension mode, an excessively stiff response is predicted by these models [Kabele, 2009]. This numerical artifact is often attributed to the inability of these models to account for the effect of the individual cracks, mainly after localization is initiated at a certain location of the structure. Kullaa [1997] proposed to simulate the appearance of the discrete cracks by dividing the elements intersected by the predicted crack paths, and subsequently connecting these elements with interface elements. The crack paths are predicted with a continuum model that integrates both plasticity and smeared cracking concepts. The individual crack-based approach proposed by Kabele [2009] adopts the traction-separation law in 2D, assuming independent opening and sliding modes, to approach the localization problem and achieve more accurate predictions of the experimental results when complex non-proportional loading cases are considered, such as in shear beams. Trüb [2011] proposes a solution based on the extended finite element method (XFEM) to simulate the discontinuity created by the macro-cracks, which are the result of the coalescence of the micro-cracks simulated by the smeared cracking approach. Other important feature of the behavior of SHCC and its consequence for the numerical modeling is reported by Suryanto et al. [2008], and deals with the influence of the alteration of the principal stress directions on the tensile behavior of SHCC. The authors developed a space averaged constitutive model to multi-directional cracking condition based on bending tests with SHCC plate initially cracked in a certain direction and subsequently loaded in a different direction at changing angles. The experimental results showed that the behavior in bending depends on the angle of the initial crack direction. The constitutive model was based on the Mindlin plate finite element.

The number of research studies directed to the numerical modeling of SHCC members and structures is still not extensive. The research in this field is currently more focused on the study of the composite material properties at the smaller size-scales, such as the size-scale that is typically adopted for the laboratory specimens. Even less frequent are the numerical models capable of simulating general 3D states of stress, probably because the number of experimental research studies dealing with the characterization of the tri-axial behavior of SHCC are also somewhat scarce.

In this research, the strategy adopted to approach the problem of simulating the no-linear behavior of SHCC departs from the nonlinear models typically used for concrete. The classical theory of elasto-plasticity applied to the case of 3D states of stress and considering associated plasticity with generalized hardening (including hardening and softening) will be adopted to simulate the behavior of SHCC in a phenomenological perspective. As such, the representative overall composite tensile stress-strain response presented in Chapter 2 summarizes most of the information used to define the constitutive model. Some shortcomings of this strategy may be anticipated, mostly associated with the adoption of continuum models to simulate the behavior of a material where cracking eventually localizes, as these models are unable to simulate individual cracks. However, such strategy may contribute with a step forward on the exploration of the possibilities to simulate the 3D behavior of SHCC materials, by adopting a single yield surface to characterize the hardening process for any loading configuration. The information about the micro- and meso-structure of the composite material can subsequently be incorporated to provide the necessary capabilities for predicting important composite behavior parameters, such as the determination of crack opening and spacing fields, or even the scaling of the tensile stress-strain relationship to suit the local size-scale at any point of the structure. For this purpose the 4-parameter failure criterion recommended by CEB-FIP Model Code Comité Euro-international du Béton [1993] to estimate the strength of concrete under multi-axial states of stress will be adopted. This failure criterion, also known as the Ottosen failure criterion, captures well the failure of concrete and other granular materials in three-dimensional states of stress, as demonstrated experimentally by several researchers. Concrete strength is estimated also considering the effect of the confining pressure, and the variation of the failure stresses with the hydrostatic stress is well captured.

5.1.1 Numerical elasto-plasticity and failure criteria for concrete

Concrete is a highly nonlinear material, with great dependence on the confining stresses and very sensitive to tri-axial states of stress. This type of behavior is also shared by other granular and quasi-brittle materials. The characterization of the material behavior of concrete is based on the reproduction of simple states of stress or strain in representative specimens, which are object of standardized experimental procedures that guide the determination of basic mechanical parameters. Concrete behavior in real structures is estimated using structural models that rely on a very limited number of mechanical parameters, mostly the compressive and tensile strengths, the Young's modulus and the Poisson's coefficient. Although the real behavior of concrete is complex and difficult to simulate, a good compromise may be achieved with reasonably simple models and few mechanical parameters.

The interaction of the various stress components in concrete determines its strength. The installed tensile, compressive or shear stresses can not be considered separately, since concrete strength will depend on the interaction of all stress components. For example, considering that a concrete with a tensile strength of f_c' and a pure shear strength of $0.08f_c'$ is tested in mixed compression-shear test, it would fail at a compressive stress of $0.5f_c'$ for a shear stress of $0.5f_c'$ [Chen, 1982]. Consequently, the concept of a mathematical relationship of interaction between all stress components that allows the separation of the stress space into the admissible and the non-admissible states of stress is very convenient. The pioneering works of Tresca, von Mises and several other scientists helped in the past to develop plasticity theory as a scientific field in solid mechanics. Originally inspired on the behavior of metals, soon the usefulness of plasticity theory to describe the nonlinear behavior of many other types of materials was revealed. Several interaction functions, known as failure criteria, have been proposed for different materials including concrete, assuming the shape of surfaces in the 3D stress space.

The well known highly nonlinear behavior of concrete is still a great challenge for material and structural modeling disciplines. Formulations based on fracture mechanics, damage or plasticity have been proposed for decades, and their refinement has increased gradually with time. The perfect model is though, even theoretically, unreachable, given the complexity of mechanical behavior and strength of disordered materials, like concrete. If such a kind of model would exist, its huge complexity would compromise its efficiency. A good balance between practical usefulness and accuracy of constitutive modeling is permanently searched, considering the actual computational and knowledge limitations.

5.1.2 The stress invariants

The definition of the failure criterion of isotropic materials as a function of the state of stress must be independent of the coordinate system chosen to describe the stress tensor. Therefore, one possibility is to define such a function with respect to the principal stresses [Chen, 1982]:

$$f(\sigma_1, \sigma_2, \sigma_3) = 0 \tag{5.1}$$

Failure of most materials is difficult to explain based on the principal stresses. Alternatively, the principal stress invariants have assumed a prominent role on the description of failure of materials and on the establishment of failure functions. Since every invariant symmetric function of the state of stress can be expressed in terms of the three principal stress invariants I_1, J_2, and J_3 (which will be defined subsequently), the failure function can be alternatively described by [Chen, 1982]:

$$f(I_1, J_2, J_3) = 0 \tag{5.2}$$

According to classic continuum mechanics, the stress invariants are involved in the eigenvectors-eigenvalues problem of determining the principal stresses, σ, and principal directions, n_j, of a generic stress tensor, σ_{ij}, defined in a certain coordinate system:

$$(\sigma_{ij} - \sigma\delta_{ij})n_j = 0 \tag{5.3}$$

where δ_{ij} represents the Kronecker delta.

The eigenvalues, or the principal stresses, σ, are the roots of the following characteristic equation:

$$\sigma^3 - I_1\sigma^2 + I_2\sigma - I_3 = 0 \tag{5.4}$$

where I_1, I_2 and I_3 are the first, second and third principal stress invariants:

$$\begin{aligned} I_1 &= \boldsymbol{tr}\,(\sigma_{ij}) = \sigma_{ii} \\ I_2 &= \frac{1}{2}\,(\sigma_{ii}\sigma_{jj} - \sigma_{ij}\sigma_{ji}) \\ I_3 &= |\sigma_{ij}| = \frac{1}{3}\sigma_{ij}\sigma_{jk}\sigma_{ki} - \frac{1}{2}I_1\sigma_{ij}\sigma_{ji} + \frac{1}{6}I_1^3 \end{aligned} \tag{5.5}$$

The deviatoric stress tensor, s_{ij}, represents a state of pure shear, and can be expressed as the deviation from the purely hydrostatic state of stress:

$$s_{ij} = \sigma_{ij} - \sigma_m\delta_{ij} \tag{5.6}$$

where σ_m represents the hydrostatic stress:

$$\sigma_m = \frac{1}{3}\sigma_{ii} = \frac{1}{3}I_1 \tag{5.7}$$

The characteristic equation of the eigenvector-eigenvalue problem can also be established considering the deviatoric stress tensor, similarly to equation 5.4:

$$s^3 - J_1s^2 - J_2s - J_3 = 0 \tag{5.8}$$

The characteristic equation involves, in this case, the deviatoric stress invariants J_1, J_2 and J_3, described by the following expressions:

$$J_1 = \boldsymbol{tr}\left(s_{ij}\right) = s_{ii} = 0$$
$$J_2 = \frac{1}{2}s_{ij}s_{ji} = \frac{1}{2}I_1^2 - I_2 \tag{5.9}$$
$$J_3 = |s_{ij}| = \frac{2}{27}I_1^3 - \frac{1}{3}I_1 I_2 + I_3$$

I_1, I_2, I_3, J_1, J_2 and J_3 are scalar invariants independently of the chosen coordinate system, what makes them very useful to the definition of generic failure criterion. In addition, it is possible to provide a geometrical and a physical interpretation to these stress invariants, specially the I_1, J_2 and J_3 stress invariants, which are of the first, second and third degree in stress, respectively. In fact, while it is possible to express every invariant symmetric function in terms of these three principal stress invariants, I_1 represents a purely hydrostatic state of stress, as opposed to J_2 and J_3 that represent the invariants of a pure shear state of stress.

5.1.3 Geometric interpretation of the stress invariants

The physical and geometrical interpretation of the stress tensor invariants is simplified by the concepts of the octahedral stresses. At one point inside the stressed body, the octahedral planes consist of the planes which make equal angles with each of the principal stress directions. The normal stress on this plane is called the octahedral normal stress, σ_{oct}, and the shear stress on this plane called the octahedral shear stress, τ_{oct}. It can be shown that the octahedral stresses are given by the following expressions:

$$\sigma_{oct} = \frac{1}{3}I_1 = \sigma_m \tag{5.10}$$

$$\tau_{oct} = \sqrt{\frac{2}{3}J_2} \tag{5.11}$$

The direction of the octahedral shear stress is given by the Lode angle, θ, that is defined by the following equation:

$$cos3\theta = \frac{\sqrt{2}J_3}{\tau_{oct}^3} \tag{5.12}$$

The relevance of the Lode angle originates from the procedure used to directly evaluate the roots of the characteristic equations described earlier, the equations 5.4 and 5.8. These equations have a similar structure to the following trigonometric identity [Chen, 1982]:

$$cos^3\theta - \frac{3}{4}cos\theta - \frac{1}{4}cos3\theta = 0 \tag{5.13}$$

If $s = \rho\ cos\theta$ is substituted into equation 5.13, the following equation is obtained:

$$cos^3\theta - \frac{J_2}{\rho^2}cos\theta - \frac{J_3}{\rho^3} = 0 \tag{5.14}$$

From the comparison of equations 5.13 and 5.14 results:

$$\rho = \frac{2}{\sqrt{3}}\sqrt{J_2} \tag{5.15}$$

$$\cos 3\theta = \frac{4J_3}{\rho^3} = \frac{3\sqrt{3}}{2}\frac{J_3}{J_2^{3/2}} \tag{5.16}$$

Considering the periodicity of the function $cos(3\theta \pm 2n\pi)$ and that θ_0 is the first root of equation 5.14 for an angle 3θ in the range 0 to π, then $0 \leq \theta \leq \frac{\pi}{3}$ and the three principal stresses are denoted by:

$$cos\left(\theta_0\right) \qquad cos\left(\theta_0 - \frac{2}{3}\pi\right) \qquad cos\left(\theta_0 + \frac{2}{3}\pi\right) \tag{5.17}$$

and the three principal stresses of σ_{ij} and s_{ij} can be calculated by assuming that $s_i = \rho cos(\theta_i)$:

$$\begin{bmatrix} s_1 \\ s_2 \\ s_3 \end{bmatrix} = \begin{bmatrix} \sigma_1 \\ \sigma_2 \\ \sigma_3 \end{bmatrix} - \begin{bmatrix} \sigma_m \\ \sigma_m \\ \sigma_m \end{bmatrix} = \frac{2}{\sqrt{3}}\sqrt{J_2}\begin{bmatrix} cos\left(\theta_0\right) \\ cos\left(\theta_0 - \frac{2}{3}\pi\right) \\ cos\left(\theta_0 + \frac{2}{3}\pi\right) \end{bmatrix} \tag{5.18}$$

where $\sigma_1 \geq \sigma_2 \geq \sigma_3$. The three stress invariants present in equation 5.18 are $\sigma_m = \frac{1}{3}I_1$, $\sqrt{J_2}$ and θ_0. Therefore the failure criteria can also be defined as a function of these three stress invariants, $f\left(\sigma_m, \sqrt{J_2}, \theta_0\right) = 0$, alternatively to the aforementioned form $f\left(I_1, J_2, J_3\right) = 0$.

The interpretation of failure criteria defined in terms of the stress invariants is simplified by the geometrical interpretation of the stress state and the stress invariants in the three-dimensional space. The stress state at a point $P\left(\sigma_1, \sigma_2, \sigma_3\right)$ may be geometrically represented by treating the three principal stresses σ_1, σ_2 and σ_3 as the coordinates of a point in the three-dimensional space (Figure 5.1). As subsequently explained, independently of the orientation of the principal directions this representation is sufficient to characterize the geometry of stress in the point P, and will be the same for any stress state as long as the principal stress values are the same. Therefore, this representation of the stress space does not consider the orientation of the local stress but only its geometry, consequently its usefulness is restricted to isotropic materials where the failure criteria are invariant functions of the stress state.

Vector $\boldsymbol{OP}$ may be considered as a representation of the state of stress, with the components $\boldsymbol{ON}$ and $\boldsymbol{NP}$. The component $\boldsymbol{ON}$ represents the hydrostatic part, while the component $\boldsymbol{NP}$ represents the deviatoric part of $\boldsymbol{OP}$. The hydrostatic axis is defined as the diagonal at equal angles relatively to the three coordinate axis. At every point of this diagonal, $\sigma_1 = \sigma_2 = \sigma_3$. The unit vector along this diagonal, $\boldsymbol{e}$, is therefore:

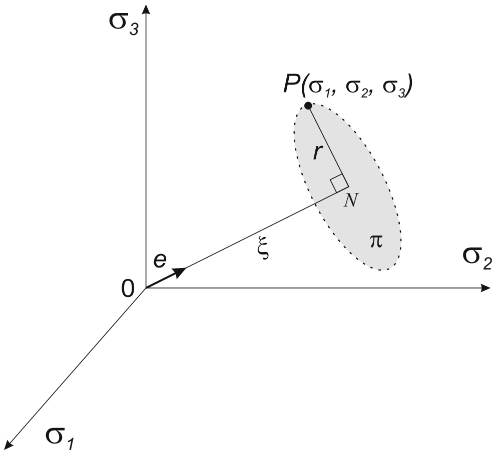

Figure 5.1: Representation and decomposition of the stress state $P\left(\sigma_1, \sigma_2, \sigma_3\right)$ in the principal stress space.

$$e = \frac{1}{\sqrt{3}} \left[1 \ 1 \ 1\right] \tag{5.19}$$

The planes which are perpendicular to the hydrostatic axis are called the deviatoric, octahedral, or π planes. Disregarding the hydrostatic stress component, any stress point on a π plane represents the deviatoric component of the stress state, or a pure shear state. The length of $\boldsymbol{ON}$ (hydrostatic component) is then described by:

$$|\boldsymbol{ON}| = \xi = \boldsymbol{OP} \cdot \boldsymbol{e} = [\sigma_1 \ \sigma_2 \ \sigma_3] \frac{1}{\sqrt{3}} \begin{bmatrix} 1 \\ 1 \\ 1 \end{bmatrix} \tag{5.20}$$

$$\xi = \frac{I_1}{\sqrt{3}} = \sqrt{3}\,\sigma_m = \sqrt{3}\,\sigma_{oct} \tag{5.21}$$

and $\boldsymbol{ON}$ vector components are:

$$\boldsymbol{ON} = [\sigma_m \ \sigma_m \ \sigma_m] = \frac{I_1}{3}\,[1 \ 1 \ 1] \tag{5.22}$$

Vector $\boldsymbol{NP}$ (deviatoric component) is therefore described by:

$$\boldsymbol{NP} = \boldsymbol{OP} - \boldsymbol{ON} = [\sigma_1 \ \sigma_2 \ \sigma_3] - \frac{I_1}{3}\,[1 \ 1 \ 1] \tag{5.23}$$

$$= [s_1 \ s_2 \ s_3] \tag{5.24}$$

and the length of $\boldsymbol{NP}$ is given by:

$$|\boldsymbol{NP}|^2 = r^2 = s_1^2 + s_2^2 + s_3^2 = 2J_2 \tag{5.25}$$

$$r^2 = 2J_2 = 3\tau_{oct}^2 \tag{5.26}$$

The geometric interpretation of the third deviatoric stress invariant, J_3, is also possible at the level of the deviatoric plane. In the present context it is of interest the interpretation involving the geometric meaning of the Lode angle, which contains J_3. For this purpose, the visualization of the deviatoric plane as the plane of the paper requires the projection of the coordinate axes on the plane of the paper. Also known as the Haigh-Westergaard stress space, in this representation the three axes corresponding to the three principal stresses are projected to the plane of the paper, becoming equally spaced and forming equal angles of 120 ° or $2\pi/3$. The coordinate axis corresponding to the fist principal stress, σ_1, is typically considered as the vertical axis (Figure 5.2).

The angle θ is measured from the positive σ_1 and lies in the deviatoric plane. The unit vector $\boldsymbol{i}$ has its origin at N and takes the direction of the projection of the σ_1 axis on the deviatoric plane, with the components:

$$\boldsymbol{i} = \frac{1}{\sqrt{6}}\,[2 \ -1 \ -1] \tag{5.27}$$

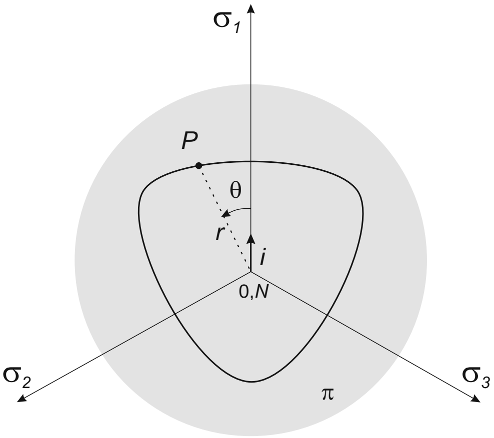

Figure 5.2: Representation of the state of stress P and failure surface in the Haigh-Westergaard stress space.

Considering that:

$$\boldsymbol{NP} \cdot \boldsymbol{i} = r cos\theta \tag{5.28}$$

the θ angle may be obtained by the following expression:

$$cos\theta = \frac{1}{\sqrt{2J_2}} \left[s_1 \; s_2 \; s_3 \right] \frac{1}{\sqrt{6}} \left[\begin{array}{c} 2 \\ -1 \\ -1 \end{array} \right] = \tag{5.29}$$

$$= \frac{\sqrt{3}}{2} \frac{s_1}{\sqrt{J_2}} = \frac{2\sigma_1 + \sigma_2 + \sigma_3}{2\sqrt{3}\sqrt{J_2}} \tag{5.30}$$

Considering that the principal stresses are ordered from the largest to the smallest value, $\sigma_1 \geq \sigma_2 \geq \sigma_3$, then $0 \leq \theta \leq 2\pi/3$. The Lode angle can then be derived by considering again the trigonometric identity:

$$cos3\theta = 4cos^3\theta - 3cos\theta \tag{5.31}$$

by which it is obtained, as in equation 5.16, the following equation:

$$\cos 3\theta = \frac{3\sqrt{3}}{2} \frac{J_3}{J_2^{3/2}} = \frac{\sqrt{2}J_3}{\tau_{oct}^3} \tag{5.32}$$

As a result, the failure surface before represented as a function of the three principal stresses, $f\left(\sigma_1, \sigma_2, \sigma_3\right)$, or the stress invariants, $f\left(I_1, J_2, J_3\right)$, can also be represented either by $f(\xi, r, \theta)$ or $f(\sigma_{oct}, \tau_{oct}, \theta)$, with the benefit of a more convenient geometrical interpretation.

5.1.4 Characteristics of the failure surfaces of concrete

Since the previous works of Kupfer [Kupfer et al., 1969] it is recognized that the experimental results of concrete tested under multiaxial loading are best fit by the failure surfaces which are dependent of all three stress invariants (I_1, J_2 and J_3) as variables [Chen, 1982]. The hydrostatic pressure dependence and the interaction between shear and normal stresses in concrete are properly taken into account in this fashion. The first models applied to concrete were very simple and approximated, because they were only taking into account the influence of hydrostatic pressure. The Rankine criterion, in the class of the one-parameter models (with the maximum tensile stress determining the failure), or the Mohr-Coloumb criterion, in the class of two-parameter models (with failure determined by both cohesion and the internal friction angle), had straight-line envelopes in the meridian planes and non-smooth 3D surfaces. Other more refined three-parameter models were subsequently proposed, showing smooth failure surfaces, like the William-Warnke criterion [Willam and Warnke, 1974], but they were still preserving the straight-line envelopes in the meridian planes.

The experimental results obtained from tri-axial testing of concrete have shown that the failure functions should have a curved shape in the meridian planes, as presented in Figure 5.3. Furthermore, the failure surface should be nearly triangular for low hydrostatic stresses and gradually becoming increasingly rounded, almost circular for high hydrostatic stresses. This shape is conceptually shown in Figure 5.2.

5.2 The Ottosen failure criterion

The four-parameter model proposed by Ottosen in 1975 Ottosen [1980], while depending on the three stress invariants (I_1, J_2 and J_3), was one of the first proposed failure criteria to show good ability to fit the bi-axial test results of Kupfer et al. [1969]. Smoothness, convexity, curved meridians and a gradual transition from an almost triangular shape to almost circular in the deviatoric plane for increasing of

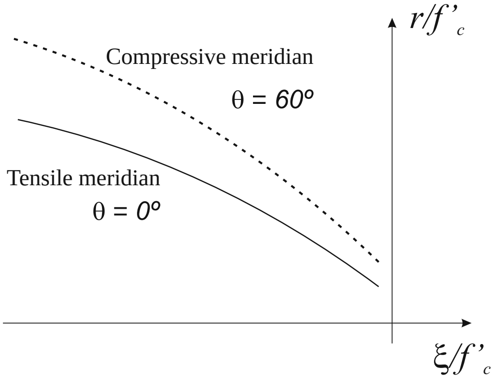

Figure 5.3: Representation of the rounded envelopes of the failure surface at the compressive and tensile meridian planes. The ξ and r coordinates are normalized with respect to the compressive strength, f_c'.

hydrostatic pressure, make the Ottosen failure criterion a good candidate for the simulation of concrete failure under tri-axial states of stress (see fig. 5.5). The Ottosen failure criterion is also recommended by Comité Euro-international du Béton [1993] as the failure criterion to determine the rupture of concrete under tri-axial states of stress. The following equation shows the dependence of the Ottosen failure criterion on the three stress invariants, I_1, J_2 and J_3, or alternatively $cos3\theta$:

$$f(I_1, J_2, cos3\theta) = \alpha\frac{J_2}{f_c^2} + \lambda\frac{\sqrt{J_2}}{f_c} + \beta\frac{I_1}{f_c} - 1 = 0 \tag{5.33}$$

where α and β are constants and $\lambda = \lambda(cos3\theta) > 0$ is the Ottosen variable that is a function of the Lode angle.

The Ottosen failure surface has curved meridians and a smooth non-circular cross-section. In the deviatoric planes, the Ottosen failure curve exhibits the gradual transition from an almost triangular shape for low hydrostatic stresses, to an almost circular shape for high hydrostatic stresses, in good agreement with the available tri-axial test results for concrete. Since the shape of the curved meridians is determined by the parameters α and β, and the shape of the non-circular cross-section is defined by the parameter λ, which in turn is determined by the constants $\lambda_t = \lambda(\theta = 0\,°)$ and $\lambda_c = \lambda(\theta = 60\,°)$, it follows that the Ottosen failure criterion is a four-parameter model [Chen, 1982; Jirásek and Bažant, 2001]. In Figure 5.4 the envelope of the Ottosen failure surface in the meridian planes is shown. In Figure 5.5 the transition from the almost triangular to the almost circular shape of the failure criterion in the deviatoric planes is shown. The four parameters of the Ottosen criterion can be fitted to the experimental results available [Ottosen, 1980]. In the present case, the expressions of the four parameters that define the Ottosen failure criterion were taken from [Comité Euro-international du Béton, 1993]

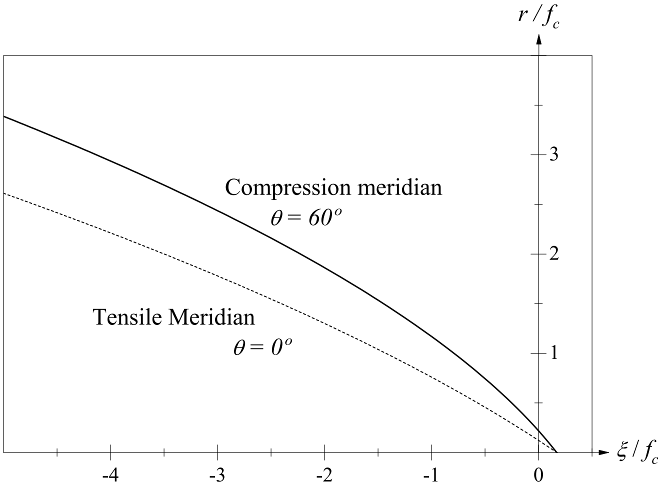

Figure 5.4: Representation of the compressive and tensile meridional planes of the Ottosen failure criterion.

The identification of the model parameters from standard tests is relatively simple, and this is not always the case when dealing with failure surfaces in the three-dimensional stress space. The Ottosen failure criterion also shows great ability to closely fit all the experimental data from concrete tri-axial testing [Ottosen, 1980]. Therefore, it is usually one of the preferred criteria to assess the multi-axial behavior of concrete. Other more recent alternatives were proposed, of more refined failure functions dealing with specific cases of loading in concrete, such as high hydrostatic stresses (Grassl et al. [2002]; Papanikolaou and Kappos [2007]), but the classic philosophy is generally preserved.

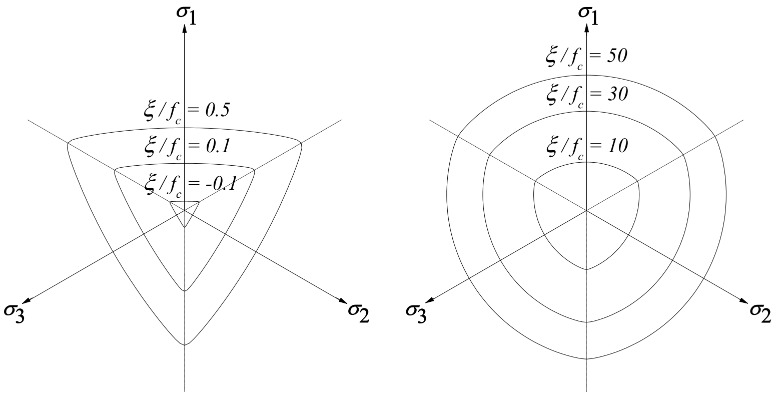

(a) (b)

Figure 5.5: Representation of the Ottosen yield criterion in the deviatoric planes using the Haigh-Westergaard stress space, for (a) low and (b) high hydrostatic stress.

5.2.1 Hardening

Perfect elasto-plastic materials yield at a constant stress while subjected to uni-axial loading. During plastic flow under multi-axial loading, the stress state can move along the yield surface and the surface itself remains unchanged. The hardening/softening (referred as "hardening" in the generalized sense) behavior of concrete while under uni-axial loading is quite different from this ideally perfect elasto-plastic type of behavior. While plastic deformation is taking place, the stress level is not constant and it actually increases (hardens) initially, and decreases (softens) subsequently after the peak stress is reached. Correspondingly, assuming that while plastic flow is taking place the stress state is moving along the yield surface, increasing/decreasing stress levels will determine changes in size and/or shape of the initial yield surface. The initial yield surface is therefore responsible for determining the onset of the plastic process, therefore it is usually designated as the elastic limit envelope. Intermediate states of the surface are typically called loading surfaces.

The change of the size or shape of the loading surface during hardening is controlled by one or more internal parameters. The hardening law defines the motion of the loading surfaces after yielding is reached, typically based on the material mechanical behavior for simple states of stress, such as the uni-axial stress-strain behavior. The simplest approach to hardening was first introduced by Odqvist [1933] *in* [Jirásek and Bažant, 2001], and is known as isotropic hardening. It determines that the evolution of the loading surface occurs in similar configurations with respect to the origin. It is, however, well known that this form of hardening is insufficient to reproduce cyclic and reversed types of loading or directional anisotropy induced by plastic flow [Hofstetter and Mang, 1995]. These are especially relevant in concrete, where kinematic and mixed hardening allow the better description of these behaviors, with the associated cost of an increased number of parameters needed to characterize the expansion and translation of the loading surfaces.

This research aims at analyzing the behavior of the Ottosen failure criterion when utilized as the loading surface with generalized hardening. An increased difficulty emerges when the Ottosen failure criterion is generalized in a hardening/softening framework, since the equation of the loading surface does not fit the general form of the isotropic models, where the hardening parameter is explicitly defined. For this reason, the particular measures needed to formulate adequately the set of equations used in the numerical implementation is addressed. Furthermore, there is the interest of studying how a constitutive model for concrete behaves, if based in the adoption of the uni-axial compressive law and the multi-axial failure criterion, both proposed by the Comité Euro-international du Béton [1993]. In a subsequent stage, the behavior of the model is also tested to assess the applicability of the adopted strategy to address the generalized hardening in tension and in compression in a decoupled fashion, while utilizing a single yield surface.

5.3 Model implementation considering one hardening parameter

The Ottosen yield criterion may be used as a loading surface when expressed as a function of the stress tensor $\boldsymbol{\sigma}$ and the hardening parameter $\tilde{\sigma}$ [Zienkiewicz et al., 2005; Zienkiewicz and Taylor, 2005]. Alternatively to equation 5.33, the Ottosen yield criterion including the hardening parameter may be written as:

$$f(\boldsymbol{\sigma},\tilde{\sigma}) = \left[\alpha J_2 + \tilde{\sigma}\left(\lambda\sqrt{J_2} + \beta I_1\right)\right]^{\frac{1}{2}} - \tilde{\sigma} \tag{5.34}$$

The stress tensor may be represented by the commonly referred engineering form, by a six component vector in the (x, y, z) coordinate system.

$$\boldsymbol{\sigma} = \{\sigma_x \ \sigma_y \ \sigma_z \ \tau_{yz} \ \tau_{xz} \ \tau_{xy}\} \tag{5.35}$$

The function adopted to define the hardening parameter is based on the law proposed by Comité Euro-international du Béton [1993] for uni-axial compression behavior of concrete (see fig. 5.6).

This curve is defined with respect to the compressive strain, ϵ_c, by two equations, one that is valid for compressive strains below $\epsilon_{c,lim}$, and the other for compressive strains exceeding $\epsilon_{c,lim}$. The expression that defines $\epsilon_{c,lim}$ is [Comité Euro-international du Béton, 1993]:

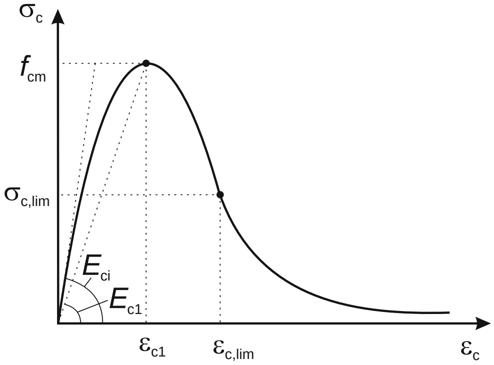

Figure 5.6: Hardening function for a concrete with $40MPa$ of compressive strength.

$$\frac{\epsilon_{c,lim}}{\epsilon_{c1}} = \frac{1}{2}\left(\frac{1}{2}\frac{E_{ci}}{E_{c1}}+1\right)\left[\frac{1}{4}\left(\frac{1}{2}\frac{E_{ci}}{E_{c1}}+1\right)^2-\frac{1}{2}\right]^{1/2} \tag{5.36}$$

Then, if $\epsilon_c < \epsilon_{c,lim}$:

$$\sigma_c = -\frac{\dfrac{E_{ci}}{E_{c1}}\dfrac{\epsilon_c}{\epsilon_{c1}}-\left(\dfrac{\epsilon_c}{\epsilon_{c1}}\right)^2}{1+\left(\dfrac{E_{ci}}{E_{c1}}-2\right)\dfrac{\epsilon_c}{\epsilon_{c1}}}f_{cm} \tag{5.37}$$

and if $\epsilon_c \geq \epsilon_{c,lim}$:

$$\sigma_c = \frac{-f_{cm}}{\left(\dfrac{1}{\dfrac{\epsilon_{c,lim}}{\epsilon_{c1}}}\xi-\dfrac{2}{\left(\dfrac{\epsilon_{c,lim}}{\epsilon_{c1}}\right)^2}\right)\left(\dfrac{\epsilon_c}{\epsilon_{c1}}\right)^2+\left(\dfrac{4}{\dfrac{\epsilon_{c,lim}}{\epsilon_{c1}}}-\xi\right)\dfrac{\epsilon_c}{\epsilon_{c1}}} \tag{5.38}$$

with :

$$\xi = \frac{4\left[\left(\frac{\epsilon_{c,lim}}{\epsilon_{c1}}\right)^2\left(\frac{E_{ci}}{E_{c1}}-2\right)+2\frac{\epsilon_{c,lim}}{\epsilon_{c1}}-\frac{E_{ci}}{E_{c1}}\right]}{\left[\frac{\epsilon_{c,lim}}{\epsilon_{c1}}\left(\frac{E_{ci}}{E_{c1}}-2\right)+1\right]^2} \tag{5.39}$$

Considering that the total axial deformation, ϵ_c is composed of the elastic, σ_c/E_c, and the plastic, $\widetilde{\epsilon_c}$, components, the hardening law may be obtained from the original uni-axial compression law by subtracting the elastic part from the total compressive strain, ϵ_c at each load level:

$$\widetilde{\epsilon_c} = \epsilon_c - \frac{\sigma_c}{E_{ci}} \tag{5.40}$$

The resulting hardening law (see Figure 5.7) is therefore constituted by two different polynomials, one of second-order that is valid for $\widetilde{\epsilon} < \widetilde{\epsilon}_{lim}$, and one of third-order that is valid for $\widetilde{\epsilon} < \widetilde{\epsilon}_{lim}$, merging both curves at the point $(\widetilde{\epsilon}_{lim}, \widetilde{\sigma}_{lim})$. As such:

$$\widetilde{\sigma}_{lim} = \sigma_{c,lim} = \frac{f_{cm}}{2} \tag{5.41}$$

$$\widetilde{\epsilon}_{lim} = \epsilon_{c,lim} - \frac{\sigma_{c,lim}}{E_{ci}} \tag{5.42}$$

The coefficient α defines the value of the initial value of the hardening function, $\widetilde{\sigma}_0$:

$$\widetilde{\sigma}_0 = \alpha f_{cm} \tag{5.43}$$

$$\tag{5.44}$$

The hardening modulus in compression, h, consists of the derivative of the hardening function, $\widetilde{\sigma}$, in each domain, with respect to the equivalent plastic strain, $\widetilde{\epsilon}$. As an example, in Figure 5.8 the hardening function and hardening modulus values are presented considering the typical values for concrete of $f_{cm} = 40$ MPa and $\epsilon_{c1} = 0.0022$. In addition, the uni-axial compressive behavior is considered as linear elastic until a compressive stress of 12 MPa is achieved. Therefore, $\alpha = 0.3$.

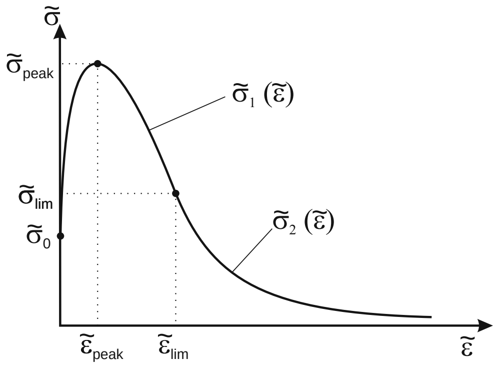

Figure 5.7: Hardening function derived from the Comité Euro-international du Béton [1993] uni-axial compression behavior law.

The parameters of the Ottosen yield function are essentially defined with respect to the uni-axial compressive and tensile strengths of the material. Implicit is the curve fitting that is carried out to obtain the coefficients of the equations of these parameters, that take into account the experimental results obtained for the bi-axial and the tri-axial compressive strengths [Ottosen, 1980; Chen, 1982]. For the present research, as recommended by the Comité Euro-international du Béton [1993] the uni-axial compressive and tensile strength medium values are used to calculate the values of all parameters, that is, f_{cm} and f_{ctm} respectively. The referred parameters, presented in equation 5.34, are described by the following equations [Comité Euro-international du Béton, 1993]:

$$\begin{aligned} \alpha &= \frac{1}{9K^{1.4}} \\ \beta &= \frac{1}{3.7K^{1.1}} \\ K &= \frac{f_{ctm}}{f_{cm}} \end{aligned} \tag{5.45}$$

and

$$\lambda = \begin{cases} c_1 \cos\left[\frac{\pi}{3} - \frac{1}{3}\arccos\left(-c_2\cos 3\theta\right)\right] & \text{for} \quad \cos 3\theta \leq 0 \ , \\ c_1 \cos\left[\frac{1}{3}\arccos\left(c_2\cos 3\theta\right)\right] & \text{for} \quad \cos 3\theta > 0 \ . \end{cases} \tag{5.46}$$

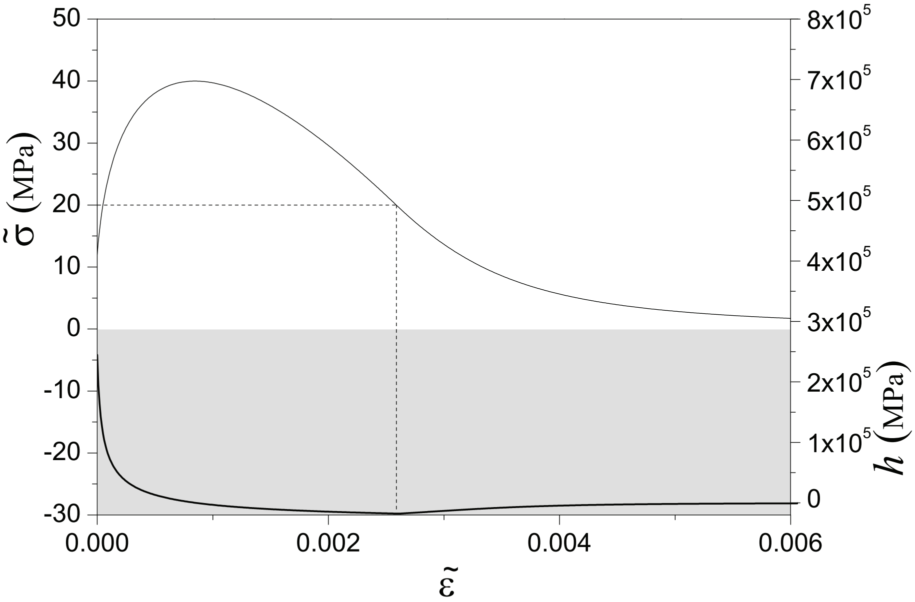

Figure 5.8: Hardening function, $\widetilde{\sigma}$, and hardening modulus, h, evolution as a function of the equivalent plastic strain, $\widetilde{\epsilon}$.

where,

$$\begin{aligned} c_1 &= \frac{1}{0.7K^{0.9}} \\ c_2 &= 1 - 6.8(K - 0.07)^2 \\ \cos 3\theta &= \frac{3\sqrt{3}}{2} \frac{J_3}{J_2^{\frac{3}{2}}} \end{aligned} \tag{5.47}$$

The I_1, J_2 and J_3 variables represent, respectively, the first, the second deviatoric and the third deviatoric stress invariants. The corresponding equations are, in the (x, y, z) coordinate system:

$$
\begin{aligned}
I_1 =& \sigma_{xx} + \sigma_{yy} + \sigma_{zz} \\
J_2 =& \frac{1}{3}\left(\sigma_x^2 + \sigma_y^2 + \sigma_z^2 - \sigma_x\sigma_y - \sigma_x\sigma_z - \sigma_y\sigma_z + 3\tau_{yz}^2 + 3\tau_{xz}^2 + 3\tau_{xy}^2\right) \\
J_3 =& \frac{2}{27}\left(\sigma_x^3 + \sigma_y^3 + \sigma_z^3\right) - \frac{1}{9}\left(\sigma_x^2\sigma_y + \sigma_x^2\sigma_z + \sigma_y^2\sigma_x + \sigma_y^2\sigma_z + \sigma_z^2\sigma_x + \sigma_z^2\sigma_y\right) + \\
& + \frac{4}{9}\sigma_x\sigma_y\sigma_z - \frac{2}{3}\left(\sigma_x\tau_{yz}^2 + \sigma_y\tau_{xz}^2 + \sigma_z\tau_{xy}^2\right) + \\
& + \frac{1}{3}\left(\sigma_x\tau_{xy}^2 + \sigma_x\tau_{xz}^2 + \sigma_y\tau_{xy}^2 + \sigma_y\tau_{yz}^2 + \sigma_z\tau_{xz}^2 + \sigma_z\tau_{yz}^2\right) + 2\tau_{yz}\tau_{xz}\tau_{xy}
\end{aligned} \tag{5.48}
$$

According to the principles of plasticity theory, the flux vector $\boldsymbol{a}$, which consists of the vector that is perpendicular to the yield surface, is composed of the six derivatives of the yield function with respect to each of the six stress components:

$$
\boldsymbol{a} = \left\{ \frac{\partial f(\boldsymbol{\sigma},\tilde{\sigma})}{\partial \sigma_x} \quad \frac{\partial f(\boldsymbol{\sigma},\tilde{\sigma})}{\partial \sigma_y} \quad \frac{\partial f(\boldsymbol{\sigma},\tilde{\sigma})}{\partial \sigma_z} \quad \frac{\partial f(\boldsymbol{\sigma},\tilde{\sigma})}{\partial \tau_{yz}} \quad \frac{\partial f(\boldsymbol{\sigma},\tilde{\sigma})}{\partial \tau_{xz}} \quad \frac{\partial f(\boldsymbol{\sigma},\tilde{\sigma})}{\partial \tau_{xy}} \right\} \tag{5.49}
$$

The equation that defines each of the six components of the flux vector $\boldsymbol{a}$ is the following:

$$
a_i = \frac{\partial f(\boldsymbol{\sigma},\tilde{\sigma})}{\partial \sigma_i} = \frac{\alpha\dfrac{\partial J_2}{\partial \sigma_i} + \tilde{\sigma}\left(\dfrac{\partial \lambda}{\partial \sigma_i}\sqrt{J_2} + \dfrac{1}{2}\lambda\ J_2^{-\frac{1}{2}}\ \dfrac{\partial J_2}{\partial \sigma_i} + \beta\dfrac{\partial I_1}{\partial \sigma_i}\right)}{2\left[\alpha J_2 + \tilde{\sigma}\left(\lambda\sqrt{J_2} + \beta I_1\right)\right]^{\frac{1}{2}}} \tag{5.50}
$$

The entire definition of the flux vector $\boldsymbol{a}$ entails the definition of the first derivatives of the λ parameter with respect to the stress components. It is also necessary to define the first derivatives of the stress invariants I_1 , J_2 and J_3. Further details about the derivatives of the λ parameter and of the stress invariants are included in Appendix A.

5.3.1 The Return-mapping Algorithm

The material nonlinear analysis by the finite element method (FEM) problem is resolved by establishing the system of equilibrium equations in the incremental form. In this fashion, the stress increment at the new load step $n+1$, $\Delta\boldsymbol{\sigma}_{n+1}$, is defined by the constitutive relation established also in the incremental form (eq.5.51). In this equation, $\boldsymbol{D}$ represents the constitutive matrix, and $\Delta\boldsymbol{\epsilon}_{n+1}$ and $\Delta\boldsymbol{\epsilon}_{n+1}^p$ represent, respectively, the total strain and the plastic strain increments within the load step $n+1$:

$$\Delta\boldsymbol{\sigma}_{n+1} = \boldsymbol{D}\left(\Delta\boldsymbol{\epsilon}_{n+1} - \Delta\boldsymbol{\epsilon}^{p}_{n+1}\right) \tag{5.51}$$

At the onset of the new load step, the total strain increment is known and given by the main FEM incremental-iterative algorithm used to solve the equilibrium equations. The plastic strain increment, however, is yet unknown, and the procedure used to determine the strain increment at the load step is, figuratively speaking, referred to as the *return to the yield surface*.

The implicit backward Euler algorithm is the most widely used method to return to the yield surface, essentially because it avoids the accumulation of errors during the approximation of the solution that is typical of other forward methods. The implicit backward Euler algorithm consists of finding a first approximation of the solution, the trial stress increment, assuming that the total strain increment is elastic. This first approximation to the solution assumes, therefore, that the plastic strain increment is null and the total plastic strain at the load step $n+1$ is the same as the one obtained in the previous load step, n. The hardening parameter is also assumed to have the value of the previous load step:

$$\begin{aligned}
\Delta\boldsymbol{\sigma}^{trial}_{n+1} &= \boldsymbol{D}\left(\Delta\boldsymbol{\epsilon}_{n+1} - \Delta\boldsymbol{\epsilon}^{p,\ trial}_{n+1}\right)\\
\boldsymbol{\sigma}^{trial}_{n+1} &= \boldsymbol{\sigma}_{n} + \Delta\boldsymbol{\sigma}^{trial}_{n+1}\\
\boldsymbol{\epsilon}^{p,\ trial}_{n+1} &= \boldsymbol{\epsilon}^{p}_{n}\\
\tilde{\sigma}^{trial}_{n+1} &= \tilde{\sigma}_{n}
\end{aligned} \tag{5.52}$$

Following these assumptions, the initial value of the yielding function is computed for the trial values of load step $n+1$:

$$f^{trial}_{n+1} = f^{trial}_{n+1}\left(\boldsymbol{\sigma}^{trial}_{n+1}\ ,\quad \tilde{\sigma}^{trial}_{n+1}\right) \tag{5.53}$$

Then, the two possible solutions determine the behavior of the material. If the yield function assumes a non-negative value, and reminding that only static loading is being considered, then the material enters the elasto-plastic regime:

$$\begin{cases}
\text{if}\ \ f^{trial}_{n+1} < 0 \quad \text{then} \quad \tilde{\sigma}_{n+1} = \tilde{\sigma}^{trial}_{n+1}\ \text{(elastic behaviour)}\ ,\\[2ex]
\text{if}\ \ f^{trial}_{n+1} \geq 0 \quad \text{then} \quad \tilde{\sigma}_{n+1} \neq \tilde{\sigma}^{trial}_{n+1}\ \text{(elasto-plastic behaviour)}\ .
\end{cases} \tag{5.54}$$

Whenever the material enters the elasto-plastic regime, the total plastic strains and the internal variables have to change. In this fashion, their new values for the load step $n+1$ may be computed as follows:

$$\begin{cases} \boldsymbol{\epsilon}^p_{n+1} = \boldsymbol{\epsilon}^p_n + \Delta\boldsymbol{\epsilon}^p_{n+1} \quad \text{with} \quad \Delta\boldsymbol{\epsilon}^p_{n+1} = \Delta\lambda_{n+1}\,\dfrac{\partial f_{n+1}}{\partial \boldsymbol{\sigma}_{n+1}}\ , \\ \\ \tilde{\epsilon}_{n+1} = \tilde{\epsilon}_n + \Delta\tilde{\epsilon}_{n+1} \quad \text{with} \quad \Delta\tilde{\epsilon}_{n+1} = -\Delta\lambda_{n+1}\,\dfrac{\partial f_{n+1}}{\partial \tilde{\sigma}_{n+1}}\ . \end{cases} \tag{5.55}$$

The first equation is derived from the flow rule, which determines that the plastic strain increment, $\boldsymbol{\epsilon}^p_{n+1}$, has the same direction as the flux vector, $\boldsymbol{a}$, if associated plasticity is considered. $\Delta\lambda_{n+1}$ is the plastic multiplier increment at the load step $n+1$, and must assume a non-negative value. In a thermodynamical framework, the second equation, or the evolution law, is derived from the second thermodynamical law, or dissipation inequality, assuming the convexity of the loading surface and that no thermal exchanges or viscous processes exist. For further details see Ristinmaa et al. [2007].

Once $\Delta\boldsymbol{\epsilon}^p_{n+1}$ is calculated, the final state of stress $\Delta\sigma_{n+1}$ corresponding to the load step $n+1$ may be computed as follows:

$$\boldsymbol{\sigma}_{n+1} = \boldsymbol{\sigma}^{trial}_{n+1} - \boldsymbol{D}\Delta\boldsymbol{\epsilon}^p_{n+1} \tag{5.56}$$

$$= \boldsymbol{\sigma}^{trial}_{n+1} - \Delta\lambda_{n+1}\,\boldsymbol{D}\frac{\partial f_{n+1}}{\partial \boldsymbol{\sigma}_{n+1}} \tag{5.57}$$

$$\tag{5.58}$$

The use of the backward Euler iteration scheme implies the need to determine the $\Delta\boldsymbol{\epsilon}^p_{n+1}$ and $\Delta\tilde{\epsilon}_{n+1}$ by an iterative procedure. Within this procedure, the aim is to minimize the residues $r^{(k)}_{f,\ n+1}, r^{(k)}_{\boldsymbol{\epsilon},\ n+1}$ and $r^{(k)}_{\tilde{\epsilon},\ n+1}$, expressed by the following equations:

$$\begin{aligned} r^{(k)}_{f,\ n+1} &= f^{(k)}_{n+1}\left(\boldsymbol{\sigma}^{(k)}_{n+1},\ \tilde{\sigma}^{(k)}_{n+1}\right) \\ r^{(k)}_{\boldsymbol{\epsilon},\ n+1} &= -\left(\boldsymbol{\epsilon}^p_{n+1}\right)^{(k)} + \boldsymbol{\epsilon}^p_n + \Delta\lambda^{(k)}_{n+1}\,\frac{\partial f^{(k)}_{n+1}}{\partial \boldsymbol{\sigma}^{(k)}_{n+1}} \\ r^{(k)}_{\tilde{\epsilon},\ n+1} &= -\left(\tilde{\epsilon}_{n+1}\right)^{(k)} + \tilde{\epsilon}_n - \Delta\lambda^{(k)}_{n+1}\,\frac{\partial f^{(k)}_{n+1}}{\partial \tilde{\sigma}^{(k)}_{n+1}} \end{aligned} \tag{5.59}$$

In each of these three equations, the k variable represents the iteration step within the iterative process to find the solutions of $\Delta\boldsymbol{\sigma}_{n+1}$, $\Delta\boldsymbol{\epsilon}^{p}_{n+1}$ and $\Delta\tilde{\epsilon}_{n+1}$ variables. These solutions lead to a simultaneous decrease of the $r_{f,\ n+1}$, $r_{\boldsymbol{\epsilon},\ n+1}$ and $r_{\tilde{\epsilon},\ n+1}$ residues below a predefined tolerance.

At the first step of the iterative procedure, ($k = 1$), the residues $r^{(k=1)}_{\boldsymbol{\epsilon},\ n+1}$ and $r^{(k=1)}_{\tilde{\epsilon},\ n+1}$ are null, and the residue $r^{(k=1)}_{f,\ n+1}$ is obtained from equation 5.60:

$$r^{(k=1)}_{f,\ n+1} = f^{(k=1)}_{n+1}\left(\boldsymbol{\sigma}^{trial}_{n+1},\ \tilde{\sigma}_{n}\right) \tag{5.60}$$

The use of the Newton-Raphson scheme for the solution of the system of three equations requires the linearization of the equations. By differentiating, one obtains:

$$\begin{aligned}
r^{(k)}_{f,\ n+1} + \frac{\partial f^{(k)}_{n+1}}{\partial \boldsymbol{\sigma}^{(k)}_{n+1}} d\boldsymbol{\sigma}^{(k+1)}_{n+1} + \frac{\partial f^{(k)}_{n+1}}{\partial \tilde{\sigma}^{(k)}_{n+1}}\, d\tilde{\sigma}^{(k+1)}_{n+1} &= 0\\
r^{(k)}_{\boldsymbol{\epsilon},\ n+1} - d\boldsymbol{\epsilon}^{p,\ (k+1)}_{n+1} + d\lambda^{(k+1)}_{n+1}\, \frac{\partial f^{(k)}_{n+1}}{\partial \boldsymbol{\sigma}^{(k)}_{n+1}} + \Delta\lambda^{(k)}_{n+1}\left[\frac{\partial^2 f^{(k)}_{n+1}}{\partial\left(\boldsymbol{\sigma}^{(k)}_{n+1}\right)^2} d\boldsymbol{\sigma}^{(k+1)}_{n+1} + \right.&\\
\left.\frac{\partial^2 f^{(k)}_{n+1}}{\partial \boldsymbol{\sigma}^{(k)}_{n+1}\ \partial \tilde{\sigma}^{(k)}_{n+1}}\ d\tilde{\sigma}^{(k+1)}_{n+1}\right] &= 0 \qquad (5.61)\\
r^{(k)}_{\tilde{\epsilon},\ n+1} - d\tilde{\epsilon}^{(k+1)}_{n+1} - d\lambda^{(k+1)}_{n+1}\, \frac{\partial f^{(k)}_{n+1}}{\partial \tilde{\sigma}^{(k)}_{n+1}} - \Delta\lambda^{(k)}_{n+1}\left[\frac{\partial^2 f^{(k)}_{n+1}}{\partial\left(\tilde{\sigma}^{(k)}_{n+1}\right)^2} d\tilde{\sigma}^{(k+1)}_{n+1} + \right.&\\
\left.\frac{\partial^2 f^{(k)}_{n+1}}{\partial \tilde{\sigma}^{(k)}_{n+1} \partial \boldsymbol{\sigma}^{(k)}_{n+1}} d\boldsymbol{\sigma}^{(k+1)}_{n+1}\right] &= 0
\end{aligned}$$

The first of these equations is also known as the consistency condition, and determines that, during plastic flow, the point representing the state of stress must remain on the yield surface. Another common way to represent the problem of minimization of the three residues is by constructing the Jacobian $\boldsymbol{J}$ and solving the following system of linear equations:

$$\boldsymbol{J}^{(k)}_{n+1} \begin{bmatrix} d\boldsymbol{\sigma}^{(k+1)}_{n+1} \\ d\tilde{\epsilon}^{(k+1)}_{n+1} \\ d\lambda^{(k+1)}_{n+1} \end{bmatrix} = \begin{bmatrix} -r^{(k)}_{f,\ n+1} \\ -r^{(k)}_{\boldsymbol{\epsilon},\ n+1} \\ -r^{(k)}_{\tilde{\epsilon},\ n+1} \end{bmatrix} \tag{5.62}$$

The process of returning to the yield surface for a prescribed generic strain increment at the load step $n+1$ is illustrated in Figure 5.9. As shown, the path followed to return to the yield surface is orthogonal, at each increment, to the tentative final solution, in contrast to other forward solution algorithms. The error $e^{(k)}$ at each iteration decreases until the final solution is found, for which $f_{n+1} = 0$.

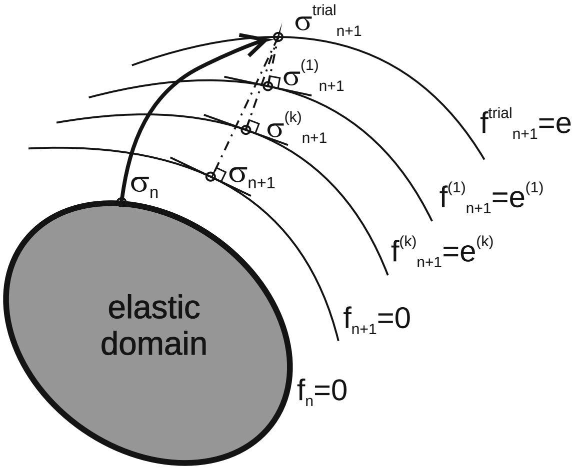

Figure 5.9: Schematic representation of the backward Euler iteration scheme, utilized to return to the yield surface and find the solution for an elasto-plastic strain increment.

In the present case, the Jacobian may be represented by the following matrix:

$$\boldsymbol{J}_{n+1}^{(k)} = \begin{bmatrix} \dfrac{\partial F_1}{\partial \boldsymbol{\sigma}_{n+1}} & \dfrac{\partial F_1}{\partial \tilde{\epsilon}_{n+1}} & \dfrac{\partial F_1}{\partial \lambda_{n+1}} \\[2ex] \dfrac{\partial F_2}{\partial \boldsymbol{\sigma}_{n+1}} & \dfrac{\partial F_2}{\partial \tilde{\epsilon}_{n+1}} & \dfrac{\partial F_2}{\partial \lambda_{n+1}} \\[2ex] \dfrac{\partial F_3}{\partial \boldsymbol{\sigma}_{n+1}} & \dfrac{\partial F_3}{\partial \tilde{\epsilon}_{n+1}} & \dfrac{\partial F_3}{\partial \lambda_{n+1}} \end{bmatrix}^{(k)}$$

The functions F_1, F_2 and F_3 are extracted from the equations of the residues

$r^{(k)}_{f,\ n+1}$, $r^{(k)}_{\boldsymbol{\epsilon},\ n+1}$ and $r^{(k)}_{\tilde{\epsilon},\ n+1}$ (eqs.(5.63)). They may be expressed as follows:

$$
\begin{aligned}
F_1^{(k)} &= f_{n+1}^{(k)}\left(\boldsymbol{\sigma}_{n+1}^{(k)},\ \tilde{\sigma}_{n+1}^{(k)}\right)\\
F_2^{(k)} &= \boldsymbol{D}^{-1}\Delta\boldsymbol{\sigma}_{n+1}^{(k)} + \Delta\lambda_{n+1}^{(k)}\ \frac{\partial f_{n+1}^{(k)}}{\partial \boldsymbol{\sigma}_{n+1}^{(k)}}\\
F_3^{(k)} &= -\Delta\tilde{\epsilon}_{n+1}^{(k)} - \Delta\lambda_{n+1}^{(k)}\ \frac{\partial f_{n+1}^{(k)}}{\partial \tilde{\sigma}_{n+1}^{(k)}}
\end{aligned}
\tag{5.63}
$$

In eq.(5.63), the term ' $-\left(\tilde{\epsilon}^p_{n+1}\right)^{(k)} + \tilde{\epsilon}^p_n$ ' was replaced by ' $-\Delta\tilde{\epsilon}^{(k)}_{n+1}$ '. In eq.(5.63), the term ' $-\left(\boldsymbol{\epsilon}^p_{n+1}\right)^{(k)} + \boldsymbol{\epsilon}^p_n$ ' was replaced by ' $\boldsymbol{D}^{-1}\Delta\boldsymbol{\sigma}^{(k)}_{n+1}$ ', and the equivalence of both terms is further explained. According to the flow rule, the plastic strain vector at the load step '$n+1$' may be defined on the basis of the plastic strain of the former load step, 'n', by the equation:

$$
\boldsymbol{\epsilon}^p_{n+1} = \boldsymbol{\epsilon}^p_n + \Delta\boldsymbol{\epsilon}^p_{n+1}\ , \tag{5.64}
$$

with the term $\Delta\boldsymbol{\epsilon}^p_{n+1}$ being defined by the equation already described in the previous section:

$$
\Delta\boldsymbol{\epsilon}^p_{n+1} = \Delta\lambda_{n+1}\ \frac{\partial f_{n+1}}{\partial \boldsymbol{\sigma}_{n+1}} \tag{5.65}
$$

Once the plastic strains $\boldsymbol{\epsilon}^p_{n+1}$ are known, the final stresses of the corresponding load step may be computed from the equation:

$$
\boldsymbol{\sigma}_{n+1} = \boldsymbol{\sigma}^{trial}_{n+1} - \boldsymbol{D}\Delta\boldsymbol{\epsilon}^p_{n+1}\ , \tag{5.66}
$$

which may be combined with eq(5.65) to yield:

$$
\boldsymbol{\sigma}_{n+1} - \boldsymbol{\sigma}^{trial}_{n+1} + \Delta\lambda_{n+1}\ \boldsymbol{D}\ \frac{\partial f_{n+1}}{\partial \boldsymbol{\sigma}_{n+1}} = 0\ , \tag{5.67}
$$

rearranging, and adopting the incremental form, yields:

$$
r^{(k)}_{\boldsymbol{\epsilon},\ n+1} = \boldsymbol{D}^{-1}\left(\boldsymbol{\sigma}^{(k)}_{n+1} - \boldsymbol{\sigma}^{trial}_{n+1}\right) + \Delta\lambda^{(k)}_{n+1}\ \frac{\partial f^{(k)}_{n+1}}{\partial \boldsymbol{\sigma}^{(k)}_{n+1}} \tag{5.68}
$$

Finally, the converged values of the unknowns at the step $n{+}1$ are obtained trough the successive summation of the increments determined at each iteration from the linear system of eqs.(5.62), that is:

$$\begin{aligned} \boldsymbol{\sigma}_{n+1}^{(k)} &= \boldsymbol{\sigma}_n + \sum_{i=1}^{k} d\boldsymbol{\sigma}_{n+1}^{(i)} \\ \tilde{\epsilon}_{n+1}^{(k)} &= \tilde{\epsilon}_n + \sum_{i=1}^{k} d\tilde{\epsilon}_{n+1}^{(i)} \\ \Delta\lambda_{n+1}^{(k)} &= \sum_{i=1}^{k} d\lambda_{n+1}^{(i)} \end{aligned} \tag{5.69}$$

5.3.2 First and second order derivatives

The implementation of the equations described previously requires the definition of all the first and the second order derivatives, namely:

- the remaining first order derivatives of the functions F_1, F_2 and F_3 with respect to the stress vector $\boldsymbol{\sigma}$, to the equivalent plastic strain $\tilde{\epsilon}$, and to the plastic multiplier λ;

- the fist order derivative of the loading function f with respect to the hardening parameter, $\tilde{\sigma}$;

- the second order derivatives of the loading function f, of the Ottosen lambda parameter and of the stress tensor invariants (I_1, J_2 and J_3) with respect to the stress vector $\boldsymbol{\sigma}$, and to the hardening function $\tilde{\sigma}$.

The derivation of these functions is included in the Appendix A.

5.3.3 The Consistent Tangent Elasto-plastic Constitutive Matrix

The integration of the FEM equilibrium equations within the Newton-Raphson incremental-iterative algorithm framework is typically carried out using the so-called consistent tangent constitutive matrix. The predicted initial solution is more close to the final solution, therefore this procedure contributes to a faster convergence of the algorithm to the equilibrium solution of the combination increment Simo and Hughes [1988]. For this purpose, the equations in which the derivation of the tangent constitutive matrix is based are the yield function, as a function of the stress vector and the hardening parameter,

$$f_{n+1} = f_{n+1}(\boldsymbol{\sigma}, \tilde{\sigma}) \ , \tag{5.70}$$

the constitutive equation, in the incremental form:

$$\Delta\boldsymbol{\sigma}_{n+1} = \boldsymbol{D}\left(\Delta\boldsymbol{\epsilon}_{n+1} - \Delta\boldsymbol{\epsilon}^{p}_{n+1}\right) \ , \tag{5.71}$$

the flow rule:

$$\Delta\boldsymbol{\epsilon}^{p}_{n+1} = \Delta\lambda_{n+1} \, \frac{\partial f_{n+1}}{\partial \boldsymbol{\sigma}_{n+1}} \ , \tag{5.72}$$

and the evolution law:

$$\Delta\tilde{\epsilon}_{n+1} = -\Delta\lambda_{n+1} \, \frac{\partial f_{n+1}}{\partial \tilde{\sigma}_{n+1}} \ . \tag{5.73}$$

To avoid the extensive exposition in the present chapter, the derivation of the consistent tangent elasto-plastic constitutive matrix for the general return-mapping algorithm is included in the Appendix A. The final equation is given, in a condensed expression, by:

$$d\boldsymbol{\sigma}_{n+1} = \left(\boldsymbol{H} - \sum_{i=1}^{2}\sum_{i=1}^{2} a_{ij} \ \boldsymbol{c}_i \boldsymbol{c}_j\right) d\boldsymbol{\epsilon}_{n+1} \tag{5.74}$$

with:

$$\boldsymbol{H} = \left(\boldsymbol{D}^{-1} + \Delta\lambda_{n+1} \frac{\partial^2 f_{n+1}}{\partial \boldsymbol{\sigma}^2_{n+1}} \right)^{-1} \tag{5.75}$$

and (see Appendix A for further details):

$$\boldsymbol{D}_{ep} = \boldsymbol{H} - \sum_{i=1}^{2} \sum_{i=1}^{2} a_{ij} \; \boldsymbol{c}_i \boldsymbol{c}_j \; , \tag{5.76}$$

The elasto-plastic constitutive matrix, $\boldsymbol{D}_{ep}$, coincides with the elastic constitutive matrix when the behavior remains elastic, as it can be demonstrated by substituting, in the previous equations (see Appendix A), the $\Delta\lambda_{n+1}$ parameter by 0.

Despite formally appealing and theoretically much more efficient (e.g. quadratic convergence within the Newton-Raphson incremental-iterative procedure), the derived consistent tangent elasto-plastic matrix is considerably more difficult to determine and numerically more demanding, with increased risk of instability mainly associated with the loss of non-singularity when the material enters the softening stage. Alternatively, in the cases where a simpler procedure is preferred, the more common form of the consistent tangent constitutive matrix can be determined. With this procedure, however, quadratic convergence is not guaranteed. Further details are included in Appendix A.

5.4 Numerical model response in compression

In figure 5.10 the deviatoric plane of the loading surface is depicted for two distinct levels of the hydrostatic stress. The type of concrete considered has a compressive strength of 40 MPa. In the first diagram, the Figure 5.10(a), the trace of the loading surfaces in the deviatoric plane are shown when the hardening parameter assumes the values of 10, 20, 30 and 40 MPa. The deviatoric plane is determined for a hydrostatic stress of 10% of the compressive strength, what may be considered as a low value. In the second diagram, the Figure 5.10(b), the trace of the loading surfaces in the deviatoric plane is shown for the same values of the hardening parameter, 10, 20, 30 and 40 MPa. In this case the deviatoric plane is obtained for a hydrostatic stress 10 times higher than the compressive strength, and may be considered as a high value of the normalized hydrostatic pressure.

In eq.(5.34) the effect of the hardening parameter on the expansion or contraction of the loading surface is not explicitly defined. In fact, the equation of this loading surface does not follow the typical form of isotropic loading surfaces, where the hardening parameter effect on the expansion or contraction of the loading surface is explicit Odqvist [1933] (*in* Jirásek and Bažant [2001]):

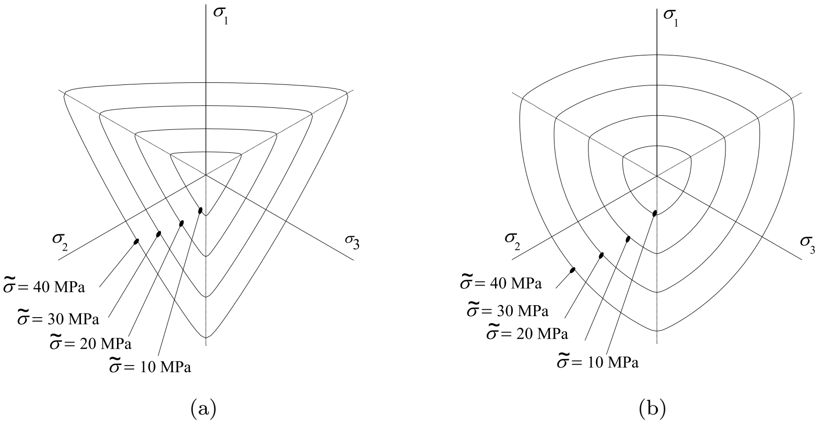

Figure 5.10: Representation of the loading function in the Haigh-Westergaard stress space, for concrete of $f_c = 40$ MPa. Deviatoric planes for hardening parameter values of 10, 20, 30 and 40 MPa: (a) for low hydrostatic stress ($I_1/f_c = 0.1$) and (b) high hydrostatic stress ($I_1/f_c = 10.0$).

$$f(\boldsymbol{\sigma}, \tilde{\sigma}) = F(\boldsymbol{\sigma}) - \tilde{\sigma} \tag{5.77}$$

It may be observed from figures 5.10, however, that the different loading surfaces are self-similar with respect to the origin, as demonstrated by the essentially parallel deviatoric curves obtained for both low and high hydrostatic pressure levels.

The elasto-plastic model above described was implemented in a Finite Element Method based software called FEMIX [Sena-Cruz et al., 2007]. The 8-node cubic element with 4 integration points was used to assess the numerical model response in uni-axial and bi-axial compressive tests. The elastic stage of the material behavior was reduced to only 10% of the ultimate strength in uni-axial compression ($0.1f_{cm}$).

To simulate the uni-axial compression test, the procedure consisted on prescribing a constant displacement increment in the direction of x_3. Both cube faces perpendicular to x_1 and x_2 were kept free. In the case of the bi-axial test, similar displacement increments were prescribed in x_3 and x_2, while the cube faces perpendicular to x_1 were kept free.

The behavior of concrete when submitted to tri-axial states of stress was investigated by several researchers (see for example Kupfer et al. [1969]; van Mier [1997]; Grassl et al. [2002]; Papanikolaou and Kappos [2007]). For reference, the experimental results obtained by Kupfer et al. [1969] for a concrete with a compressive strength $f_c = 32.06MPa$ and by Hussein and Marzouk [2000] for a concrete with a compressive strength $f_c = 96.0MPa$ are selected as representatives of, respectively, a moderate strength concrete and a high strength concrete. In Figure 5.11 the stress-strain results obtained for the uni-axial and bi-axial tests are shown and compared with the experimental results obtained by Kupfer et al. [1969]. In Figure 5.12 the stress-strain results obtained for the uni-axial and bi-axial tests are shown and compared with the experimental results obtained by Hussein and Marzouk [2000].

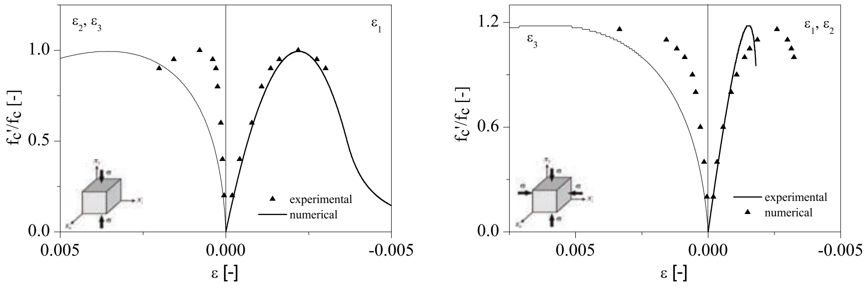

(a) (b)

Figure 5.11: Compressive strain-normalized stress numerical response compared with the experimental results of Kupfer et al. [1969] considering the (a) uni-axial and (b) equibi-axial compression tests.

In the case of the moderate-strength concrete, the uni-axial stress-strain curve is almost identical to the results obtained by Kupfer et al. [1969].When comparing the numerical and experimental results in the case of the high strength concrete, the numerical response is somewhat more brittle and does not follow entirely the experimental results up to the peak. Probably this is due to the difficulty of the hardening function, which is defined based on the uni-axial compressive law for concrete by Comité Euro-international du Béton [1993], to fit the uni-axial experimental results. In particular, the results presented by Hussein and Marzouk [2000] indicate that the compressive strain at the peak compressive stress is 0.0033, which is significantly higher than the prescription of the Comité Euro-international du Béton [1993] for the compressive strain at peak of about 0.0022, or even the more recent value of 0.0028 [Fédération International du Béton, 2010].

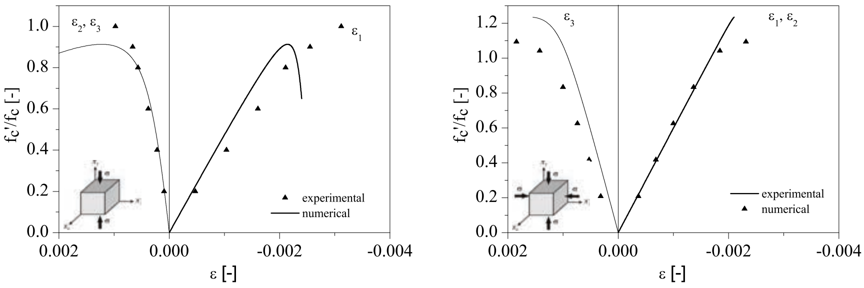

(a) (b)

Figure 5.12: Compressive strain-normalized stress numerical response compared with the experimental results of Hussein and Marzouk [2000] considering the (a) uni-axial and (b) equibi-axial compression tests.

In the case of the bi-axial compression, the results obtained are somewhat more brittle than expected, when comparing these with the experimental results. The relation between the peak stress in the bi-axial and the uni-axial compression tests are close, however, to the values obtained experimentally. In the present case, the value obtained was of 1.185. In fact this value may change with the concrete strength, as suggested by Papanikolaou and Kappos [2007].

In Figure 5.13 the results obtained in terms of the volumetric strains are compared to the experiments for both types of concrete.

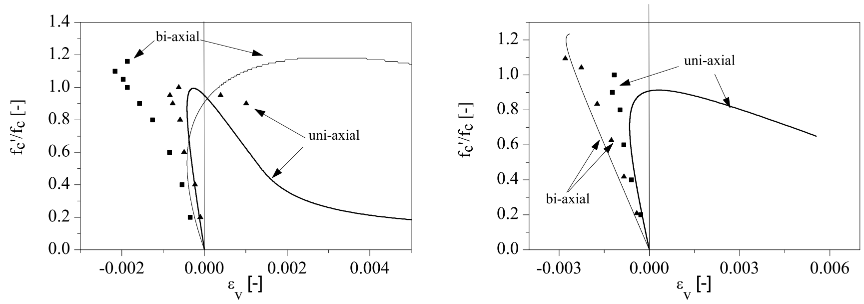

(a) (b)

Figure 5.13: Volumetric strain-normalized stress numerical response compared with the experimental results of (a) Kupfer et al. [1969] and (b) Hussein and Marzouk [2000].

The results of figure 5.13 show that the experimentally observed behavior of the material in terms of volume change is approximately captured, with an initial decrease in volumetric strain, followed by a gradual increase that becomes more pronounced for higher load values and during softening. These volumetric changes are more pronounced in the bi-axial test, in agreement with the experimentally observed. It seems, however, that the obtained values are somewhat underestimated, since experimental results indicate a more significant decrease of volumetric strain during hardening. Probably this difference could be attenuated by altering the load at which the behavior shifts from elastic to plastic, since the volumetric deformation becomes clearly more significant after plastic flow is initiated.

5.5 Model implementation considering two hardening parameters

The shape of the trace of Ottosen yield surface on the deviatoric plane is determined by the coefficient K, or the ratio between the tensile and compressive strengths (eq. 5.45). Originally the Ottosen yield function was developed to estimate concrete failure, under generic tri-axial states of stress, therefore it is not natural to consider that K may change during loading, particularly during plastic flow. Considering the hypothesis of utilizing the Ottosen yield function to simultate hardening both in compression and in tension, the ratio between the equivalent strength in tension and in compression will change during plastic flow. Therefore, the idea of using the coefficient K to simulate the possibility of having both tensile and compressive hardening merged into a single yield curve is very attractive, both formally and for practical reasons. In this context, K is redefined to become the ratio between the hardening parameters in tension, $\widetilde{\sigma_t}$, and in compression, $\widetilde{\sigma_c}$:

$$K\left(\widetilde{\sigma_t}, \widetilde{\sigma_c}\right) = \frac{\widetilde{\sigma_t}}{\widetilde{\sigma_c}} \tag{5.78}$$

The hardening function in compression remains the same, as presented in the previous section. The hardening function in tension is defined considering the tensile stress-strain results obtained in Chapter 2 using dogbone specimens (Figure 5.14). The tensile behavior is approximated to a bi-linear tensile stress-strain relationship until the ultimate tensile stress, σ_{tu}, is reached at a tensile strain ϵ_{tu}. The tensile behavior is elastic until the initial cracking tensile stress, σ_{t0}, is reached at a tensile strain ϵ_{t0}. The Young's modulus in the elastic part, E_{ti}, is assumed as equal to the Young's modulus in compression, E_{ci}.

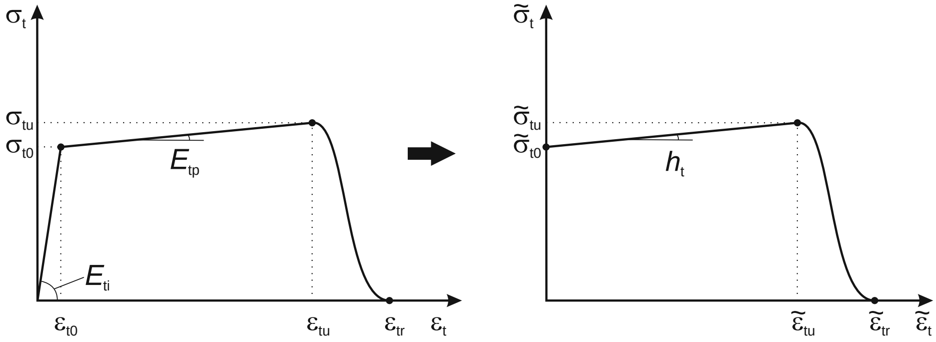

Figure 5.14: Schematic representation of the tensile stress-strain response obtained from uni-axial tensile testing, and corresponding hardening function in tension.

The hardening function in tension, $\widetilde{\sigma}_t\left(\widetilde{\epsilon}_t\right)$, is obtained from the tensile stress-strain relationship following the same procedure as previously described for the hardening function in compression. The hardening parameter in tension, $\widetilde{\sigma}_t$, is defined as a function of the equivalent plastic strain in tension by assuming the following relationship between the uni-axial tensile strain, ϵ_t, and the equivalent tensile strain, $\widetilde{\epsilon}_t$:

$$\widetilde{\epsilon}_t = \epsilon_t - \frac{\sigma_t}{E_{ti}} \tag{5.79}$$

The hardening function in tension is defined by two distinct equations. For $\widetilde{\sigma}_t < \widetilde{\sigma}_{tu}$, the hardening function is described by the equation:

$$\widetilde{\sigma}_{t1} = \frac{\sigma_{t0} + \left(\widetilde{\epsilon}_t - \dfrac{\sigma_{t0}}{E_{ti}}\right) E_{tp}}{1 - \dfrac{E_{tp}}{E_{ti}}} \tag{5.80}$$

with:

$$E_{tp} = \frac{\sigma_{tu} - \sigma_{t0}}{\epsilon_{tu} - \epsilon_{t0}} \tag{5.81}$$

and the hardening modulus, h_{t1}, is described by the following equation:

$$h_{t1} = \frac{E_{tp}}{1 - \dfrac{E_{tp}}{E_{ti}}} \tag{5.82}$$

For $\widetilde{\sigma}_t \geq \widetilde{\sigma}_{tu}$ the material enters the softening regime and the equation that describes this portion of the hardening function in tension is a spline. The initial inclination of the spline, at σ_{tu}, is equal to h_{t1}, and the final inclination is zero. The residual value of the equivalent tensile stress, $\widetilde{\epsilon}_{tr}$ is defined with respect to $\widetilde{\epsilon}_{tu}$, and typically assumed as 0.3. Further details about the equations defining $\widetilde{\sigma}_{t2}$ and h_{t2} may be found at [Pereira et al., 2012]

The return-mapping algorithm presented previously in section 5.3.1 must be altered to consider the possibility of the occurrence of hardening both in tension and in compression. In the general case of a tri-axial loading configuration, hardening can occur exclusively in tension, in compression or both in tension and in compression. Therefore it is necessary to define the contribution of each hardening parameter in the overall plastic flow process. One way to tackle this problem is to define the increment of each hardening parameter at a certain load step with a weight factor, based on the principal stress components [Lee and Fenves, 1998]. Essentially, the concept consists on considering that the increments of each hardening variable, that is, the equivalent plastic strains in compression and in tension, are proportional to the weight of the maximum compressive and tensile principal stresses respectively, at a certain load step. Therefore, the evolution law previously adopted (eq. 5.55) is replaced by the new equation:

$$\begin{bmatrix} \Delta\widetilde{\epsilon}_{t,n+1} \\ \Delta\widetilde{\epsilon}_{c,n+1} \end{bmatrix} = \begin{bmatrix} 0 & 0 & r\left(\widehat{\boldsymbol{\sigma}}_{n+1}\right) & 0 & 0 & 0 \\ -\left(1 - r\left(\widehat{\boldsymbol{\sigma}}_{n+1}\right)\right) & 0 & 0 & 0 & 0 & 0 \end{bmatrix} \Delta\widehat{\boldsymbol{\epsilon}}^{p}_{n+1} \tag{5.83}$$

where $\widehat{\boldsymbol{\sigma}}_{n+1}$ is the vector that contains the three eigenvalues of the stress tensor in ascending order, and $\Delta\widehat{\boldsymbol{\epsilon}}^{p}_{n+1}$ is the vector that contains the three eigenvalues of the plastic strain increment tensor, also in ascending order, both at the load step $n+1$. As previously discussed, it is convenient to describe the evolution law as a function of the stress increment at the load step $n+1$, therefore:

$$\begin{aligned} \Delta\widehat{\boldsymbol{\epsilon}}^{p}_{n+1} &= \boldsymbol{A}_{\epsilon}\Delta\boldsymbol{\epsilon}^{p}_{n+1} \\ &= -\boldsymbol{A}_{\boldsymbol{\epsilon}}\left(\boldsymbol{D}_{\boldsymbol{e}}\right)^{-1}\Delta\boldsymbol{\sigma}_{n+1} \end{aligned} \tag{5.84}$$

where $\boldsymbol{A}_\epsilon$ represents the transformation matrix of the plastic strain increment vector from (x, y, z) to the principal stress directions [Pereira et al., 2012].

The weight factor r is a scalar quantity, such that $0 \leq r \leq 1$, and is defined as [Lee and Fenves, 1998]:

$$r\left(\widehat{\boldsymbol{\sigma}}_{n+1}\right) = \begin{cases} 0 & \text{if } \Delta\boldsymbol{\sigma}_{n+1} = 0 \\ \dfrac{\displaystyle\sum_{i=1}^{3} \langle \widehat{\sigma}_i \rangle}{\displaystyle\sum_{i=1}^{3} |\widehat{\sigma}_i|} & \text{otherwise} \end{cases} \tag{5.85}$$

where $\langle x \rangle$ denotes the Macaulay bracket function:

$$\langle x \rangle = \frac{|x| + x}{2} \tag{5.86}$$

As in previous equations, r may also be defined as a function of the stress vector, by assuming that:

$$\widehat{\boldsymbol{\sigma}}_{n+1} = \boldsymbol{A}_\sigma \ \boldsymbol{\sigma}_{n+1} \tag{5.87}$$

where $\boldsymbol{A}_\sigma$ represents the transformation matrix of the stress vector at load step $n+1$ from (x, y, z) to the principal stress directions.

Lastly, the new evolution law presented in eq. 5.84 can be integrated in the return-mapping algorithm, and the system of equations to solve will be:

$$\boldsymbol{J}_{n+1}^{(k)} \begin{bmatrix} d\boldsymbol{\sigma}_{n+1}^{(k+1)} \\ d\tilde{\epsilon}_{c,n+1}^{(k+1)} \\ d\tilde{\epsilon}_{t,n+1}^{(k+1)} \\ d\lambda_{n+1}^{(k+1)} \end{bmatrix} = \begin{bmatrix} -r_{f,\ n+1}^{(k)} \\ -r_{\boldsymbol{\epsilon},\ n+1}^{(k)} \\ -r_{\tilde{\epsilon}_t,\ n+1}^{(k)} \\ -r_{\tilde{\epsilon}_c,\ n+1}^{(k)} \end{bmatrix} \tag{5.88}$$

with:

$$\boldsymbol{J}_{n+1}^{(k)} = \begin{bmatrix} \dfrac{\partial F_1}{\partial \boldsymbol{\sigma}_{n+1}} & \dfrac{\partial F_1}{\partial \tilde{\epsilon}_{t,n+1}} & \dfrac{\partial F_1}{\partial \tilde{\epsilon}_{c,n+1}} & \dfrac{\partial F_1}{\partial \lambda_{n+1}} \\ \dfrac{\partial F_2}{\partial \boldsymbol{\sigma}_{n+1}} & \dfrac{\partial F_2}{\partial \tilde{\epsilon}_{t,n+1}} & \dfrac{\partial F_2}{\partial \tilde{\epsilon}_{c,n+1}} & \dfrac{\partial F_2}{\partial \lambda_{n+1}} \\ \dfrac{\partial F_3}{\partial \boldsymbol{\sigma}_{n+1}} & \dfrac{\partial F_3}{\partial \tilde{\epsilon}_{t,n+1}} & \dfrac{\partial F_3}{\partial \tilde{\epsilon}_{c,n+1}} & \dfrac{\partial F_3}{\partial \lambda_{n+1}} \\ \dfrac{\partial F_4}{\partial \boldsymbol{\sigma}_{n+1}} & \dfrac{\partial F_4}{\partial \tilde{\epsilon}_{t,n+1}} & \dfrac{\partial F_4}{\partial \tilde{\epsilon}_{c,n+1}} & \dfrac{\partial F_4}{\partial \lambda_{n+1}} \end{bmatrix}^{(k)}$$

and:

$$\begin{aligned} F_1^{(k)} &= f_{n+1}^{(k)}\left(\boldsymbol{\sigma}_{n+1}^{(k)},\ \tilde{\sigma}_{t,n+1}^{(k)},\ \tilde{\sigma}_{c,n+1}^{(k)}\right) \\ F_2^{(k)} &= \boldsymbol{D}^{-1}\Delta\boldsymbol{\sigma}_{n+1}^{(k)} + \Delta\lambda_{n+1}^{(k)}\ \frac{\partial f_{n+1}^{(k)}}{\partial \boldsymbol{\sigma}_{n+1}^{(k)}} \\ F_3^{(k)} &= -\Delta\tilde{\epsilon}_{t,n+1}^{(k)} - \widehat{\boldsymbol{h}}_t\left(\widehat{\boldsymbol{\sigma}}_{n+1}^{(k)}\right)\ \boldsymbol{A}_\epsilon\ \boldsymbol{D}^{-1}\ \Delta\boldsymbol{\sigma}_{n+1}^{(k)} \\ F_4^{(k)} &= -\Delta\tilde{\epsilon}_{c,n+1}^{(k)} - \widehat{\boldsymbol{h}}_c\left(\widehat{\boldsymbol{\sigma}}_{n+1}^{(k)}\right)\ \boldsymbol{A}_\epsilon\ \boldsymbol{D}^{-1}\ \Delta\boldsymbol{\sigma}_{n+1}^{(k)} \end{aligned} \tag{5.89}$$

with:

$$\begin{bmatrix} \widehat{\boldsymbol{h}}_t\left(\widehat{\boldsymbol{\sigma}}_{n+1}^{(k)}\right) \\ \widehat{\boldsymbol{h}}_c\left(\widehat{\boldsymbol{\sigma}}_{n+1}^{(k)}\right) \end{bmatrix} = \begin{bmatrix} 0 & 0 & r\left(\widehat{\boldsymbol{\sigma}}_{n+1}^{(k)}\right) & 0 & 0 & 0 \\ -\left(1 - r\left(\widehat{\boldsymbol{\sigma}}_{n+1}^{(k)}\right)\right) & 0 & 0 & 0 & 0 & 0 \end{bmatrix} \tag{5.90}$$

The residues at each iteration are defined by:

$$\begin{aligned} r_{f,\ n+1}^{(k)} &= f_{n+1}^{(k)}\left(\boldsymbol{\sigma}_{n+1}^{(k)},\ \tilde{\sigma}_{t,n+1}^{(k)},\ \tilde{\sigma}_{c,n+1}^{(k)}\right) \\ r_{\boldsymbol{\epsilon},\ n+1}^{(k)} &= -\left(\boldsymbol{\epsilon}_{n+1}^{p}\right)^{(k)} + \boldsymbol{\epsilon}_{n}^{p} + \Delta\lambda_{n+1}^{(k)}\ \frac{\partial f_{n+1}^{(k)}}{\partial \boldsymbol{\sigma}_{n+1}^{(k)}} \\ r_{\tilde{\epsilon}_t,\ n+1}^{(k)} &= -\left(\tilde{\epsilon}_{t,n+1}\right)^{(k)} + \tilde{\epsilon}_{t,n} - \widehat{\boldsymbol{h}}_t\left(\widehat{\boldsymbol{\sigma}}_{n+1}^{(k)}\right)\ \boldsymbol{A}_\epsilon\ \boldsymbol{D}^{-1}\ \Delta\boldsymbol{\sigma}_{n+1}^{(k)} \\ r_{\tilde{\epsilon}_c,\ n+1}^{(k)} &= -\left(\tilde{\epsilon}_{c,n+1}\right)^{(k)} + \tilde{\epsilon}_{c,n} - \widehat{\boldsymbol{h}}_c\left(\widehat{\boldsymbol{\sigma}}_{n+1}^{(k)}\right)\ \boldsymbol{A}_\epsilon\ \boldsymbol{D}^{-1}\ \Delta\boldsymbol{\sigma}_{n+1}^{(k)} \end{aligned} \tag{5.91}$$

The first and second order derivatives of the aforementioned functions with respect to the hardening parameters in tension and in compression were derived, considering the equation 5.78 and adapting the equations derived for the single hardening parameter case (see Appendix 1). A detailed description of these equations may be found at [Pereira et al., 2012].

5.6 Numerical model response in compression and in tension

To understand the behavior of the implemented two-hardening parameter model, let us start by analyzing the behavior of the yield surface for the plane stress case. Considering that $\sigma_3 = 0$, and that the stress states will be represented on the principal stress space σ_1, σ_2, the loading surfaces obtained considering that hardening in compression is occuring are presented in Figure 5.15. The evolution of hardening in compression seems to comply with the requirements, mostly that the tensile quadrant remains unchanged while the compressive quadrant expands. Although the shape of the surface is altered during the expansion, this change does not seem to be significant and the yielding curve remains smooth and convex. However, in a closer observation it can be identified a slight distortion of the shape of the curve and a change of the uni-axial compressive stress while the yield surface expands. For example, the yielding curve obtained when the hardening parameter in compression is 60 MPa intersects the (σ_1) at a slightly lower value than 60 MPa.

Let us now consider a variation of the hardening parameter in tension, while the hardening parameter in compression is kept unchanged. In Figure 5.16 the yielding function is represented for two distinct values of the hardening parameter in compression, $\widetilde{\sigma}_c = 30$MPa and $\widetilde{\sigma}_c = 60$MPa. For each of these two yielding curves the hardening parameter in tension will be altered from $\widetilde{\sigma}_t = 4$ MPa to $\widetilde{\sigma}_t = 3$ MPa and $\widetilde{\sigma}_t = 5$ MPa. Considering the magnitude of the tensile stresses typically encountered in SHCC materials, this range of values for the present evaluation is sufficient.

As shown in Figure 5.16, the movement of the yielding curve in the direction of the tensile stress quadrant affects the shape of the yielding curve in the compression quadrant. For lower values of the hardening parameter ($f'_c = 30$ MPa) this effect is not significant, and the yielding stress in uni-axial compression remains unchanged. However, for higher values of the hardening parameter ($f'_c = 60$ MPa), the slight change of the hardening parameter in tension affects and alters the yielding curve shape. For example, when the hardening parameter in tension is moved from 4 MPa

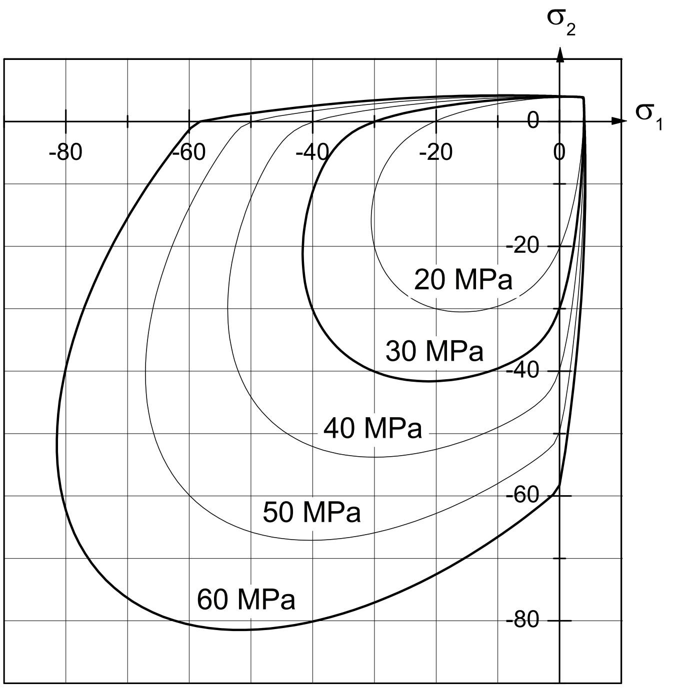

Figure 5.15: Yielding functions obtained for different values of the hardening parameter in compression, while keeping the hardening parameter in tension unchanged, $\widetilde{\sigma}_t = 4$ MPa.

to 3 MPa, without changing the hardening parameter in compression, the yielding stress in uni-axial compression is no longer 60 MPa but approximately 50 MPa. Because the coefficients of the parameters that define the Ottosen yield surface provided by the Comité Euro-international du Béton [1993] were curve-fitted to experimental data and to a ratio between the tensile and the compressive strengths of about 0.1, these results seem to indicate that, to obtain more precise results, the parameters of the Ottosen yield surface would have to be updated every time that the ratio between the hardening parameters in tension and in compression deviates too much from 0.1.

To compare the numerical response with the experimental results of Kupfer et al. [1969] for a low strength concrete and of Hussein and Marzouk [2000] for a high strength concrete, the procedure adopted previously was slightly altered. The careful analysis of the experimental results above referred allowed to assume that, with reasonable approximation, the material behavior is elastic until the compressive stress

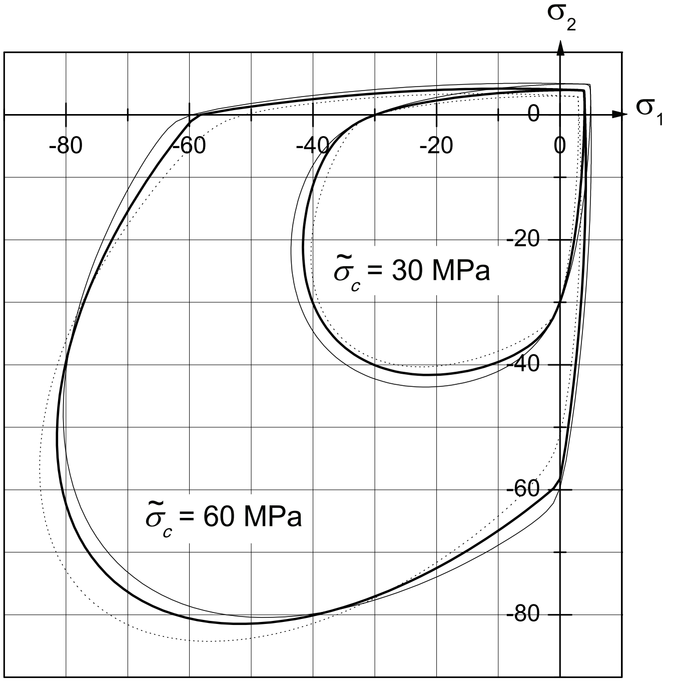

Figure 5.16: Yielding functions obtained for two different values of the hardening parameter in compression ($\widetilde{\sigma}_c = 30$ MPa and $\widetilde{\sigma}_c = 60$ MPa). In each case, the yielding functions are presented for three different values of the hardening paramenter in tension: $\widetilde{\sigma}_t = 3$ MPa (dashed line), $\widetilde{\sigma}_t = 4$ MPa (solid thick line), and $\widetilde{\sigma}_t = 5$ MPa (solid thin line).

of $0.8 f_c$ was reached, before the peak stress. As such, although only the hardening parameter in compression is activated in these simulations the results obtained are somewhat different. Furthermore, the hardening function in compression was adapted to allow the prescription of the value of 0.0032 to the compressive strain at peak stress. The numerical responses are compared with the experimental results in Figure 5.17.

Both in the case of the uni-axial and the bi-axial tests the numerical responses seem to approximate better than before the experimental results. However, it seems that the transition from the elastic to the elasto-plastic regime occurs in a less smooth way. If the transition from the elastic to the elasto-plastic regime is occurring at

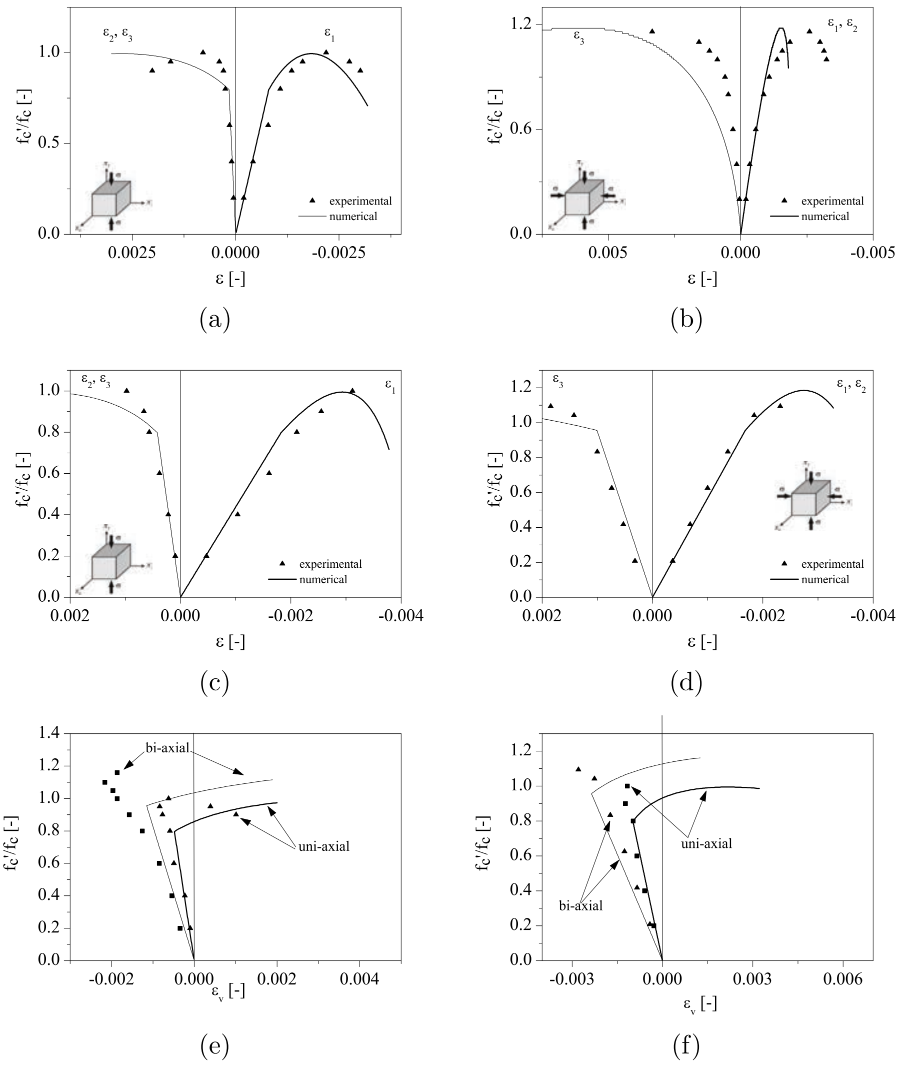

(a) (b)

(c) (d)

(e) (f)

Figure 5.17: Compressive strain-normalized stress numerical response compared with the experimental results of Kupfer et al. [1969], considering the (a) uni-axial and (b) equibi-axial compression tests, compared with the experimental results of Hussein and Marzouk [2000] considering the (c) uni-axial and (d) equibi-axial compression tests, and volumetric strain-normalized stress numerical response compared with the experimental results of (e) Kupfer et al. [1969] and (f) Hussein and Marzouk [2000].

higher stress, the difference between the Young's modulus and the hardening modulus, is grater, therefore justifying this observation.

The discrepancies between the numerical responses and experimental results for the volumetric behavior also seem slightly diminished. The overall trend is essentially captured, but the deformation perpendicularly to the loading direction is generally overestimated.

To assess the behavior of the model regarding tensile hardening, the single finite element was tested at an increasing tensile deformation, following the same procedure as before. The adopted tensile properties were: initial cracking tensile stress, $\sigma_{t0} = 3.5$ MPa, ultimate tensile stress, $\sigma_{tu} = 4.0$ MPa, ultimate tensile strain, $\epsilon_{tu} = 0.05$, Young's modulus $E_{ti} = E_{ci} = 20.0$ GPa. The following tensile stress-strain curve was obtained:

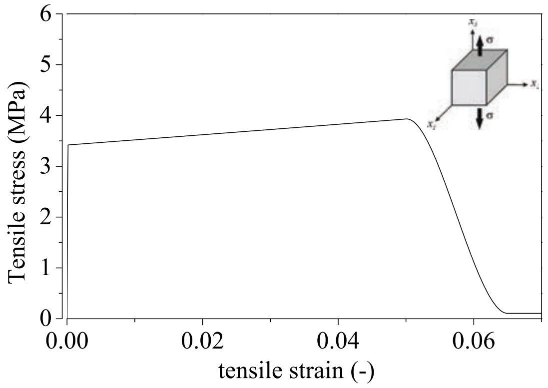

Figure 5.18: Tensile strain-stress numerical response obtained with a single element.

The response obtained in Figure 5.18 is essentially identical to the experimental results and the initial data utilized to define the hardening law in tension. As such, considering also the previous results obtained in compression, the numerical model showed reasonable ability to simulate the behavior of SHCC material at various different states of stress.

5.7 Applications of the model to simulate SHCC behavior

The numerical model above exposed was utilized to simulate the experimental results of the direct tension tests of dogbone-shaped specimens and of the eccentric tension tests of CT specimens. The material considered is the cementitious matrix composite reinforced with 2% of PVA fibers, that was experimentally characterized in the previous chapters. The material properties adopted were the following:

- Young's modulus, $E_c = E_t = 20.0$ GPa;
- Poisson's ratio, $\nu = 0.2$;
- Compressive strength, $\sigma_c = 60.0$ MPa;
- Strain at compressive peak stress, $\epsilon_{c1} = 0.0042$;
- Parameter that defines the initial yielding compressive stress, $\alpha = 0.4$;
- Initial cracking tensile stress, $\sigma_{t0} = 3.5$ MPa;
- Tensile strength, $\sigma_{tu} = 4.0$ MPa;
- Strain at ultimate tensile stress, $\epsilon_{tu} = 0.04$;

5.7.1 Direct tension of dogbone-shaped specimens

A finite element model was constructed to simulate the experimental behavior obtained with the direct tension testing of the dogbone-shaped specimens in Chapter 2. Due to the symmetry of loading and boundary conditions, only one quarter of the specimen was discretized. The model is composed of 20-node cubic elements, 6 in length, 2 in width and 1 in depth. The adopted finite element mesh and support conditions in the (x, y) plane are presented in Figure 5.19. The curvature of the necking region of the dogbone was approximated using 2 elements. Although more elements could have been used to obtain a smoother approximation of the curved shape at this region, the influence on the results at the level of the straight middle portion of the specimen would not be significant, in the present context. All degrees of freedom were restrained on the bottom of the necking region, to simulate the fixed connection provided to the specimen by the hydraulic clamps. The deformed mesh and the x_2 displacement field at peak load are presented in Figure 5.20.

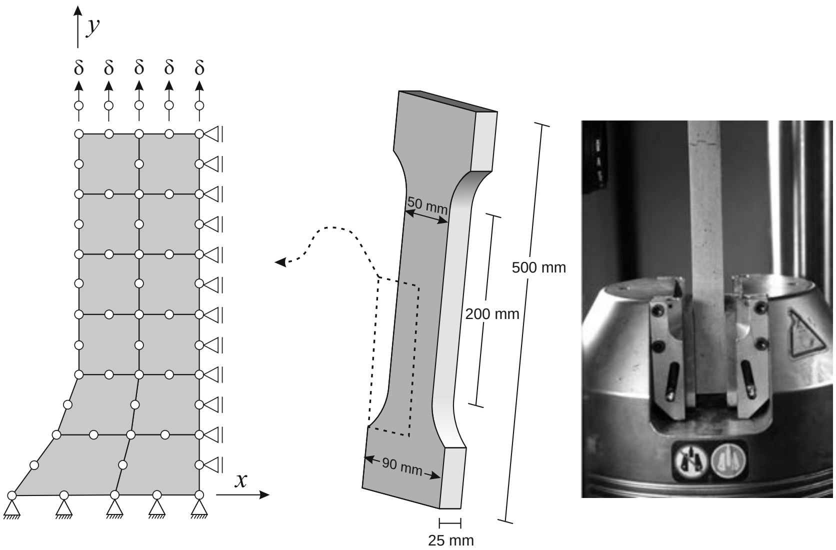

Figure 5.19: FE mesh constructed to simulate the dogbone-shaped direct tension test results, and image of the supports used during testing (Figure 2.6).

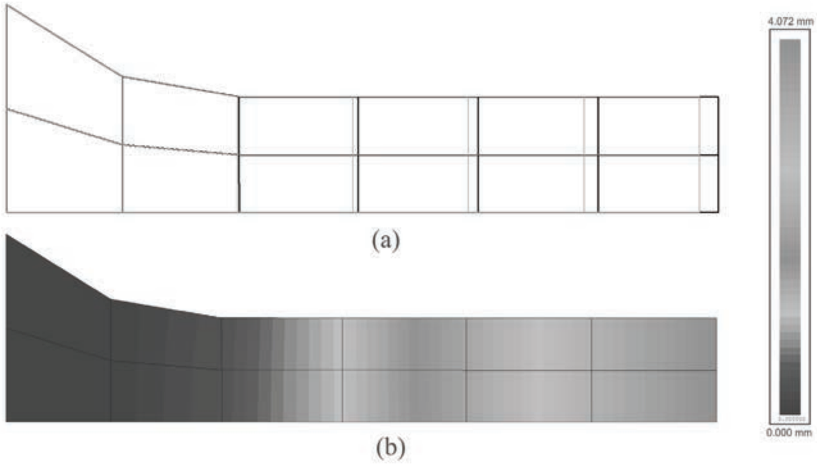

Figure 5.20: Numerical simulation of the dogbone direct tension test: (a) deformed mesh and (b) x_2 displacement field, both at peak load.

The deformed mesh shows that the mesh lines orthogonal to the longitudinal axis of the specimen remain essentially parallel after deformation (see Figure 5.20 (a)). At the necking region of the dogbone the orthogonal mesh lines are slightly curved, as confirmed by the x_2 displacement field, and a slight curvature of the x_2 displacement contour lines is observed. The finite elements in the mesh are essentially subjected to a pure tensile state of stress. Consequently this type of test is not especially demanding to the numerical model, considering that the experimental results of direct tension tests were used to calibrate the model. The computation of the solution was carried out up to the peak load, where the hardening parameter reached its maximum value and the tensile strain reached 4%. The computation of the solution for the subsequent load steps was not carried out, as the solution at each load step became increasingly slow. Since the simulation of the entire tensile hardening-softening response was possible, in a previous stage, using a single element, probably the complexity of the equations to be resolved would require the optimization of the solving algorithm in a numerical perspective. This point was not further explored in the context of the present research, but will be object of attention in future work.

The tensile stress-strain response obtained is presented in Figure 5.21:

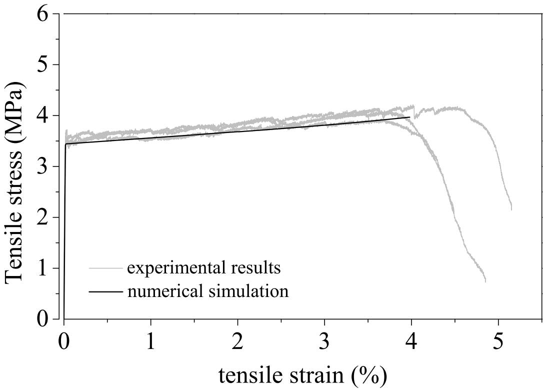

Figure 5.21: Numerical results obtained with the elasto-plasticity model compared with the experimental results of the dogbone-shaped specimens in direct tension (Section 2.7).

As shown, the response obtained in Figure 5.21 is essentially identical to the experimental results obtained. The numerical model showed adequate ability to simulate the behavior of SHCC material under predominantly tensile states of stress, in this case up to the ultimate tensile stress, σ_{tu}.

5.7.2 Eccentric tensile tests of CT specimens

To extend this analysis, a finite element model of the CTT was also constructed to simulate the results presented in the former chapter. As discussed previously, the direct tension test is not especially demanding in terms of simulation, considering the discussed features of the numerical model implemented. In contrast the CT test, where the localization of cracking is strongly induced, poses a challenge that is significantly more demanding to the type of model used, which is known for its limitations on the simulation of problems where localization is dominant. In this context, this research is focused on identifying the limits of the model in its current state of development, and providing indications for future refinements and further development.

The FE model was composed of 20-node cubic elements. The adopted finite element mesh and support conditions in the (x, y) plane are presented in Figure 5.22:

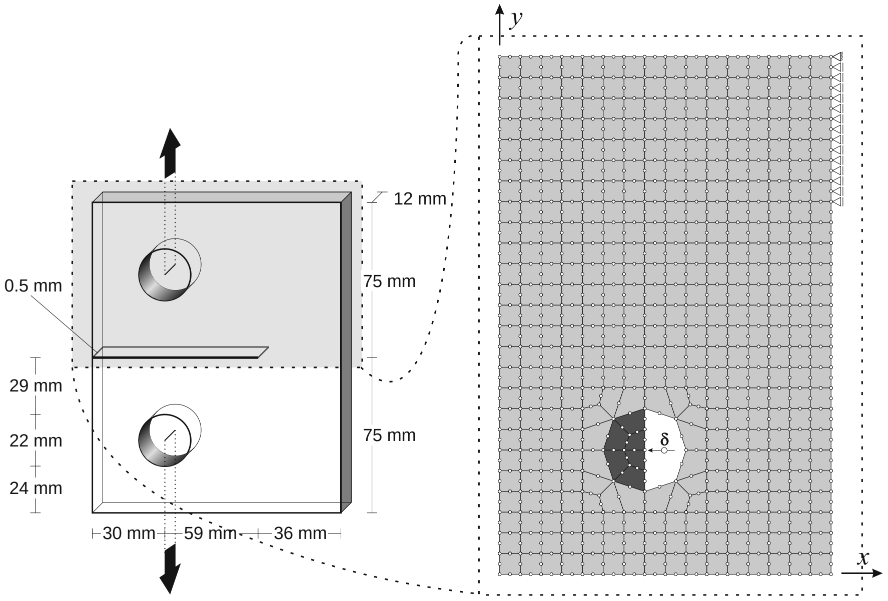

Figure 5.22: FE mesh constructed to simulate the CT test results, and image of the supports used during testing (Figure 2.6).

The deformed mesh and the x_3 displacement field obtained at peak load are presented in Figure 5.23. The x_3 displacement, that is perpendicular to the plane of the paper, is greatly affected by the plastic deformation. As discussed previously, the uni-axial and bi-axial numerical results obtained with a single finite element showed that the plastic deformation in the loading direction is accompanied by a pronounced plastic deformation in the orthogonal direction(s). This behavior is the consequence of the type of yielding surface that was utilized to determine the plastic strain, assumed as co-linear to the flux vector, and typical of granular materials. Therefore, the x_3 displacement field reveals two zones of pronounced plastic deformation, the first one close to the notch tip and the second in the compression side of the ligament, as expected. It is also possible to observe that the element immediately below the tip of the notch is already considerably distorted. This distortion of the element, that is caused by the absence of a cracking localization mechanism in the model, may originate artificial stiffening of the numerical response and difficult the numerical solution at subsequent load steps.

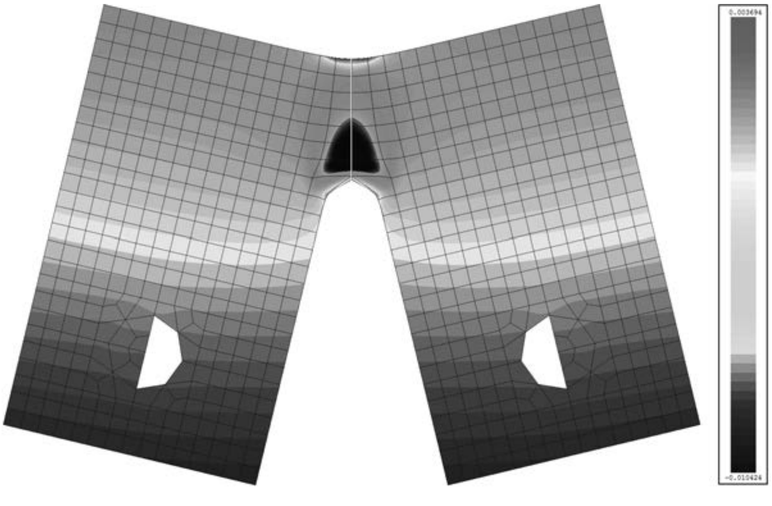

Figure 5.23: Results of the numerical simulation of the CT test, showing the deformed mesh and x_3 displacement field at the last computed load step. The regions of high plastic deformation near the notch tip and at the top of the ligament region are revealed.

The numerical response obtained is compared to the experimental results in Figure 5.24. In addition, the numerical response obtained with the FE model adopted in Chapter 3 and 4, where interface elements were utilized to simulate the initiation and propagation of a crack at the ligament region, are also presented in Figure 5.24.

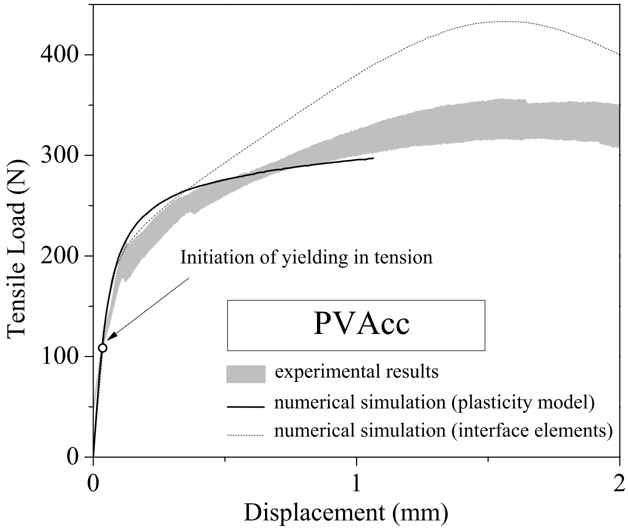

Figure 5.24: Numerical results obtained with the elasto-plasticity model compared with the numerical results obtained with the fracture model of the previous chapter and the scatter of experimental results.

As shown, the numerical response obtained with the plasticity model is approximately identical to the experimental at the initial stage of loading. Yielding in tension is initiated at a load of 105 N on the finite element that is located immediately above the notch tip. The numerical model captures well the experimental response up to a load of about 200 N, obtained at a displacement of 0.100 mm. From this point onwards, the numerical response overestimates the stiffness of the responses observed in the experimental results. In a subsequent stage, the gradual loss of stiffness at increasing displacement of the numerical response is observed, and at a displacement of about 0.500 mm the numerical response meets again the range of the obtained experimental results. Although the experimental results are reasonably approximated at higher displacements, the lower stiffness shown by the numerical response becomes evident. Due to the strong localization inducing effect of the long notch in the CT specimens, probably the results can not be considered as mesh objective, and the size of the finite elements are determining the width of the band at which yielding is occurring. If the yielding band is constant and approximately equal to the size of the finite element in x_2 direction, this constrain may result in both excessive or moderate stiffness of the numerical response, when compared to the experimental response, depending on the stage of the loading process considered.

5.8 Conclusions

The utility and applicability of the Ottossen failure criterion as a loading surface to the modeling of the nonlinear behavior of concrete under multi-axial states of stress was addressed. The Ottosen failure criterion was generalized in a hardening/softening framework for both tensile and compressive hardening. Increased complexity of the system of equations to be resolved was obtained, since the equation of the loading surface does not comply with the simpler form of the isotropic models, where the hardening parameter is explicitly defined. It was possible to confirm, however, that the loading surfaces remain self-similar with respect to the origin, if hardening in compression occurs. When considering tensile hardening, though, a slight change of the shape of the yielding surface occurs, and consequently the value of the yielding stress in uni-axial compression changes slightly too. These observations suggest that, for a more precise definition of the yielding conditions, the parameters that define the Ottosen yield surface should be continuously updated. This updating must consider the continuous evolution of the ratio between the hardening parameters in tension and in compression, among other mechanical characteristics, and should be based on experimental results.

The adoption of alternative strategies, such as the consideration of more than one yielding surface that merge at a pre-defined stress locus, would allow the full decoupling of tensile and compressive hardening effect on the yielding surface, while maintaining the uni-axial yielding stress. However, in exchange additional problems may emerge when defining the evolution of the yield surface for the mixed stress increments. In the present case, the results seem to suggest that, with additional refinement, the single yielding surface to define hardening for any type of loading is a viable solution, although additional complexity may result when refining the model.

In general, the elasto-plasticity model was able to capture the main features of uni-axial and bi-axial compressive behavior, as well as the uni-axial tensile behavior. The numerical stress-strain responses agree reasonably well with the experimental results available in the literature, and the model approximates well the expected behavior. The bi-axial results in terms of stress-strain showed a relatively more brittle response than expected, when compared with the experimental results obtained by other researchers. In terms of volumetric deformations, the overall behavior obtained follows essentially the expected, with the initial decrease in volume followed by a growing increase, in the last stages of hardening and during softening. The predicted volumetric deformations appear, though, somewhat overestimated in terms of volume decrease, mainly in the pre-peak regions. The experimental uni-axial tensile response was precisely simulated by the numerical model, including the softening stage, when the behavior of the numerical model was assessed by considering a single finite element. The simulation of the softening behavior of the dogbone-shaped specimen was not accomplished, though, and the progressive slowing down of the solution procedure at each load step was pronounced. This suggests that the numerical solution algorithm should be object of attention in future developments. In addition, the absence of a mechanism, in the numerical model, to simulate the process of cracking localization and the appearance of discontinuities on the displacement field limit the maximum imposed displacement that can be simulated. This is also a feature of the model that will be object of attention in future developments.

The consideration of a isotropic evolution of hardening roughly approximates the experimental evidence. It is feasible to consider that, if for example tensile hardening occurs in one direction, the tensile properties of the material in the orthogonal directions are somewhat affected. The current version of the model, by considering isotropic hardening evolution, prescribes similar modification of the material properties for any direction considered, therefore load reversals or alterations of the principal stress directions do not influence the numerical model responses. In the case of compression loading this is not particularly important, but for tensile loading the simulation of induced anisotropy due to cracking would be an important requirement. As mentioned in introductory section of this chapter, the results available in the literature dealing with the characterization of the induced anisotropy due to the alteration of the principal directions is scarce, and more developments in this field are expected in the near future. These results are necessary to the definition of interaction relationships between the evolution of hardening in tension at different directions. The future development of a multi-directional yielding criterion for the evolution of hardening in tension should be based on solid experimental evidence. Until now, the scarce experimental results available are restricted to the bi-axial tensile case, and for this case spacial averaged constitutive models to multi-directional cracking were already proposed, as discussed in the introductory section of this chapter. Developments in this field are, therefore, expected in the near future, including the consideration of tri-axial tensile states of stress.

Bibliography

Bolander, J. and Hirosaka, H. (1995). Simulation of fracture in cement-based composites. *Cem Conc Comp*, 17(2):135–145.

Bolander, J. and Saito, S. (1997). Discrete modeling of short-fiber reinforcement in cementitious composites. *Advanced Cement Based Materials*, 6(3-4):76–86.

Chen, W. (1982). *Plasticity in reinforced concrete.* McGraw Hill.

Comité Euro-international du Béton (1993). *CEB-FIP model code 1990: design code.* Number 213-214. T. Telford.

Cunha, V., Barros, J., and Sena-Cruz, J. (2012). A finite element model with discrete embedded elements for fibre reinforced composites. *Computers & structures*, 94-95:22–33.

Fédération International du Béton (2010). *Model Code 2010.* Number vol. 1 in Model Code 2010. International Federation for Structural Concrete (fib).

Grassl, P., Lundgren, K., and Gylltoft, K. (2002). Concrete in compression: a plasticity theory with a novel hardening law. *International Journal of Solids and Structures*, 39(20):5205–5223.

Han, T.-S., Feenstra, P. H., and Billington, S. L. (2003). Simulation of highly ductile fiber-reinforced cement-based composite components under cyclic loading. *ACI STRUCTURAL JOURNAL*, 100(PART 6):749–757.

Hofstetter, G. and Mang, H. (1995). *Computational mechanics of reinforced concrete structures.* Fundamentals and advances in the engineering sciences. Friedr. Vieweg and Sohn Verlagsgesellschaft mbH.

Hussein, A. and Marzouk, H. (2000). Behavior of high-strength concrete under biaxial stresses. *ACI Mater J*, 97(1):27–36.

Jirásek, M. and Bažant, Z. (2001). *Inelastic Analysis of Structures.* Wiley.

Kabele, P. (2007). Multiscale framework for modeling of fracture in high performance fiber reinforced cementitious composites. *Engineering Fracture Mechanics*, 74(1-2):194–209.

Kabele, P. (2009). Finite element fracture analysis of reinforced shcc members. In van Zijl, G. and Boshoff, W., editors, *Advances in Cement-Based Materials*, volume International Conference on Advanced Concrete Materials, pages 237–244, Stellenbosch, South Africa.

Karihaloo, B. and Wang, J. (2000). Mechanics of fibre-reinforced cementitious composites. *Computers & Structures*, 76(1-3):19–34.

Kullaa, J. (1997). Finite element modelling of fibre-reinforced brittle materials. *HERON -ENGLISH EDITION-*, 42(2):75–96.

Kunieda, M., Ueda, N., Nakamura, H., and Ogura, H. (2011). Tensile fracture process of strain hardening cementitious composites by means of three-dimensional meso-scale analysis. *Cem Concr Compos Cement & concrete composites*, 33(9):956–965.

Kupfer, H., HK, Hilsdorf, H., and Rusch, H. (1969). Behaviour of concrete under biaxial states of stress. *Am Concrete Inst-J*, 66(8):656–66.

Lee, J. and Fenves, G. (1998). Plastic-damage model for cyclic loading of concrete structures. *Journal of Engineering Mechanics*, 124(8):892–900.

Odqvist, F. (1933). Hardening of potamic iron similar fields. a contribution to plasticity theory. *Z. Angew. Math. Mech.*, 13:360–363.

Ottosen, N. (1980). Nonlinear finite element analysis of concrete structures. Technical report, Riso Natinal Labortory - Denmark.

Papanikolaou, V. K. and Kappos, A. J. (2007). Confinement-sensitive plasticity constitutive model for concrete in triaxial compression. *Int. J. Solids Struct.*, 44(21):7021–7048.

Pereira, E. B., Barros, J., and Fischer, G. (2012). Development of a 3d 4-parameter elasto-plasticity model with hardening in tension and in compression to the numerical simulation of the structural behavior of strain hardening cementitous composites. Technical report, University of Minho.

Ristinmaa, M., Wallin, M., and Ottosen, N. S. (2007). Thermodynamic format and heat generation of isotropic hardening plasticity. *Acta Mechanica*, 194(1-4):103–121.

Schlangen, E., Prabowo, H., Sierra-Beltran, M., and Qian, Z. (2009). A model for building a design tool for ductile fibre reinforced materials. In *Advances in Cement-Based Materials*, pages 307–312–. CRC Press.

Sena-Cruz, J., Barros, J. A. O., Azevedo, A. F. M., and Gouveia, A. V. (2007). Numerical simulation of the nonlinear behavior of rc beams strengthened with nsm cfrp strips. In *Proceedings of CMNE/CILAMCE 2007 - Iberian latin american congress on computational methods in engineering*. Associação Portuguesa de Mecânica Teórica, Aplicada e Computacional (APMTAC).

Simo, J. and Hughes, T. (1988). *Elastoplasticity and viscoplasticity: computational aspects.* Springer.

Suryanto, B., Maekawa, K., and Nagai, K. (2008). Numerical analysis of secondary rotated cracking behavior of fiber reinforced cementitious composite plate. In *Creep, Shrinkage and Durability Mechanics of Concrete and Concrete Structures, Two Volume Set*, pages 557–563–. Taylor & Francis.

Trüb, M. (2011). *Numerical Modeling of High Performance Fiber Reinforced Cementitious Composites.* PhD thesis, Institute of Structural Engineering - ETH Zürich.

van Mier, J. (1997). *Fracture processes of concrete: assesment of material parameters for fracture models.* New directions in civil engineering. CRC Press.

van Zijl, G. (2009). Computational modelling of strain-hardening cement composites (shcc). In *Advances in Cement-Based Materials*, pages 263–270–. CRC Press.

Vorel, J. and Boshoff, W. (2009). Numerical modelling of strain hardening fibre-reinforced composites. In *Advances in Cement-Based Materials*, pages 271–278–. CRC Press.

Willam, K. and Warnke, E. (1974). Constitutive model for the triaxial behaviour of concrete. In *Proc. Intl. Assoc. Bridge Structl. Engrs*, volume Report 19, Section III, page 30, Zurich.

Zienkiewicz, O. C. and Taylor, R. L. (2005). *The finite element method for solid and structural mechanics.* Elsevier Butterworth-Heinemann, Amsterdam ; Boston :.

Zienkiewicz, O. C., Taylor, R. L., and Zhu, J. Z. (2005). *The finite element method: its basis and fundamentals.* Elsevier Butterworth-Heinemann,, Amsterdam ; Boston :.

CHAPTER 6

Final remarks

The present investigation concerning the mechanical behavior of Strain Hardening Cementitious Composites was mostly dedicated to the characterization of the cracking processes at the material meso-scale level. To this purpose, considering the typical procedures utilized to characterize the mechanical behavior of these materials in tension and the theoretical background that explains their pseudo-strain hardening behavior in tension, it became appropriate and necessary to define a strategy for the characterization of the tensile stress-crack opening behavior of these materials. Therefore, in a first stage, the most important accomplishments are related to the definition of the Single Crack Tension Test (SCTT) and may be summarized by the following:

- Definition of a specimen geometry, testing parameters and boundary conditions necessary to obtain a single crack on SHCC specimens tested in tension;
- Characterization of the topological features of the obtained single cracks with considerable resolution, using an image-based deformation analysis system. Confirmation of the uniqueness of the crack plane, and verification of the mechanical responses obtained by means of numerical simulations based on the tensile stress-crack opening responses obtained;
- Characterization of the crack profiles obtained with the SCTT, both using the image-based deformation analysis system and the results of the numerical simulation;
- Characterization of the behavior of an individual crack in multiply-cracked

SHCC specimens in direct tension, using the image-based deformation analysis; establishment of the correspondence between the results obtained with the SCTT and the behavior of an individual crack in multiply-cracked specimens;

- Identification of the most important features of the tensile stress-crack opening behavior on SHCC and their relation with the micro-mechanical properties of the composite;
- Evaluation of the effect of different fiber and fiber-matrix interaction properties on the tensile stress-crack opening behavior of the composites;

The SCTT showed reasonable robustness and high sensitivity to important composite parameters, therefore it may be regarded as a valid contribution for both the design and the numerical modeling activities of SHCC materials. Furthermore, the results obtained support the recommendation of this type of test to assess the bridging stress-crack opening law, which is regarded as a central piece of information in most micro-mechanical models proposed in the literature characterize and design these materials.

In future developments the study of the influence of the predominant direction of fiber orientation on the tensile stress-crack opening response may be considered. Also, the exploration of techniques to further reduce the thickness of the notches may be welcomed, since the development of new composites that are more demanding with regards to the conditions necessary to initiate and propagate a single crack may be anticipated. In addition, the investigation of the conditions necessary to adapt this type of test to other types of fibers and aggregates, of different sizes and natures, may be considered.

Subsequently, the investigation reported in this thesis was dedicated to the characterization of fracture properties and crack propagation in SHCC. The importance of the cracking processes on the tensile behavior of SHCC motivated the development of a testing setup to characterize with increased resolution the initiation and propagation of cracks. The specimen geometry adopted was based on the Compact Tension Specimen, and a high resolution camera was adapted to the image-based deformation system to enhance the resolution of the interpolated displacement fields. The utilization of this setup to the investigation of the near crack tip displacement fields led to the following developments:

- Definition of a specimen geometry, testing parameters and boundary conditions of the Compact Tension Test (CTT), based on the Compact Tension Specimen, to characterize the fracture processes in cementitious composites;

- Topological characterization of the cracking processes and crack propagation at the surface of CT specimens of various cementitious composites, with resolutions of the order of the micrometer;
- Identification of typical behaviors of crack initiation, propagation, branching and smearing, and their relation with the type of fiber reinforcement, the characteristics of the cementitious matrix and the type of aggregates used;
- Characterization and discussion of the nature of the fracture process zone in cementitious matrix composites;
- Utilization of the real crack patterns to explain the discrepancies between the experimental and the simulated mechanical behaviors; discussion about the viability of using back analysis to extract the fracture parameters of SHCC materials from typical fracture tests;

The CTT has shown valuable characteristics to serve as a complimentary characterization test setup, providing information about the most important properties of the cracking processes and crack propagation in in cementitious composites. The CTT also contributes to the mechanical characterization of cementitious composites, providing the mechanical response for loading conditions other than pure tension. CTT may be further explored to complement the characterization of the cracking processes in SHCC materials, in particular by altering the testing boundary conditions and the size of the specimen. These developments may consider the conceptual tests of classical approaches to the problem of crack propagation by linear elastic fracture mechanics.

The comparison of the mechanical behavior of different cementitious composites was carried out subsequently using both the SCTT and the CTT test setups previously discussed. The tensile stress-crack opening responses obtained with the SCTT were utilized to simulate the mechanical CTT responses, to further verify the objective character of the tensile stress-crack opening relationships derived with the SCTT. Different combinations of fiber reinforcements, including the utilization of multiple fiber types in the same composite, and different cementitious matrices were investigated and the main findings are:

- The detailed analysis of the tensile results have clearly shown that fibers of different sizes and of different natures show an effective contribution to crack restraining at clearly differentiated length scales of the cracking process; the experimental results also support the conception of a multi-scale nature of the cracking process in cementitious composites, which should be related to the different length scales of the material;

- The effect of combining different fiber types on the tensile response of the composite is clearly revealed by the SCTT, with the formation of distinct tensile hardening-softening sequences in the tensile response, as a result of the effective contribution of each fiber type at different length scales of the cracking process;
- Based on the SCTT, a systematic procedure was explored to objectively quantify the beneficial result and possible synergistic effect of combining different fiber types in hybrid fiber reinforced cementitious composites; the possibility of obtaining synergistic effects as a result of the combination of different types of fibers to control the cracking process at different length scales was also discussed, based on the experimental results;
- The results obtained seem to indicate that, when multiple types of fibers are combined in the cementitious composite, the preservation of the synchronism in the activation of the different types of fibers is essential to obtain optimal tensile performance;

The combination of both the SCTT and the CTT tests, together with the high resolution image-based deformation analysis system, have resulted in a conveninet set of experimental results to support the characterization and understanding of the fracture behavior of SHCC materials, both in the case of the single fiber type and in the hybrid formulations. To further explore the multiple peak feature observed in the tensile stress-crack opening response when multiple types of fibers are combined, the addition of even more different fiber types in the same composite to explore new different types of tensile behaviors, and the adoption of different cementitious matrices are left open for future research.

The last part of this research was dedicated to the numerical simulation of the nonlinear behavior of SHCC materials at the structural scale. The number of studies available in the literature specifically dedicated to the nonlinear behavior of SHCC is still limited, but a few strategies have already been reported to reproduce well the experiments conducted in structural members under different loading configurations. In this research, the adopted strategy was based on elasto-plasticity. The 4-parameter Ottosen failure criterion was generalized to consider hardening/softening in tension and in compression to the simulation of general tri-axial states of stress. The most important findings are:

- The Ottosen yielding surface, when generalized to consider hardening/softening in tension and in compression, simulates reasonably well the uni-axial and bi-axial compressive behavior of cementitious composites, as well as the uni-axial tensile behavior of fiber reinforced cementitious composites exhibiting pseudo-strain hardening;

- The variation of the hardening parameter in compression is accompanied by the change of the shape of the yielding surface; this change accommodates well all the requisites related to the process of hardening in tension; the variation of the hardening parameter in tension is limited to a certain range of possible values, and in some cases the change of the shape of the yielding surface may lead to the slight variation of the uni-axial compressive yielding stresses; to avoid this artifact a continuous updating of the yielding surface parameters may be required;

- The numerical model was able to simulate well the tensile behavior up to the peak load of the dogbone-shaped specimens in direct tension; the simulation of the load-displacement response of the CT specimen was stiffer than expected in the early stage of the elasto-plastic response, and too soft in the last computed load steps; the need to simulate cracking localization and discontinuities on the displacement field became clear;

As discussed previously, the further refinement of the numerical model developed should consider the incorporation of a mechanism to accommodate discontinuities in the displacement field caused by cracking localization, if the simulation of the entire response of structural members is required. Furthermore, the algorithmic details of the procedure used to find the solution at each load step seem to require further development and optimization. Additionally, the subsequent simulation of the structural behavior of members subjected to different loading conditions is essential to ascertain the capabilities of the model. This status of development of the model was, though, not possible to fit in the contents of the present research, and is therefore left for future developments. It is, however, anticipated the need to incorporate the tensile stress-crack opening responses obtained with the SCTT in the numerical model, whether as a means to scale the tensile stress-strain response considering the size of the elements or the length scale of the structural members, or to describe the traction-separation laws required to simulate the coalescence of discontinuities on the displacement fields of the finite element model, or even to compute fields of crack opening/spacing distributions, which are of great importance to the modeling of deterioration and time-dependent phenomena.

APPENDIX A

Numerical model auxiliary equations

A.1 First and second order derivatives

A.1.1 First order derivatives of the stress invariants

The first order derivatives of the stress invariants I_1 , J_2 and $J_3$are described by the following expressions:

$$\frac{\partial I_1}{\partial \sigma_x} = \frac{\partial I_1}{\partial \sigma_y} = \frac{\partial I_1}{\partial \sigma_z} = 1 \ ; \quad \frac{\partial I_1}{\partial \tau_{yz}} = \frac{\partial I_1}{\partial \tau_{xz}} = \frac{\partial I_1}{\partial \tau_{xy}} = 0 \tag{A.1}$$

for J_2:

$$\begin{aligned} \frac{\partial J_2}{\partial \sigma_x} &= \frac{1}{3}\left(2\sigma_x - \sigma_y - \sigma_z\right) & \frac{\partial J_2}{\partial \tau_{yz}} &= 2\tau_{yz} \\ \frac{\partial J_2}{\partial \sigma_y} &= \frac{1}{3}\left(2\sigma_y - \sigma_x - \sigma_z\right) & \frac{\partial J_2}{\partial \tau_{xz}} &= 2\tau_{xz} \\ \frac{\partial J_2}{\partial \sigma_z} &= \frac{1}{3}\left(2\sigma_z - \sigma_x - \sigma_y\right) & \frac{\partial J_2}{\partial \tau_{xy}} &= 2\tau_{xy} \end{aligned} \tag{A.2}$$

and for J_3:

$$\begin{aligned}
\frac{\partial J_3}{\partial \sigma_x} &= \frac{1}{9}\left(2\sigma_x^2 - \sigma_y^2 - \sigma_z^2 - 2\sigma_x\sigma_y - 2\sigma_x\sigma_z + 4\sigma_y\sigma_z\right) \\
&+ \frac{1}{3}\left(\tau_{xy}^2 + \tau_{xz}^2 - 2\tau_{yz}^2\right) \\
\frac{\partial J_3}{\partial \sigma_y} &= \frac{1}{9}\left(2\sigma_y^2 - \sigma_x^2 - \sigma_z^2 - 2\sigma_x\sigma_y - 2\sigma_y\sigma_z + 4\sigma_x\sigma_z\right) \\
&+ \frac{1}{3}\left(\tau_{xy}^2 + \tau_{yz}^2 - 2\tau_{xz}^2\right) \\
\frac{\partial J_3}{\partial \sigma_z} &= \frac{1}{9}\left(2\sigma_z^2 - \sigma_x^2 - \sigma_y^2 - 2\sigma_x\sigma_z - 2\sigma_y\sigma_z + 4\sigma_x\sigma_y\right) \\
&+ \frac{1}{3}\left(\tau_{xz}^2 + \tau_{yz}^2 - 2\tau_{xy}^2\right) \\
\frac{\partial J_3}{\partial \tau_{yz}} &= \frac{2}{3}\,\tau_{yz}\left(\sigma_y + \sigma_z - 2\sigma_x\right) + 2\tau_{xy}\tau_{xz} \\
\frac{\partial J_3}{\partial \tau_{xz}} &= \frac{2}{3}\,\tau_{xz}\left(\sigma_x + \sigma_z - 2\sigma_y\right) + 2\tau_{xy}\tau_{yz} \\
\frac{\partial J_3}{\partial \tau_{xy}} &= \frac{2}{3}\,\tau_{xy}\left(\sigma_x + \sigma_y - 2\sigma_z\right) + 2\tau_{xz}\tau_{yz}
\end{aligned} \tag{A.3}$$

A.1.2 Second Order Derivatives of the Stress Tensor Invariants

The first stress invariant (I_1), has its all second order derivatives, with respect to the six stress vector components, null. For the second deviatoric stress invariant, reminding that the 1^{st}, the 2^{nd} and the 3^{rd} stress components are, respectively, σ_x, σ_y and σ_z, and that the 4^{th}, $5th$ and $6th$ stress components are, correspondingly, τ_{yz}, τ_{xz} and τ_{xy}, it is obtained:

If $i \leq 3$, with k and l smaller than 4, one obtains:

$$\frac{\partial}{\partial \sigma_j}\left(\frac{\partial J_2}{\partial \sigma_i}\right) = \frac{\partial}{\partial \sigma_j}\left[\frac{1}{3}\left(2\sigma_i - \sigma_k - \sigma_l\right)\right], \tag{A.4}$$

and:

$$\frac{\partial}{\partial \sigma_j}\left(\frac{\partial J_2}{\partial \sigma_i}\right) = \begin{cases} \dfrac{2}{3} & \text{for} \quad j = i \ , \\ -\dfrac{1}{3} & \text{for} \quad j \neq i \quad \text{and} \quad j \leq 3 \ , \\ 0 & \text{for} \quad j > 3 \ . \end{cases} \tag{A.5}$$

If $i > 3$, one obtains:

$$\frac{\partial}{\partial \sigma_j}\left(\frac{\partial J_2}{\partial \sigma_i}\right) = \frac{\partial}{\partial \sigma_j}\left(2\sigma_i\right), \tag{A.6}$$

and:

$$\frac{\partial}{\partial \sigma_j}\left(\frac{\partial J_2}{\partial \sigma_i}\right) = \begin{cases} 2 & \text{for} \quad j = i \ , \\ 0 & \text{for} \quad j \neq i \ . \end{cases} \tag{A.7}$$

where σ_j represents the generic j^{th} component of the stress vector. For the third deviatoric stress invariant J_3:

If $i \leq 3$, with k and l not exceeding 3, one obtains:

$$\begin{aligned} \frac{\partial}{\partial \sigma_j}\left(\frac{\partial J_3}{\partial \sigma_i}\right) = \frac{\partial}{\partial \sigma_j}\Bigg(\frac{1}{9}\,\big(2\sigma_i^2 - \sigma_k^2 - \sigma_l^2 - 2\sigma_i\sigma_k - 2\sigma_i\sigma_l \, + \\ + \, 4\sigma_k\sigma_l\big) + \frac{1}{3}\left(\sigma_u^2 + \sigma_v^2 - 2\sigma_{i+3}^2\right)\Bigg) \ , \end{aligned} \tag{A.8}$$

and:

$$\frac{\partial}{\partial \sigma_j}\left(\frac{\partial J_3}{\partial \sigma_i}\right) = \begin{cases} \dfrac{2}{9}\ \left(2\sigma_j - \sigma_k - \sigma_l\right) & \text{for} \quad j = i \ , \\ \dfrac{2}{9}\ \left(2\sigma_k - \sigma_i - \sigma_j\right) & \text{for} \quad j \neq i \quad \text{and} \quad j \leq 3 \ , \\ -\dfrac{4}{3}\ \sigma_j & \text{for} \quad j > 3 \quad \text{and} \quad j = i + 3 \ , \\ \dfrac{2}{3}\ \sigma_j & \text{for} \quad j > 3 \quad \text{and} \quad j \neq i + 3 \ . \end{cases} \tag{A.9}$$

If $i > 3$, one obtains:

$$\frac{\partial}{\partial \sigma_j}\left(\frac{\partial J_3}{\partial \sigma_i}\right) = \frac{\partial}{\partial \sigma_j}\left(\frac{2}{3}\,\sigma_i\Big(\sigma_u + \sigma_v - 2\sigma_{i-3}\Big) + 2\sigma_k\sigma_l\right), \tag{A.10}$$

and:

$$\frac{\partial}{\partial \sigma_j}\left(\frac{\partial J_3}{\partial \sigma_i}\right) = \begin{cases} -\dfrac{4}{3}\sigma_j & \text{for} \quad j = i-3 \ , \\ \dfrac{2}{3}\sigma_j & \text{for} \quad j \neq i-3 \text{ and } j \leq 3 \ , \\ \dfrac{2}{3}\Big(\sigma_k + \sigma_l - 2\sigma_{i-3}\Big) & \text{for} \quad j = i \ , \ j > 3 \text{ and } k, l \leq 3 \ , \\ 2\sigma_k & \text{for} \quad j \neq i \ , \ j > 3 \text{ and } k > 3 \ . \end{cases} \tag{A.11}$$

A.1.3 First order derivatives of the λ parameter (Ottosen Yield Function)

In equation (A.12) the λ parameter is defined for the two possible domains of the Lode angle ($\cos 3\theta$):

$$\begin{aligned} &\text{for} \cos 3\theta \leq 0 \ : \\ &\quad \frac{\partial \lambda}{\partial \sigma_i} = \frac{\sqrt{3}}{2}\, c_1\, c_2\, \frac{\sin\left[\dfrac{\pi}{3} - \dfrac{1}{3}\arccos\left(-c_2\cos 3\theta\right)\right]\left(J_2^{\frac{3}{2}}\,\dfrac{\partial J_3}{\partial \sigma_i} - \dfrac{3}{2}\sqrt{J_2}\;J_3\,\dfrac{\partial J_2}{\partial \sigma_i}\right)}{J_2^3\sqrt{1-\left(c_2\cos 3\theta\right)^2}} \\ &\text{for} \cos 3\theta > 0 \ : \\ &\quad \frac{\partial \lambda}{\partial \sigma_i} = \frac{\sqrt{3}}{2}\, c_1\, c_2\, \frac{\sin\left[\dfrac{1}{3}\arccos\left(c_2\cos 3\theta\right)\right]\left(J_2^{\frac{3}{2}}\,\dfrac{\partial J_3}{\partial \sigma_i} - \dfrac{3}{2}\sqrt{J_2}\;J_3\,\dfrac{\partial J_2}{\partial \sigma_i}\right)}{J_2^3\sqrt{1-\left(c_2\cos 3\theta\right)^2}} \end{aligned} \tag{A.12}$$

A.1.4 Second Order Derivatives of the λ parameter (Ottosen Yield Function)

The second order derivatives of the λ parameter with respect to the stress vector components are obtained as follows, when $\cos 3\theta \leq 0$:

$$\frac{\partial}{\partial \sigma_j}\left(\frac{\partial \lambda}{\partial \sigma_i}\right) = \frac{\partial}{\partial \sigma_j}\left[\frac{\sqrt{3}}{2}\, c_1\, c_2\, \underbrace{\sin\left[\frac{\pi}{3} - \frac{1}{3}\, \arccos\left(-c_2 \cos 3\theta\right)\right]}_{\text{function g}} \cdot \right.$$
$$\left. \cdot \underbrace{\frac{J_2^{\frac{3}{2}}\, \dfrac{\partial J_3}{\partial \sigma_i} - \dfrac{3}{2}\, J_2^{\frac{1}{2}}\, J_3\, \dfrac{\partial J_2}{\partial \sigma_i}}{J_2^3\, \sqrt{1 - \left(c_2 \cos 3\theta\right)^2}}}_{\text{function h}}\right], \tag{A.13}$$

with:

$$\frac{\partial \lambda}{\partial \sigma_i} = \frac{\sqrt{3}}{2}\, c_1\, c_2 \cdot \mathrm{g}\left(\sigma_i\right) \cdot \mathrm{h}\left(\sigma_i\right)\ . \tag{A.14}$$

After some algebraic operations, one obtains:

$$\frac{\partial}{\partial \sigma_j}\left(\frac{\partial \lambda}{\partial \sigma_i}\right) = \frac{\sqrt{3}}{2}\, c_1\, c_2 \cdot \left(\frac{\partial \mathrm{g}(\sigma_i)}{\partial \sigma_j}\, \mathrm{h}(\sigma_i) + \mathrm{g}(\sigma_i)\, \frac{\partial \mathrm{h}(\sigma_i)}{\partial \sigma_j}\right)\ , \tag{A.15}$$

where:

$$\frac{\partial \mathrm{g}(\sigma_i)}{\partial \sigma_j} = -\frac{\sqrt{3}}{2}\, c_2 \cos\left[\frac{\pi}{3} - \frac{1}{3} \arccos\left(-c_2 \cos 3\theta\right)\right] \cdot \frac{J_2^{\frac{3}{2}}\, \dfrac{\partial J_3}{\partial \sigma_j} - \dfrac{3}{2}\, J_2^{\frac{1}{2}}\, J_3\, \dfrac{\partial J_2}{\partial \sigma_j}}{J_2^3\, \sqrt{1 - \left(c_2 \cos 3\theta\right)^2}} \tag{A.16}$$

and:

$$
\begin{aligned}
\frac{\partial \mathrm{h}(\sigma_i)}{\partial \sigma_j} = \Bigg[& \frac{\partial}{\partial \sigma_j}\left(J_2^{\frac{3}{2}}\ \frac{\partial J_3}{\partial \sigma_i} - \frac{3}{2}\ J_2^{\frac{1}{2}}\ J_3\ \frac{\partial J_2}{\partial \sigma_i} \right) \cdot J_2^3\ \sqrt{1-(c_2 \cos 3\theta)^2}\ - \\
& - \left(3\ J_2^2\ \frac{\partial J_2}{\partial \sigma_j}\ \sqrt{1-(c_2\ \cos 3\theta)^2}\ - \frac{3\sqrt{3}}{2}\ c_2\ cos3\theta\ \frac{J_2^{\frac{3}{2}}\ \dfrac{\partial J_3}{\partial \sigma_j} - \dfrac{3}{2}\ J_2^{\frac{1}{2}}\ J_3\ \dfrac{\partial J_2}{\partial \sigma_j}}{\sqrt{1-(c_2 \cos 3\theta)^2}} \right) \cdot \\
& \cdot \left(J_2^{\frac{3}{2}}\ \frac{\partial J_3}{\partial \sigma_j} - \frac{3}{2}\ J_2^{\frac{1}{2}}\ J_3\ \frac{\partial J_2}{\partial \sigma_j} \right) \Bigg] \cdot \left(J_2^3 \sqrt{1-(c_2 \cos 3\theta)^2} \right)^{-2}\ ,
\end{aligned}
\tag{A.17}
$$

with:

$$
\begin{aligned}
\frac{\partial}{\partial \sigma_j}\left(J_2^{\frac{3}{2}}\ \frac{\partial J_3}{\partial \sigma_i} - \frac{3}{2}\ J_2^{\frac{1}{2}}\ J_3\ \frac{\partial J_2}{\partial \sigma_i} \right) = & \frac{3}{2}\ J_2^{\frac{1}{2}}\ \frac{\partial J_2}{\partial \sigma_j} \frac{\partial J_3}{\partial \sigma_i} + \frac{\partial}{\partial \sigma_j}\left(\frac{\partial J_3}{\partial \sigma_i} \right) J_2^{\frac{3}{2}} - \\
& - \frac{3}{2}\ \frac{1}{2}\ J_2^{-\frac{1}{2}}\ \frac{\partial J_2}{\partial \sigma_j}\ J_3\ \frac{\partial J_2}{\partial \sigma_i} - \frac{3}{2}\ J_2^{\frac{1}{2}}\ \frac{\partial J_3}{\partial \sigma_j} \frac{\partial J_2}{\partial \sigma_i} - \frac{3}{2}\ J_2^{\frac{1}{2}}\ J_3 \frac{\partial}{\partial \sigma_j} \frac{\partial J_2}{\partial \sigma_i}\ .
\end{aligned}
\tag{A.18}
$$

When $\cos 3\theta > 0$, the same expressions presented above are applied but the term “ $\left[\frac{\pi}{3} - \frac{1}{3} \arccos\left(-c_2 \cos 3\theta\right)\right]$ “ is substituted by “ $\left[\frac{1}{3} \arccos\left(c_2 \cos 3\theta\right)\right]$ “:

$$
\begin{aligned}
& \frac{\partial}{\partial \sigma_j}\left(\sin\left[\frac{\pi}{3} - \frac{1}{3}\ \arccos\left(-c_2 \cos 3\theta\right) \right] \right) = \\
& = \cos\left[\frac{\pi}{3} - \frac{1}{3}\ \arccos\left(-c_2 \cos 3\theta\right) \right] \cdot \frac{\partial}{\partial \sigma_j}\left(\frac{\pi}{3} - \frac{1}{3}\ \arccos\left(-c_2 \cos 3\theta\right) \right) \\
& = \cos\left[\frac{\pi}{3} - \frac{1}{3}\ \arccos\left(-c_2 \cos 3\theta\right) \right] \cdot \left(-\frac{1}{3} \right)\ \frac{-1}{\sqrt{1-(-c_2 \cos 3\theta)^2}}\ \cdot\ \frac{\partial}{\partial \sigma_j}\left(-c_2 \cos 3\theta\right) \\
& = -\frac{\sqrt{3}}{2}\ c_2\ \cos\left[\frac{\pi}{3} - \frac{1}{3}\ \arccos\left(-c_2 \cos 3\theta\right) \right] \cdot \frac{J_2^{\frac{3}{2}}\ \dfrac{\partial J_3}{\partial \sigma_j}\ -\ \dfrac{3}{2}\sqrt{J_2}\ J_3\ \dfrac{\partial J_2}{\partial \sigma_j}}{J_2^3\ \sqrt{1-(c_2\ \cos 3\theta)^2}}\ ,
\end{aligned}
\tag{A.19}
$$

with:

$$\begin{aligned}\frac{\partial}{\partial \sigma_j}\Big(\cos 3\theta\Big) &= \frac{\partial}{\partial \sigma_j}\left(\frac{3\sqrt{3}}{2}\cdot\frac{J_3}{J_2^{\frac{3}{2}}}\right)\\ &= \frac{3\sqrt{3}}{2}\left(\frac{\partial J_3}{\partial \sigma_j}\,J_2^{-\frac{3}{2}} + \left(-\frac{3}{2}\right)J_2^{-\frac{5}{2}}\,\frac{\partial J_2}{\partial \sigma_j}\,J_3\right)\,.\end{aligned} \tag{A.20}$$

A.1.5 First and second order derivatives of the Ottosen Yield Function

The derivatives of the Ottosen Yield function must with respect to the stress vector components are given by the following equation:

$$\frac{\partial}{\partial \sigma_j}\left(\frac{\partial f(\boldsymbol{\sigma},\,\tilde{\sigma})}{\partial \sigma_i}\right) = \frac{1}{2}\,\frac{\partial}{\partial \sigma_j}\left[\underbrace{\left[\alpha\,\frac{\partial J_2}{\partial \sigma_i} + \tilde{\sigma}\left(\frac{\partial \lambda}{\partial \sigma_i}\,J_2^{\frac{1}{2}} + \frac{1}{2}\,\lambda\,\frac{\partial J_2}{\partial \sigma_i}\,J_2^{-\frac{1}{2}} + \beta\,\frac{\partial I_1}{\partial \sigma_i}\right)\right]}_{\text{function g}}\cdot \cdot \underbrace{\left[\alpha\,J_2 + \tilde{\sigma}\,\left(\lambda\,J_2^{\frac{1}{2}} + \beta I_1\right)\right]^{-\frac{1}{2}}}_{\text{function h}}\right], \tag{A.21}$$

with:

$$\frac{\partial f(\boldsymbol{\sigma},\,\tilde{\sigma})}{\partial \sigma_i} = \frac{1}{2}\left[\mathrm{g}(\boldsymbol{\sigma},\,\tilde{\sigma})\cdot \mathrm{h}(\boldsymbol{\sigma},\,\tilde{\sigma})\right]\,. \tag{A.22}$$

To facilitate the presentation of the final expression, one assumes that:

$$\frac{\partial}{\partial \sigma_j}\left(\frac{\partial f(\boldsymbol{\sigma},\,\tilde{\sigma})}{\partial \sigma_i}\right) = \frac{1}{2}\left(\frac{\partial \mathrm{g}(\boldsymbol{\sigma},\,\tilde{\sigma})}{\partial \sigma_j}\,\mathrm{h}(\boldsymbol{\sigma},\,\tilde{\sigma}) + \mathrm{g}(\boldsymbol{\sigma},\,\tilde{\sigma})\,\frac{\partial \mathrm{h}(\boldsymbol{\sigma},\,\tilde{\sigma})}{\partial \sigma_j}\right)\,, \tag{A.23}$$

where:

$$\begin{aligned}\frac{\partial \mathrm{g}\left(\boldsymbol{\sigma},\ \tilde{\sigma}\right)}{\partial \sigma_j} = \alpha\ \frac{\partial}{\partial \sigma_j}\left(\frac{\partial J_2}{\partial \sigma_i}\right) + \tilde{\sigma}\Bigg[& \frac{\partial}{\partial \sigma_j}\left(\frac{\partial \lambda}{\partial \sigma_i}\right)\ J_2^{\frac{1}{2}} + \frac{1}{2}\ \frac{\partial \lambda}{\partial \sigma_i}\ J_2^{-\frac{1}{2}}\ \frac{\partial J_2}{\partial \sigma_j} + \\ & \frac{1}{2}\left(\frac{\partial \lambda}{\partial \sigma_j}\ \frac{\partial J_2}{\partial \sigma_i}\ J_2^{-\frac{1}{2}} - \frac{1}{2}\ \lambda\ J^{-\frac{3}{2}}\ \frac{\partial J_2}{\partial \sigma_i}\ \frac{\partial J_2}{\partial \sigma_j} + \right. \\ & \left. \lambda\ \frac{\partial}{\partial \sigma_j}\left(\frac{\partial J_2}{\partial \sigma_i}\right) J_2^{-\frac{1}{2}}\right) + \beta\ \frac{\partial}{\partial \sigma_j}\left(\frac{\partial I_1}{\partial \sigma_i}\right)\Bigg]\ ,\end{aligned} \tag{A.24}$$

and:

$$\begin{aligned}\frac{\partial \mathrm{h}\left(\boldsymbol{\sigma},\ \tilde{\sigma}\right)}{\partial \sigma_j} = -\frac{1}{2}\left[\alpha\ \frac{\partial J_2}{\partial \sigma_j} + \tilde{\sigma}\left(\frac{\partial \lambda}{\partial \sigma_j}\ J_2^{\frac{1}{2}} + \frac{1}{2}\ \lambda\ \frac{\partial J_2}{\partial \sigma_j}\ J_2^{-\frac{1}{2}} + \beta\ \frac{\partial I_1}{\partial \sigma_j}\right)\right] \cdot \\ \cdot \left[\alpha\ J_2\ + \tilde{\sigma}\left(\lambda\ \sqrt{J_2}\ + \beta\ I_1\right)\right]^{-\frac{3}{2}}\ .\end{aligned} \tag{A.25}$$

A.1.6 First and second order derivatives of F_1, F_2 and F_3

The functions F_1, F_2 and F_3, need to be derived with respect to the unknown variables of the linear system of equations, and those are the stress vector components $\boldsymbol{\sigma}_{n+1}$, the hardening parameter $\tilde{\epsilon}_{n+1}$ and the plastic multiplier λ_{n+1}. With respect to the stress vector components $\boldsymbol{\sigma}_{n+1}$, one has:

$$\frac{\partial F_1^{(k)}}{\partial \boldsymbol{\sigma}_{n+1}^{(k)}} = \frac{\partial f_{n+1}^{(k)}}{\partial \boldsymbol{\sigma}_{n+1}^{(k)}}\ , \tag{A.26a}$$

$$\frac{\partial F_2^{(k)}}{\partial \boldsymbol{\sigma}_{n+1}^{(k)}} = \boldsymbol{D}^{-1} + \Delta\lambda_{n+1}^{(k)}\ \frac{\partial^2 f_{n+1}^{(k)}}{\partial\left(\boldsymbol{\sigma}_{n+1}^{(k)}\right)^2}\ , \tag{A.26b}$$

$$\frac{\partial F_3^{(k)}}{\partial \boldsymbol{\sigma}_{n+1}^{(k)}} = -\Delta\lambda_{n+1}^{(k)}\ \frac{\partial^2 f_{n+1}^{(k)}}{\partial \tilde{\sigma}_{n+1}^{(k)} \partial \boldsymbol{\sigma}_{n+1}^{(k)}}\ , \tag{A.26c}$$

with respect to the hardening parameter $\tilde{\epsilon}_{n+1}$, one obtains:

$$\frac{\partial F_1^{(k)}}{\partial \tilde{\epsilon}_{n+1}^{(k)}} = \frac{\partial f_{n+1}^{(k)}}{\partial \tilde{\sigma}_{n+1}^{(k)}} \, \frac{\partial \tilde{\sigma}_{n+1}^{(k)}}{\partial \tilde{\epsilon}_{n+1}^{(k)}} \ , \tag{A.27a}$$

$$\frac{\partial F_2^{(k)}}{\partial \tilde{\epsilon}_{n+1}^{(k)}} = \Delta\lambda_{n+1}^{(k)} \, \frac{\partial^2 f_{n+1}^{(k)}}{\partial \boldsymbol{\sigma}_{n+1}^{(k)} \, \partial \tilde{\sigma}_{n+1}^{(k)}} \, \frac{\partial \tilde{\sigma}_{n+1}^{(k)}}{\partial \tilde{\epsilon}_{n+1}^{(k)}} \ , \tag{A.27b}$$

$$\frac{\partial F_3^{(k)}}{\partial \tilde{\epsilon}_{n+1}^{(k)}} = -1 - \Delta\lambda_{n+1}^{(k)} \, \frac{\partial^2 f_{n+1}^{(k)}}{\partial \left(\tilde{\sigma}_{n+1}^{(k)}\right)^2} \, \frac{\partial \tilde{\sigma}_{n+1}^{(k)}}{\partial \tilde{\epsilon}_{n+1}^{(k)}} \ , \tag{A.27c}$$

and with respect to the plastic multiplier λ_{n+1}, the result is:

$$\frac{\partial F_1^{(k)}}{\partial \lambda_{n+1}^{(k)}} = 0 \ , \tag{A.28a}$$

$$\frac{\partial F_2^{(k)}}{\partial \lambda_{n+1}^{(k)}} = \frac{\partial f_{n+1}^{(k)}}{\partial \boldsymbol{\sigma}_{n+1}^{(k)}} \ , \tag{A.28b}$$

$$\frac{\partial F_3^{(k)}}{\partial \lambda_{n+1}^{(k)}} = -\frac{\partial f_{n+1}^{(k)}}{\partial \tilde{\sigma}_{n+1}^{(k)}} \ . \tag{A.28c}$$

Of interest is the fact that, when comparing the system of linearized equations (5.89) obtained from the equations of the residues $r_{f,\ n+1}^{(k)}, r_{\boldsymbol{\epsilon},\ n+1}^{(k)}$ and $r_{\tilde{\epsilon},\ n+1}^{(k)}$ (5.63), and the system of linear equations (5.62) obtained when using the Jacobian, in the former they are obtained differentiating with respect to the stress vector components $\boldsymbol{\sigma}_{n+1}$, the hardening function $\tilde{\sigma}_{n+1}$ and the plastic multiplier λ_{n+1}, as in the latter they are obtained deriving in order to the stress vector components $\boldsymbol{\sigma}_{n+1}$, the hardening parameter $\tilde{\epsilon}_{n+1}$ and the plastic multiplier λ_{n+1}. It is, however, straightforward to observe that they lead to the same result, by the following:

$$\tilde{\sigma} = \tilde{\sigma}(\tilde{\epsilon}) \tag{A.29}$$

consequently:

$$d\tilde{\sigma} = \frac{\partial \tilde{\sigma}}{\partial \tilde{\epsilon}} \cdot d\tilde{\epsilon} \tag{A.30}$$

By substituting (A.30) in (5.89) a similar system of equations is obtained.

A.1.6.1 Derivatives with respect to the Hardening Parameter $\tilde{\sigma}$

The first order derivative of the Ottosen Yield Function with respect to the Hardening Parameter is given by:

$$\begin{aligned}\frac{\partial f\left(\boldsymbol{\sigma},\ \tilde{\sigma}\right)}{\partial \tilde{\sigma}} &= \frac{\partial}{\partial \tilde{\sigma}}\left[\left[\alpha\ J_2\ +\ \tilde{\sigma}\ \left(\lambda\sqrt{J_2}\ +\ \beta\ I_1\right)\right]^{\frac{1}{2}}\ -\ \tilde{\sigma}\right] \\ &= \frac{1}{2}\left[\alpha\ J_2\ +\ \tilde{\sigma}\ \left(\lambda\sqrt{J_2}\ +\ \beta\ I_1\right)\right]^{-\frac{1}{2}}\cdot\left(\lambda\sqrt{J_2}\ +\ \beta\ I_1\right)\ -\ 1\ .\end{aligned} \tag{A.31}$$

The second order derivative of the Ottosen Yield Function with respect to the Hardening Parameter is obtained by the following:

$$\frac{\partial}{\partial \tilde{\sigma}}\left(\frac{\partial f\left(\boldsymbol{\sigma},\ \tilde{\sigma}\right)}{\partial \tilde{\sigma}}\right) = \left(-\frac{1}{4}\right)\cdot\left[\alpha\ J_2\ +\ \tilde{\sigma}\ \left(\lambda\sqrt{J_2}\ +\ \beta\ I_1\right)\right]^{-\frac{3}{2}}\cdot\left(\lambda\sqrt{J_2}\ +\ \beta\ I_1\right)^2 . \tag{A.32}$$

The second order derivative of the Ottosen Yield Function (A.31) with respect to the Hardening Parameter may be obtained as follows:

$$\frac{\partial}{\partial \tilde{\sigma}}\left(\frac{\partial f\left(\boldsymbol{\sigma},\ \tilde{\sigma}\right)}{\partial \sigma_i}\right) = \frac{\partial}{\partial \tilde{\sigma}}\left[\frac{1}{2}\ \frac{\overbrace{\alpha\ \frac{\partial J_2}{\partial \sigma_i}\ +\ \tilde{\sigma}\ \left(\frac{\partial \lambda}{\partial \sigma_i}\sqrt{J_2}\ +\ \frac{1}{2}\lambda\ J_2^{-\frac{1}{2}}\frac{\partial J_2}{\partial \sigma_i}\ +\ \beta\ \frac{\partial I_1}{\partial \sigma_i}\right)}^{\text{function g}}}{\underbrace{\sqrt{\alpha\ J_2\ +\ \tilde{\sigma}\ \left(\lambda\sqrt{J_2}\ +\ \beta\ I_1\right)}}_{\text{function h}}}\right] , \tag{A.33}$$

with:

$$\frac{\partial f\left(\boldsymbol{\sigma},\ \tilde{\sigma}\right)}{\partial \sigma_i} = \frac{1}{2}\ \frac{\mathrm{g}\left(\boldsymbol{\sigma},\ \tilde{\sigma}\right)}{\mathrm{h}\left(\boldsymbol{\sigma},\ \tilde{\sigma}\right)}\ . \tag{A.34}$$

Making use of the chain rule, one obtains:

$$\frac{\partial}{\partial \tilde{\sigma}}\left(\frac{\partial f\left(\boldsymbol{\sigma},\ \tilde{\sigma}\right)}{\partial \sigma_i}\right) = \frac{1}{2}\ \frac{\frac{\partial \mathrm{g}\left(\boldsymbol{\sigma},\ \tilde{\sigma}\right)}{\partial \tilde{\sigma}}\ \mathrm{h}\left(\boldsymbol{\sigma},\ \tilde{\sigma}\right) - \mathrm{g}\left(\boldsymbol{\sigma},\ \tilde{\sigma}\right)\ \frac{\partial \mathrm{h}\left(\boldsymbol{\sigma},\ \tilde{\sigma}\right)}{\partial \tilde{\sigma}}}{\mathrm{h}^2\left(\boldsymbol{\sigma},\ \tilde{\sigma}\right)}\ , \tag{A.35}$$

with:

$$\frac{\partial \mathrm{g}\left(\boldsymbol{\sigma},\ \tilde{\sigma}\right)}{\partial \tilde{\sigma}} = \frac{\partial \lambda}{\partial \sigma_i}\sqrt{J_2} \ + \ \frac{1}{2}\ \lambda\ J_2^{-\frac{1}{2}}\ \frac{\partial J_2}{\partial \sigma_i} + \beta\ \frac{\partial I_1}{\partial \sigma_i}\ , \tag{A.36}$$

and:

$$\frac{\partial \mathrm{h}\left(\boldsymbol{\sigma},\ \tilde{\sigma}\right)}{\partial \tilde{\sigma}} = \frac{1}{2}\left[\alpha\ J_2\ +\ \tilde{\sigma}\ \left(\lambda\sqrt{J_2}\ +\ \beta\ I_1\right)\right]^{-\frac{1}{2}} \cdot\ \left(\lambda\sqrt{J_2}\ +\ \beta I_1\right)\ . \tag{A.37}$$

Finally, the first order derivative, with respect to the stress vector components, of the first order derivative of the Ottosen Yield Function with respect to the Hardening Parameter is described by the following equation:

$$\frac{\partial}{\partial \sigma_i}\left(\frac{\partial f\left(\boldsymbol{\sigma},\ \tilde{\sigma}\right)}{\partial \tilde{\sigma}}\right) = \frac{\partial}{\partial \sigma_i}\left(\underbrace{\frac{1}{2}\left[\alpha\ J_2\ +\ \tilde{\sigma}\ \left(\lambda\sqrt{J_2}\ +\ \beta\ I_1\right)\right]^{-\frac{1}{2}}}_{\text{function g}} \cdot \underbrace{\left(\lambda\sqrt{J_2}\ +\ \beta\ I_1\right)}_{\text{function h}}\right)\ , \tag{A.38}$$

with:

$$\frac{\partial f\left(\boldsymbol{\sigma},\ \tilde{\sigma}\right)}{\partial \tilde{\sigma}} = \mathrm{g}\left(\boldsymbol{\sigma},\ \tilde{\sigma}\right)\cdot \mathrm{h}\left(\boldsymbol{\sigma},\ \tilde{\sigma}\right)\ . \tag{A.39}$$

After some algebraic operations, one obtains:

$$\frac{\partial}{\partial \sigma_i}\left(\frac{\partial f\left(\boldsymbol{\sigma},\ \tilde{\sigma}\right)}{\partial \tilde{\sigma}}\right) = \frac{\partial \mathrm{g}\left(\boldsymbol{\sigma},\ \tilde{\sigma}\right)}{\partial \sigma_i}\ \mathrm{h}\left(\boldsymbol{\sigma},\ \tilde{\sigma}\right) + \mathrm{g}\left(\boldsymbol{\sigma},\ \tilde{\sigma}\right)\ \frac{\partial \mathrm{h}\left(\boldsymbol{\sigma},\ \tilde{\sigma}\right)}{\partial \sigma_i}\ , \tag{A.40}$$

with:

$$\begin{aligned} \frac{\partial \mathrm{g}\left(\boldsymbol{\sigma},\ \tilde{\sigma}\right)}{\partial \sigma_i} = & -\frac{1}{4}\left[\alpha\ J_2\ +\ \tilde{\sigma}\ \left(\lambda\sqrt{J_2}\ +\ \beta\ I_1\right)\right]^{-\frac{3}{2}} \cdot \left[\alpha\ \frac{\partial J_2}{\partial \sigma_i} + \right. \\ & \left. +\ \tilde{\sigma}\ \left(\frac{\partial \lambda}{\partial \sigma_i}\sqrt{J_2}\ +\ \frac{1}{2}\ \lambda\ J_2^{-\frac{1}{2}}\ \frac{\partial J_2}{\partial \sigma_i} + \beta\ \frac{\partial I_1}{\partial \sigma_i}\right)\right]\ , \end{aligned} \tag{A.41}$$

and:

$$\frac{\partial \mathrm{h}\left(\boldsymbol{\sigma},\ \tilde{\sigma}\right)}{\partial \sigma_i} = \frac{\partial \lambda}{\partial \sigma_i}\sqrt{J_2}\ + \lambda\ J_2^{-\frac{1}{2}}\ \frac{1}{2}\frac{\partial J_2}{\partial \sigma_i} + \beta\ \frac{\partial I_1}{\partial \sigma_i}\ , \tag{A.42}$$

A few simple algebraic operations allow to demonstrate that $\frac{\partial}{\partial\tilde{\sigma}}\left(\frac{\partial \mathrm{f}(\boldsymbol{\sigma},\,\tilde{\sigma})}{\partial\boldsymbol{\sigma}}\right) = \frac{\partial}{\partial\boldsymbol{\sigma}}\left(\frac{\partial \mathrm{f}(\boldsymbol{\sigma},\,\tilde{\sigma})}{\partial\tilde{\sigma}}\right)$.

A.2 The Consistent Tangent Elasto-plastic Constitutive Matrix

For the integration of the FEM equilibrium equations within the Newton-Raphson incremental-iterative algorithm, it is desirable to obtain and use the consistent tangent constitutive matrix. This procedure contributes to the faster convergence to the equilibrium solution, and approximates better the trial stress when plastic flow is occurring. The derivation of the tangent constitutive matrix is based on the following equations: the yield function, as a function of the stress vector and the hardening parameter,

$$f_{n+1} = f_{n+1}(\boldsymbol{\sigma}, \tilde{\sigma}) \ , \tag{A.43}$$

the constitutive equation, in the incremental form:

$$\Delta\boldsymbol{\sigma}_{n+1} = \boldsymbol{D} \cdot \left(\Delta\boldsymbol{\epsilon}_{n+1} - \Delta\boldsymbol{\epsilon}^{p}_{n+1}\right) \ , \tag{A.44}$$

the flow rule:

$$\Delta\boldsymbol{\epsilon}^{p}_{n+1} = \Delta\lambda_{n+1}\,\frac{\partial f_{n+1}}{\partial\boldsymbol{\sigma}_{n+1}} \tag{A.45}$$

and the hardening law:

$$\Delta\tilde{\epsilon}_{n+1} = -\Delta\lambda_{n+1}\,\frac{\partial f_{n+1}}{\partial\tilde{\sigma}_{n+1}} \ . \tag{A.46}$$

The derivation of the consistent tangent matrix for the general return-mapping algorithm requires the determination of the total differentials df_{n+1}, $d\boldsymbol{\sigma}_{n+1}$, $d\boldsymbol{\epsilon}_{n+1}$, and $d\tilde{\epsilon}_{n+1}$. As such, for the yield function one obtains:

$$df_{n+1} = \frac{\partial f_{n+1}}{\partial \boldsymbol{\sigma}_{n+1}} \cdot d\boldsymbol{\sigma}_{n+1} + \frac{\partial f_{n+1}}{\partial \tilde{\sigma}_{n+1}} \cdot d\tilde{\sigma}_{n+1} \ , \tag{A.47}$$

and for the constitutive equation:

$$d\boldsymbol{\sigma}_{n+1} = \boldsymbol{D} \cdot \left(d\boldsymbol{\epsilon}_{n+1} - d\boldsymbol{\epsilon}^{p}_{n+1} \right) \ , \tag{A.48}$$

for the flow rule:

$$d\boldsymbol{\epsilon}^{p}_{n+1} = d\lambda_{n+1} \ \frac{\partial f_{n+1}}{\partial \boldsymbol{\sigma}_{n+1}} + \Delta\lambda_{n+1} \left(\frac{\partial^2 f_{n+1}}{\partial \boldsymbol{\sigma}^2_{n+1}} \cdot d\boldsymbol{\sigma}_{n+1} + \frac{\partial^2 f_{n+1}}{\partial \boldsymbol{\sigma}_{n+1} \partial \tilde{\sigma}_{n+1}} \cdot d\tilde{\sigma}_{n+1} \right) \ , \tag{A.49}$$

and for the hardening law:

$$d\tilde{\epsilon}_{n+1} = d\lambda_{n+1} \ \frac{\partial f_{n+1}}{\partial \tilde{\sigma}_{n+1}} + \Delta\lambda_{n+1} \left(\frac{\partial^2 f_{n+1}}{\partial \tilde{\sigma}^2_{n+1}} \cdot d\tilde{\sigma}_{n+1} + \frac{\partial^2 f_{n+1}}{\partial \tilde{\sigma}_{n+1} \partial \boldsymbol{\sigma}_{n+1}} \cdot d\boldsymbol{\sigma}_{n+1} \right) \ . \tag{A.50}$$

All $n + 1$ values correspond to the converged values at the end of the Newton-Raphson iterative procedure, carried out to determine the equilibrium solution of the load step $n + 1$, for each integration point.

Substituting (A.49) in (A.48), after some algebraic operations, one obtains:

$$d\boldsymbol{\sigma}_{n+1} = \boldsymbol{H} \ \cdot \left(d\boldsymbol{\epsilon}_{n+1} - d\lambda_{n+1} \ \frac{\partial f_{n+1}}{\partial \boldsymbol{\sigma}_{n+1}} - \Delta\lambda_{n+1} \frac{\partial^2 f_{n+1}}{\partial \boldsymbol{\sigma}_{n+1} \partial \tilde{\sigma}_{n+1}} \ d\tilde{\sigma}_{n+1} \right) \ , \tag{A.51}$$

where $\boldsymbol{H} = \left(\boldsymbol{D}^{-1} + \Delta\lambda_{n+1} \frac{\partial^2 f_{n+1}}{\partial \boldsymbol{\sigma}^2_{n+1}} \right)^{-1}$ represents the elasto-plastic constitutive tensor. Substituting the expression (A.51) in (A.47) and reminding that while plastic deformation is occuring, for a specific converged solution of a load step $df_{n+1} = 0$, then one obtains:

$$\begin{aligned} \frac{\partial f_{n+1}}{\partial \boldsymbol{\sigma}_{n+1}} \ \cdot \ \boldsymbol{H} \ \cdot \ d\boldsymbol{\epsilon}_{n+1} \ &= d\lambda_{n+1} \ \frac{\partial f_{n+1}}{\partial \boldsymbol{\sigma}_{n+1}} \ \cdot \ \boldsymbol{H} \ \cdot \ \frac{\partial f_{n+1}}{\partial \boldsymbol{\sigma}_{n+1}} + \\ &+ \left(\Delta\lambda_{n+1} \ \frac{\partial f_{n+1}}{\partial \boldsymbol{\sigma}_{n+1}} \ \cdot \ \boldsymbol{H} \ \cdot \ \frac{\partial^2 f_{n+1}}{\partial \boldsymbol{\sigma}_{n+1} \partial \tilde{\sigma}_{n+1}} \ - \ \frac{\partial f_{n+1}}{\partial \tilde{\sigma}_{n+1}} \right) \ d\tilde{\sigma}_{n+1} \ . \end{aligned} \tag{A.52}$$

Substituting equation (A.51) into equation (A.50), and using the relation $d\tilde{\sigma} = h \ d\tilde{\epsilon}$, after some simplifications one obtains:

$$\begin{aligned}&\left(-\frac{\partial f_{n+1}}{\partial \tilde{\sigma}_{n+1}} + \Delta\lambda_{n+1} \, \frac{\partial^2 f_{n+1}}{\partial \tilde{\sigma}_{n+1} \partial \boldsymbol{\sigma}_{n+1}} \cdot \boldsymbol{H} \cdot \frac{\partial f_{n+1}}{\partial \boldsymbol{\sigma}_{n+1}}\right) d\lambda_{n+1} + \left(-h \, \Delta\lambda_{n+1}\right. \\ &\quad \left. \frac{\partial^2 f_{n+1}}{\partial \tilde{\sigma}^2_{n+1}} + h \, \Delta\lambda^2_{n+1} \, \frac{\partial^2 f_{n+1}}{\partial \tilde{\sigma}_{n+1} \partial \boldsymbol{\sigma}_{n+1}} \cdot \boldsymbol{H} \cdot \frac{\partial^2 f_{n+1}}{\partial \boldsymbol{\sigma}_{n+1} \partial \tilde{\sigma}_{n+1}} + 1\right) d\tilde{\epsilon}_{n+1} = \\ &\quad = \Delta\lambda_{n+1} \, \frac{\partial^2 f_{n+1}}{\partial \tilde{\sigma}_{n+1} \partial \boldsymbol{\sigma}_{n+1}} \cdot \boldsymbol{H} \cdot d\boldsymbol{\epsilon}_{n+1} \, .\end{aligned} \tag{A.53}$$

In order to be possible the substitution of equation (A.52) and equation (A.53) into equation (A.51), they both must be described explicitly with respect to $(d\lambda_{n+1})$ and $(\Delta\lambda_{n+1} \; \tilde{\epsilon}_{n+1})$. In this fashion, one obtains, for equation (A.52):

$$\begin{aligned}&\left(\frac{\partial f_{n+1}}{\partial \boldsymbol{\sigma}_{n+1}} \cdot \boldsymbol{H} \cdot \frac{\partial f_{n+1}}{\partial \boldsymbol{\sigma}_{n+1}}\right) d\lambda_{n+1} + \left(h \, \frac{\partial f_{n+1}}{\partial \boldsymbol{\sigma}_{n+1}} \cdot \boldsymbol{H} \cdot \frac{\partial^2 f_{n+1}}{\partial \boldsymbol{\sigma}_{n+1} \partial \tilde{\sigma}_{n+1}} - \right. \\ &\quad \left. - \frac{h}{\Delta\lambda_{n+1}} \frac{\partial f_{n+1}}{\partial \tilde{\sigma}_{n+1}}\right) \Delta\lambda_{n+1} \, d\tilde{\epsilon}_{n+1} = \frac{\partial f_{n+1}}{\partial \boldsymbol{\sigma}_{n+1}} \cdot \boldsymbol{H} \cdot d\boldsymbol{\epsilon}_{n+1} \, ,\end{aligned} \tag{A.54}$$

and for equation (A.53):

$$\begin{aligned}&\left(-\frac{h}{\Delta\lambda_{n+1}} \frac{\partial f_{n+1}}{\partial \tilde{\sigma}_{n+1}} + h \, \frac{\partial^2 f_{n+1}}{\partial \tilde{\sigma}_{n+1} \partial \boldsymbol{\sigma}_{n+1}} \cdot \boldsymbol{H} \cdot \frac{\partial f_{n+1}}{\partial \boldsymbol{\sigma}_{n+1}}\right) d\lambda_{n+1} + \left(\frac{-h^2}{\Delta\lambda_{n+1}} \frac{\partial^2 f_{n+1}}{\partial \tilde{\sigma}^2_{n+1}} + \right. \\ &\quad \left. h^2 \, \frac{\partial^2 f_{n+1}}{\partial \tilde{\sigma}_{n+1} \partial \boldsymbol{\sigma}_{n+1}} \cdot \boldsymbol{H} \cdot \frac{\partial^2 f_{n+1}}{\partial \boldsymbol{\sigma}_{n+1} \partial \tilde{\sigma}_{n+1}} + \frac{h}{\Delta\lambda^2_{n+1}}\right) \Delta\lambda_{n+1} \, d\tilde{\epsilon}_{n+1} = \\ &\quad = h \, \frac{\partial^2 f_{n+1}}{\partial \tilde{\sigma}_{n+1} \partial \boldsymbol{\sigma}_{n+1}} \cdot \boldsymbol{H} \cdot d\boldsymbol{\epsilon}_{n+1} \, .\end{aligned} \tag{A.55}$$

The values of $(d\lambda_{n+1})$ and $(\Delta\lambda_{n+1} \; \tilde{\epsilon}_{n+1})$ may be obtained by solving the system of the two equations (A.54) and (A.55), by the following:

$$\begin{bmatrix} d\lambda_{n+1} \\ \Delta\lambda_{n+1} \; d\tilde{\epsilon}_{n+1} \end{bmatrix} = \begin{bmatrix} A_{11} & A_{12} \\ A_{21} & A_{22} \end{bmatrix}^{-1} \cdot \begin{bmatrix} B_1 \\ B_2 \end{bmatrix} \tag{A.56}$$

with:

$$A_{11} = \frac{\partial f_{n+1}}{\partial \boldsymbol{\sigma}_{n+1}} \cdot \boldsymbol{H} \cdot \frac{\partial f_{n+1}}{\partial \boldsymbol{\sigma}_{n+1}} \, , \tag{A.57}$$

$$A_{12} = h \, \frac{\partial f_{n+1}}{\partial \boldsymbol{\sigma}_{n+1}} \cdot \boldsymbol{H} \cdot \frac{\partial^2 f_{n+1}}{\partial \boldsymbol{\sigma}_{n+1} \partial \tilde{\sigma}_{n+1}} - \frac{h}{\Delta\lambda_{n+1}} \frac{\partial f_{n+1}}{\partial \tilde{\sigma}_{n+1}} \, , \tag{A.58}$$

$$A_{21} = -\frac{h}{\Delta\lambda_{n+1}} \frac{\partial f_{n+1}}{\partial \tilde{\sigma}_{n+1}} \; + \; h \; \frac{\partial^2 f_{n+1}}{\partial \tilde{\sigma}_{n+1} \partial \boldsymbol{\sigma}_{n+1}} \cdot \boldsymbol{H} \cdot \frac{\partial f_{n+1}}{\partial \boldsymbol{\sigma}_{n+1}} \; , \tag{A.59}$$

$$A_{22} = \frac{-h^2}{\Delta\lambda_{n+1}} \frac{\partial^2 f_{n+1}}{\partial \tilde{\sigma}^2_{n+1}} \; + h^2 \; \frac{\partial^2 f_{n+1}}{\partial \tilde{\sigma}_{n+1} \partial \boldsymbol{\sigma}_{n+1}} \cdot \boldsymbol{H} \cdot \frac{\partial^2 f_{n+1}}{\partial \boldsymbol{\sigma}_{n+1} \partial \tilde{\sigma}_{n+1}} + \frac{h}{\Delta\lambda^2_{n+1}} \; , \tag{A.60}$$

$$B_1 = \; \frac{\partial f_{n+1}}{\partial \boldsymbol{\sigma}_{n+1}} \cdot \boldsymbol{H} \cdot d\boldsymbol{\epsilon}_{n+1} \; , \tag{A.61}$$

$$B_2 = \; h \; \frac{\partial^2 f_{n+1}}{\partial \tilde{\sigma}_{n+1} \partial \boldsymbol{\sigma}_{n+1}} \cdot \boldsymbol{H} \cdot d\boldsymbol{\epsilon}_{n+1} \; . \tag{A.62}$$

If now it is assumed that:

$$\begin{bmatrix} A_{11} & A_{12} \\ A_{21} & A_{22} \end{bmatrix}^{-1} = \begin{bmatrix} a_{11} & a_{12} \\ a_{21} & a_{22} \end{bmatrix} \; , \tag{A.63}$$

then, using the matrix inversion algebra to compute the inverse of a second rank matrix, one obtains:

$$a_{11} = \frac{A_{22}}{A_{11} \; A_{22} - A_{12} \; A_{12}} \; , \tag{A.64}$$

$$a_{12} = a_{21} = -\frac{A_{12}}{A_{11} \; A_{22} - A_{12} \; A_{12}} \; , \tag{A.65}$$

$$a_{22} = \frac{A_{11}}{A_{11} \; A_{22} - A_{12} \; A_{12}} \; , \tag{A.66}$$

This may be written in the following format:

$$\begin{bmatrix} B_1 \\ B_2 \end{bmatrix} = \begin{bmatrix} \boldsymbol{b}_1 \\ \boldsymbol{b}_2 \end{bmatrix} \cdot \; d\boldsymbol{\epsilon}_{n+1} \; , \tag{A.67}$$

based on the equations (A.56) and (A.67), one may rewrite the equation (A.51) as follows:

$$d\boldsymbol{\sigma}_{n+1} = \boldsymbol{H} \cdot \left(\boldsymbol{I} - \frac{\partial f_{n+1}}{\partial \boldsymbol{\sigma}_{n+1}} \left(a_{11}\ \boldsymbol{b}_1 + a_{12}\ \boldsymbol{b}_2 \right) - \ h\ \frac{\partial^2 f_{n+1}}{\partial \boldsymbol{\sigma}_{n+1} \partial \tilde{\sigma}_{n+1}} \left(a_{21}\ \boldsymbol{b}_1 + a_{22}\ \boldsymbol{b}_2 \right) \right) \cdot d\boldsymbol{\epsilon}_{n+1}\ , \tag{A.68}$$

or rearranging:

$$\begin{aligned} d\boldsymbol{\sigma}_{n+1} = \Bigg(& \boldsymbol{H}\ -\ a_{11}\ \boldsymbol{H} \cdot \frac{\partial f_{n+1}}{\partial \boldsymbol{\sigma}_{n+1}} \frac{\partial f_{n+1}}{\partial \boldsymbol{\sigma}_{n+1}} \cdot \boldsymbol{H}\ -\ h\ a_{12}\ \boldsymbol{H} \cdot \frac{\partial f_{n+1}}{\partial \boldsymbol{\sigma}_{n+1}} \frac{\partial^2 f_{n+1}}{\partial \tilde{\sigma}_{n+1} \partial \boldsymbol{\sigma}_{n+1}} \cdot \boldsymbol{H}\ - \\ & -\ h\ a_{21}\ \boldsymbol{H} \cdot \frac{\partial^2 f_{n+1}}{\partial \boldsymbol{\sigma}_{n+1} \tilde{\sigma}_{n+1}} \frac{\partial f_{n+1}}{\partial \boldsymbol{\sigma}_{n+1}} \cdot \boldsymbol{H}\ -\ h^2\ a_{22}\ \boldsymbol{H} \cdot \frac{\partial^2 f_{n+1}}{\partial \boldsymbol{\sigma}_{n+1} \partial \tilde{\sigma}_{n+1}} \frac{\partial^2 f_{n+1}}{\partial \tilde{\sigma}_{n+1} \partial \boldsymbol{\sigma}_{n+1}} \cdot \boldsymbol{H} \Bigg)\ . \end{aligned} \tag{A.69}$$

or, in a condensed form:

$$d\boldsymbol{\sigma}_{n+1} = \left(\boldsymbol{H} - \sum_{i=1}^{2} \sum_{i=1}^{2} a_{ij}\ \boldsymbol{c}_i \boldsymbol{c}_j \right) \cdot d\boldsymbol{\epsilon}_{n+1} \tag{A.70}$$

with:

$$\boldsymbol{c}_1 = \boldsymbol{H} \cdot \frac{\partial f_{n+1}}{\partial \boldsymbol{\sigma}_{n+1}}\ \ ;\ \ \boldsymbol{c}_2 =\ h\ \boldsymbol{H} \cdot \frac{\partial^2 f_{n+1}}{\partial \tilde{\sigma}_{n+1} \partial \boldsymbol{\sigma}_{n+1}}\ . \tag{A.71}$$

Lastly, the equation that defined the consistent tangent constitutive matrix is the following:

$$\boldsymbol{D}_{ep} = \boldsymbol{H} - \sum_{i=1}^{2} \sum_{i=1}^{2} a_{ij}\ \boldsymbol{c}_i \boldsymbol{c}_j\ , \tag{A.72}$$

and coincides with the elastic constitutive matrix when the behavior remains elastic, as it can be easily demonstrated by replacing in the previous equations the $\Delta\lambda_{n+1}$ parameter by 0.